ISSN 1983-4195

50 YEARS IBRACON

IBRACON Structures and Materials Journal

Revista IBRACON de Estruturas e Materiais

Volume 15, Number 2
April 2022

ISSN 1983-4195
Volume 15, Number 2

Editorial

The Brazilian Concrete Institute (IBRACON) is celebrating its Jubilee. Fifty years dedicated to developing and spreading knowledge and networking in the concrete industry. The IBRACON Structures and Materials Journal (ISMJ) is a proud part of this journey. Celebrating this moment, in 2022 one of the editors-in-chief along the journal history is invited to write one editorial. I am glad to write in this issue.

In 2007 two separated journals (the Structural Journal, and the Materials Journal) were created, and later merged into the current one-journal version in 2008. In this period 81 issues and 766 documents were published citing 17,217 references. Considering only the SciELO database (ISMJ official repository), an amazing number of 2,549,899 accesses to one of the journal documents is recorded. The five most accessed papers are:

Title	# Of views
Sistema de reforço à punção de lajes lisas de concreto armado com polímeros reforçados com fibra de carbono (PRFC). Vol.07, n.4. Aug, 2014. p.592-625. *Santos, G. S. ; Nicácio, W. G.; Lima, A. W.; Melo, G. S. S. A.*	50713
Proteção catódica de estruturas de concreto. Vol.06, n.2. Apr, 2013. p.178-193 *Araujo, A.; Panossian, Z.; Lourenço, Z.*	48390
Use of Electrochemical Impedance Spectroscopy (EIS) to monitoring the corrosion of reinforced concrete. Vol.08, n.4. Aug, 2015. p.529-546. *Ribeiro, D. V.; Souza, C. A. C.; Abrantes, J. C. C.*	44965
Strength and deformability of hollow concrete blocks: correlation of block and cylindrical sample test results. Vol.02, n.1. Mar, 2009. p.85-99. *Barbosa, C. S.; Hanai, J. B.*	38777
Behavior of reinforced concrete beams reinforced with GFRP bars. Vol.01, n.3. Sep, 2008. p.285-295. *Tavares, D. H.; Giongo, J. S.; Paultre, P.*	37996

Most of the authors are from Brazil, but since the ISMJ changes towards a greater international insertion and choice to publish only in English from 2020, there is an expressive number of authors from all the Americas and Iberia, and an increasing number of authors coming from other parts of Europe, Asia, Africa, and Oceania. The journal is honored to have published authors from all continents, as much as is honored to also have editors from all continents. The figure below illustrates the authors distribution. The full data is available at https://analytics.scielo.org/?journal=1983-4195.

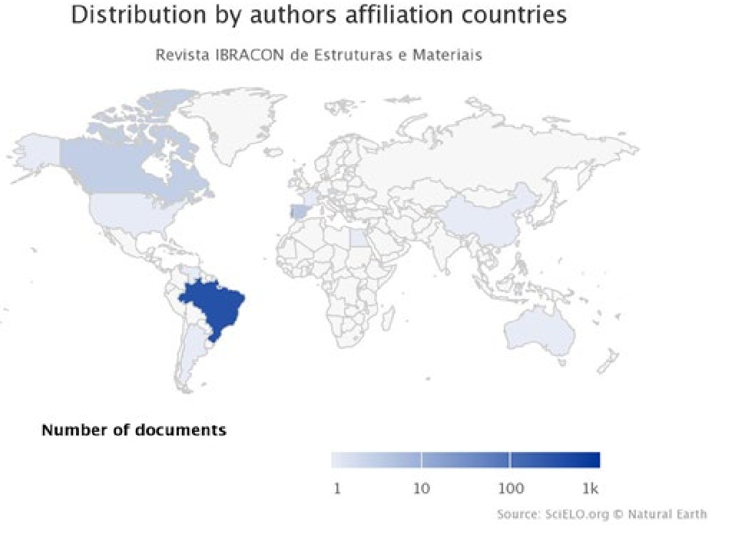

ISMJ is included in the SciELO project to be part of the Scopus database. While we do not have yet the answer from Scopus, we can look at the Google metrics (https://scholar.google.com/citations?user=SiuOxYsAAAAJ&hl=en). Along the years there were 4,288 citations of the journal papers, with 3,330 citations since 2017. The all-time h-index is equal to 23, and the h5-index is equal to 18. Almost 80% of the journal citations are from the last five years, and, even considering we are in the beginning of the year, the journal h5-index is close to its all-time h-index high, reflecting its growing impact.

Considering the year of 2021 some relevant information is:

- Submission to first-decision time = 50 days (papers submitted in 2021)
- Submission to acceptance time = 171 days (papers submitted from 2019 & published in 2021)
- Acceptance to publication time = about 3 weeks.
- Number of papers received in 2021 = 259 papers
- Paper acceptance = 37,7% (papers submitted in 2021 with a decision)

Over years the IBRACON Journal has built a reputation in Latin America as one of the most important scientific publications in Civil Engineering. This recognition is also observed worldwide in recent years.

This month, I would like to welcome our new Associate Editors, thanking them for bringing their excellence, reputation, and dedication to ISJM, Dr. Carmen Andrade (Polytechnic University of Catalonia, Spain), Dr. Pedro Castro Borges (Center for Research and Advanced Studies of the National Polytechnic Institute, Mexico), Dr. Maria Positieri (National Technological University, Argentina).

As part of the 2022 celebration, we are happy to announce that the issue V15N6 (November 2022) will be a Special Edition on Concrete Sustainability. Dr. Edna Possan (Federal University for Latin American Integration, Brazil) and Dr. Mark Alexander (University of Cape Town, South Africa) are the invited Editors-in-Chief for the Special Edition. Please check the Call for Contributions at the journal website: http://ismj.org.

Thank you

Guilherme A. Parsekian
Editor-in-Chief

ISSN 1983-4195
Volume 15, Number 2
April 2022

IBRACON Structures and Materials Journal
Revista IBRACON de Estruturas e Materiais

Contents

Cover: Parametric Tower

Courtesy: Marcela Noronha P. de O. e Sousa

IBRACON

Ibracon Structures and Materials Journal is published bimonthly (February, April, June, August, October, and December) by IBRACON.

IBRACON
Instituto Brasileiro do Concreto Founded in 1972

Av. Queiroz Filho, nº 1700 — sala 407/408
Torre D — Villa Lobos Office Park
CEP 05319-000 — São Paulo, SP — Brazil
Phone: +55 11 3735-0202
Fax: +55 11 3733-2190
E-mail: riem@ibracon.org.br
Website: http://www.ibracon.org.br

Cover design & Layout: Editora Cubo
www.editoracubo.com.br

Aims and Scope

Aims and Scope

The IBRACON Structures and Materials Journal (in Portuguese: Revista IBRACON de Estruturas e Materiais) is a technical and scientific divulgation vehicle of IBRACON (Brazilian Concrete Institute), published every two months. Each issue has 12 to 15 articles and, possibly, a technical note and/or a technical discussion regarding a previously published paper. All contributions are reviewed and approved by professionals with recognized scientific competence in the area. The IBRACON Structures and Materials Journal is an open access Journal, free of charges for authors and readers.

Objectives

The IBRACON Structures and Materials Journal´s main objectives are:

- Present current developments and advances in concrete structures and materials.
- Make possible the better understanding of structural concrete behavior, supplying subsidies for a continuous interaction among researchers, producers, and users.
- Stimulate the development of scientific and technological research in the areas of concrete structures and materials, through papers peer-reviewed by a qualified Editorial Board.
- Promote the interaction among researchers, constructors and users of concrete structures and materials and the development of Civil Construction.
- Provide a vehicle of communication of high technical level for researchers and designers in the areas of concrete structures and materials.

Submission Procedure

The procedure to submit and revise the contributions, as well as the formats, are detailed in the Journal Website (ismj.org).

The papers and the technical notes are revised by at least two reviewers indicated by the editors. Discussions and replies are accepted for publication after a review by the editors and at least one member of the Editorial Board. In case of disagreement between the reviewer and the authors, the contribution will be sent to a specialist in the area, not necessarily linked to the Editorial Board. Conflict of interests is carefully handled by the Editors.

Contribution Types

The Journal will publish original papers, short technical notes, and paper discussions. Original papers will be accepted if they are in accordance with the objectives of the Journal and present quality of information and presentation. A technical note is a brief manuscript. It may present a new feature of research, development, or technological application in the areas of Concrete Structures and Materials, and Civil Construction. This is an opportunity to be used by industries, companies, universities, institutions of research, researchers, and professionals willing to promote their works and products under development.

A discussion is received no later than 3 months after the publication of the paper or technical note. The discussion must be limited to the topic addressed in the published paper and must not be offensive. The right of reply is granted to the Authors. The discussions and the replies are published in the subsequent issues of the Journal.

The submission file should be in accordance with the paper template available at the Journal Website. It is recommended that the length of the papers does not exceed 25 pages. Where available, URLs for the references should be provided.

The IBRACON Structures and Materials Journal will conduct the review process for manuscripts submitted in English. Titles, abstracts, and keywords are presented in English, and in Portuguese or Spanish. Articles and technical notes are peer-reviewed and only published after approval of the reviewers and the Editorial Board.

Once accepted, an article is typeset according to the journal layout. The author will be required to review and approve the galleys before publishing. At this stage only typesetting errors will be considered.

Internet Access

The IBRACON Structures and Materials Journal Webpage is available at http://ismj.org.

Sponsors

The funds for the maintenance of the Journal are currently obtained from the IBRACON. The Journal is not supposed to be maintained with funds from private sponsorship, which could diminish the credit of the publications.

Photocopying

Photocopying in Brazil. Brazilian Copyright Law is applicable to users in Brazil. IBRACON holds the copyright of contributions in the journal unless stated otherwise at the bottom of the first page of any contribution. Where IBRACON holds the copyright, authorization to photocopy items for internal or personal use, or the internal or personal use of specific clients, is granted for libraries and other users registered at IBRACON.

Copyright

IBRACON

Av. Queiroz Filho, 1700 – sala 407/408 – Torre D
Villa Lobos Office Park
05319-000 – Vila Hamburguesa
São Paulo – SP
Phone: +55 (11) 3735-0202
E-mail: riem@ibracon.org.br

Disclaimer

Papers and other contributions and the statements made, or opinions expressed therein are published on the understanding that the authors of the contribution are the only responsible for the opinions expressed in them and that their publication does not necessarily reflect the views of IBRACON or of the Journal Editorial Board.

Editorial Board

Direction

Rev. IBRACON Estrut. Mater., vol. 15, no. 2, e15201, 2022

IBRACON Structures and Materials Journal
Revista IBRACON de Estruturas e Materiais
ISSN 1983-4195 ismj.org

ORIGINAL ARTICLE

Eco-efficient steel slag concretes: an alternative to achieve circular economy

Concretos ecoeficientes de escória de aciaria: uma alternativa para alcançar a econômica circular

Laís Cristina Barbosa Costa[a]
Marcela Aguiar Nogueira[a]
Larissa Caroline Ferreira[a]
Fernanda Pereira da Fonseca Elói[a]
José Maria Franco de Carvalho[b]
Ricardo André Fiorotti Peixoto[a]

[a]Universidade Federal de Ouro Preto – UFOP, Laboratório de Materiais de Construção Civil, Ouro Preto, MG, Brasil
[b]Universidade Federal de Viçosa – UFV, Laboratório de Materiais Compósitos, Viçosa, MG, Brasil

Received 01 April 2021
Accepted 19 July 2021

Abstract: Annually billions of tonnes of aggregates are extracted to apply in civil construction generating environmental impacts and energy consumption. So, based on circular economy principles applying residues as aggregates is a good solution to reduce the mining activity and to generate a more efficient destination for the residues. Thus, this research aims to evaluate the technical, economic, and environmental performance of concretes produced entirely with steel slag aggregates. The concretes were characterized through physical properties, as specific gravity, water absorption, compressive and tensile strength. Durability tests (expansibility) were also conducted. The authors analyzed the cost assessment and environmental impact of steel slag concrete production as well. The incorporation of steel slag increases the compressive and tensile strength of concrete, analyzed in different ages. Additionally, the steel slag does not present expansibility when confined in the concrete matrix. The entire replacement of natural aggregates for steel slag allowed to reduce in 31% the cement consumption, a decrease of 140 kg/m^3, for the same strength class. The environmental analysis showed that the incorporation of steel slag aggregates reduced the cement intensity of concrete and its impact. Regarding the cost assessment, the mixtures with steel slag presented a lower cost compared to the conventional one. These results indicate that steel slag aggregates could be used in a cleaner production of concrete, replacing natural aggregates with no injury. This research provides the feasibility of using steel slag aggregates in a cleaner and cheaper concrete production and contribute to the promotion of sustainable solutions for the construction sector through the circular economy principles.

Keywords: steel slag aggregate, compressive strength, cement intensity; circular economy.

Resumo: Anualmente bilhões de toneladas de agregados são extraídos para aplicação na construção civil, resultando em impactos ambientais e significativo consumo de energia. Assim, baseando-se nos princípios da economia circular, aplicar resíduos como agregados para construção civil é uma boa alternativa para reduzir a extração de recursos naturais e gerar uma destinação mais eficiente para os resíduos. Assim, essa pesquisa objetiva analisar o desempenho técnico, econômico e ambiental de concretos produzidos inteiramente com agregado de escória de aciaria. Os concretos foram caracterizados quanto suas propriedades físicas, como massa específica, absorção de água e resistência à compressão e tração. Ensaios de durabilidade (expansão) também foram realizados. Também foram analisados os custos do concreto de escória de aciaria e o seu impacto ambiental, através da intensidade de ligantes. Os concretos foram avaliados mecanicamente em diferentes idades, sendo observado que a incorporação de escória de aciaria aumenta a resistência à compressão e tração das matrizes. Além disso, em ensaios acelerados, a escória de aciaria não apresentou expansibilidade. A substituição total dos agregados naturais por escória de aciaria permitiu reduzir em 31% o consumo de concreto e cimento, o que representa um decréscimo de 140 kg/m^3 para a mesma classe de

Corresponding author: Laís Cristina Barbosa Costa. E-mail: lais.cristina.costa@gmail.com
Financial support: National Council for Scientific and Technological Development (CNPq, grant number 140896/2019-8).
Conflict of interest: Nothing to declare.

resistência. Foi observado também que a incorporação de escória de aciaria reduz a intensidade de cimento das misturas e que essas possuem menor custo de produção comparado ao convencional. Esses resultados indicam que os agregados de escória de aciaria podem ser utilizados substituindo os agregados naturais sem causar danos. Este trabalho avalia a viabilidade de usar agregados de escória de aciaria na produção mais limpa de concretos, podendo contribuir para a promoção de soluções sustentáveis para o setor da construção através dos princípios da economia circular.

Palavras-chave: agregado de escória de aciaria, resistência à compressão, intensidade de ligantes, economia circular.

How to cite: L. C. B. Costa, M. A. Nogueira, L. C. Ferreira, F. P. F. Elói, J. M. F. Carvalho, and R. A. F. Peixoto, "Eco-efficient steel slag concretes: an alternative to achieve circular economy," *Rev. IBRACON Estrut. Mater.*, vol. 15, no. 2, e15201, 2022, https://doi.org/10.1590/S1983-41952022000200001

1 INTRODUCTION

Gonçalves et al. [1] reported the economic feasibility of a steel slag processing plant to produce fine and coarse aggregates for civil construction. The viability of this processing plant is mostly related to the steel slag low cost of purchasing and the availability of the metallic material in steel slag (around 30 wt.%) that can be sold. The utilization of steel slag as aggregate follows the circular economy practices aiding to reduce the environmental impact of all industry related in the processes, stimulating innovation, and optimizing the resource supplies. Due to the circular economy, the metallic material recovered returns to the productive chain, and the construction sector reduces its demand for raw materials. Also, historically the communities grow around industries, so the use of steel slag as aggregates could contribute for the local economy to strengthen, job creation and generation of new sustainable businesses.

Additionally, the incorporation of steel slag and other recycled aggregates assists in the reduction of the effects of natural aggregates extraction. The various types of coarse aggregates come from activities with significant water consumption, and affects the landscape and the existing biota [2]. The mining of river sand, used as fine aggregate, causes contamination of the water, increases turbidity, changes the geometry of the riverbed (including the flow) and damages flora and fauna [3].

Besides all these damages related to the mining of natural aggregates, it is important to highlight that the same river basin used for the sand extraction is demanded to supply the population with potable water, among other activities as agriculture and industry. Usually, the rivers cross cities and the sand extraction occurs near the urban centers, thus the consequences of this activity are close to the population with direct impact such as floods, visual and water pollution.

In Brazil, the Paraiba do Sul river has its sources in São Paulo passing through Minas Gerais and ending in Rio de Janeiro, states with a high rate of urbanization and participation in national GDP [4], [5]. This river basin provides water for 8.7 million people only in the metropolitan region of Rio de Janeiro [6], although the Paraiba do Sul river is the major reserve of sand in São Paulo state. Considering this environmental issue, the search for alternative solutions to replace the natural aggregates has raised, although some recycled aggregates possibilities are not easily available or drop with some concrete properties failing in the technical or economic analysis.

In 2017 the global production of steel generated around 1 billion tonnes of byproducts and residues, with 28% as steel slag [7]. The incorporation of steel slag as fine aggregate has potential to reduce the river sand extraction. Currently, around 28% of all existing mines in Brazil produce river sand [8].

The incorporation of steel slag as coarse and fine aggregate enhances the mechanical properties of concretes allowing increases of 20-40% in compressive strength compared to conventional concretes [9]–[15]. The higher hardness and better surface properties of steel slag particles promote this strength gain [16]–[20]. Some authors reported increases of about 40% in the compressive strength of conventional strength concretes (f_{ck}<40 MPa) produced with total replacement of the conventional coarse aggregate and partial substitution of the fine aggregate (0-55%) with steel slag [9], [10], [21]–[23]. Additionally, many researchers evaluated the steel slag incorporation in precast elements such as structural masonry blocks [24], pavers [14], and its use as soil stabilizer [25]. Despite all available information, site-cast concretes produced with full replacement of natural aggregates by steel slag aggregates (coarse and fine) are still rare, but some spare results indicated the viability of eco-efficient concretes with steel slag aggregates [26].

However, the few existing papers related to steel slag concretes ignore environmental and economic parameters, focusing only on the technical feasibility. Answering the demand to incorporate circular economy concepts in the construction sector, the authors evaluate the technical, economic, and environmental performance of concretes produced with full replacement of natural aggregates by steel slag aggregates (coarse and fine fraction). These analyses had a fundamental relevance for the real applicability of this residue that contributes to cleaner production in the construction and steel industry.

2 METHODOLOGY

2.1 Materials

For the production of the concretes, the chosen Portland cement was the Brazilian type CP IV – RS, called Portland-pozzolanic cement (PPC) due to partial substitution of clinker (15-50%) by pozzolanic material [27]. This blended cement already has a reduced environmental impact, contributing to the production of a cleaner concrete. The specific gravity of the cement CP IV is 3.01 g/cm^3, and the chemical composition is indicated in Table 1.

Table 1. Chemical composition of Portland cement CP IV

SiO_2	Al_2O_3	CaO	SO_3	MgO	K_2O	Fe_2O_3	TiO_2	MnO	Other
19.2%	5.5%	64.5%	4.3%	0.8%	0.9%	3.6%	0.3%	0.4%	0.5%

The conventional coarse and fine aggregates used in the production of the reference concretes were, respectively, gneiss gravel (4.8-12.5 mm) and quartz river sand (0-4.8mm). A basic oxygen furnace steel industry located in João Monlevade provided the steel slag in particle sizes of 0-4.8 mm and 4.8-12.5 mm, used as aggregates in the steel slag concrete.

This steel slag was subjected to a magnetic separation process to reduce its metallic iron content. To reduce the expansive oxides present in steel slag, Diniz et al. [25], Adegoloye et al. [28] and Pellegrino and Gaddo [21] verified the efficiency of the weathering process for periods superior to six months. The steel slag available for this research was subjected to four years of weathering through wet-dry cycles in a stockyard. Later in the experimental program, the stability of the steel slag applied in this research will be evaluated through macro and micro analysis. The appropriated treatment of steel slag is mandatory to allow its utilization without any future damage to the structures [29].

The particle size distribution of the reference and of steel slag aggregates (as received) differ. The particle size distribution of an aggregate is an important factor for the concrete properties. This affects the cement consumption, workability, mechanical performance, and many other properties [30], [31]. Therefore, this physical difference difficult the analysis of the technical, environmental and economic impact caused by the application of steel slag as aggregates in concrete. To physically adequate the aggregates, they had their particle size distributions equalized through sieving. The granulometry was chosen seeking for the minimum adjustment in both aggregates following the specifications of the standard NBR 7211 [32]. Figure 1 presents the particle size distribution used for the reference aggregate and for the steel slag aggregate (coarse and fine fraction).

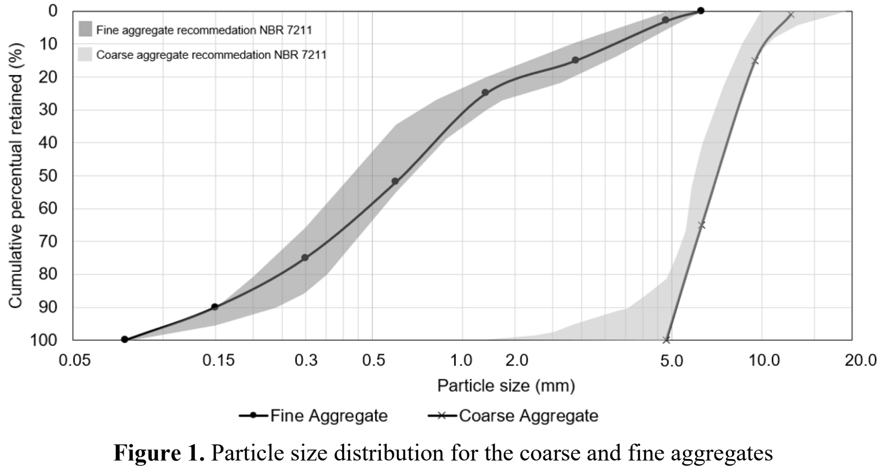

Figure 1. Particle size distribution for the coarse and fine aggregates

The complete physical characterization of the aggregates is shown in Table 2. The procedures were performed following the respective standard. The high specific gravity and bulk density of steel slag aggregates are due to their chemical composition, rich in metallic oxides as CaO, SiO_2 e Fe_2O_3 [14].

Table 2. Physical characterization of steel slag and reference aggregates

	Fine Aggregates		Coarse Aggregates		Procedure Standard
	Steel slag	Reference	Steel slag	Reference	
Specific gravity (g/cm^3)	3.74	2.68	3.58	2.61	NBR 9776 [33]/ NBR NM 53 [34]
Bulk density (g/cm^3)	2.22	1.63	1.77	1.44	NBR NM 45 [35]
Material finer than 75µm (%)	8.06	6.26	1.93	0.81	NBR NM 46 [36]
Crushing strength (%)	-		89.41.	82.90	NBR 9938 [37]
Shape Index	-		1.47	1.81	NBR 7809 [38]

Tap water from the public system of Ouro Preto (Brazil) was used in concrete production. A superplasticizer based in ether polycarboxylate was used to aid in the plasticity of the concretes and to reduce the water content.

2.2 Microstructural analysis of the steel slag stability

To verify the stability of the steel slag used in this experimental program, its chemical, mineralogical and thermal characterization was performed. For these procedures, a sample of steel slag was grounded in a ball mill (200 rpm, 180 minutes) and latter in a planetary ball mill (400 rpm, 15 minutes) until the material passed through the 45µm sieve. Additionally, this sample has a D50 below 10 µm that ensures the accuracy of these analyses [39].

The chemical characterization proceeded through x-ray fluorescence (PANalytical Epsilon3x) analyses. The mineralogical characterization was done by x-ray diffraction (Bruker D2 Phaser) with the setup: CuKα radiation, 40kV, 30mA, step size of 0.01° and 1 second per step, in a 2θ range of 5-70°. The software PANalytical X'pert HighScore Plus V3.0 was used for mineral phase identification and quantification based in Rietveld refinement with ICDD PDF4+database. 10 wt.% of Fluorite (analytical grade, 99% of purity) was used as an internal standard. The thermogravimetric and differential thermal analysis were evaluated simultaneously (TG/DTA - Shimadzu DTG-60H) using an atmosphere of inert N2 in a range from 25-1000°C with a heating rate of 10°C/min.

2.3 Mix proportions and technical characterization of the concretes

Physically identical concretes were designed by setting equally the design parameters. No specific strength classes were targeted, but instead, a small and a high cement content (310 kg/m^3 and 450 kg/m^3) were fixed, with the respective water/cement ratio of 0.62 and 0.44. The mix design procedure selected was the Brazilian widely used methodology IPT/EPUSP [40], with a mortar content of 59% set for all concretes. In the mix design, the specific gravity was considered to ensure the equivalent volume of aggregates in both conventional and steel slag concretes.

Concretes with similar workability allow the same applicability. Because of that, the concrete had a fixed slump. The slump test was realized according to the Brazilian standard NBR NM 67 [41]. The slump value adopted was 70 ± 10mm for the concretes with a cement consumption of 310kg/m^3 and 90 ± 10mm for those with 450kg/m^3 cement consumption.

Table 3 lists the concrete compositions and their respective slump test results. The code that identifies the produced concretes are REF for reference aggregates and BOFS for the basic oxygen furnace steel slag concretes.

Table 3. Mix Design of the steel slag and reference concretes produced

Code	Cement (kg/m^3)	Fine Aggregate (kg/m^3)	Coarse Aggregate (kg/m^3)	Water (kg/m^3)	Superplasticizer (%)	Slump (mm)
REF-310	310	936.65	866.31	190.65	0.40	70
BOFS-310	310	1376.40	1171.86	190.65	0.25	70
REF-450	450	818.00	881.36	198.00	0.58	80
BOFS-450	450	1224.77	1163.83	198.00	0.35	100

The superplasticizer dosage was empirical to achieve the required workability. Although, the saturation point of this chemical admixture combined with the cement type used was evaluated through a viscosity test proposed by

Carvalho et al. [26], based on Aïtcin [22]. The saturation point was 0.7%. All the mixtures required a low superplasticizer content for the desired workability.

The order of material input in the mixing procedure was coarse aggregate, cement, and fine aggregate, each one with 1/3 of the total mixing water. The superplasticizer was previously dissolved in the mixing water. The mixing time between material inputs was set in 30 seconds. An additional mixing time of 5 minutes was performed after the last material input. A 120-liter inclined-axis concrete mixer was used. The total mixing and sampling time was one hour.

For the physical characterization of the concretes, Ø50 × 100 mm cylindrical specimens were cast and compacted in a flow table with 20 drops (1 drop/second). The specimens were maintained in a moisture chamber with a controlled environment (95% relative humidity and 23°C) as required by the Brazilian standard NBR 9479 [42]. The tests were done after curing times of 28, 42 and 84 days.

Table 4 presents the concrete characterization program with the respective standards and the number of specimens evaluated. The maximum relative standard deviation of compressive strength was used to verify the reliability of the compressive strength results, in accordance with NBR 7215 [46].

Table 4. Characterization program of hardened concrete

Procedure	Age	Repetitions	Standard
Compressive Strength	28, 42 and 84 days	4 specimens	NBR 5739 [43]
Tensile strength by diametral compression	28, 42 and 84 days	4 specimens	NBR 7222 [44]
Specific gravity	28 days	3 specimens	NBR 9778 [45]
Water absorption	28 days	3 specimens	NBR 9778 [45]
Expansibility (Wet-Dry cycle)	28 days	4 specimens	-

The expansibility test to evaluate the durability of the steel slag aggregates in cement-based composites was developed through a wet-dry cycle experiment. The concrete specimens were subjected to 24 hour wet-dry cycles, comprising 24 hours in a wet chamber (24 ± 2 °C, 98% RH., EQUILAM SSUM) and 24 hour in local conditions (22 ± 2 °C, 35 ± 5% RH.), for a total period of 180 days. The dimensional variation was measured with a caliper ruler (precision 0.001mm), always at the same time. For the mechanical tests, a hydraulic press EMIC DL 2000 (load cell 200kN, 0.3MPa/s) was used, while the specific gravity and water absorption test were carried out with a SOLOTEST oven and wet bath.

2.4 Economic evaluation

The cost estimate of the concrete components considered the Brazilian National System of Costs Survey and Indexes of Construction (SINAPI) referring to February 2021 [47]. The unitary cost measured in volume was converted to mass and adjusted. This system collects information about the Brazilian construction sector since 1969, and it is recognized as a trustable source for the elaboration of construction estimates. For the steel slag aggregates, the value was obtained from a specialized processing plant in the metropolitan region of Belo Horizonte (Brazil). The economic viability of this plant was reported by Gonçalves et al. [1].

The concrete cost estimates were calculated for the mixture designed with the cost of the concrete components. The steel industry distribution in the Southeast Region of Brazil shows that most of the plants is located around the capitals or close to big cities. This Region is responsible for 52% of the Brazilian GDP [5] and has the country's biggest urbanization rate of 93% [4]. Also, the Southeast Region has around 42% of the Brazilian population. The metropolitan areas of the four states capitals concentrate 20% of the country's total population [48]. This proximity and the economic relevance of this region indicates that the steel slag generated could be used in the fabrication of concrete in the principal capitals of Brazil contributing to sustainable development in a circular economy model. Also, the last United Nations report included an adjustment in the human development index considering the carbon dioxide emission and material footprint [49]. This change reinforces the need to search for technological alternatives that contributes with circular economy principles, aiding to the stimulation of new sustainable businesses.

On a previous analysis Gonçalves [50] verified the economic feasibility of installation and operation of steel slag processing plant considering the impacts of stockyard and all previous steps related to the production of steel slag aggregate. Gonçalves [50] proposed that the processing plant should be a center of distribution of steel slag aggregated powered by steel slag provided for steel industries in the region. The maximum range of 150 kilometers between the processing plant and the steel industry allow the feasibility of the process. Figure 2 shows the map of the Southeast

Region with the location of the steel industries (in gray), the state capitals (in black), and their respective radial distances.

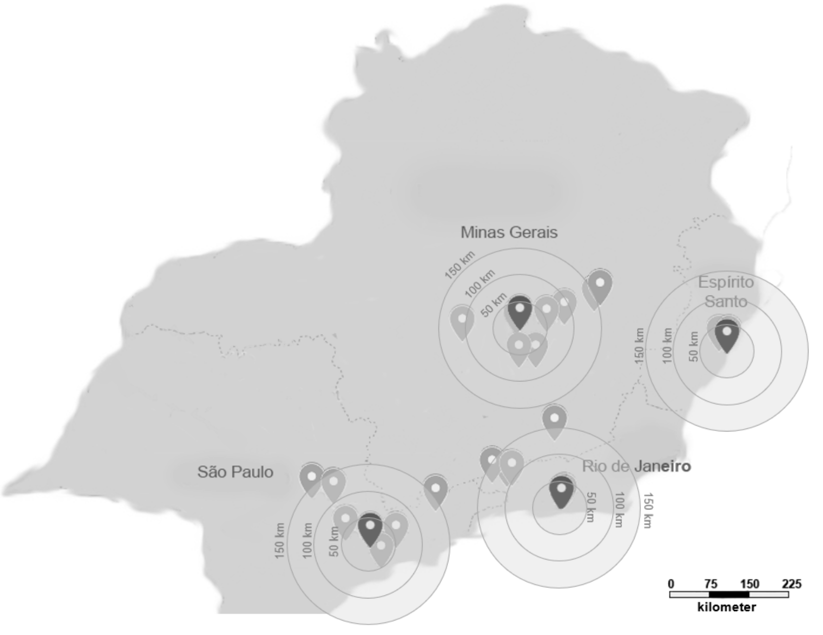

Figure 2. Map of Brazil's Southeast Region with the location of the steel industries and radial distances of the capital cities.

Figure 2 shows that all the steel industries located in the Brazilian southeast region are closer to the capitals under the range of 150 km required for the feasibility of steel slag processing plants [50]. The economic evaluation performed in this research considered the costs related after the production of steel slag aggregate, and the previous expenses are considered by Gonçalves [50]. This research assumes that the supply of construction material in the capitals, will have the same logistics both for steel slag aggregates and for the conventional aggregates. Because of that the expenses with transportation are not considered, as also indicated by the SINAPI.

2.5 Characterization of the environmental performance

An initial environmental performance of the concretes produced was evaluated through the cement intensity index proposed by Damineli et al. [51]. This coefficient is defined as the relation between the binder consumption (Portland cement, kg/m^3) of a concrete and its performance. The performance parameter chosen is the compressive strength.

All the concretes produced in this research have fixed cement consumption, so their CO_2 emission related to cement production are equal. The steel slag aggregate environmental performance is indirectly analyzed through its contribution to the enhancement of compressive strength, which could enable the production of concretes with lower cement content, allowing the reductions in CO_2 emission.

Additionally, the boundary conditions stablished for the economic evaluation are applied in the environmental analysis.

3 RESULTS AND DISCUSSION

3.1 Microstructural analysis of the steel slag stability

Table 5 shows the chemical and mineralogical composition of the steel slag. The BOF steel slag is basically composed by calcium, siliceous, iron and aluminum. Its chemical composition and phases are similar to the reported in literature [12], [52]–[55].

Table 5. Chemical and mineralogical composition of steel slag

Chemical composition		Mineralogical composition	
CaO	36.2%	Brownmillerite - *$Ca_2(Al,Fe)_2O_5$*	4.9%
SiO_2	13.4%	Calcite – $CaCO_3$	4.8%
MgO	4.9%	Larnite - Ca_2SiO_4	6.3%
P_2O_5	1.5%	Wustite - FeO	4.4%
Al_2O_3	3.6%	Periclase - MgO	4.1%
MnO	3.7%	Akermanite - $Ca_2Mg(Si_2O_7)$	2.3%
Fe_2O_3	34.5%	Merwinite - $Ca_3Mg(SiO_4)_2$	1.0%
Outros	2.2%	Amorphous	72.2%

There is a general concern about the high content of lime (CaO), periclase (MgO) and wustite (FeO) in steel slag, due to their expansiveness. Because of that, weathering processes are important to neutralize these expansive oxides, as indicated in literature [16]–[18]. The mineralogical phase identification of the steel slag (Table 5) shows low content of expansive oxides (lime, periclase, and wustite). Most of the calcium, iron, and magnesium are combined in other phases, this confirms the efficiency of weathering and the stability of steel slag. Also, it is noteworthy that these expansive oxides are confined in the inner of steel slag particles, the sample preparation allows the access to the expansive oxides.

Figure 3 presents the thermal analysis of the steel slag. In this sample, it is noticed three main loss ranges emphasized in the DTG curve. The first range indicates the release of adsorbed or free water. The second one relates to the dehydration of calcium hydroxide ($Ca(OH)_2$). The third one represents the decarbonation of the calcium carbonate ($CaCO_3$). The phases detected in the thermal analysis are also comprised in the DRX characterization (Table 5), as expected.

The content of the phases in the TG/DTA analysis are quantify through the mass loss related to the corresponding phase decomposition. It is known that 74.09g of calcium hydroxide releases 18.01g of water and 100.09g of calcium carbonate releases 44.01g of carbon dioxide during their decomposition. Thus, the content of $Ca(OH)_2$ and $CaCO_3$ are, respectively, 0.16% and 6.10%, in good accordance with the DRX result (Table 5).

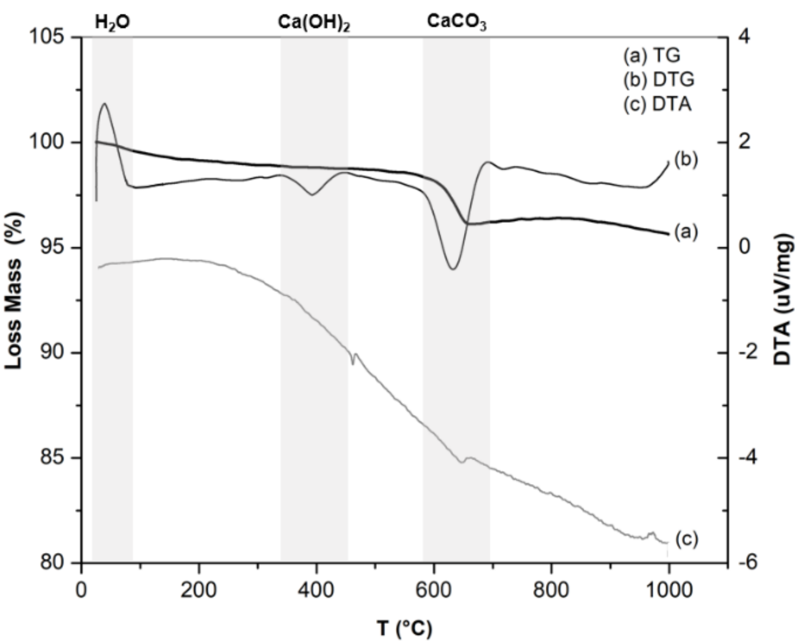

Figure 3. TG/DTA curves for the steel slag used

When generated, the steel slag has a high content of lime that, in contact with the water, forms calcium hydroxide. During the weathering process, the remaining lime and the calcium hydroxide are transformed into calcite, which could form a white layer outside the steel slag [56]. Thus, weathered steel slag usually has none or low content of calcium hydroxide [28], [57]. The TG/DTA result (Figure 3) and the mineralogical characterization (Table 5) present a low content of $Ca(OH)_2$ explained for the longtime of weathering of the steel slag. The low content of calcium hydroxide and expansive oxides (Table 5) are indicatives of the stability of the steel slag and the efficiency of the weathering process.

Additionally, it is known that the reactivity (reaction rate) of a material is directly related with the specific surface [58], [59]. Only the steel slag in a powder fraction (<75µm), with high surface, has the reactivity needed to hydrate the expansive oxides implying in a dilution of these compounds in the matrix. According to Table 5, the sum of expansive oxides percentages (CaO, MgO, and FeO) is 8.6%. Artificial aggregates have a content 75-µm finer material under 10%, according to NBR 7211 [32]. Thus, the expansive oxides represent approximately 0.86 wt.% in all concrete mass, which allows to consider the steel slag as a stable aggregate.

3.2 Technical characterization of the concretes

Table 6 shows the results of the specific gravity of the produced concretes. As expected, the steel slag concretes presented a higher specific gravity. Neverless, the increase of 38% observed between the specific gravity of steel slag and reference aggregates become a difference of only 25% in the concrete specific gravity. The NBR 8953 [60] classifies the reference and steel slag concrete as normal-weight concretes (2-2.8 g/cm^3), which allows the use of the alternative concrete in typical structural applications, as columns and beans. Also, the increase in cement consumption does not affect the specific gravity of reference or steel slag concretes since the majority of the mixture volume is composed of aggregates.

Table 6. Specific gravity of the produced concretes

Concrete type	Specific gravity (g/cm^3)
REF-310	2.14
BOFS-310	2.80
REF-450	2.22
BOFS-450	2.83

The results of the water absorption test are shown in Figure 4. This property measures the permeable pores of the matrixes being indicative of their porosity. The full replacement of reference aggregates by steel slag led to a reduction in water absorption. The reduction in water absorption with the steel slag incorporation is probably related to the morphology of the aggregate. The reference coarse aggregates are elongated with a high shape index (1.81), while the steel slag is spherical with a shape index 18% smaller (1.48). In elongated aggregates the water tends to accumulate in their vicinity generating a more porous interfacial transition zone [31], [61].

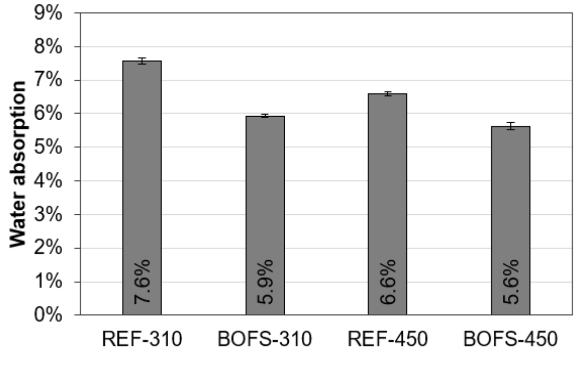

Figure 4. Water absorption of the concretes produced in the hardened state

Figure 5 presents the compressive strength of the concretes with ages of 28, 42 and 84 days. All the data presents a good correlation with the water absorption results (Figure 4). The incorporation of steel slag improved the mechanical performance of the concrete produced in all ages. This result is coherent with the literature, that reports enhancement in mechanical performance in concretes produced with steel slag aggregates [10], [21], [62], [63]. However, in this research, the mechanical performance of concrete was improved through total replacement of reference aggregates with steel slag, which can lead to a reduction in the extraction of aggregates by the construction sector and contributes with the recycling of this residue.

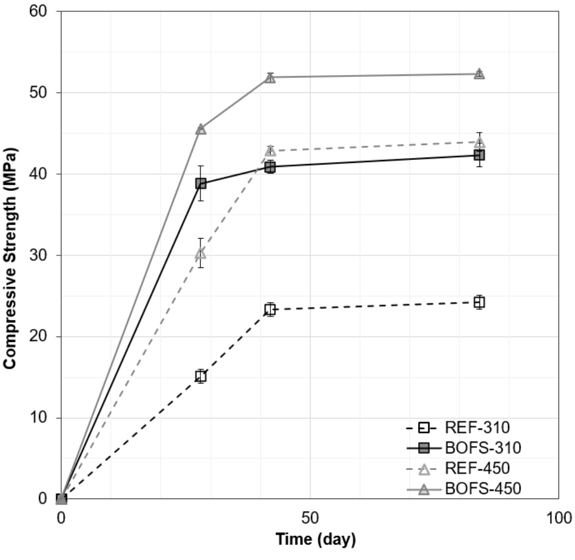

Figure 5. Compressive strength of the produced concretes

In general, the good performance of BOFS concretes is explained by the better crushing strength of the steel slag aggregate compared to reference one (7% higher), and the better shape index (closer to 1 - cubic morphology). The aggregates had a significant contribution in compressive strength, mostly in the concretes with compressive strength up to 40 MPa, where the rupture happens in the mortar [61]. Due to the equalization of concrete parameters (cement content, water/cement ratio, and mortar content), it was possible to evaluate the performance of the concretes in the same comparison basis.

At 28 days, BOFS-310 and BOFS-450 showed compressive strength about 156% and 50% higher than the relative reference concrete. In older ages (42- and 84 days), the steel slag incorporation improved the compressive strength of the concrete to a lesser extent. The strength enhancement was greater than the specific gravity increase (~30%) provided by incorporation of steel slag aggregates, offsetting any doubts about the higher structural weight by using steel slag.

These mechanical performance results indicate that it is possible to improve the mechanical performance of the matrixes using lower cement content, also reducing the hazardous activity of aggregate extraction through the steel slag incorporation. The lower cement content contributes to reducing the cement production that demands expensive milling and heating processes resulting in large CO_2 emissions.

The enhancement in compressive strength in the steel slag concretes with higher cement content (450 kg/m^3) is smaller, because of the strength class of these concretes (higher than 40 MPa). In this case, the rupture happens in the coarse aggregate, because both concretes had the same mortar content and cement consumption. This explains the smaller difference in the results.

Another reason for the better mechanical performance of BOFS concrete is the significant content of material finer than 75μm in the fine steel slag aggregate. This finer material on both aggregates are in accordance with the normative requirements of NBR 7211 [32], although the BOFS aggregate has a content around 50% higher than REF. The steel slag powder can refine the microstructure of the cement-based composite and has cementitious properties, as stated by the literature. Carvalho et al. [26] and Roslan et al. [64] reported that the full replacement of cement by steel slag powder increased the compressive strength of the specimens. Also, Wang and Yan [65] observed that the hydration of steel slag powder generated similar products of the cement hydration and some small reactivity of steel slag material finer than 75μm is reported in literature [18]. Additionally, the mineralogical composition of steel slag (Table 5) indicates a high amorphous phase content that could aid in this compressive strength.

The surface of the steel slag aggregate can also contribute to the improvement of compressive strength. Figure 6 shows images of the surface of steel slag and reference coarse aggregates obtained with a microscope. The rough surface of steel slag can increase the micro-adherence between aggregates and mortar. Additionally, this surface allows better hydration of the cement, and a smaller interfacial transition zone (ITZ) is formed, as reported by Brand and Roesler [66].

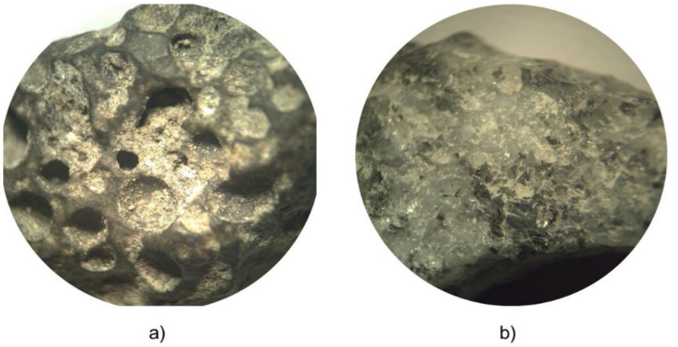

Figure 6. Microscopy images of aggregates, 15x magnification (a) steel slag (b) gneiss coarse aggregate

Overall, both concretes (REF and BOFS) present an increase in the compressive strength between 28 and 42 days. This occurs due to the use of a blended Portland cement with a high content of pozzolanic materials (up to 15% of clinker replacement). Supplementary cementitious materials, as pozzolanas, had a low rate of reaction with a higher effect in older ages [31], [67]. The increase in the compressive strength between 28 and 42 days is higher in the REF concrete. The BOFS concretes had a matrix more densely packed, due to the material finer than 75µm, the shape, and the aggregate surface texture. On another hand, the reference aggregates are unfavorable for the densification of the matrix, thus the effect of pozzolanic material is emphasized. At the age of 84 days, the concrete strength is like the 42 days, indicating an almost constant behavior for both aggregates (BOFS and REF).

The tensile strength of the concretes produced at the age of 28, 42 and 84 days is indicated in Figure 7. In general, the tensile strength increases in the same manner as the compressive strength. The ITZ and the aggregate's shape and surface affect the tensile strength of concrete [68]. Then, the utilization of steel slag aggregates increases the tensile strength of concrete due to their higher strength, with a better shape index and with the contribution of possible cementitious action by the material finer than 75 µm attached in the aggregates.

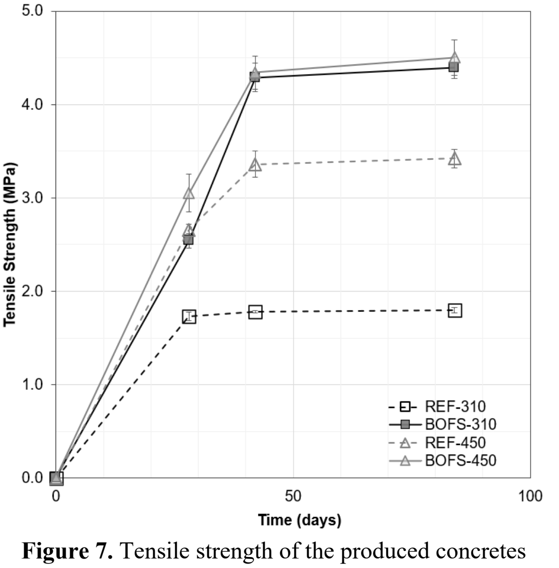

Figure 7. Tensile strength of the produced concretes

Figure 8 shows the dimensional variation of concrete specimens produced with steel slag and reference aggregates. The maximum length variation in the BOFS and REF sample occurs at 30 days being respectively ~0.02‰ and ~0.01‰.

Both concretes showed similar behaviors. This small dimensional variation confirms the stability of steel slag aggregates provided for the weathering process; this result agrees with the findings of Silva et al. [14]. Also, this result reinforces the discussion about the mineralogical composition of steel slag (Table 2). Only the pulverulent material has the reactivity needed to hydrate the expansive oxides generating a dilution of these compounds.

The literature reports that the hydration of MgO, CaO, and FeO generates volumetric expansions of approximately 119.5%, 99.4%, and 109.6%, respectively (Weast, 1987). However, the BOFS sample maintained intact during the test time. This implies that the confinement tension of cement paste is enough to avoid cracks and efflorescence in the cementitious matrixes containing low contents of expansive oxides.

The enhancement in the compressive strength of BOFS concrete at older ages (Figure 5) is another indication of the potential applicability of steel slag aggregates to produce cleaner concretes, where its use does not imply reduction in the concrete performance.

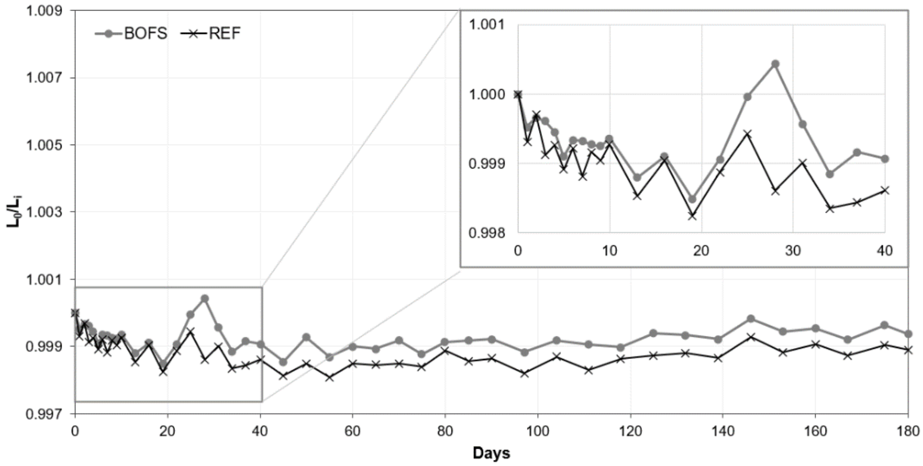

Figure 8. Expansibility of concrete specimens

3.3 Economic evaluation

Table 7 shows the average cost of the concrete insume. The steel slag cost is equivalent to 6% of the reference coarse aggregate cost. Despite the demand of processing the steel slag, this aggregate still presenting a competitive price. This is due to the high efficiency in the recuperation of metallic material in the processing plant, the value spent in the purchase and processing of steel slag is equal to 24% of the amount obtained by the sale of the metallic material [1]. Additionally, the reuse of the metallic material aids to reduce the supply of raw materials and the waste generation in this processing plant. Incorporating steel slag aggregates in construction sector also has other indirect benefit as creating jobs, boosting the economy grow of local communities, besides other social aspects.

Table 7. Current prices of the concrete inputs in Brazil (reference year: 2020)

Material	Average price/unit
Cement CP IV RS	USD 4.90/ 50 kg bag
Medium River sand	USD 12.56/tonne
Gneiss gravel	USD 16.83/tonne
Steel slag aggregate	USD 1.00/tonne

The cost of the production of 1 m^3 of concrete is indicated in Table 8. The benefit of using steel slag aggregates is clearer in the concretes with smaller cement consumption. These concretes have a higher volume of aggregates that generates a higher reduction in the cost. The production of BOFS-310 concrete is 36% more economical than REF-310; for the BOFS-450 the cost decrease is 27% compared to REF-450. Considering the already reported economic feasibility for the installation of steel slag processing plants [1], the reduced cost for the fabrication of the steel slag concrete is another indicative of the feasibility of using the steel slag aggregates.

Also, for the same cement consumption the concretes produced with steel slag have a higher compressive strength (Figure 5), so the cost per MPa of steel slag concretes is significantly smaller than the reference concretes. For a real situation, with a specific compressive strength class, the cost saving using steel slag aggregate is higher, since it will demand a smaller cement consumption to produce some concrete with the same compressive strength.

Table 8. Estimate cost of the concretes produced in this work

Concrete type	Average price for 1 cubic meter produced	Cost per MPa
REF-310	48.62 USD	2.08 USD/m^3
BOFS-310	31.52 USD	0.77 USD/m^3
REF-450	61.58 USD	1.44 USD/m^3
BOFS-450	45.16 USD	0.87 USD/m^3

3.4 Environmental performance

The results of the cement intensity of the produced concretes are listed in Table 9. Steel slag concretes had a lower cement intensity than the reference one. This result was expected since the cement consumption was fixed and the compressive strength of these concretes was higher. Additionally, the research used a blended cement with a low content of clinker (50-85 wt.%). It is known that it is possible to save 830 kg of CO_2 for each tonne of clinker displaced [69]. Thus, despite all the results the concretes produced already have a higher eco-efficiency.

Table 9. Cement intensity of steel slag and reference concretes produced

Concrete Type	Cement intensity (kg/m^3/MPa)
REF-310	13.29
BOFS-310	7.58
REF-450	10.50
BOFS-450	8.67

Daminieli et al. [51] analyzed several concrete data from around the world and observed that, in general, the cement intensity is in a range of 5-20 kg/m^3/MPa. The concretes produced in this work are among this limit. In general, the lowest binder intensities reported by Daminieli et al. [51], around 4 kg/m^3/MPa, is related to high strength concretes (superior to 200 MPa) with the incorporation of silica fume, high packing densities, and very low water/cement ratio. These are very specialized concretes that have little applicability. Besides, the steel slag concretes produced are in the regular range [51], the complete replacement of the conventional aggregates to steel slag aggregates generated a reduction in cement intensity of 43% and 17% for the concretes with 310 kg/m^3 and 450 kg/m^3, respectively.

Although the compressive strength class of BOFS-310 is equivalent to REF-450, this indicates that to produce a steel slag concrete with a compressive strength like the REF-310 is required a small amount of cement. Then, it is proposed a correction factor in the cement intensity (Cbi). Equation 1 indicates the calculation of the Cbi. The application of the Cbi in the cement intensity obtained for BOFS-310 indicates a new value of 5.22 kg/m^3/MPa, closer to the inferior limit of Daminieli et al. [51].

$$f_{c310}^{BOFS} = f_{c450}^{REF}\ ; Cbi = \frac{310}{450} = 0.69 \tag{1}$$

Carvalho et al. [52] studied concretes produced with steel slag aggregate and a fine fraction of steel slag in replacement of cement finding a cement intensity around 3.5 kg/m^3/MPa. This low cement intensity is attributed to the fine fraction of steel slag that requires grinding in a ball mill with at least 200 rpm for more than 180 minutes. Then, a cement intensity around 8 kg/m^3/MPa of BOFS concretes with less or no processing is an excellent result that could represent a greater environmental performance than a concrete with a cement intensity of 3 kg/m^3/MPa.

Although the cement intensity only measures the environmental effect of cement production, all concrete produced in this research has the same cement consumption. Considering this, an initial environmental performance related to the aggregate replacement could be indirectly considered. In general, the use of steel slag in this research represents a significant reduction in the CO_2 emission due to a thereduction in cement consumption without using expensive gridding procedures or materials. The total replacement of reference aggregates to steel slag represents an effective and easy way to reduce the environmental impact of the construction sector, contributing to the production of cleaner concretes. Probably the combination of steel slag aggregates with mineral admixtures producing high strength concretes can generates a more significant reduction in the cement intensity.

3.5 Consideration about feasibility

Figure 9 summarizes the main data obtained in this research. For the elaboration of the radar chart, all the results were normalized to a scale of 1 to 5. The mixture design with the best performance in the parameter received grade 5, and the others were proportionally calculated on this scale. In this way, the most external curve represents the concrete mixture that encompasses the best technical characteristics, the small cost, and the lower environmental impact. The steel slag concretes are closer to the outside limit, although the main difference is the cost. Stands out that the reduction in the cost of concrete production is particularly important in Brazil, which has a housing deficit of 6 million units, mostly (84%) for low-income families [70]. Because of that, the BOFS-310 is established as the best mixture design. Also, the BOFS-310 had the smallest cement intensity (7.58 kg/m^3/MPa) showing its eco-efficiency. Anyway, steel slag aggregate revealed a solution to a cleaner production of concrete in construction sector, contributing to the reduction of natural aggregates mining and the consequent effects in society. The reference concretes were hatched to simplify the analysis.

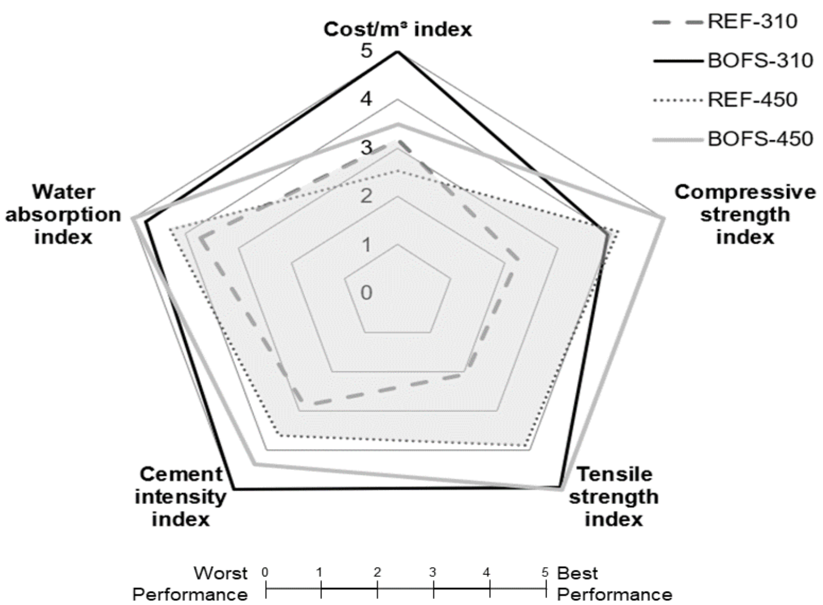

Figure 9. Radar chart of the technical, economic and environmental performance analysis of the concretes. Parameters are normalized, where 5 is the best performance and 0 the worst one.

4 CONCLUSION

This work evaluates a cleaner production solution for the steel slag residue which contributes to the promotion of new strategies of circular economy. The steel slag (BOFS fine and coarse fraction) entirely replaced the conventional aggregates in the production of eco-efficient concretes. Besides the experimental program to evaluate the durability, mechanical and physical properties of the steel slag concrete, this work evaluated the economic and environmental impact of this material. The main findings of this work are:

- The novel data collected in the microstructural analysis of the steel slag stability through different techniques (FRX, DRX and TG/DTA) indicated the weathered stage of this residue. Additionally, the expansive oxides are accessible and reactive only in a powder condition (<75µm), which implies in a significant dilution of this compound in the matrix and its hazardous potential.

- The BOFS aggregates improve the compressive and tensile strength of the concrete due to its hardness and morphology. Additionally, the material finer than 75µm presented in the steel slag aggregate contributes to the densification of the matrix acting as a cementitious material. These results associated with the broad explanation about the steel slag microstructure is important to better understand the various gaps remaining related to the expansiveness of steel slag and the efficiency of weathering processes.
- The BOFS concrete has a similar compressive strength compared to reference one with a reduction of 140 kg/m^3 (~31%) in the cement content. This enhancement in the mechanical performance of concrete is the main responsible for the lower environmental impact that results in a more eco-efficient product.
- For the cost estimation, the concretes produced with steel slag aggregates presented a cost 27-36% lower than the reference ones. This results in the production of a cement-based composite more accessible for low-income constructions.
- The cost and environmental analysis of steel slag aggregates are new in the literature and indicated that this material is a preferable alternative to the natural aggregates.

The physical properties results, and expansibility test conducted indicated that steel slag aggregates could be used in structural elements. This aggregate allows the production of concrete with lower content of Portland cement implying in a decrease of CO_2 emission by the construction industry. Additionally, the steel slag aggregate has a lower production cost compared to the extraction of natural aggregates reducing the total cost of concrete production.

Brazil has a housing deficit of more than 6 million of dwellings, mostly of low-income families [70], so the steel slag aggregates could aid in the housing problem, since the BOFS concrete is more resistant, durable and have smaller cost than regular concrete. It is important to point out that historically many communities are born around industries, so the use of steel slag aggregate in construction sector aids strengthening the economy through job creation and generation of sustainable businesses.

Besides all the contributions listed above, the use of steel slag aggregates also comprises an economic opportunity for new cleaner businesses that could provide environmental and social benefits. The results presented in this work adds in a definition of new strategies for circular economy. It is mandatory to update the productive system and seek for ways to expand the economy in a sustainable way. The use of steel slag as aggregate is an alternative for the resource scarcity contributing for reduction in the demand for natural resources of the construction sector and steel industry.

ACKNOWLEDGMENTS

We gratefully acknowledge the Ministry of Science, Technology, Innovation and Communications, the National Council for Scientific and Technological Development (CNPq) and the agencies CAPES and FAPEMIG for providing financial support. We are also grateful for the infrastructure and collaboration of the Research Group on Solid Waste - RECICLOS – CNPq.

REFERENCES

[1] D. Gonçalves, W. Fontes, J. Mendes, G. Silva, and R. Peixoto, "Evaluation of the economic feasibility of a processing plant for steelmaking slag," *Waste Manag. Res.*, vol. 34, no. 2, pp. 107–112, 2016.

[2] M. Alexander and S. Mindess, *Aggregates in Concrete.* New York: CRC Press, 2005.

[3] D. Padmalal, K. Maya, S. Sreebha, and R. Sreeja, "Environmental effects of river sand mining: a case from the river catchments of Vembanad lake, Southwest coast of India," *Environmental Geology*, vol. 54, no. 4, pp. 879–889, 2008.

[4] Instituto Brasileiro de Geografia e Estatística, *Censo Demográfico*. Rio de Janeiro: IBGE, 2010.

[5] Instituto Brasileiro de Geografia e Estatística, *Contas Regionais do Brasil*. Rio de Janeiro: IBGE, 2016.

[6] C. Carvalho, *Extração de Areia Vai Aumentar no Paraíba do Sul*. Brasília: Agência Nacional de Águas, 2019.

[7] Instituto Aço Brasil, *Relatório de Sustentabilidade 2016-2017*. Rio de Janeiro: IABR, 2018.

[8] Brasil. Ministério de Minas e Energia. Departamento Nacional de Produção Mineral, *Universo da Mineração Brasileira 2006*. Brasilia: DNPM, 2007.

[9] S. Monosi, M. Ruello, and D. Sani, "Electric arc furnace slag as natural aggregate replacement in concrete production," *Cement Concr. Compos.*, vol. 66, pp. 66–72, 2016.

[10] J. San-José, I. Vegas, I. Arribas, and I. Marcos, "The performance of steel-making slag concretes in the hardened state," *Mater. Des.*, vol. 60, pp. 612–619, 2014.

[11] H. Beshr, A. A. Almusallam, and M. Maslehuddin, "Effect of coarse aggregate quality on the mechanical properties of high strength concrete," *Constr. Build. Mater.*, vol. 17, no. 2, pp. 97–103, 2003.

[12] I. Papayianni and E. Anastasiou, "Production of high-strength concrete using high volume of industrial by-products," *Constr. Build. Mater.*, vol. 24, no. 8, pp. 1412–1417, 2010.

[13] C. Pellegrino, P. Cavagnis, F. Faleschini, and K. Brunelli, "Properties of concretes with Black/Oxidizing Electric Arc Furnace slag aggregate," *Cement Concr. Compos.*, vol. 37, pp. 232–240, 2013.

[14] M. Silva, B. Souza, J. Mendes, G. Brigolini, S. Silva, and R. Peixoto, "Feasibility study of steel slag aggregates in precast concrete pavers," *ACI Mater. J.*, vol. 113, no. 4, pp. 439–446, 2016.

[15] H. Andrade, J. Carvalho, L. Costa, F. Elói, K. Silva, and R. Peixoto, "Mechanical performance and resistance to carbonation of steel slag reinforced concrete," *Constr. Build. Mater.*, vol. 298, pp. 123910, 2021.

[16] I. Grubeša, I. Barisic, A. Fucic, and S. Bansode, *Characteristics and Uses of Steel Slag in Building Construction*, 1st ed. Cambridge: Woodhead Publ., 2016.

[17] Y. Jiang, T. Ling, C. Shi, and S. Pan, "Characteristics of steel slags and their use in cement and concrete: a review," *Resour. Conserv. Recycling*, vol. 136, pp. 187–197, 2018.

[18] A. Martins et al., "Steel slags in cement-based composites: an ultimate review on characterization, applications and performance," *Constr. Build. Mater.*, vol. 291, pp. 123265, 2021.

[19] G. Wang, *The Utilization of Slag in Civil Infrastructure Construction*. Cambridge: Woodhead Publ., 2016.

[20] I. Z. Yildirim and M. Prezzi, "Chemical, mineralogical, and morphological properties of steel slag," *Adv. Civ. Eng.*, vol. 2011, pp. 1–3, 2011.

[21] C. Pellegrino and V. Gaddo, "Mechanical and durability characteristics of concrete containing EAF slag as aggregates," *Cement Concr. Compos.*, vol. 31, no. 9, pp. 663–671, 2009.

[22] P.-C. Aïtcin, "Cements of yesterday and today concrete of tomorrow," *Cement Concr. Res.*, vol. 29, no. 9, pp. 1349–1359, Nov 2000.

[23] Y. Guo, J. Xie, J. Zhao, and K. Zuo, "Utilization of unprocessed steel slag as fine aggregate in normal- and high-strength concrete," *Constr. Build. Mater.*, vol. 204, pp. 41–49, 2019.

[24] R. Januzzi, L. Costa, R. Peixoto, and A. Cury, "Study of the mechanical behavior of prisms composed by two blocks produced with eletrical steel slag for structural masonry," *Mason. Int.*, vol. 31, pp. 80–87, 2019.

[25] D. Diniz, J. Carvalho, J. Mendes and R. Peixoto, "Blast oxygen furnace slag as chemical soil stabilizer for use in roads," *J. Mater. Civ. Eng.*, vol. 29, no. 9, pp. 1–7.

[26] J. Carvalho, T. Melo, W. Fontes, J. Batista, G. Brigolini, and R. Peixoto, "More eco-efficient concrete: an approach on optimization and use of waste-based supplementary cementing materials," *Constr. Build. Mater.*, vol. 206, pp. 397–409, 2019.

[27] Associação Brasileira de Normas Técnicas,, *Cimento Portland – Requisitos*, NBR 16665, 2018.

[28] G. Adegoloye, A.-L. Beaucour, S. Ortola, and A. Noumowe, "Mineralogical composition of EAF slag and stabilised AOD slag aggregates and dimensional stability of slag aggregate concretes," *Constr. Build. Mater.*, vol. 115, pp. 171–178, 2016.

[29] J. Guo, Y. Bao, and M. Wang, "Steel slag in China: treatment, recycling, and management," *Waste Manag.*, vol. 78, pp. 318–330, 2018.

[30] J. F. Young, S. Mindess, R. J. Gray, and A. Bentur, *The Science and Technology of Civil Engineering Materials*. New Jersey: Prentice Hall, 1998.

[31] P. K. Mehta and P. J. M. Monteiro, *Concrete: Microstrucuture, Properties and Materials*. New York: McGraw-Hill, 2006.

[32] Associação Brasileira de Normas Técnicas, *Agregado para Concreto – Especificação*, ABNT NBR 7211, 2009.

[33] Associação Brasileira de Normas Técnicas, *Aggregate – Determination of Fine Aggregate Specific Gravity by Chapman Vessel – Method of Test*, ABNT NBR 9776, 1986.

[34] Associação Brasileira de Normas Técnicas, *Agregado Graúdo – Determinação de Massa Específica, Massa Específica Aparente e Absorção de Água*, ABNT NBR NM 53, 2009.

[35] Associação Brasileira de Normas Técnicas, *Agregados – Determinação da Massa Unitária e do Volume de Vazios*, ABNT NBR NM 45, 2006.

[36] Associação Brasileira de Normas Técnicas, *Agregados – Determinação do Material Fino que Passa Através da Peneira 75 Micrometro, por Lavagem*, ABNT NBR NM 46, 2003.

[37] Associação Brasileira de Normas Técnicas, *Agregados – Determinação da Resistência ao Esmagamento de Agregados Graúdos – Método de Ensaio*, ABNT NBR 9938, 2013.

[38] Associação Brasileira de Normas Técnicas, *Agregado Graúdo – Determinação do Índice de Forma pelo Método do Paquímetro – Método de Ensaio*, ABNT NBR 7809, 2019.

[39] K. Scrivener, R. Snellings, and B. Lothenbach, *A Practical Guide to Microstructural Analysis of Cementitious Materials*. Boca Raton: CRC Press, 2016.

[40] P. Helene and P. Terzian, *Manual de Dosagem e Controle do Concreto*, 1a ed. São Paulo: Pini, 1992.

[41] Associação Brasileira de Normas Técnicas, *Concreto – Determinação da Consistência pelo Abatimento do Tronco de Cone*, ABNT NBR NM 67, 1998.

[42] Associação Brasileira de Normas Técnicas, *Argamassa e Concreto – Câmaras Úmidas e Tanques para Cura de Corpos-de-Prova*, ABNT NBR 9479, 2006.

[43] Associação Brasileira de Normas Técnicas, *Concreto – Ensaio de Compressão de Corpos de Prova Cilíndricos*, ABNT NBR 5739, 2018.

[44] Associação Brasileira de Normas Técnicas, *Concreto e Argamassa – Determinação da Resistência à Tração por Compressão Diametral de Corpos de Prova Cilíndricos*, ABNT NBR 7222, 2011.

[45] Associação Brasileira de Normas Técnicas, *Argamassa e Concreto Endurecidos – Determinação da Absorção de Água, Índice de Vazios e Massa Específica*, ABNT NBR 9778, 2005.

[46] Associação Brasileira de Normas Técnicas, *Cimento Portland – Determinação da Resistência à Compressão*, ABNT NBR 7215, 2014.

[47] Sistema Nacional de Pesquisa de Custos e Índices da Construção Civil, *Relatório de Insumos e Composições- FEV/2021: Minas Gerais, Rio de Janeiro e São Paulo*. Rio de Janeiro: SINAPI, 2021.

[48] Instituto Brasileiro de Geografia e Estatística, *Estimativas da População dos Municípios com Data de 1° de Julho de 2018*. Rio de Janeiro: IBGE, 2018.

[49] United Nations Development Programme, *Human Development Report 2020 – The Next Frontier: Human Development and the Anthropocene*. New York: UNDP, 2020.

[50] D. R. R. Gonçalves, "Análise da viabilidade econômica via simulação de Monte Carlo para utilização da escória de aciaria como agregado na fabricação de pré-fabricados para a construção civil – ecoblocos," M.S. thesis, Univ. Fed. Ouro Preto, Ouro Preto, 2015.

[51] B. Damineli, F. Kemeid, P. Aguiar, and V. John, "Measuring the eco-efficiency of cement use," *Cement Concr. Compos.*, vol. 32, no. 8, pp. 555–562, 2010.

[52] J. Carvalho, W. Fontes, C. Azevedo, G. Brigolini, and R. Peixoto, "Enhancing the eco-efficiency of concrete using engineered recycled mineral admixtures and recycled aggregates," *J. Clean. Prod.*, vol. 257, pp. 120530, 2020.

[53] L. Franco, J. Mendes, L. Costa, R. Pira, and R. Peixoto, "Design and thermal evaluation of a social housing model conceived with bioclimatic principles and recycled aggregates," *Sustain. Cities Soc.*, vol. 51, pp. 101725, 2019.

[54] A. Santamaria, A. Orbe, J. San José, and J. González, "A study on the durability of structural concrete incorporating electric steelmaking slags," *Constr. Build. Mater.*, vol. 161, pp. 94–111, 2018.

[55] C. Li, Z. Chen, S. Wu, B. Li, J. Xie, and Y. Xiao, "Effects of steel slag fillers on the rheological properties of asphalt mastic," *Constr. Build. Mater.*, vol. 145, pp. 383–391, 2017.

[56] N. Palankar, A. Shankar, and B. Mithun, "Durability studies on eco-friendly concrete mixes incorporating steel slag as coarse aggregates," *J. Clean. Prod.*, vol. 129, pp. 437–448, 2016.

[57] D. Graffitti, "Evaluation of free lime content in steel slag (in portuguese)," M.S. thesis, Univ. Fed. Porto Alegre, Porto Alegre, 2002.

[58] J. Benezet and A. Benhassaine, "Grinding and pozzolanic reactivity of quartz powders," *Powder Technol.*, vol. 105, no. 1–3, pp. 167–171, 1999.

[59] E. Gutman, *Mechanochemistry of Materials*. Cambridge: Cambridge Int. Sci. Publ., 1998.

[60] Associação Brasileira de Normas Técnicas, *Concrete for Structural Use: Density, Strength and Consistence Classification*, ABNT NBR 8953, 2015.

[61] J. F. Lamond and J. H. Pielert, *Significance of Tests and Properties of Concrete and Concrete-Making Materials*. Bridgeport: ASTM International, 2006.

[62] E. Anastasiou, K. Filikas, and M. Stefanidou, "Utilization of fine recycled aggregates in concrete with fly ash and steel slag," *Constr. Build. Mater.*, vol. 50, pp. 154–161, 2014.

[63] Y. Biskri, D. Achoura, N. Chelghoum, and M. Mouret, "Mechanical and durability characteristics of High Performance Concrete containing steel slag and crystalized slag as aggregates," *Constr. Build. Mater.*, vol. 150, pp. 167–178, 2017.

[64] N. Roslan, M. Ismail, Z. Abdul-Majid, S. Ghoreishiamiri, and B. Muhammad, "Performance of steel slag and steel sludge in concrete," *Constr. Build. Mater.*, vol. 104, pp. 16–24, 2016.

[65] Q. Wang and P. Yan, "Hydration properties of basic oxygen furnace steel slag," *Constr. Build. Mater.*, vol. 24, no. 7, pp. 1134–1140, 2010.

[66] A. Brand and J. Roesler, "Interfacial transition zone of cement composites with steel furnace slag aggregates," *Cement Concr. Compos.*, vol. 86, pp. 117–129, 2018.

[67] J. Skibsted and R. Snellings, "Reactivity of supplementary cementitious materials (SCMs) in cement blends," *Cement Concr. Res.*, vol. 124, pp. 105799, 2019.

[68] H. Reinhardt, "Factors affecting the tensile properties of concrete," in *Understanding the Tensile Properties of Concrete*, J. Weerheijm, Ed., Oxford: Woodhead Publ., 2013, pp. 19–51. http://dx.doi.org/10.1533/9780857097538.1.19.

[69] International Energy Agency Staff, *Energy Technology Perspectives 2017: Catalysing Energy Technology Transformations.* Paris: IEA, 2017.

[70] Fundação João Pinheiro, *Déficit Habitacional no Brasil 2013-2014*. Belo Horizonte: Cent. Estat. Inf., 2016.

Author contributions: LCBC: conceptualization, formal analysis, investigation, methodology, writing; MAN: methodology, writing. LCF: methodology, writing; FPFE: methodology, writing; JMFC: methodology, resources, supervision, writing; RAFP: supervision, resources, funding acquisition, writing.

Editors: Lia Pimentel, Guilherme Aris Parsekian.

IBRACON Structures and Materials Journal
Revista IBRACON de Estruturas e Materiais
ISSN 1983-4195 ismj.org

ORIGINAL ARTICLE

Applicability of the 500°C isotherm method in determining the strength of reinforced concrete beams after fire

Aplicabilidade do método dos 500°C na determinação da resistência de vigas em concreto armado após incêndio

Leonardo Medeiros da Costa[a]
José Jeferson do Rêgo Silva[b]
Tiago Ancelmo de Carvalho Pires de Oliveira[b]
Dayse Cavalcanti de Lemos Duarte[c]

[a]Universidade Estadual da Paraíba – UEPB, Departamento de Engenharia Civil, Araruna, PB, Brasil
[b]Universidade Federal de Pernambuco – UFPE, Departamento de Engenharia Civil, Recife, PE, Brasil
[c]Universidade Federal de Pernambuco – UFPE, Departamento de Engenharia Mecânica, Recife, PE, Brasil

Received 03 March 2021
Accepted 02 August 2021

Abstract: A procedure to estimate the residual bending moment and the shear load capacity after fire in reinforced concrete beams was evaluated. The calculation method is based on the 500ºC Isotherm Method, adopting the reduction coefficients proposed by Van Coile et al. (2014) for the steel yield strength. The proposed method validation was done from experimental results of 62 reinforced concrete beams available in the literature. It was possible to observe a good approximation of the analytical method with the experimental data. For the bending moment an average ratio M_r^{ana} / M_r^{exp} of 1.04 and standard deviation of 0.15 was found. For the shear force an average ratio V_r^{ana} / V_r^{exp} of 0.85 and standard deviation of 0.23 was found.

Keywords: residual strength, shear, bending moment, after fire.

Resumo: Um procedimento para estimar a capacidade residual após incêndio para o momento fletor e o cisalhamento em vigas de concreto armado foi avaliado. O método de cálculo é baseado no Método das Isotermas dos 500ºC, adotando os coeficientes de redução propostos por Van Coile et al. (2014) para resistência ao escoamento do aço. A validação foi feita com resultados experimentais de 62 vigas disponíveis na literatura e foi possível observar uma boa aproximação com os dados experimentais, apresentando para o momento fletor uma relação média M_r^{ana} / M_r^{exp} de 1.04 e desvio padrão médio de 0.15, e para o esforço cortante uma relação média V_r^{ana} / V_r^{exp} de 0.85 e desvio padrão médio de 0.23.

Palavras-chave: resistência residual, cisalhamento, momento fletor, após incêndio.

How to cite: L. M. Costa, J. J. R. Silva, T. A. C. P. Oliveira, and D. C. L. Duarte, "Applicability of the 500°C isotherm method in determining the strength of reinforced concrete beams after fire", *Rev. IBRACON Estrut. Mater.*, vol. 15, no. 2, e15202, 2022, https://doi.org/10.1590/S1983-41952022000200002

1 INTRODUCTION

It is known that fires can cause serious damage to reinforced concrete structural elements. In particular, the beams and slabs are located at the top of the building and are more prone to fire damage, as highlighted by Yang et al. [1]. In the absence of a failure during the fire, measuring the level of damage caused after a fire is essential in deciding either to release the use, to repair or to demolish the structure.

Corresponding author: Leonardo Medeiros da Costa. E-mail: leonardom.costa@yahoo.com.br
Financial support: None.
Conflict of interest: Nothing to declare.

Determining the residual capacity of reinforced concrete (RC) beams involves understanding the effects of temperature on concrete and steel. Concrete has a good fire performance due to its low thermal conductivity and high thermal capacity but presents loss on the residual strength depending on the severity of the fire [2], [3]. After fire temperatures between 500 and 600ºC, the steel recovers its strength to room temperatures, as indicated by Neves et al. [4] and Van Coile et al. [5], respectively.

Molkens et al. [6] note that for most fires in buildings with concrete structure, the structural elements do not collapse during the fire exposure. However, after fire a change in the critical failure mode can occur. Thanaraj et al. [7] reported experimental series where the elements started to fail due to shear. This same behavior is observed by Diab [8] reporting that shear failure can be critical on reinforced concrete beams after fire, being an aggravating factor that this is sudden type of rupture. This tendency to shear failure in RC beams after fire occurs in elements with low compressive strength concrete, decreasing the shear capacity of the elements because concrete is an important part of shear strength. Other factors such as w/c ratio, density and reinforcement percentage are also an influence on the failure mode [7].

In the ABNT NBR 15200 [9], Eurocode 1 1-2 [10] and Eurocode 2 1-2 [11] standards, there is no clear recommendation on the assessment of residual load capacity in reinforced concrete elements after a fire situation. In the literature, some authors have proposed analytical formulations to determine the residual strength of reinforced concrete beams and the most relevant references in this regard are here presented.

The residual strength after fire of other materials such as high-strength mortar, wood, and masonry is reported in the literature. Cülfik and Özturan [12] observed a significant loss on mortars residual strength for temperatures up to 600ºC and almost full strength loss for temperatures up to 900ºC. Sciarretta [13] numerically analyzed masonry walls after fire and found satisfactory results compared to experimental results available in the literature.

Hsu and Lin [14] proposed an approach based on the ACI 318 [15] considering the deformation compatibility to evaluating the residual load capacity of beams exposed to fire. It was observed that the reduction on the bending moment and shear force capacity are different: the shear capacity after fire is about 53.0% and 40.8% of the initial capacity, while the residual bending moment is about 65.13% and 52.83% of the initial capacity, when the beams are exposed to fire for 120 and 180 minutes, respectively.

Kodur et al. [16] presented a simplified approach for calculating residual flexural strength of reinforced concrete beams based on ACI 318 [17], applying the reduction factors for the strength of steel and concrete. The maximum temperature and duration of the fire were estimated through visual observations of the exposed concrete. As a result, the residual bending moment was conservative.

Bai and Wang [18] proposed a method based on the design at room temperature for the residual flexural strength of reinforced concrete beams after fire, considering reducing the concrete and reinforcement steel sections to compensate the damage caused by the fire. In a parametric study, they concluded that the initial strength of concrete and steel have few influences on the residual strength results. The percentual strength reduction after fire exposure is near for all the strength values analyzed.

Xu et al. [19]–[21] presented experimental studies analyzing the residual strength after fire to shear and the bending moment of reinforced concrete beams with rectangular and “T” sections. In Xu et al. [20] a study on estimating of the resistance after fire is presented based on the Chinese code [22], reducing the strengths of concrete and steel as a function of temperature.

Numerical simulations were developed by Kodur and Agrawal [23], Sun et al. [24] and Cai et al. [25], but refined analysis requires a high computational cost. As it is possible to observe in the available literature, few analytical models to estimate the residual strength of reinforced concrete beams after fire are formulated. Even more scarce is the analysis of post-fire shear capacity, as research is often conditioned to the verification of flexural strength.

The present paper aims to validate the application of a simplified procedure to estimate the bending moment and the shear capacity in reinforced concrete beams after fire. The method is based on the 500ºC Isotherm Method [11], adopting the reduction coefficients proposed by Van Coile et al. [5] to the yield strength of steel.

2 **EXPERIMENTAL DATA**

2.1 **Post-fire moment capacity**

A total of 22 beams tested experimentally were used to verify the method for determining the post-fire moment capacity and are available in the literature. The beams were heated on three faces, without load during the heating phase and tested post-fire with four-point bending, Figure 1. All beams failed in flexure. More details are present in Thanaraj et al. [7], Xu et al. [20] and Pereira et al. [26]. It is noteworthy to mention that only beams that lost strength after fire are included in the validation. RC beams under short-time heating and low peak temperatures tended to have no relevant loss of strength.

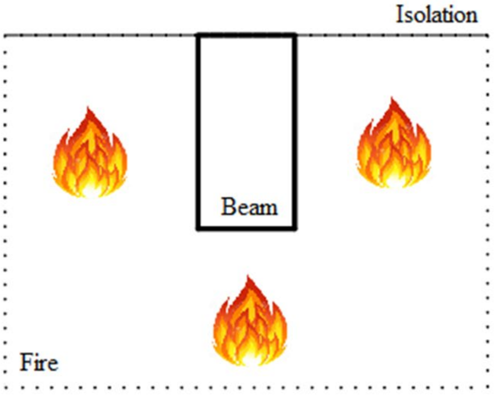

(a)

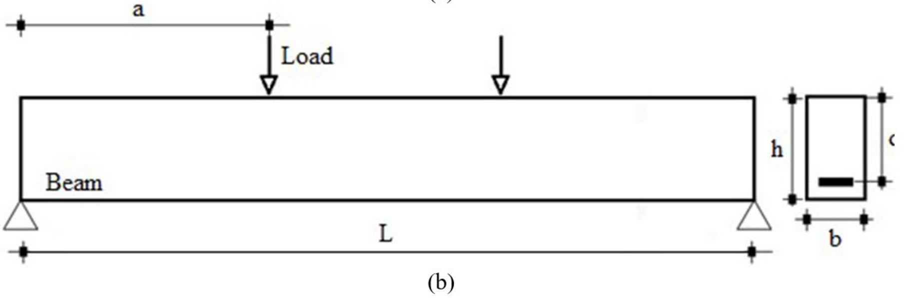

(b)

Figure 1. Tests (a) heating phase on cross section and (b) four-point bending after fire

The parameters considered in the beams were: cross section, concrete strength, time of exposure to fire, transverse reinforcement ratio (ρ_t), longitudinal reinforcement ratio (ρ_l) and shear span (ξ), see Table 1

Where: A_s : area of longitudinal reinforcement; A_{sw} : area of transverse reinforcement area; s : stirrups spacing

Table 1. Identification and characteristics of beams analyzed by bending

Ref.	ID.	Cross Section	Fire curve	Time	fc	$\rho_l = \frac{A_s}{b \cdot h}$	$\rho_t = \frac{A_{sw}}{b \cdot s}$	$\xi = a / d$
-	-	-	-	(min)	(MPa)	%	%	-
[20]	L5	25x40	ISO 834	60	41.2	1.47%	0.27%	1.51
[20]	L6	25x40	ISO 834	60	41.2	1.47%	0.27%	1.71
[20]	L7	25x40	ISO 834	60	41.2	1.47%	0.27%	2.22
[20]	L9	25x40	ISO 834	120	41.2	1.47%	0.27%	3.31
[26]	REC15_210	12x20	NS	210	47.6	0.65%	0.79%	1.43
[26]	REC30_210	12x20	NS	210	47.6	0.65%	0.79%	1.57
[7]	M20-60	20x20	ISO 834	60	27.09	0.39%	0.62%	1.23
[7]	M20-120	20x20	ISO 834	120	27.09	0.39%	0.62%	1.23
[7]	M20-180	20x20	ISO 834	180	27.09	0.39%	0.62%	1.23
[7]	M20-240	20x20	ISO 834	240	27.09	0.39%	0.62%	1.23
[7]	M30-60	20x20	ISO 834	60	37.8	0.39%	0.62%	1.23

Table 1. Continued…

Ref.	ID.	Cross Section	Fire curve	Time	f_c	$\rho_l = \frac{A_s}{b \cdot h}$	$\rho_t = \frac{A_{sw}}{b \cdot s}$	$\xi = a / d$
-	-	-	-	(min)	(MPa)	%	%	-
[7]	M30-120	20x20	ISO 834	120	37.8	0.39%	0.62%	1.23
[7]	M30-180	20x20	ISO 834	180	37.8	0.39%	0.62%	1.23
[7]	M30-240	20x20	ISO 834	240	37.8	0.39%	0.62%	1.23
[7]	M40-60	20x20	ISO 834	60	47.31	0.39%	0.62%	1.23
[7]	M40-120	20x20	ISO 834	120	47.31	0.39%	0.62%	1.23
[7]	M40-180	20x20	ISO 834	180	47.31	0.39%	0.62%	1.23
[7]	M40-240	20x20	ISO 834	240	47.31	0.39%	0.62%	1.23
[7]	M50-60	20x20	ISO 834	60	56.67	0.39%	0.62%	1.23
[7]	M50-120	20x20	ISO 834	120	56.67	0.39%	0.62%	1.23
[7]	M50-180	20x20	ISO 834	180	56.67	0.39%	0.62%	1.23
[7]	M50-240	20x20	ISO 834	240	56.67	0.39%	0.62%	1.23

NS – Non-Standard

The influence of the ratio (a / d) on the post-fire moment capacity in the tested beams was not identified. The procedure was also shown to be applicable to non-standard fire curves. As expected, longer times of exposure to fire resulted in greater resistance reductions, especially for concretes of lower resistance. The compressive strength also influenced the failure mode.

2.2 **Post-fire shear capacity**

A total of 40 beams tested experimentally with results available in the literature were used in the validation of the procedure to estimate the post-fire shear capacity of reinforced concrete beams. The beams were heated on three faces, without load during the heating phase and tested post-fire with four-point bending. The identification and characteristics of the beams are shown in Table 2.

Table 2. Identification and characteristics of the beams analyzed to shear

Ref.	ID.	Cross Section	Fire curve	Time	f_c	$\rho_l = \frac{A_s}{b \cdot h}$	$\rho_t = \frac{A_{sw}}{b \cdot s}$	ξ=a/d	a / L
-	-	(cm)	-	(min)	(MPa)	(%)	(%)	-	-
[27]	V120	20x30	ISO 834	120	17.1	0.75%	0.14%	4.4	0.25
[27]	V60	20x30	ISO 834	60	17.1	0.75%	0.14%	4.4	0.25
[27]	V90	20x30	ISO 834	90	17.1	0.75%	0.14%	4.4	0.25
[14]	test nº17	30x45	ASTM E119	60	34.7	2.53%	0.00%	1.5	0.36
[14]	test nº18	30x45	ASTM E119	180	34.7	2.53%	0.00%	1.5	0.36
[14]	test nº2	20x30	ASTM E119	60	34.7	1.90%	0.00%	1.5	0.33
[14]	test nº27	20x30	ASTM E119	60	60.5	1.90%	0.00%	1.5	0.33
[14]	test nº28	20x30	ASTM E119	180	62.5	1.90%	0.00%	1.5	0.33

Table 2. Continued…

Ref.	ID.	Cross Section	Fire curve	Time	f_c	$\rho_l = \frac{A_s}{b \cdot h}$	$\rho_t = \frac{A_{sw}}{b \cdot s}$	ξ=a/d	a / L
-	-	(cm)	-	(min)	(MPa)	(%)	(%)	-	-
[14]	test nº3	20x30	ASTM E119	180	34.7	1.90%	0.00%	1.5	0.33
[14]	test nº32	20x30	ASTM E119	60	65.2	3.80%	0.00%	1.5	0.32
[14]	test nº33	20x30	ASTM E119	180	66.5	3.80%	0.00%	1.5	0.32
[14]	test nº8	20x30	ASTM E119	60	35.8	3.80%	0.00%	1.5	0.32
[14]	test nº9	20x30	ASTM E119	180	35.8	3.80%	0.00%	1.5	0.32
[14]	test nº14	20x30	ASTM E119	60	34.7	1.90%	0.98%	1.5	0.33
[14]	test nº15	20x30	ASTM E119	180	34.7	1.90%	0.98%	1.5	0.33
[14]	test nº23	30x45	ASTM E119	180	34.7	2.53%	0.98%	1.5	0.36
[14]	test nº11	20x30	ASTM E119	60	35.8	3.80%	0.00%	4.0	0.41
[14]	test nº12	20x30	ASTM E119	180	35.8	3.80%	0.00%	4.0	0.41
[14]	test nº20	30x45	ASTM E119	60	35.8	5.47%	0.00%	4.0	0.44
[14]	test nº21	30x45	ASTM E119	180	35.8	5.47%	0.00%	4.0	0.44
[14]	test nº30	20x30	ASTM E119	60	71.6	1.90%	0.00%	4.0	0.42
[14]	test nº35	20x30	ASTM E119	60	65.7	3.80%	0.00%	4.0	0.41
[14]	test nº25	30x45	ASTM E119	180	35.8	5.47%	0.52%	4.0	0.44
[20]	L4	25x40	ISO 834	60	41.2	1.47%	0.00%	2.2	0.36
[21]	L4	20x30	ISO 834	60	51.5	3.27%	0.17%	2.7	0.50
[28]	B5-2.1-f120	25x40	ISO 834	120	31.6	1.96%	0.00%	2.1	0.21
[28]	B5-2.1-f60	25x40	ISO 834	60	31.6	1.96%	0.00%	2.1	0.21
[28]	B5-2.1-f90	25x40	ISO 834	90	31.6	1.96%	0.00%	2.1	0.21
[28]	B6-2.1-f90	25x40	ISO 834	90	31.6	1.61%	0.00%	2.1	0.21
[28]	B7-2.1-f90	25x40	ISO 834	90	31.6	1.47%	0.00%	2.1	0.21
[28]	B4-2.1-f90	25x40	ISO 834	90	31.6	1.96%	0.20%	2.1	0.21
[28]	B1-2.1-f120	25x40	ISO 834	120	31.6	1.96%	0.27%	2.1	0.21
[28]	B1-2.1-f60	25x40	ISO 834	60	31.6	1.96%	0.27%	2.1	0.21
[28]	B1-2.1-f90	25x40	ISO 834	90	31.6	1.96%	0.27%	2.1	0.21
[28]	B2-2.1-f90	25x40	ISO 834	90	31.6	1.61%	0.27%	2.1	0.21
[28]	B3-2.1-f90	25x40	ISO 834	90	31.6	1.47%	0.27%	2.1	0.21
[28]	B5-2.6-f90	25x40	ISO 834	90	31.6	1.96%	0.00%	2.6	0.26
[28]	B1-2.6-f90	25x40	ISO 834	90	31.6	1.96%	0.27%	2.6	0.26
[28]	B5-3.3-f90	25x40	ISO 834	90	31.6	1.96%	0.00%	3.3	0.32
[28]	B1-3.3-f90	25x40	ISO 834	90	31.6	1.96%	0.27%	3.3	0.32

* ρ_t =0.00%: no stirrups

A relevant parameter is the ratio (a/d) that can modify the shear failure mode in reinforced concrete beams, as highlighted by Nakamura et al. [29]. Plasencia et al. [30] state that the failure of beams with ratio ($a/d<2$) was due to the rupture of the compression strut. This behavior was also observed in the post-fire shear capacity based on the experimental data presented, where the residual strength was influenced by the distance of the load applied to the support (a), effective height (d) and free span of the beam (L).

It is pertinent to observe that the formulations consider the shear span ($\xi = a/d$) and the ration (a/L) in the expressions to contemplate the "arc effect" that is promoted by the distance between the applied load and the support. It is also observed that the presence of stirrups changes the behavior of reinforced concrete beams, the calculation method being different for beams with or without transverse reinforcement.

3 PROPOSED PROCEDURE

The 500°C Isotherm method is applied to estimate the behaviour in fire situation and not to estimate the residual load bearing capacity of RC beams. The purpose of this paper is to extrapolate and verify its applicability in post fire situation.

The simplified method proved to be applicable to estimate the residual strength of RC beams independent of two important phenomena of concrete: (1) strength of concrete preheated to high temperature is after cooling (residual strength) lower than the strength at high temperature [31] and (2) concrete exposed to simultaneous action of high temperature and compressive stresses loses its strength much slower than concrete heated only (without compression) [32].

Figure 2 shows a flowchart for determining the residual strength of RC beams.

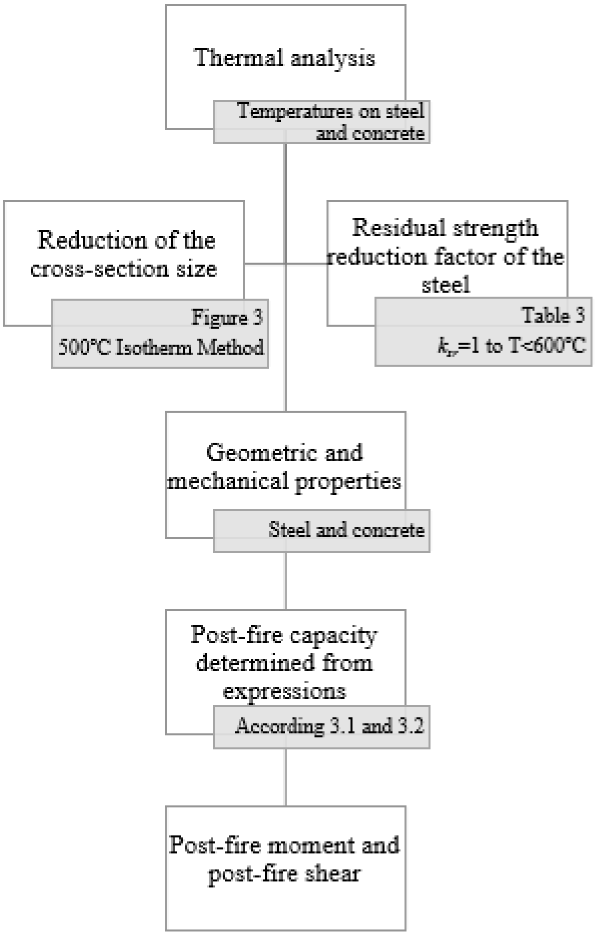

Figure 2. Procedure for determining residual strength

Thermal analyses are conducted first to obtain the temperature evolution in the cross section determined by FEM, through ABAQUS software, with 2D elements of 4 nodes (DC2D4) and 10x10mm mesh. The model accounts for the properties changes with the increase in temperature, considering the variation in conductivity and specific heat of the concrete (1.5% humidity) according to NBR15200 [9], as well as the emissivity of 0.7 and the heat transfer coefficient per convection of 25W/m²ºC.

The residual strength for the concrete was determined according to the 500ºC Isotherm Method [11]. In Figure 3, it is possible to identify the variables for a beam with three faces exposed to fire, where b_{fi} : it is the reduced width of the beam after fire (cm); d_{fi} : is the effective height of the beam after fire (cm); d_{500} : depth of the 500ºC isotherm (cm).

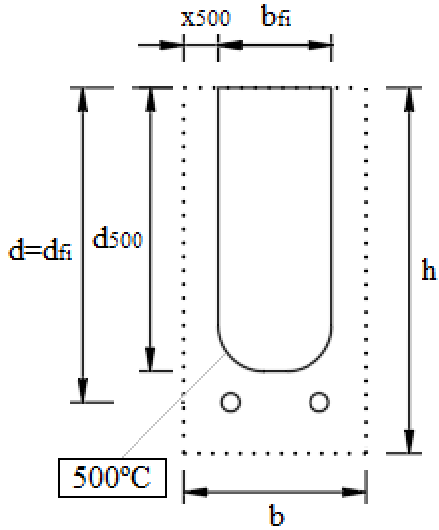

Figure 3. 500ºC Isotherm. (Source: Adapted [11])

Steel reinforcement bars have reduced strength using reduction factors (k_{sr}) proposed in Van Coile et al. [5] determined by a stochastic model based on experimental results, as shown in Table 3.

Table 3. Reduction factor for residual strength of steel

T (ºC)	20	50	100	200	400	550	600	700	850
k_{sr}	1	1	1	1	1	1	1	0.7	0.6

Source: Adapted from [5]

It is possible to notice that after fire, the steel reinforcement has a good capacity to recover its initial strength for temperatures up to 600ºC.

The longitudinal steel bars have the temperature measured on their axis, and the respective reducing coefficient is applied. The transverse steel bars had the reduction factor as a function of temperature at the point recommended in Eurocode 2 1-1 [33] to find point "P" at height $h_{c,ef}$ whose value is given by Equation 1:

$$h_{c,ef} = \min\left[2.5\left(h - d_{500}\right), \frac{\left(h - y_\theta\right)}{3}, \frac{h}{2}\right] \tag{1}$$

Where: $h_{c,ef}$: is the height at point P from the beam bottom (cm); h : is the height of the beam (cm); y_θ : is the position of the neutral axis after a fire (cm).

The height ($h_{c,ef}$) refers to the region where the first shear cracks tend to appear. Other authors such as Xiang et al. [34] used the temperature at mean height of the stirrup and Diab [8] and Cai et al. [25] used the average over the height of the stirrup.

3.1 Post-fire moment capacity

The post-fire bending moment is determined from the 500ºC isotherm depth (d_{500}), width of the reduced section (b_{fi}) and the effective depth (d_{fi}) which remains the same as the cross section at room temperature. Figure 4 shows the balance of forces in the bending section.

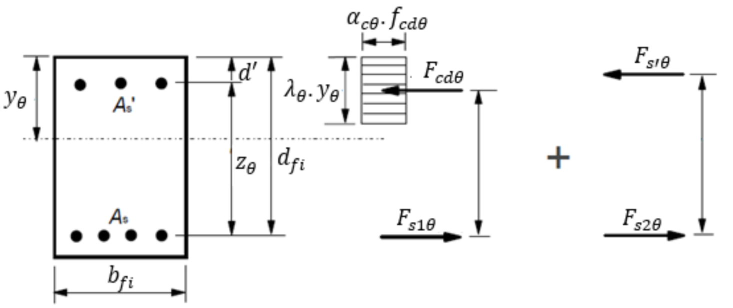

Figure 4. Equilibrium of forces in the bending section. (Source: Adapted [9])

Applying the balance of forces in the cross section, the concrete and steel forces can be calculated, in a procedure like the guidelines of NBR 6118 [35]. The coefficients α_c, γ_c e γ_s were adopted equal to 1 and λ_θ equal to 0.8.

3.2 **Post-fire shear capacity**

The estimated of the residual shear capacity after fire was based on the Model I proposed by the Brazilian standard [35] at room temperature that follows the model of classic truss with stirrups at 90º and compression struts at 45º.

Equations 2 to 7 presented below were adjusted based on the observation of the experimental behavior of the beams analyzed and include the relationships ($\xi = a/d$) and (a/L) in the formulation, discussed in section 2.

a) For beams without stirrups ($V_r^{ana} = V_{c\theta}$ *)*

$$V_{c\theta} = \frac{V_{Rd2}}{\xi}, \quad \xi \le 2 \text{ The failure occurs in the compression strut of concrete with a value proportional to } \xi. \tag{2}$$

$V_{c0} \cdot \xi^{-a/L}$, $\quad 2 < \xi \le 3.5$ The rupture occurs in the diagonal tension under the influence of a.

V_{c0}, $\quad \xi > 3.5$ Concrete is not influenced by ξ.

Where:

$$V_{c0} = 0.6 \cdot \frac{f_{ct}}{\gamma_c} \cdot b_{fi} \cdot d_{500} \tag{3}$$

$$V_{Rd2} = 0.27 \cdot \alpha_{v2} \cdot \frac{f_{ck}}{\gamma_c} \cdot b_{fi} \cdot d_{500} \tag{4}$$

$$\alpha_{v2} = 1 - \frac{f_{ck}}{250} \tag{5}$$

Where: V_r^{ana} : is the residual shear force; V_{Rd2} : is the shear force relative to the compression strut of concrete; V_{c0} : it is part resisted by complementary mechanisms.

b) For beams with stirrups ($V_r^{ana} = V_{R\theta}$ *)*

In the case of deep beams ($\xi \le 2$) with shear reinforcement, the contribution of steel is reduced to smaller ξ. (Hayashikawa et al. [36] apud Nakamura et al. [29]).

$V_{R\theta} =$

$$\frac{V_{Rd2}}{\xi^{1+a/L}} + \frac{V_{sw}}{\xi}, \ \xi \le 2$$

Shear capacity provided by compressive strength of the concrete in the strut and the steel loses efficiency due to the proximity of the load applied with the support.

$$\frac{V_{c0}}{\xi^{1-a/L}} + V_{sw}, \ 2 < \xi \le 3.5 \tag{6}$$

Shear capacity provided by complementary mechanisms of concrete and steel has its effective contribution.

$$V_{c0} + V_{sw}, \ \xi > 3.5$$

Concrete and steel are not influenced by ξ.

$$V_{sw} = \frac{A_{sw}}{s} \cdot k_{sr} \cdot \frac{f_{yk}}{\gamma_s} \cdot d_{500} \tag{7}$$

Where: V_{sw} : shear capacity provided by shear reinforcement. The coefficients γ_c and γ_s equal to 1.

4 RESULTS AND DISCUSSIONS

4.1 Post-fire moment capacity

Table 4 presents the results found for the residual bending moment and the relationships M_r^{ana} / M_r^{exp} between the analytical model and the experimental data.

Table 4. Analytical and experimental results for bending moment

Ref.	ID.	M_r^{exp}	M_{r1}^{ana}	M_{r1}^{ana} / M_r^{exp}
-	-	(kNm)	(kNm)	-
[20]	L5	196.0	210.9	1.08
[20]	L6	200.0	210.9	1.05
[20]	L7	197.0	210.9	1.07
[20]	L9	167.0	169.6	1.02
[26]	REC15_210	13.1	10.5	0.80
[26]	REC30_210	12.2	10.6	0.87
[7]	M20-60	9.2	11.8	1.28
[7]	M20-120	6.5	8.1	1.24

Table 4. Continued…

Ref.	ID.	M_r^{exp}	M_{r1}^{ana}	M_{r1}^{ana} / M_r^{exp}
-	-	(kNm)	(kNm)	-
[7]	M20-180	5.6	6.9	1.23
[7]	M20-240	5.2	6.0	1.16
[7]	M30-60	11.3	12.0	1.06
[7]	M30-120	7.5	8.2	1.09
[7]	M30-180	5.8	7.0	1.21
[7]	M30-240	4.9	6.1	1.24
[7]	M40-60	13.6	12.2	0.89
[7]	M40-120	8.7	8.3	0.95
[7]	M40-180	7.0	7.1	1.01
[7]	M40-240	5.5	6.2	1.12
[7]	M50-60	15.8	12.3	0.78
[7]	M50-120	9.8	8.3	0.85
[7]	M50-180	8.0	7.1	0.89
[7]	M50-240	6.9	6.2	0.90
		Mean		*1.04*
		Standard Deviation		*0.15*
		Confidence Interval		*0.98-1.08*

The analytical-experimental results compiled in Table 4 result in an average ratio M_{r1}^{ana} / M_r^{exp} of 1.04 with a standard deviation of 0.15. The confidence interval was calculated with a 95% confidence level. Figure 5 plots the residual strength compared to the safety margin of ± 10%. Some samples of [7] showed a $M_{r1}^{ana} / M_r^{exp} > 1.2$ ratio, which may have been caused by the small cross-sectional dimensions of the beams and because exposure to the fire curve for a longer time.

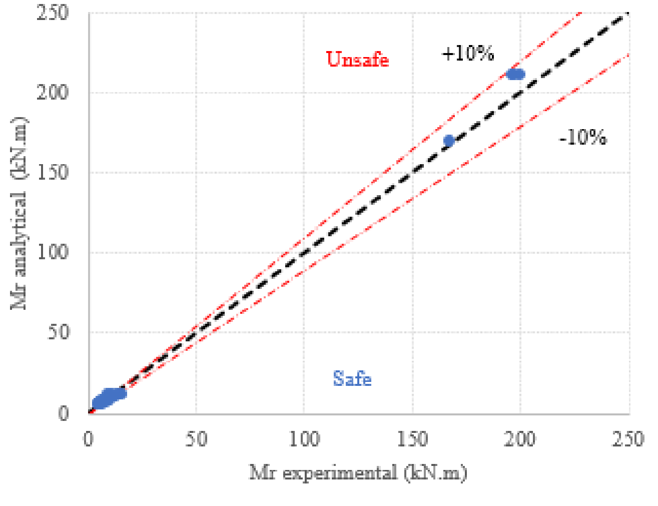

Figure 5. Post-fire moment capacity: analytical vs. experimental.

Figure 6 presents the results without the data from [20], which allows to analyze in more detail the group of beams that had a lower failure load and that consist of most of the data. The difference between the moments is justified by the large width dimension of the cross section (25x40cm) of the samples from [20].

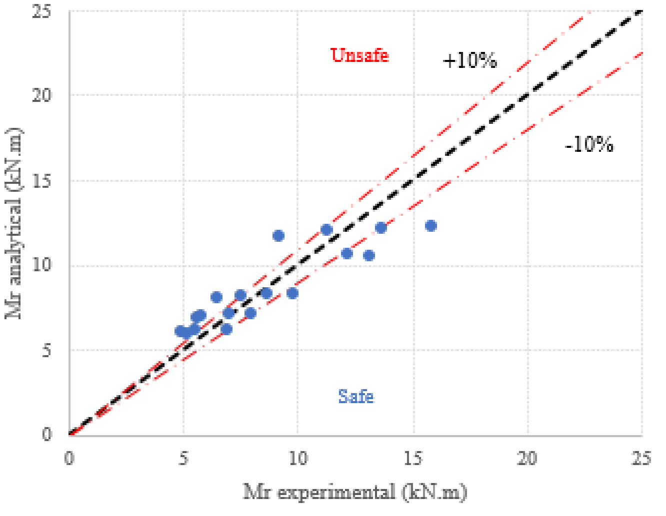

Figure 6. Post-fire moment capacity: analytical vs. experimental.

It is noteworthy to point that 14 beams showed a ratio $M_{r1}^{ana} / M_{r}^{exp}$ greater than 1, with an average value of 1.13.

It is suggested, then, the proposition of a correction factor equal to 1.2 to match the model results, resulting in an average ratio $M_{r2}^{ana} / M_{r}^{exp}$ of 0.86 with a standard deviation of 0.13. Figure 7 shows the results corrected by the coefficient.

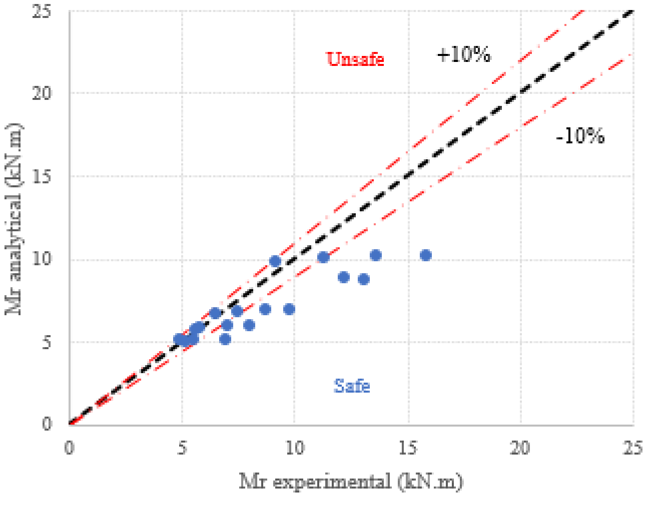

Figure 7. Post-fire moment capacity: analytical vs. experimental.

A total of 5 beams (22.72%) presented analytical results with ratio $M_{r2}^{ana} / M_{r}^{exp}$ greater than 1, with an average value of 1.04 and coefficient of variation of 1.92%. No value was greater than the safety margin of 1.1. According to Coelho et al. [37], even though this may indicate that the results are less safe, they converge with the philosophy presented in the Eurocodes, where a prediction model must predict the phenomenon on its average, with the security of the model provided by safety factors. Therefore, the analytical procedure to measure the residual bending moment in reinforced concrete beams after fire, although simplified, can predict the bending resistance of beams after fire.

4.2 Post-fire shear capacity

Table 5 presents the results found for the shear by the analytical model compared to the experimental results through the ratio $V_{r1}^{ana} / V_{r}^{exp}$.

Table 5. Analytical and experimental results for shear force

Ref.	ID.	V_r^{exp}	V_{r1}^{ana}	V_{r1}^{ana} / V_r^{exp}
-	-	(kN)	(kN)	-
[24]	V120	47.4	45.9	0.97
[24]	V60	71.9	71.7	1.00
[24]	V90	61.9	55.0	0.89
[11]	test nº17	468.3	484.1	1.03
[11]	test nº18	279.0	387.3	1.39
[11]	test nº2	213.9	209.8	0.98
[11]	test nº27	337.5	321.9	0.95
[11]	test nº28	229.5	136.7	0.60
[11]	test nº3	188.8	87.1	0.46
[11]	test nº32	471.4	312.3	0.66
[11]	test nº33	246.5	140.5	0.57
[11]	test nº8	321.0	198.8	0.62
[11]	test nº9	220.7	89.4	0.41
[11]	test nº14	270.6	326.4	1.21
[11]	test nº15	243.1	139.7	0.57
[11]	test nº23	467.6	462.3	0.99
[11]	test nº11	89.2	49.3	0.55
[11]	test nº12	41.3	22.2	0.54
[11]	test nº20	211.9	123.2	0.58
[11]	test nº21	117.2	98.5	0.84
[11]	test nº30	89.8	75.8	0.84
[11]	test nº35	130.3	67.5	0.52
[11]	test nº25	311.1	195.6	0.63
[17]	L4	97.0	80.0	0.82
[18]	L4	147.0	50.4	0.34
[25]	B5-2.1-f120	60.0	65.1	1.08
[25]	B5-2.1-f60	80.0	76.6	0.96
[25]	B5-2.1-f90	71.3	72.8	1.02
[25]	B6-2.1-f90	79.0	72.8	0.92
[25]	B7-2.1-f90	80.0	72.8	0.91
[25]	B4-2.1-f90	132.5	114.7	0.87

Table 5. Continued…

Ref.	ID.	V_r^{exp}	V_{r1}^{ana}	V_{r1}^{ana} / V_r^{exp}
-	-	(kN)	(kN)	-
[25]	B1-2.1-f120	132.5	132.4	1.00
[25]	B1-2.1-f60	145.0	139.8	0.96
[25]	B1-2.1-f90	137.5	137.3	1.00
[25]	B2-2.1-f90	135.0	137.3	1.02
[25]	B3-2.1-f90	130.0	137.3	1.06
[25]	B5-2.6-f90	70.0	66.4	0.95
[25]	B1-2.6-f90	125.0	131.9	1.06
[25]	B5-3.3-f90	55.0	57.5	1.05
[25]	B1-3.3-f90	115.0	128.1	1.10
		Mean		0.85
		Standard deviation		0.23
		Confidence Interval		0.78-0.92

Figure 8 presents the results found experimentally and analytically for all the beams analyzed.

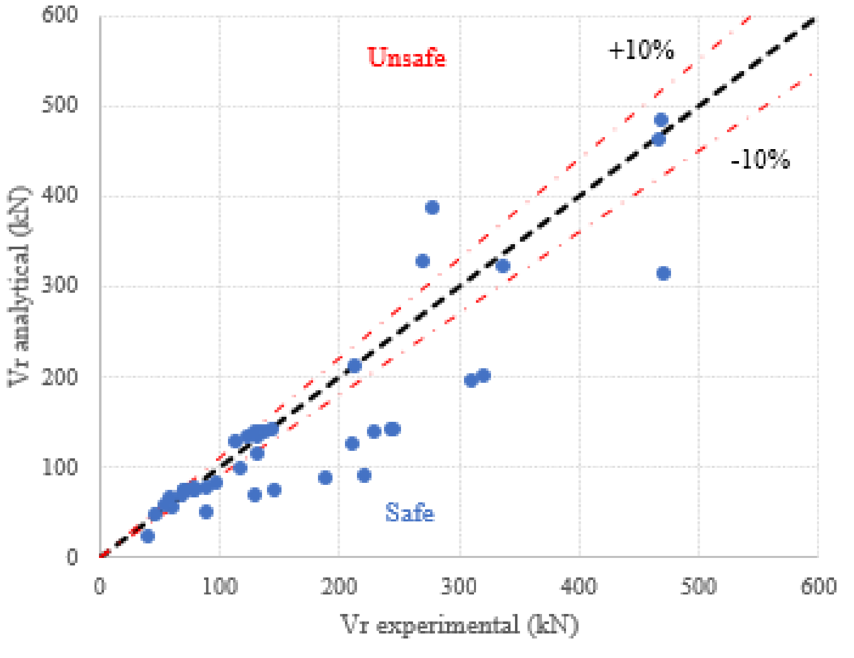

Figure 8. Residual shear force: analytical vs. experimental.

Analyzing the data in Table 5, it is possible to find an average ratio of $V_{r1}^{ana} / V_r^{exp} = 0.85$ and an average standard deviation of 0.23. The confidence interval was calculated with a 95% confidence level. A total of 47.5% of the beams are within the range V_{r1}^{ana} / V_r^{exp} of 0.90 and 1.10 and only two beams (5%) outside the adopted safety margin ($V_{r1}^{ana} / V_r^{exp} > 1.1$): the samples "test nº14" and "test nº18".

The results showed to be more conservative for samples submitted to longer fire times (180min), however, due to the sudden and undesirable shear failure, it is prudent that the procedure has this premise. The analytical proposal, therefore, succeeds to estimate with reasonable precision and with safety the residual shear capacity of reinforced concrete beams after fire.

5 CONCLUSIONS

The study evaluated an analytical procedure for determining residual capacity for the bending moment and shear force of reinforced concrete beams after fire. The proposal was evaluated from experimental results of 62 reinforced concrete beams available in the literature. With the results, it is possible to conclude:

- The 500ºC isotherm method associated with the reduction coefficients presented here allows the assessment of residual strength to the bending moment with a correction factor of 1.2;
- The shear residual capacity to considering the influence of the ratio (a/d) applied to the 500ºC isotherm method and associated with the reduction coefficients presented here made it possible to predict shear capacity without the need for a correction factor;
- Shear capacity after fire can become the primary failure mode and needs to be considered in the analysis of strength after fire.

REFERENCES

[1] Y. Yang, S. Feng, Y. Xue, Y. Yu, H. Wang, and Y. Chen, "Experimental study on shear behavior of fire-damaged reinforced concrete T-beams retrofitted with prestressed steel straps," *Constr. Build. Mater.*, vol. 209, pp. 644–654, 2019, http://dx.doi.org/10.1016/j.conbuildmat.2019.03.054.

[2] J. Wróblewska and R. Kowalski, "Assessing concrete strength in fire-damaged structures," *Constr. Build. Mater.*, vol. 254, pp. 119122, 2020, http://dx.doi.org/10.1016/j.conbuildmat.2020.119122.

[3] M. Usman, M. Yaqub, M. Auzair, W. Khaliq, M. Noman, and A. Afaq, "Restorability of strength and stiffness of fire damaged concrete using various composite confinement techniques," *Constr. Build. Mater.*, vol. 272, pp. 121984, 2021, http://dx.doi.org/10.1016/j.conbuildmat.2020.121984.

[4] I. C. Neves, J. C. Rodrigues, and A. P. Loureiro, "Mechanical properties of reinforcing and prestressing steels after heating," *J. Mater. Civ. Eng.*, vol. 8, no. 4, pp. 189–194, 1996, http://dx.doi.org/10.1061/(ASCE)0899-1561(1996)8:4(189).

[5] R. Van Coile, R. Caspeele, and L. Taerwe, "Towards a reliability-based post-fire assessment method for concrete slabs incorporating information from inspection," *Struct. Concr.*, vol. 15, no. 3, pp. 395–407, 2014, http://dx.doi.org/10.1002/suco.201300084.

[6] T. Molkens, R. Van Coile, and T. Gernay, "Assessment of damage and residual load bearing capacity of a concrete slab after fire: Applied reliability-based methodology," *Eng. Struct.*, vol. 150, pp. 969–985, 2017, http://dx.doi.org/10.1016/j.engstruct.2017.07.078.

[7] D. P. Thanaraj, N. Anand, P. Arulraj, and K. Al-Jabri, "Investigation on structural and thermal performance of reinforced concrete beams exposed to standard fire," *J. Build. Eng.*, vol. 32, pp. 101764, 2020, http://dx.doi.org/10.1016/j.jobe.2020.101764.

[8] M. Diab, "Shear capacity of reinforced concrete beams at elevated temperatures," M.S. thesis, The Sch. Graduate and Postdoc. Stud., Western Univ.London, Ontario, Canada, 2014.

[9] Associação Brasileira de Normas Técnicas, *Projeto de Estruturas de Concreto em Situação de Incêndio*, NBR 15200, 2012.

[10] European Committee for Standardization, *Eurocode 1: Actions on Structures - Part 1-2: General Actions – Actions on Structures Exposed to Fire*, EN 1991-1-2, 2002.

[11] European Committee for Standardization, *Eurocode 2: Design of Concrete Structures - Part 1-2: General Rules – Structural Fire Design*, EN 1992-1-2, 2004.

[12] M. S. Cülfik and T. Özturan, "Effect of elevated temperatures on the residual mechanical properties of high-performance mortar," *Cement Concr. Res.*, vol. 32, no. 5, pp. 809–816, 2002, http://dx.doi.org/10.1016/S0008-8846(02)00709-3.

[13] F. Sciarretta, "Modeling of mechanical damage in traditional brickwork walls after fire exposure," *Adv. Mat. Res.*, vol. 919-921, pp. 495–499, 2014, http://dx.doi.org/10.4028/www.scientific.net/AMR.919-921.495.

[14] J. H. Hsu and C. S. Lin, "Effect of fire on the residual mechanical properties and structural performance of reinforced concrete beams," *J. Fire Prot. Eng.*, vol. 18, no. 4, pp. 245–274, Nov 2008, http://dx.doi.org/10.1177/1042391507077171.

[15] American Concrete Institute. *Building Code Requirements for Structural Concrete and Commentary*, ACI 318R-02, 2002.

[16] V. K. R. Kodur, M. B. Dwaikat, and R. S. Fike, "An approach for evaluating the residual strength of fire-exposed RC beams," *Mag. Concr. Res.*, vol. 62, no. 7, pp. 479–488, 2010, http://dx.doi.org/10.1680/macr.2010.62.7.479.

[17] American Concrete Institute, *Building Code Requirements for Reinforced Concrete*, ACI 318-08, 2008.

[18] L. Bai and Z. Wang, "Residual bearing capacity of reinforced concrete member after exposure to high temperature," *Adv. Mat. Res.*, vol. 368, no. 373, pp. 577–581, Oct 2011, http://dx.doi.org/10.4028/www.scientific.net/AMR.368-373.577.

[19] Y. Xu, B. Wu, M. Jiang, and X. Huang, "Experimental study on residual flexural behavior of reinforced concrete beams after exposure to fire," *Adv. Mat. Res.*, vol. 457-458, pp. 183–187, Jan 2012. [Online]. Available: 10.4028/www.scientific.net/AMR.457-458.183

[20] Y. Xu, B. Wu, R. Wang, M. Jiang, and Y. Luo, "Experimental study on residual performance of reinforced concrete beams after fire," *J. Build. Struct.*, vol. 34, no. 8, 2013.

[21] Y. Xu, X. Peng, Y. Dong, Y. Luo, and B. Lin, "Experimental study on shear behavior of reinforced concrete beams strengthened with CFRP sheet after fire," *J. Build. Struct. China*, vol. 36, no. 2, 2015. http://dx.doi.org/10.14006/j.jzjgxb.2015.02.015.

[22] GB, *Code for Design of Concrete Structures*, GB 50010, 2010.

[23] V. K. R. Kodur and A. Agrawal, "An approach for evaluating residual capacity of reinforced concrete beams exposed to fire," *Eng. Struct.*, vol. 110, pp. 293–306, Nov 2016, http://dx.doi.org/10.1016/j.engstruct.2015.11.047.

[24] R. Sun, B. Xie, R. Perera, and Y. Pan, "Modeling of reinforced concrete beams exposed to fire by using a spectral approach," *Adv. Mater. Sci. Eng.*, vol. 2018, pp. 1–12, 2018, http://dx.doi.org/10.1155/2018/6936371.

[25] B. Cai, L.-F. Xu, and F. Fu, "Shear resistance prediction of post-fire reinforced concrete beams using artificial neural network," *Int. J. Concr. Struct. Mater.*, vol. 13, no. 1, pp. 46, 2019, http://dx.doi.org/10.1186/s40069-019-0358-8.

[26] R. G. Pereira, T. A. C. Pires, D. C. L. Duarte, and J. J. R. Silva, "Assess of residual mechanical resistance of reinforced concrete beams after fire," *Rev. ALCONPAT*, vol. 9, no. 1, 2018, http://dx.doi.org/10.21041/ra.v9i1.299.

[27] A. Kumar and V. Kumar, "Behaviour of RCC beams after exposure to elevated temperatures," *J. Inst. Eng.*, vol. 84, pp. 165–170, 2003.

[28] Y. Song et al., "Residual shear capacity of reinforced concrete beams after fire exposure," *KSCE J. Civ. Eng.*, vol. 24, no. 11, pp. 3330–3341, 2020, http://dx.doi.org/10.1007/s12205-020-1758-7.

[29] H. Nakamura, T. Iwamoto, L. Fu, Y. Yamamoto, T. Miura, and Y. H. Gedik, "Shear resistance mechanism evaluation of RC beams based on arch and beam actions," *J. Adv. Concr. Technol.*, vol. 16, no. 11, pp. 563–576, Nov 2018, http://dx.doi.org/10.3151/jact.16.563.

[30] G. R. Plasencia, J. D. B. Rocha, J. J. H. Santana, and L. Pudipedi, "Study of the behavior of reinforced concrete deep beams: estimate of the ultime shear capacity," *Rev. Constr.*, vol. 16, no. 1, 2017. http://dx.doi.org/10.7764/RDLC.16.1.43.

[31] R. Kowalski and P. Król, “Experimental examination of residual load bearing capacity of RC beams heated up to high temperature,” in *Proc. 6th Int. Conf. Struct. Fire*, East Lansing, Michigan, USA, 2010, pp. 254–261

[32] M. Głowacki and R. Kowalski, "An experimental approach to the estimation of stiffness changes in RC elements exposed to bending and high temperature," *Eng. Struct.*, vol. 217, pp. 110720, 2020., http://dx.doi.org/10.1016/j.engstruct.2020.110720.

[33] European Committee for Standardization, *Eurocode 2 – Design of Concrete Structures – Part 1-2: General Rules – Structural Fire Design*, EN 1992-1-1, 2004.

[34] K. Xiang, G. Wang, and H. Liu, "Shear strength of reinforced concrete beams after fire," *Appl. Mech. Mater.*, vol. 256-259, pp. 742–748, Dec 2012, http://dx.doi.org/10.4028/www.scientific.net/AMM.256-259.742.

[35] Associação Brasileira de Normas Técnicas, *Projeto de Estruturas de Concreto – Procedimento*, NBR 6118, 2014.

[36] T. Hayashikawa, F. Saido, and I. Higai, "Strength of RC deep beams with shear reinforcement," *Proc. Jpn. Concr. Inst.*, vol. 12, no. 2, pp. 319–324, 1990. In Japanese.

[37] M. R. F. Coelho, J. M. Sena-Cruz, and L. A. C. Neves, "Review on the bond behavior of FRP NSM systems in concrete," *Constr. Build. Mater.*, vol. 93, pp. 1157–1169, Sep 2015., http://dx.doi.org/10.1016/j.conbuildmat.2015.05.010.

Author contributions: LMC: conceptualization, methodology, bibliographic research, data analysis; JJRS: conceptualization, methodology, drafting, supervision; TACP: conceptualization, supervision, drafting and formal analysis, DCLD: writing and formal analysis.

Editors: Fernando S. Fonseca, Guilherme Aris Parsekian.

IBRACON Structures and Materials Journal
Revista IBRACON de Estruturas e Materiais
ISSN 1983-4195 ismj.org

ORIGINAL ARTICLE

Computational and experimental simulation to analyze loss in concrete cover by reinforcement deformation in solid slabs

Simulação computacional e experimental para análise de perdas no cobrimento de concreto por deformação da armadura em lajes maciças

Ana Paula Maran[a]
Maria Fernanda Fávero Menna Barreto[a]
Denise Carpena Coitinho Dal Molin[a]
João Ricardo Masuero[a]

[a]Universidade Federal do Rio Grande do Sul – UFRGS, Programa de Pós-graduação em Engenharia Civil – PPGCI, Porto Alegre, RS, Brasil

Received 05 November 2020
Accepted 04 August 2021

Abstract: Adequate cover thickness contributes to the correct performance of reinforced concrete structures. Spacers are recommended in standards to maintain a concrete cover; however, many regulations do not provide sufficient guidelines for their use, resulting in poor construction. A research program was developed for solid slabs through computational and experimental simulations to minimize errors in the cover by assessing different reinforcement bar diameters and spacer distribution, considering realistic element construction and standards, combining theory with practice. The results show that the use of spacers does not guarantee the design cover for some reinforcement bar diameters, as 4.2 and 5.0 mm, and regardless of the spacer distribution configuration assessed, these meshes undergo permanent deformation, thereby damaging the cover and consequently impact structural performance. Meshes of 6.3 and 8.0 mm diameters present deformation within the cover tolerance. Therefore, it is preferable to choose bigger diameters and larger mesh spacing to guarantee the projected cover, contributing to the correct performance of the structures, solving one of the major problems in this type of construction.

Keywords: cover thickness, concrete cover, spacers, simulation.

Resumo: A espessura de cobrimento adequada contribui para o desempenho das estruturas de concreto armado. Espaçadores são recomendados por normas para obter o cobrimento de concreto, entretanto, muitas dessas normas não fornecem informações suficientes para o uso destes dispositivos, resultando em falhas de construção. O programa deste trabalho foi desenvolvido para lajes maciças através de simulação computacional e experimental, como forma de minimizar erros de cobrimento avaliando diferentes diâmetros de armadura e distribuições de espaçadores, considerando a construção do elemento e as normas vigentes, combinando teoria e prática. Os resultados mostraram que o uso de espaçadores não garante o cobrimento de armadura para algumas malhas de armadura, como 4,2 e 5,0 mm, independentemente da distribuição de espaçadores avaliada, essas malhas sofrem deformação permanente elevada e, consequentemente, impactam no desempenho estrutural. Malhas com barras de diâmetro 6,3 e 8,0 mm apresentaram deformações dentro da tolerância de execução. Assim, é preferível optar pela utilização de malhas mais abertas com diâmetros maiores apara garantir o cobrimento especificado em projeto, contribuindo para o correto desempenho das estruturas, auxiliando um dos maiores problemas neste tipo de construção.

Palavras-chave: espessura de cobrimento, cobrimento de concreto, espaçadores, simulação.

How to cite: A. P. Maran, M. F. F. Menna Barreto, D. C. C. Dal Molin, and J. R. Masuero, "Computational and experimental simulation to analyze loss in concrete cover by reinforcement deformation in solid slabs," *Rev. IBRACON Estrut. Mater.*, vol. 15, no. 2, e15203, 2022, https://doi.org/10.1590/S1983-41952022000200003

Corresponding author: Ana Paula Maran. E-mail: anapaulamaran@gmail.com
Financial support: This work was supported by the Coordenação de Aperfeiçoamento de Pessoal de Nível Superior – CAPES, and the Conselho Nacional de Desenvolvimento Científico e Tecnológico – CNPq. The participation of A. P. Maran was sponsored by CAPES grant number 88882.439894/2019-01; M. F. F. Menna Barreto was sponsored by CNPq grant number 142266/2018-3 and CAPES grant number 88882.439905/2019-01.
Conflict of interest: Nothing to declare.

1 INTRODUCTION

A durable reinforced concrete structure should maintain its original shape, quality, and ease of maintenance when exposed in the environment throughout its projected service life [1]. To protect against aggressive agents, the reinforcement is encased in a concrete cover layer [2], [3], which is defined as the distance between the outer face of the structural member to the nearest bar, including the stirrup and secondary reinforcement [4], [5]. The minimum cover implemented should ensure safe transmission of bond forces, protection of steel bars against corrosion (durability) and adequate fire resistance [6].

The end of the service life of the structure or structural component is associated, among other factors, with the loss of the protection capacity of the concrete cover [3], [7]. Thus, several analysis are developed to predict the effect of the penetration of aggressive agents on the structure, as well as its durability, to assist in prevention strategies [8], [9]. Most models of service-life prediction are correlated with durability and, subsequently, cover.

The cover protection provided is only achieved by the adequate quality of the concrete (composition, production, transport, concreting, thickening, finishing and curing) and sufficient thickness (quality and distribution of the spacers) [10], [11].

The cover thickness specified in the project is related to the environmental aggressiveness class and intended working life, varying according to the standards applied in each country. For reinforced concrete slabs with at least 50 years of service life: in Brazil, nominal standardized covers vary from 20 mm to 45 mm [12]; in the U.K., from 25 mm to 60 mm [13]; and in the U.S.A., from 20 in to 75 in [4]. Moreover, such covers require a minimum execution tolerance. This tolerance, in standards, is usually related to quality and execution controls [6], [12]–[14], with inspections that include measurements of the cover, and could also be associated with the effective depth of the element [4].

Spacers are used in concrete structures to support the reinforcement and construction loads during construction, so that the required concrete cover is achieved [15], [16]. They are mentioned in the main design and execution standards for reinforced concrete structures [5], [12], [17]–[23], consisting of an essential component that is placed and left permanently in the structure in large quantities [24]–[26]. Despite its importance, limited studies have investigated the effect of spacers on the concrete structures [25], [26].

Some aspects should be considered when choosing the spacer type to be used, such as the product performance [11], the structural element to be concreted, the reinforcement characteristics [10]. Also, the spacer correct quantity and position are essential because the distance between them has a significant influence on the final cover in slabs [27]. Their distribution should consider that an excessive spacing between spacers could cause bars to flex, especially during concreting process. On the other hand, scarce spacer distances promote higher consumption of this material, spending more money, and introducing more points of weakness in the system [15], [25], [26], [28].

For slabs, the normative recommendations indicate a maximum distance of 50Ø (50 times the reinforcement diameter) limited to 100 cm for positive reinforcement, and a maximum distance of 50Ø (50 times the reinforcement diameter) limited to 50 cm for negative reinforcement [17], [19], [29].

Noncompliance in the cover thickness can be related to several factors, such as defects in design and detailing, execution, or materials supply [30]. Such factors interact with one another, so the failure in one could compromise the system [31]. For example, failure to indicate standardized specifications in the project could accumulate successive errors starting from the design stage [32].

Many researchers report the failure to obtain the cover thickness specified in the current reinforced concrete structure constructions [27], [30], [31], [33], [34], where the probability of inefficient cover varies between 38.7% and 88.8% in solid slabs [30]. In general, the design reinforcement position is not achieved even before construction [35].

Among the structural elements, the slabs are one of the most damaged elements as a result of insufficient cover thickness [27]. Unsatisfactory covers could be a consequence of uneven placement or insufficient quantity of spacers, lack of formwork leveling [35], [36], spacers with a poor performance [11], wrong choice of spacers, or workers walking through the reinforcement meshes [34]. Furthermore, the minimum cover execution tolerance value of 5 mm, which is related to a good execution quality control, are not met, being directly related to the reduction of building durability [32], [34].

In this context, this study aims to assess the influence of standards' spacers distribution to obtain the concrete cover on solid slabs, considering the reinforcement plastic deformation occurred during the construction. Then, this deformation is compared and its effects are analyzed based on the designed cover thickness. All this, considering concrete construction practices (workers walking over the reinforcement before and during the concrete construction process) and accomplished by combining factors presented in regulatory references.

2 METHODS

To achieve the main goal, a computational simulation was developed to analyze the reinforcement deformation of a solid slab mesh under temporary construction loads. After that, an experimental simulation was performed in a laboratory to validate the computational simulation.

2.1 Computational simulation

The simulation was carried out by the Displacement Method.

The slabs were chosen because they are one of the hardest elements to obtain the intended design concrete cover [30] and due to their solid characteristic they are evaluated in a number of studies [30], [32], [34]–[37]. To perform this work, the slabs with 200 x 200 cm dimensions were cast with a reinforcement mesh spacing of 20 cm. This mesh spacing was chosen because it is the largest allowed by standards, and it represents the lower stiffness between the available mesh spacing. Therefore, any mesh with a spacing smaller than 20 x 20 cm is stiffer, having a better structural performance against the concrete cover.

The meshes were composed of steel for reinforced concrete with a tensile strength of 500 MPa and 600 MPa. The diameters of the bars were 4.2 mm, 5.0 mm, 6.3 mm and 8.0 mm. The 4.2 mm diameter is permitted in welded meshes and is more common in waffle slabs. This diameter is not typically used in solid slabs, however it was considered in this laboratory investigation because it is allowed by the standard [12]. The other diameters are frequently used in solid slabs [27], [34], [37]–[39] and were chosen for verification in structural design.

The concrete covers varied from 15 to 45 mm and are typically referenced in standards and used in design for this type of structure.

The construction loads can influence the permanent deformation of the steel bars, affecting the projected cover thickness due to direct contact with the reinforcement. A load of 1 kN was considered, representing a variable construction load, equivalent to the weight of a person plus tools [40], distributed evenly by reinforcement bar surface and idealized as a rectangle of 10 x 30 cm, representing a step of a worker walking on top of the reinforcement during the concrete construction process (Figure 1).

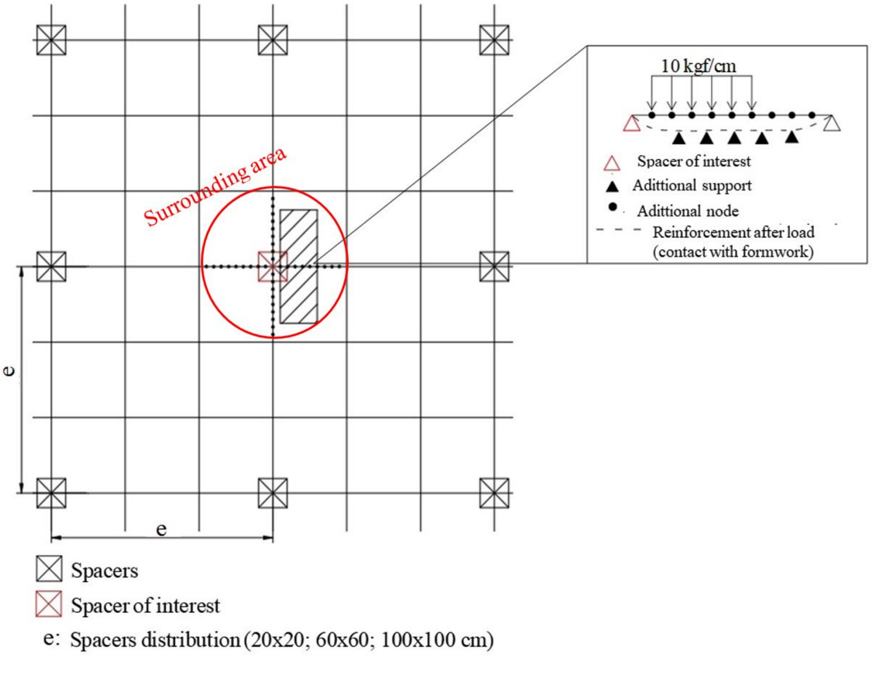

Figure 1. Load application and spacer distribution on the mesh.

Maran [32] simulated the load contribution of the wet concrete weight, and it was not considered in this study because it is minimal (0.0289 kg/cm) compared to a worker's weight (10 kg/cm). The same author reported that wet concrete weight was not significant due to their involvement and accommodation around the bars and the formwork, acting as a support for the reinforcement.

The load was applied near the spacer to consider it in only one steel bar (local effect), as a way to simulate the most critical load simulation in a more concentrated form of application. It was applied transversely to the reinforcement, equivalent to a linear load of 10 kgf/cm. The spacers were modeled as a pinned rigid support and their stiffness was not taken into account. The spacer of interest was modeled with displacement restriction in X, Y and Z directions in the mesh plane, while the other spacers had restriction only in the Y direction. The spacer distribution was made based on regulatory guidelines [17], [29]. The cover used for all configurations was 3.0 cm, as it allows a more significant displacement of the bars during the tests.

To perform the simulation, some variables were controlled that directly influence the mesh behavior, listed in Table 1.

Table 1. Variables considered in the simulation.

Variables	Levels	Units
Mesh opening	20	cm
Steel type	CA 60 and CA 50	
Reinforcement bar diameter	4.2; 5.0; 6.3; 8.0	mm
Load	10	kgf/cm
Standard spacer distribution	50Ø; Medium; 100	cm
Distribution of spacers	20x20; 60x60; 100x100	cm
Cover thickness	15; 20; 25; 30; 35; 40; 45	mm

The reinforcement mesh modeled considers a rigid union between the bars, with a coupling between torsion and bending. Nevertheless, the meshes were composed of independent steel bars with only one coupling against the vertical displacements due to the tying. To adjust this characteristic, the bar's torsional stiffness was reduced to a value close to zero. In the computer simulation, the load and displacement analysis was applied only to the lower bar of the mesh. The analyzed cover thickness included the nominal cover and the minimum cover (reduced permissible execution tolerances), to map the behavior of the mesh with the contact with the formwork.

The reinforcement mesh was modeled with nodes in the bar junctions. In the surrounding area of the central spacer, the analyzed reinforcement bars were modeled with segments of 2 cm as additional nodes, allowing, through links in these nodes, the simulation of additional formwork supports when the bar comes into contact with it (Figure 1).

If the displacement is less than the cover thickness, it means that the reinforcement does not lean against the formwork. Otherwise, if the displacement is more than the cover thickness, the steel bar leans against the formwork providing additional support and modifying the moments. As a solution, other additional supports with a prescribed displacement equal to the cover were added through iterative method update, simulating the contact of the reinforcement and the formwork.

The analysis was based on the bending moment generated by the construction load and its deformation, according to Figure 2 adopted for computational analysis.

When the bending moment is higher than the limit, it represents the plastification of the reinforcement, permanent deformations, and therefore, reduction of the design cover. The calculations of plastification moments of the bars were generated as a function of the diameter, through Equation 1 (moment of initial plastification) and Equation 2 (moment of total plastification).

$$M_{PI} = \left(\frac{\pi R^3}{4}\right) \cdot \sigma_e \tag{1}$$

$$M_{PT} = \left(\frac{4R^3}{3}\right) \cdot \sigma_e \tag{2}$$

Where: M_{PI} = initial plastification moment (kN.cm); R = radius of the steel bar (cm); σ_e = steel yield strength (kN/cm^2); M_{PT} = total plastification moment (kN.cm).

The positive and negative bending moments obtained in the simulation were compared with the bending moments of the bar plastification (Table 2).

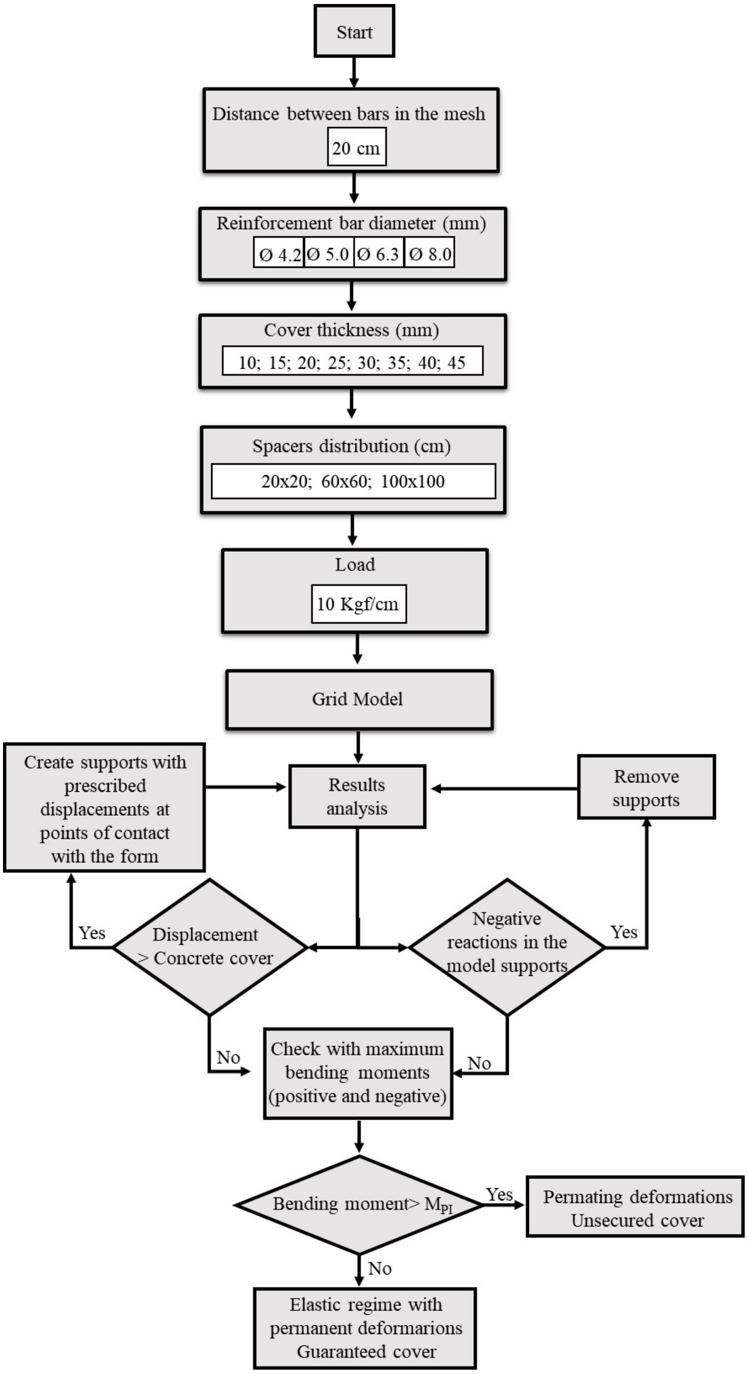

Figure 2. Simulation flowchart.

Table 2. Moment of plastification as a function of the reinforcement bar diameter.

Reinforcement bar	**Bending moment (kN.cm)**	
	M_{PI}	**M_{PT}**
(CA 60) Ø 4.2	43.64	74.09
(CA 60) Ø 5.0	73.63	125.0
(CA 50) Ø 6.3	122.74	208.37
(CA 50) Ø 8.0	251.33	426.67

Note: M_{PI} =Moment of initial plastification; M_{PT} = Moment of total plastification.

The initial plastification moment (M_{PI}) indicates when the permanent deformation begins. Bending moments were accepted below M_{PI}, as the deformation reverses after removing the load, since the deformation is elastic.

The total plastification moment (M_{PT}) defines the reinforcement resistance limit, i.e., the maximum value that the bar can support, behaving like a plastic hinge for increasing loads.

The representative diagrams of the initial and total plastification bending moments are shown in Figure 3.

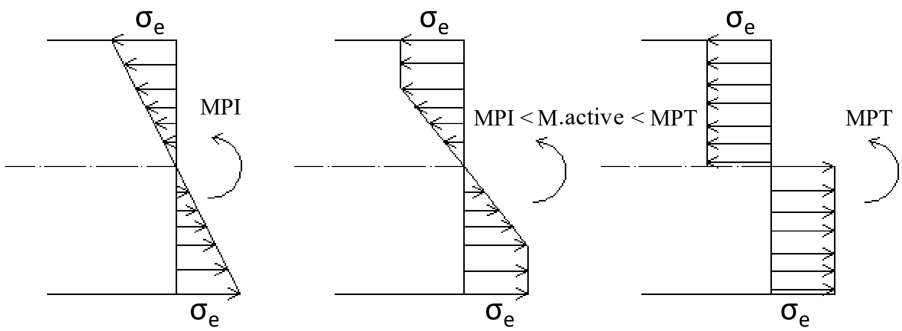

a) b) c)

Figure 3. Stress distribution in the cross-section of the bar: a) initial plastification moment; b) partial plastification moment; c) total plastification moment.

The computational simulation analysis was performed by the linear elastic regime, which allows the identification of permanent deformations, but not their magnitude. Thus, critical values of bending moments for the plastification of the steel bars were experimentally tested in the laboratory to validate the simulation results.

2.2 Experimental simulation

The experimental simulation is complementary to the computational simulation since this did not present values for the deformation of the bars, and consequently, the reduction of the cover, being restricted to the supply of the bending moment generated for comparison with the deformation moments. In addition, the experimental simulation was developed to validate the results of the computational simulation.

Reinforcement meshes with 200 x 200 cm dimensions, 20 cm opening, diameters varying from 4.2 mm to 8.0 mm, with spacer distribution of 20 cm, 60 cm and 100 cm, concrete cover of 3 cm (intermediate evaluation thickness), and tied in bars intersection with nylon clamps (facility of execution and replacement of steel bars) were reproduced in the laboratory. The load was the same one used in the simulations (1 kN), replicated as a worker steps on the reinforcement. For that, the worker weight was measured and complemented with tools until reaches the test load (1 kN). The foot was measured to confirm the 10 cm of local load application. This situation was represented in Figure 4. The cover was measured before and after the worker step with a pachymeter along the bar, in each additional nodes represented in Figure 1 and Figure 4b.

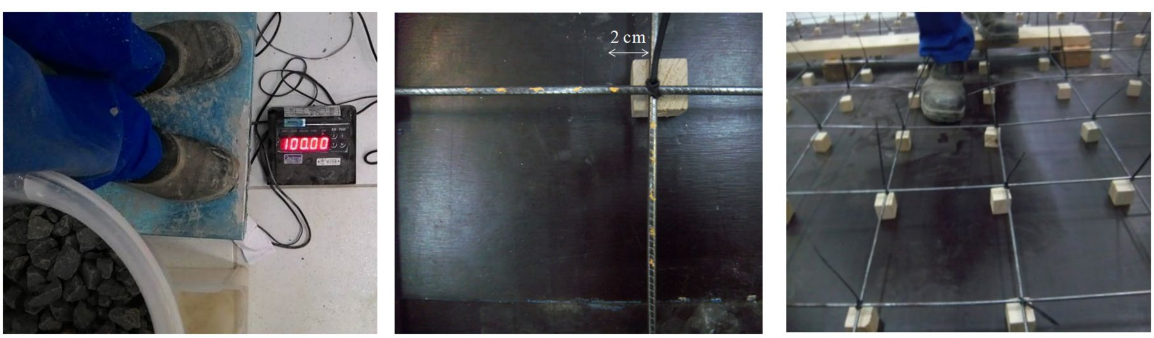

a) b) c)

Figure 4. Experimental simulation: (a) load calibration; (b) additional node; (c) deformation caused by loading application.

The load application and displacement analysis of the bar were done in the center of the mesh (spacer of interest), considering that this reinforcement had a 30 mm cover (lower bar) and the mesh's upper bar had a cover of 30 mm more the bar diameter (30 mm + Ø).

The test was directed to the two bars located at the central point. The application of the load was performed through predetermined points where each central reinforcement bar received only one load application, and then it was changed to another. For each configuration, three exchanges of central reinforcement bars were done.

3 RESULTS AND DISCUSSIONS

3.1 *Computational simulation*

The results of the computational simulations were compared with the initial and total plastification moment of the steel bar (Table 2). The effects of the construction load on the bars, relating to the worker walking on the reinforcement mesh with a 20 cm opening, are shown in Figure 5.

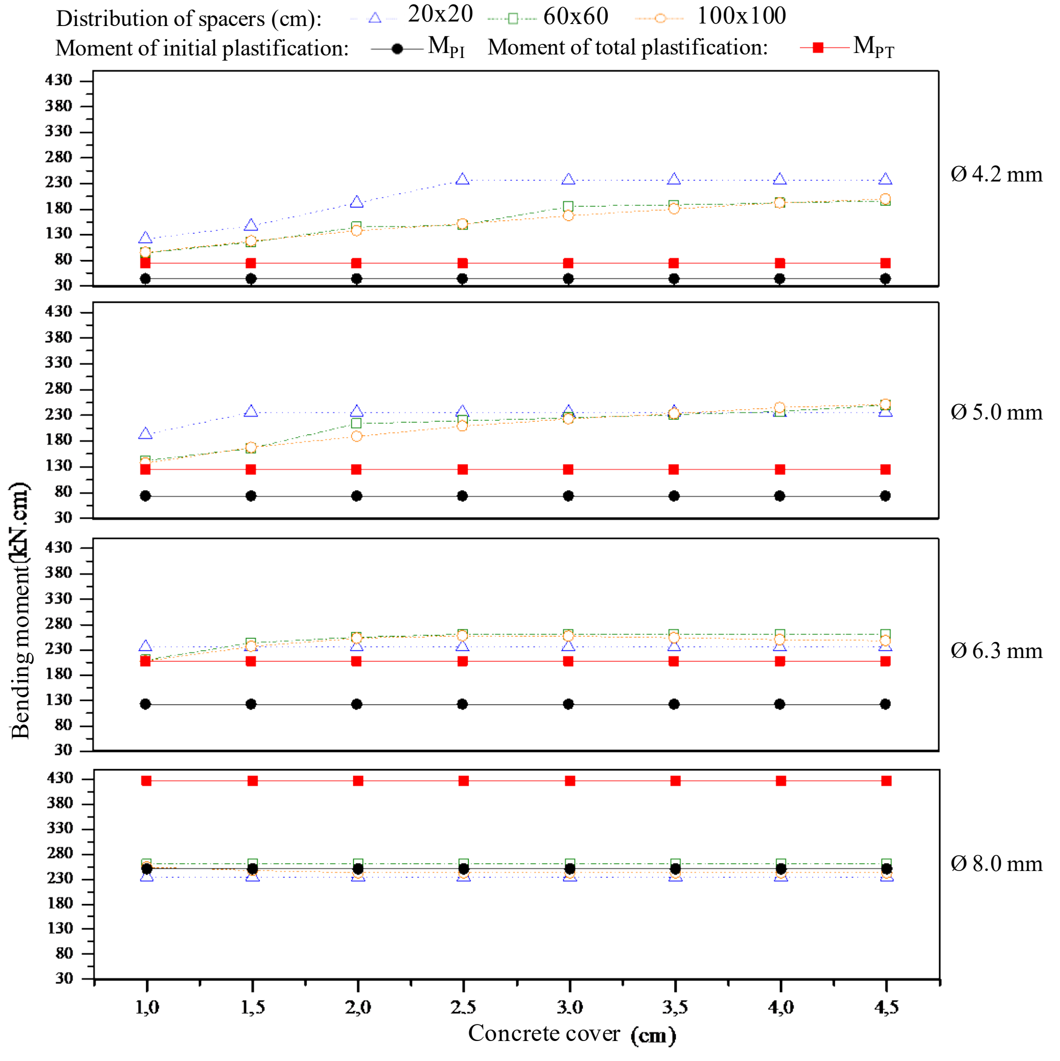

Figure 5. Behavior of the meshes with accidental loading.

Table 3 presents the comparison between reinforcement displacement (d) and concrete cover (c) to inform the formwork contact. The configurations that resulted in displacement greater than the cover mean the contact of the steel bar with the formwork. The meshes with 8.0 mm bar diameter did not come into contact with the formwork, regardless of the configuration, due to the stiffness of the reinforcement.

Table 3. Comparison between reinforcement displacement (d) and concrete cover (c).

Reinforcement bar diameter (mm)	Spacer distribution (cm)	Concrete cover (cm)							
		1	1.5	2	2.5	3	3.5	4	4.5
4.2	20x20	d > c	d > c	d > c	d > c	d > c	d > c	d > c	d > c
	60x60	d > c	d > c	d > c	d > c	d > c	d > c	d > c	d > c
	100x100	d > c	d > c	d > c	d > c	d > c	d > c	d > c	d > c
5.0	20x20	d > c	d < c	d < c	d < c	d < c	d < c	d < c	d < c
	60x60	d > c	d > c	d > c	d > c	d > c	d > c	d > c	d > c
	100x100	d > c	d > c	d > c	d > c	d > c	d > c	d > c	d > c
6.3	20x20	d < c	d < c	d < c	d < c	d < c	d < c	d < c	d < c
	60x60	d > c	d > c	d > c	d < c	d < c	d < c	d < c	d < c
	100x100	d > c	d > c	d > c	d > c	d > c	d > c	d > c	d > c
8.0	20x20	d < c	d < c	d < c	d < c	d < c	d < c	d < c	d < c
	60x60	d < c	d < c	d < c	d < c	d < c	d < c	d < c	d < c
	100x100	d < c	d < c	d < c	d < c	d < c	d < c	d < c	d < c
d < c	No contact with formwork								
d > c	Contact with formwork								

The meshes with smaller diameters (Ø 4.2, Ø 5.0), irrespective of the distribution of spacers or cover thickness, have a permanent deformation, as the bending moment generated from the application of the load is higher than the initial plastification moment and the total plastification moment calculated.

For an intermediate mesh diameter (Ø 6.3), the bending moment of the bars is close to the total plastification moment of the reinforcement but still higher. That is, there is a decrease in cover caused by the plastic deformation of the bar. However, this deformation is smaller compared to 4.0 and 5.0 mm diameters bars.

For the reinforcement with larger diameter assessed (Ø 8.0), an elastic behavior occurs with a plastification start, but all simulated configurations present bending moments much lower than the moment of total plastification, which did not happen with the meshes of the others diameters analyzed. No larger diameters were assessed than those presented in this study, probably because their behavior would be better than Ø 8.0.

In the smaller diameter bars (Ø 4.2; Ø 5.0), the bending moments are much higher than the total plastification moments, indicating that the permanent deformation of the reinforcement occurs in a generalized way, making it impossible to obtain the specified cover.

3.2 *Experimental simulation*

The initial reinforcement cover, measured before the load application, is presented in Table 4.

Table 4. Initial cover thickness in experimental simulation.

Spacer distribution (cm)	Medium concrete cover (mm)			
	Ø 4.2 mm	Ø 5.0 mm	Ø 6.3 mm	Ø 8.0 mm
20x20	30.21	30.24	30.56	30.85
60x60	30.50	30.13	31.12	30.02
100x100	29.42	29.88	30.30	30.22

After the load application, the reinforcement plastic deformations were measured. The plastic deformation was defined by the difference between the initial cover (bar without any load) and cover after application and removal load (residual deformation). The maximum displacement (Max.), which is the bigger plastic deformation between the measured points, the mean (Mean), standard deviation (SD), and coefficient of variation (COV), for each bar, with a different diameter measured, are presented in Table 5.

Table 5. Permanent displacement values in experimental simulation.

Permanent deformation of the steel bar (mm)												
Bar diameter	**Ø 4.2 mm (CA-60)**			**Ø 5.0 mm (CA-60)**			**Ø 6.3 mm (CA-50)**			**Ø 8.0 mm (CA-50)**		
Spacer Distribution (cm)	20	60	100	20	60	100	20	60	100	20	60	100
Max. (mm)	11.36	7.48	5.79	8.05	6.05	5.69	1.21	1.86	1.80	0.53	1.39	1.32
Mean (mm)	9.62	6.77	4.98	6.29	4.75	3.79	1.17	1.42	1.44	0.42	0.96	1.14
SD	2.08	0.63	0.71	1.52	1.24	1.65	0.06	0.43	0.31	0.16	0.51	0.16
COV	0.22	0.09	0.14	0.24	0.26	0.44	0.05	0.30	0.22	0.39	0.53	0.14
Formwork contact	Yes	Yes	Yes	No	Yes	Yes	No	No	Yes	No	No	No

The reinforcement bars with diameters of 4.2 mm and 5.0 mm did not present sufficient stiffness to prevent their contact with the formwork in the application of the accidental load, regardless of the distribution of spacers. It also occurs a reinforcement plastic deformation. Consequently, the bars adjacent to the load application region were lifted, uncoupling the spacer, which generally does not have an adequate fixation, making it even more challenging to obtain the design cover specified.

The meshes with 6.3 mm bars diameter lean on the formwork for the spacer distribution of 100 cm. Thus, the deformation of the mesh occurs at load application, although, to a lesser extent, compared to meshes with a diameter of 4.2 mm and 5.0 mm.

The reinforcement bars with 8.0 mm diameter did not provide contact with the formwork at any spacer's configuration. It was observed during the application of the load that the bars of the mesh perimeter lifted, allowing the displacements of the unfixed spacers.

The experimental simulations were controlled, but the situation found in the constructions is often more unfavorable, such as the deformation of the steel bars before the assembly of the reinforcements, the non-interconnection between all steel bars, the quality of spacers, among others.

3.3 *Computer simulation versus experimental simulation*

The numerical modeling presented the software limitation not to indicate the deformation of the steel bar quantitatively. However, the computer simulation allowed the mapping of critical situations with the indication of the critical bending moment and the formwork contact. Another computational program, which measures the reinforcement deformation, can be future used to compare numerically the experimental deformations obtained.

All observations during the experimental tests about the reinforcement contact with formwork are consistent with the results of the computer simulations. Also, the bending moments generated on the computational analysis are proportional to the displacements achieved in the experimental simulation.

The bars with a diameter of 4.2 mm showed a more significant deformation than the other meshes investigated, being an expected result due to the small diameter of the steel bar. It was observed that, regardless of the configuration, the bars get in contact with the formwork when the load was applied. This situation also was confirmed by the software.

Another factor that can be observed is that the international regulatory guidelines [17], [29], [41], which determine the minimum spacer distribution of 50Ø, are inefficient, since they do not mention the limitation of the reinforcement diameter used in the project. With this recommendation, the application of loads on the bar causes a positive bending moment with a value above that of the corresponding elastic limit of the material, generating permanent deformations. The formwork acts as a maximum displacement limiter. As the reinforcement, which does not have enough stiffness, the bar leans against the formwork under the action of the load applied, and smaller spacers distribution generates greater curvature and, therefore, a bigger bending moment, as shown in Figure 6.

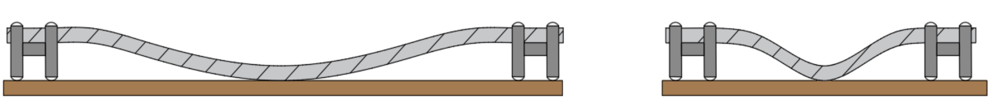

Figure 6. Deformation caused by the same loading at different distances between spacers.

The deformation caused by the worker single trampled on the reinforcement, for a mesh with 4.2 mm diameter and 50Ø spacer distribution, is much higher than the cover recommended tolerance of 10 mm in the standards. In turn, meshes of 4.2- and 5.0-mm diameters do not meet the minimum regulatory execution tolerance of 5 mm.

The meshes of diameter 6.3 mm presented deformations inside the regulatory limit of the cover execution tolerance, in which all values were below 5 mm. Thus, it is possible to state that the reinforcement with a diameter of 6.3 mm, regardless of the distribution of the spacers (until 100 cm), fulfills the regulatory guideline, making it possible to guarantee the specified cover thickness.

The deformation, resulting from the load application for the meshes, with a minimum 8.0 mm diameter bar, were satisfactory, being below the regulatory limit of the cover execution tolerance. Additionally, during the application of the load, the reinforcement had no contact with the formwork, as presented in the computer simulation.

The deformation was analyzed considering only one load application (one worker), however during the structure execution the intense traffic of workers can cause bigger deformations.

Again, the deformation values, obtained in the experimental simulation presented in the distribution of the spacers were consistent with the computational simulation, in which the smaller spacer distribution (20x20 cm) presents a higher bending moment due to the application of the accidental load compared to the larger spacing (100x100 cm).

When the bar stiffness is enough to prevent the reinforcement from leaning against the formwork, this results in a the larger spacing between spacers, less curvature, and a smaller moment.

The results indicate that for reinforcement meshes with smaller diameters bars (4.2 mm and 5.0 mm), there is no guarantee of the design cover, as they present plastic deformation higher than the minimum recommended execution tolerance (5.0 mm) in standards, irrespective of the spacers distribution.

This corroborates the situation found *in loco* by [37], in which slabs with larger reinforcement diameter, under the same conditions, presented a higher probability of meeting the minimum project cover.

As the tests were carried out computationally and laboratory experimentally with meshes with fastening in all nodes, and since this configuration only happens in practice with welded meshes, the deformations under usual execution conditions tend to be higher than those obtained in this study. To obtain the design cover, it is advisable to discontinue the use of reinforcements with these diameters with free traffic of workers on the mesh.

In more critical situations, such as in negative reinforcement, meshes with smaller diameters are very deformable, damaging the cover of the building. Thus, it is preferable to use bars with larger diameters, 8.0 mm and above to ensure the positioning and rigidity of the reinforcement during concrete construction.

For meshes with an intermediate diameter bar (6.3 mm), permanent deformations can occur, causing problems if there is no control over the spacers. Therefore, it is advisable to adhere to the international regulatory recommendation that defines the distribution of spacers as 50Ø to 100 cm until studies can corroborate the possibility of using spacings greater than 100 cm.

Finally, for meshes of diameter 8.0 mm and higher, any spacing of spacers, up to 100 cm, can be used.

4 CONCLUSIONS

This study aimed to assess the influence of the spacers distribution to obtain the reinforcement concrete cover of solid slabs, considering some factors that could affect it during the concreting process. The results obtained and the analyses carried out during this study concern solely the sample in question under the evaluated conditions.

The meshes with 4.2 mm diameter resulted in non-executable scenarios, as they presented deformations that do not exceed the standard cover execution tolerance of 10 mm, while meshes with 5.0 mm steel bars result in unworkable cover values in works that consider a high execution control, as they present deformation greater than 5 mm, irrespective of the distribution of spacers. In the daily practice of the designer, this means that the adoption of 4.2-mm meshes for slabs is not recommended, and in case of adoption of 5.0 mm diameter meshes, it is not advisable to reduce the tolerance of the concrete cover.

Although a 4.2 mm diameter is not common in solid slabs, it is permitted by standard and it is frequently designed for waffle slabs, which are constructed under the same scheme considered in this study. The design of 5.0-mm diameter meshes is very common in solid slabs as it is presented in most studies that investigate concrete covers, usually combined with a concrete cover tolerance reduction. However, mesh with 5.0-mm diameter is permitted by standards, this study proves that its performance is not satisfactory to achieve the concrete cover designed.

The intermediate 6.3 mm diameter bar showed plastification in the computer simulation, as confirmed in the experimental simulation. Nevertheless, the deformation can be considered within the tolerances of execution, as the obtained deformation were lower than those indicated in standards for the cover tolerances.

The reinforcement meshes of larger diameters, 8.0 mm and higher, presented satisfactory performance, because regardless of the distribution spacer configurations the reinforcement does not undergo significant permanent deformation.

When the traffic of workers and equipment are directly on the reinforcement, the existence of the total execution tolerance is crucial. The indicated value for a rigorous cover execution of 5 mm seems insufficient for the configurations considered for diameters smaller than or equal to 5.0 mm.

In the case of using reinforcement with diameters 4.2 or 5.0 mm, it is preferable to adopt larger diameters with larger mesh spacing, which has an equivalent reinforcement rate. For example, 5.0 mm diameter meshes with 10 cm opening are equivalent to 6.3 mm diameter meshes with 15 cm opening, so the last mesh cited is preferable to obtaining the concrete cover. In another example, it is preferable to have 8.0-mm meshes with a 20 cm opening rather than 6.3-mm meshes with a 12.5 cm opening. Although smaller open meshes were stiffer than the bigger ones, the diameter of the reinforcement is more influential, so the bigger diameters were better to achieve the concrete cover.

These small adoptions can contribute significantly to obtaining the concrete cover, a crucial aspect to structural performance, and it is not achieved in its totality without sudden changes during construction (such as the prohibition of traffic directly on the reinforcement), and thus realistic (yet temporary) construction loads need to be considered.

ACKNOWLEDGEMENTS

The authors appreciate the financial support of CAPES (Coordenação de Aperfeiçoamento de Pessoal de Nível Superior) and CNPq (Conselho Nacional de Desenvolvimento Tecnológico).

DATA AVAILABILITY STATEMENT

Some data that support the findings of this study are openly available in Lume Repositório Digital at https://lume.ufrgs.br/handle/10183/127876.

REFERENCES

[1] American Concrete Institute, "ACI 201 guide to durable concrete: reported by ACI Committee 201," *ACI Mater. J.*, 2008.

[2] B. Aïssoun, K. Khayat, and J.-L. Gallias, "Variations of sorptivity with rheological properties of concrete cover in self-consolidating concrete," *Constr. Build. Mater.*, vol. 113, pp. 113–120, 2016.

[3] R. Wasserman and A. Bentur, "Efficiency of curing technologies: strength and durability," *Mater. Struct.*, vol. 46, no. 11, pp. 1833–1842, 2013.

[4] American Concrete Institute, "ACI 318 building code requirements for structural concrete: reported by ACI Committee 318," *ACI Mater. J.*, 2019.

[5] Associação Brasileira de Normas Técnicas, *Execução de Estruturas de Concreto – Procedimento*, NBR 14931, 2004.

[6] European Committee for Standardzation, *Eurocode 2: Design of Concrete Structures – Part 1.1: General Rules and Rules for Buildings*, EN 1992-1.1, 2004

[7] Z. Cui and A. Alipour, "Concrete cover cracking and service life prediction of reinforced concrete structures in corrosive environments," *Constr. Build. Mater.*, vol. 159, pp. 652–671, 2018.

[8] K. Bhargava, A. K. Ghosh, Y. Mori, and S. Ramanujam, "Modeling of time to corrosion-induced cover cracking in reinforced concrete structures," *Cement Concr. Res.*, vol. 35, no. 11, pp. 2203–2218, 2005.

[9] C. Lu, W. Jin, and R. Liu, "Reinforcement corrosion-induced cover cracking and its time prediction for reinforced concrete structures," *J. Corros. Sci.*, vol. 53, no. 4, pp. 1337–1347, 2011.

[10] J. Vaquero, "Separadores para hormigón estructural," *Zuncho*, no. 13, 2007.

[11] M. F. F. M. Barreto, A. P. Maran, D. C. C. Dal Molin, and J. R. Masuero, "Performance evaluation of plastic spacers: proposal and development of evaluation methods," *IBRACON Struct. Mater. J.*, vol. 9, no. 6, pp. 911–9520, 2016, http://dx.doi.org/10.1590/s1983-41952016000600006.

[12] Associação Brasileira de Normas Técnicas. *Projeto de Estruturas de Concreto – Procedimento*, NBR 6118, 2014.

[13] British Standards Institution, *Concrete - Complementary British Standard to BS EN 206-1 – Part 1: Method of Specifying and Guidance for the Specifier*, BS 8500, 2006.

[14] P. Rougeau and P. Guirard, "*Durabilidade do Concreto: Bases Científicas para a Formulação de Concretos Duráveis de Acordo com o Ambiente*," G. C. Isaia, Trad., IBRACON, 2014, ch. 7.

[15] F. Muslim; H. S. Wong; N. R. Buenfeld, "The interface bond strength between reinforcement spacer and concrete" in *Young Res. Forum IV. Innov. Constr. Mater.* (Paper number 19), 2018.

[16] Concrete Reinforcing Steel Institute, *Supports for Reinforcement Used in Concrete*, 2016.

[17] España, *Instrucción Española del Hormigón Estructural (EHE) EHE 08 – Capítulo XIII – Ejecución*, 2008.

[18] Bureau of Indian Standards, *Plain and Reinforced Concrete – Code of Practic*, IS 456, 2000.

[19] American Concrete Institute, *Specifications for Structural Concrete*, ACI 301, 2016.

[20] British Standards Institution, *Spacers and Chairs for Steel Reinforcement and Their Specification – Part 1: Product Performance Requirements*, BS 7973-1, 2001.

[21] Australian Standard, *Concrete Structures*, AS 3600, 2018.

[22] Japan Society of Civil Engineers, *Standard Specification for Concrete Structures*, 2007.

[23] New Zealand Standard, *Concrete Structures Standard. Part 1 – The Design of Concrete Structures*, NZS 3101-1, 2006.

[24] U. M. Angst et al., "The steel: concrete interface," *Mater. Struct.*, vol. 50, no. 143, 2017.

[25] S. Alzyoud, H. S. Wong, and N. R. Buenfeld, "Influence of reinforcement spacers on mass transport properties and durability of concrete structures," *Cement Concr. Res.*, vol. 87, pp. 31–44, 2016, http://dx.doi.org/10.1016/j.cemconres.2016.05.006.

[26] Ø. Strømme, "Influence of cracks and spacers on chloride penetration and reinforcement corrosion in concrete," Norwegian Univ. Sci. Technol., Norwegian, 2017.

[27] A. P. Maran, M. F. F. Menna Barreto, A. B. Rohden, D. C. C. Dal Molin, and J. R. Masuero, "Assessment of cover to reinforcement in slabs using different spacer and tying distances," *IBRACON Struct. Mater. J.*, vol. 8, no. 5, pp. 625–643, 2015.

[28] F. Muslim, Z. Gu, H. S. Wong, and N. R. Buenfeld, "Effect of reinforcement spacers on mass transport properties of concrete containing supplementary cementitious materials," in *36th Cem. Concr. Sci. Conf.*, Cardiff, 2016.

[29] British Standards Institution, *Spacers and Chairs for Steel Reinforcement and Their Specification – Part 2: Fixing and Application of Spacers and Chairs and Tying of Reinforcement*, BS 7973, 2001.

[30] M. F. F. Menna Barreto, A. P. Maran, D. C. C. Dal Molin, and J. R. Masuero, *Conver to Steel in Reinforced Concrete Structures and Their Spacers*. LAMBERT Academic Publishing, 2015, 65 p.

[31] L. A. Clark, M. G. K. Shammas-Toma, D. E. Saymour, P. F. Pallet, and B. K. Marsh, "How can we get the cover we need," *Struct. Eng.*, vol. 75, no. 17, 2007.

[32] A. P. Maran, "Análise da influência da distribuição de espaçadores na garantia da espessura de cobrimento especificada em lajes de concreto armado," M.S. thesis, Univ. Fed. Rio Grande do Sul, Porto Alegre, 2015.

[33] B. Marsh, "Specification and achievement of cover to reinforcement," *Adv. Concr. Tech.*, vol. 1, pp. 1–9, 2003.

[34] V. Palm, A. P. Maran, M. F. F. Menna Barreto, D. C. C. Dal Molin, and J. R. Masuero, "Influência da distribuição de espaçadores no cobrimento e na vida útil de lajes maciças," *Ambient. Constr.*, vol. 20, no. 3, pp. 671–686, 2020.

[35] D. Campos, "Cobrimento de armadura em estruturas de concreto armado: análise comparativa entre valores antes, durante e depois da concretagem," Monograph, Univ. Fed. Rio Grande do Sul, Porto Alegre, 2013.

[36] O. S. P. Silva, "Cobrimento de armadura em estruturas de concreto armado: análise comparativa entre o valor especificado em projeto e o em execução em obras na cidade de Porto Alegre," Monograph, Univ. Fed. Rio Grande do Sul, Porto Alegre, 2012.

[37] M. F. F. Menna Barreto, A. P. Maran, D. C. C. Dal Molin, J. R. Masuero, and R. Z. Alves, "Influência do diâmetro da armadura no cobrimento final em lajes de concreto armado," in *An. 56º Cong. Bras. Concr.*, 2014.

[38] C. O. Campos, L. M. Trautwein, R. B. Gomes, and G. Melo, "Experimental study of solid RC slabs strengthened on the upper face," *IBRACON Struct. Mater. J.*, vol. 11, no. 2, pp. 255–278, 2018.

[39] F. B. Mendonça, G. S. Urgessa, L. E. N. Almeida, and A. F. F. Rocco, "Damage diagram of blast test results for determining reinforced concrete slab response for varying scaled distance, concrete strength and reinforcement ratio," *Eng. Sci.*, vol. 93, no. 1, e20200511, 2021.

[40] Associação Brasileira de Normas Técnicas, *Cargas para o Cálculo de Estruturas de Edificações*, NBR 6120, 2019.

[41] Comité Euro-International du Béton, *Spacers, Chairs and Tying of Steel Reinforcement*, Bulletin d'Information No. 201, 1990.

Author contributions: APM conceptualization, writing, methodology, data curation, formal analysis; MFFMB: writing, methodology, data curation, formal analysis; DCCDM: conceptualization, supervision, methodology; JRM: methodology, formal analysis, supervision.

Editors: Mauricio Pina Ferreira, Guilherme Aris Parsekian.

IBRACON Structures and Materials Journal
Revista IBRACON de Estruturas e Materiais
ISSN 1983-4195 ismj.org

ORIGINAL ARTICLE

Reinforced concrete structures strengthened with CFRP (ACI x FIB) - Recommendations for bending design criteria

Reforço de estruturas de concreto armado com CFRP (ACI x FIB) - Recomendações para dimensionamento à flexão

Igor Del Gaudio Orlando[a]
Túlio Nogueira Bittencourt[a]
Leila Cristina Meneghetti[a]

[a]Universidade de São Paulo – USP, Escola Politécnica, Departamento Engenharia de Estruturas e Geotécnica, São Paulo, SP, Brasil

Received 14 December 2020
Accepted 06 August 2021

Abstract: This work deals with the evaluation of the design criteria and security check (Ultimate Limit State - ULS) of the American (ACI-440.2R, 2017) and European (FIB Model Code, 2010) standards of reinforced concrete structures strengthened with Carbon Fiber Reinforced Polymers (CFRP), by the technique of Externally Bonded Reinforcement (EBR). It is intended to evaluate if, for a given database of 64 experimental tests of beams and slabs, the obtained results respect the safety conditions according to the mentioned standards, to increase the efficiency of this reinforcement technique and to lead to the establishment of regulatory design criteria in Brazil. Results show a conservative match among experimental and theoretical values calculated according to the two guidelines and it is concluded that a future regulation in Brazil on this subject should be based on the FIB Model Code.

Keywords: carbon fiber reinforced polymers (CFRP), bending strengthening, ACI-440 (2017), FIB Model Code (2010), regulation in Brazil.

Resumo: Este trabalho trata da avaliação dos critérios de dimensionamento e verificação de segurança ao Estado Limite Último (ELU) da norma americana (ACI-440.2R, 2017) e europeia (FIB Model Code, 2010) de estruturas de concreto armado reforçadas à flexão com Polímeros Reforçados com Fibras de Carbono (CFRP), pela técnica de colagem externa (EBR). Considerando uma dada base de 64 dados de ensaios experimentais de vigas e lajes, avaliou-se se os resultados obtidos respeitam as condições de segurança segundo as normas referidas, com o propósito de aumentar a eficiência dessa técnica de reforço e conduzir ao estabelecimento de critérios regulamentares de dimensionamento no Brasil. Os resultados obtidos mostram uma proximidade conservadora entre valores experimentais e teóricos calculadas de acordo com as duas recomendações e conclui-se que uma futura regulamentação no Brasil sobre esse tema deve-se ter como premissa o modelo do FIB Model Code.

Palavras-chave: polímeros reforçados com fibras de carbono (CFRP), reforço à flexão, ACI-440 (2017), FIB Model Code (2010), regulamentação no Brasil.

How to cite: I. D. G. Orlando, T. N. Bittencourt, and L. C. Meneghetti, "Reinforced concrete structures strengthened with CFRP (ACI x FIB) - Recommendations for bending design criteria," *Rev. IBRACON Estrut. Mater.*, vol. 15, no. 2, e15204, 2022, https://doi.org/10.1590/S1983-41952022000200004

1 INTRODUCTION

In recent years, the development of new materials, the improvement of execution techniques, and the greater knowledge about the behavior of structures, in conjunction with a greater concern about the durability of constructions, have made repair, strengthening, and retrofit of concrete elements one of the most evolved areas in engineering. Structures are required to sustain critical loads under challenging environmental conditions such as heavy traffic

Corresponding author: Igor Del Gaudio Orlando. E-mail: igordgorlando@gmail.com
Financial support: CNPq (Conselho Nacional de Desenvolvimento Científico e Tecnológico) - scholarship number 152486/2016-0.
Conflict of interest: Nothing to declare.

density, impact from debris flow and highly corrosive environments. Therefore, strengthening is frequently required in reinforced concrete (RC) structures to meet the adequate strength requirements and extend the service life [1].

As described by Toutanji et al. [2], one of the techniques developed during the last decades to strength reinforced concrete beams in bending is the use of fiber-reinforced polymers (FRP) through the externally bonded reinforcement (EBR) technique. Increases in the strength of global flexion from 10 to 160% were reported in prior studies [3]–[8]. These materials feature good properties of non-corrosiveness; high longitudinal tensile strength, high stiffness, high strength-to-weight ratio, insect and fungal resistance chemical attack resistance, low thermal transmissibility, and simple installation; which supported their popularization in the structural reinforcement market [9]–[13].

Currently, the use of FRPs in buildings and bridge repair, strengthening and maintenance is most pronounced due to their efficient and economical nature [14], [15]. In recent years, the construction sector has become one of the world's largest consumers of polymer composites [16]–[20], indicating that FRP materials are part of the modern construction industry.

However, in Brazil there is still no specific standard for strengthening projects related to the use of composite materials. Strengthening concrete structures with FRP are carried out following international standards and recommendations, as well as manufacturer specifications [21]. The main design recommendations for strengthening with FRP are the American Concrete Institute (ACI) - Committee 440 [22] and the European standard "FIB Model Code - Task Group 9.3" [23].

To resolve this issue and propose a Brazilian guideline, it is necessary to evaluate and discuss the design parameters and methodologies suggested in the literature and compare them with a variety of experimental results.

This study aims to provide fundamentals to assist in deciding about the design procedures to be adopted in Brazil in structural strengthening projects with FRP composites. Therefore, discussion and evaluation of both design criteria and safety factor assessment (Ultimate Limit State - ULS) of ACI-440 [22] and FIB Model Code [23] are presented and some parameters and methodology highlighted as important to be considered in the future development of code design criteria in Brazil.

2 STATE OF THE ART

This section discusses analytical design models applied to projects of concrete beams bending strengthening with FRP.

2.1 Basic design assumptions

According to ACI 440 [22] and FIB [23], the following assumptions are applied in the strengthening of bending design elements:

- The strain in the concrete and reinforcement are directly proportional to their respective distances to the neutral axis of the section. Flat sections before loading remain flat after loading (Euler-Bernoulli's assumption);
- The maximum compression strain in the concrete is 0.003 (ACI) or 0.0035 (FIB);
- The tensile strength of concrete is neglected;
- The stress vs. strain diagram of the steel is elastic-linear until its yield point, followed by perfectly plastic behavior;
- It is admitted that FRP are characterized by an elastic-linear stress-strain behavior to rupture;
- The shear strain in the adhesive layer is neglected, given that this layer is very thin with small variation in its thickness.

2.2 Rupture modes of FRP systems

The bending capacity of a reinforced member is related to its rupture mode. The following rupture modes may occur in a bending member strengthened with FRP:

- Crushing of the compressed concrete (CC) before the yielding of reinforcement;
- Yielding of reinforcement (FY) followed by the failure of the FRP system (FR);
- Yielding of reinforcement (FY) followed by the concrete crushing (CC);
- Debonding of the FRP (FD);
- Delamination of the FRP system from concrete substrate (FD).

According to Juvandes [24], the first three types constitute the group of modes where the section presents a perfect bond between adhesive, FRP and concrete interfaces until rupture (classic rupture - RC). The two remaining cases (FD) define the group of premature failure of the FRP (premature rupture - RP). Debonding is known to occur at low axial strain level of FRP, thus externally bonded systems often do not yield full tensile strength of FRP [25]–[27].

As shown by Kalfat et al. [28], different types of intermediate anchorages, including U-jacket anchors, mechanically fastened anchors, and FRP anchors, have been used to prevent early debonding failure. Metallic clamps have been used to prevent delamination and to increase ductility [29]. These anchors delay debonding by enabling the continuation of the load path between FRP concrete and increasing bond strength [30].

2.3 ACI-440.2R-17 model [22]

The strength design approach requires that the design flexural strength of a member exceed its required factored moment, as indicated by Equation 1:

$$\varnothing M_n \geq M_u \tag{1}$$

where $\varnothing$ = strength reduction factor; M_n = nominal flexural strength; and M_u = factored moment at a section.

As described previously, one of the consequences of the use of FRP in strengthened concrete structures is the reduction of the ductility of the original element. In some cases, this loss is negligible, but sections that may have significant ductility losses should be checked. For reinforced concrete elements, adequate ductility is achieved if the strain in the steel is at least equal to 0.005 at the instant of the concrete rupture or the debonding/delamination of the FRP system,

ACI-440 [22] recommends using the strength reduction factor ($\varnothing$), which is a function of the yielding strain of the steel (ε_{sy}) and the unitary net tensile strain in steel (ε_t) according to Equation 2, 3 and 4:

$$\varnothing = 0.90 \; para \; \varepsilon_t \geq 0.005 \tag{2}$$

$$\varnothing = 0.65 + \frac{0.25\left(\varepsilon_t - \varepsilon_{sy}\right)}{0.005 - \varepsilon_{sy}} \quad \text{to} \quad \varepsilon_{sy} < \varepsilon_t < 0.005 \tag{3}$$

$$\varnothing = 0.65 \; to \; \varepsilon_t \leq 0.005 \; \varepsilon_{sy} \tag{4}$$

The bending strength capacity of the section of an element strengthened with FRP can be determined through the compatibility of strain, balance of internal forces and control of the failure mode. The nominal flexural strength capacity of the section (M_n) can be calculated as Equation 5:

$$M_n = A_s f_s \left(d - \frac{\beta_1 c}{2}\right) + \psi_f A_f f_{fe} \left(h - \frac{\beta_1 c}{2}\right) + A'_s f'_s \left(\frac{\beta_1 c}{2} - d'\right) \tag{5}$$

where A_s = area of nonprestressed steel reinforcement; A'_s = area of the compression reinforcement of the section; f_s = stress in steel reinforcement; h = total height of the section; d = useful height of section; c = position of the neutral axis; A_f = FRP area; and f_{fe} = effective stress in FRP.

The application of the coefficient of reduction in the strength of the FRP, denoted by ψ_f, in the portion that simulates the contribution of FRP to the resistant moment is defined in ACI 440 [22], item "10.2.10". According to Okeil et al. [31] it is based on reliability analyses that in turn is based on the statistically calibrated properties of the bending strength.

The terms α_1 and β_1 in the equations below are parameters that define a rectangular stress block in concrete equivalent to a non-linear stress distribution. Considering α_1 = 0.85 (Whitney stress block) it is possible to obtain reasonably accurate results for a rectangular section. In addition, β_1 = 0.85, when 17MPa < f'_c < 28MPa. For f'_c > 28MPa, the value of β_1 is provided by the general expression (ACI-318), presented in Equation 6:

$$\beta_1 = 1.05 - 0.05\left(\frac{f'_c}{7}\right) \tag{6}$$

Where β_1 > 0,65. The depth of the neutral axis (c) is found by satisfying the internal balance of forces and the compatibility of strain according to the following Equation 7:

$$c = \left(\frac{A_s f_s + A_f f_e - A'_s f'_s}{\alpha_1 f'_c \beta b}\right) \tag{7}$$

The effective strain (ε_{fe}) that can be achieved by the FRP is defined as Equation 8:

$$\varepsilon_{fe} = \varepsilon_{cu}\left(\frac{d_f - c}{c}\right) - \varepsilon_{bi} \le \varepsilon_{fd} \tag{8}$$

Where ε_{bi} = pre-existing strain when the FRP is installed; d_f = effective depth of FRP; ε_{cu} = ultimate axial strain of the unconfined concrete corresponding to 0.85 f'_{c0}; and ε_{fe} = effective strain in FRP reinforcement attained at failure.

Regardless of where the neutral axis of the analyzed section is, the failure controlled by the FRP debonding may govern the procedures. Thus, to prevent crack induced debonding failure mode, the effective strain in FRP should be limited to the strain at which debonding may occur as defined in Equation 9:

$$\varepsilon_{fd} = 0.41\sqrt[2]{\frac{f'_c}{n E_f t_f}} \le 0.9\varepsilon_{fu} \tag{9}$$

where the maximum allowable strain in FRP (ε_{fd}) is a function of the thickness of each layer of FRP (t_f), the number of layers of FRP (n) and the modulus of elasticity of FRP (E_f).

As reported by Arduini and Nanni [32], it's important to note that carbon fiber stiffness, fiber direction, and number of plies can significantly affect the performance of strengthened beams. Toutanji et al. [33] observed that not only ductility of strengthened beams tends to significantly reduce with the increase on the number of bonded sheets, but also the failure mode of strengthened-specimens changes. For instance, wrapping of FRP sheets perpendicular to edges of strengthened beam (and on top of longitudinally applied FRP sheets) can be effective in anchoring bonded CFRP sheets and delays debonding of FRP strengthening system. However, though anchor system enhanced the capacity of the strengthened beam significantly, it reduces the overall ductility [34].

2.4 FIB Model Code (2010) [23]

In the FIB Model Code 2010 [23], the calculation of the resistance design moment (M_{Rd}) of the strengthened section is also based on the design principles of reinforced concrete, according to the Equation 10:

$$M_{Rd} = A_{S1} f_{yd}\left(d - \lambda x\right) + A_f E_f \varepsilon_f \left(h - \lambda x\right) + A_{S2} E_s \varepsilon_{S2}\left(\lambda x - d_2\right) \tag{10}$$

The neutral axis is determined from the compatibility of the strains and internal equilibrium of forces as Equation 11:

$$\eta f_{cd} b x + A_{s2} E_s \varepsilon_{s2} = A_{s1} f_{yd} + A_f E_{fu} \varepsilon_f \tag{11}$$

where the terms λ e η in Equations 10 and 11 are parameters that define a rectangular stress block in the concrete equivalent to a non-linear stress distribution, according to Equations 12 and 13 below. These equations provide reasonably accurate results for a rectangular section.

$$\lambda = \begin{cases} 0.8 & to\ f_{ck} \leq 50\,MPa \\ 0.8 - \dfrac{f_{ck} - 50}{400} & to\ 50 \leq f_{ck} \leq 100\,MPa \end{cases} \tag{12}$$

$$\eta = \begin{cases} 1.0 & to\ f_{ck} \leq 50\,MPa \\ 1.0 - \dfrac{f_{ck} - 50}{200} & to\ 50 \leq f_{ck} \leq 100\,MPa \end{cases} \tag{13}$$

As sudden failures with little or no warning are undesirable, the ductility index of the strengthened element must exceed a certain value. With respect to this issue, the FIB Model Code [23] gives the following limitation on the depth of the compression zone at ultimate: $\xi \leq 0,45$ (for concrete type C50⁄60 or lower) or $\xi \leq 0,35$ for concrete above C55⁄67, where:

$$\xi = \frac{c}{d} \tag{14}$$

The maximum allowable strain in the FRP to prevent debounding failure due to concrete crack may not exceed the limit indicated by the FIB Model Code [23] and supplemented by the FIB-14 [35] through the Equations 15 and 16:

$$\varepsilon_{fd} \leq 0.9\varepsilon_{fu} \tag{15}$$

$$f_{fd} = \frac{f_{fk}}{y_f} \tag{16}$$

Where y_f (FRP material partial safety factor) is given in Table 3.1 of FIB-14 [35], with y_f =1.35 for any strengthening system with low-quality control of the application on the construction site.

The maximum tensile stress in the FRP limited by the connection to concrete in a single anchorage zone (not cracked) is given by Equations 17 and 18 of FIB Model Code, 2010 [23]:

$$f_{fbm} = K_m K_b \beta_L \sqrt[2]{\frac{2E_f}{t_f} \cdot f_{cm}{}^{2/3}} \tag{17}$$

$$k_b = \sqrt[2]{\frac{2 - b_f / b}{1 + b_f / b}} \geq 1 \tag{18}$$

where t_f = thickness of the FRP layer FRP; β_L = is the anchorage length factor of the FRP; K_b : structure shape factor; b_f : FRP section width; *b*: width of the concrete section; and E_f : the modulus of elasticity of the FRP.

3 DESCRIPTION OF DATA EXTRACTED FROM THE LITERATURE

For further investigation of the design parameters, a set of 64 experimental data were selected according to the following criteria:

- Type of structural element: slab and beam;

- Reinforcement technique: EBR;
- Type of reinforcement: carbon fiber reinforced polymers (CFRP) (sheet and laminates).

The data, which are shown in Tables 1 and 2, were collected from the following experimental studies:

- Slabs: Juvandes [24], Dias [37].
- Beams: Gamino et al. [21], Dias [37], Beber [38], Brosens [39], Matthys [40], Pinto [41], Travassos [42].

Note that CFRP was employed because this type of reinforcement is widely used and studied, resulting in a greater sampling of available experimental elements. Tables 1 and 2 include the failure modes observed for the 64 collected data and the level of strain of the CFRP at the moment of rupture (ε_{fu}). For 12 experimental beam data, these strain values are unknown. It can be observed that in both slabs and beams, approximately 40% of the samples presented classic ruptures.

Table 1. Summary of the 12 experimental slab data used in this study*.

Author	Exp. Data	Type	Reinforced concrete element					CFRP System									
			b (cm)	h (cm)	A_s (cm²)	ρ_s (%)	f^{cil}_{cm} (MPa)	E_{f1} (GPa)	ε_{fk1} (‰)	b_{f1} (mm)	t_{f1} (mm)	n_{bf1}	n_{lf1}	A_{f1} (cm²)	ρ_f (%)	ε_{fu} (‰)	Type Rupt.
Dias [37]	LA3R	S.	44.0	7.6	0.85	0.31%	63.3	230	15	140	0.11	1	2	0.311	0.09%	11.1	RC
	LB1R	S.	44.0	8.1	0.85	0.28%	63.3	230	15	140	0.11	1	2	0.311	0.09%	12.0	RC
	LA4S	L.	44.0	8.0	0.85	0.29%	63.3	160	20	32	1.20	1	1	0.384	0.11%	9.7	RP
	LB2S	L.	44.0	8.5	0.85	0.27%	63.3	160	20	32	1.20	1	1	0.384	0.10%	9.2	RP
	LD3BL	L.	44.0	8.5	0.85	0.27%	49.7	150	14	32	1.40	1	1	0.448	0.12%	9.6	RP
	LD4BL	L.	44.0	8.1	0.85	0.28%	49.7	150	14	32	1.40	1	1	0.448	0.13%	10.4	RP
	LE3I	L.	44.0	8.2	0.85	0.28%	49.7	160	15	32	1.40	1	1	0.448	0.12%	8.6	RP
	LE4I	L.	44.0	7.8	0.85	0.30%	49.7	160	15	32	1.40	1	1	0.448	0.13%	10.2	RP
Juvandes [24]	LC3R	S.	44.0	8.1	0.85	0.28%	63.3	230	15	140	0.11	1	2	0.311	0.09%	10.9	RC
	LC4R	S.	44.0	7.7	0.85	0.30%	63.3	230	15	140	0.11	1	2	0.311	0.09%	10.3	RC
	LC1S	L.	44.0	8.1	0.85	0.28%	63.3	160	20	32	1.20	1	1	0.384	0.11%	10.3	RP
	LC2S	L.	44.0	8.4	0.85	0.27%	63.3	160	20	32	1.20	1	1	0.384	0.10%	11.8	RP

* RC = classical failure; RP = premature failure; ε_{fu} = ultimate FRP strain during tests; ρ_f = FRP reinforcement ratio; ρ_s = reinforcement ratio; f^{cil}_{cm} = mean compressive strength of concrete cylinders; L = Laminate; S = Sheet

Table 2. Summary of the 52 experimental beams data used in this study.

Author	Exp. Data	Type	Reinforced concrete element					CFRP System									
			b (cm)	h (cm)	A_s (cm²)	ρ_s (%)	f^{cil}_{cm} (MPa)	E_{f1} (GPa)	ε_{fk1} (‰)	b_{f1} (mm)	t_{f1} (mm)	n_{bf1}	n_{lf1}	A_{f1} (cm²)	ρ_f (%)	ε_{fu} (‰)	Type Rupt.
Dias [37]	V2	S	12.0	18.0	1.01	0.52%	41.0	240	15	70	0.11	1	2	0.155	0.07%	8.1	RP
	V3	S	12.0	18.0	1.01	0.52%	41.0	240	15	70	0.11	1	2	0.155	0.07%	8.1	RC
	V4	L	12.0	18.0	1.01	0.52%	41.0	200	11	20	1.40	1	1	0.280	0.13%	6.9	RP
	V6	L	12.0	18.0	1.01	0.52%	41.0	200	11	20	1.40	1	1	0.280	0.13%	7.2	RP
Pinto [41]	V1	L	15.0	45.0	6.03	0.98%	34.8	165	17	50	1.20	2	1	1.200	0.18%	5.2	RP
	V3	L	15.0	45.0	6.03	0.98%	38.3	165	17	50	1.20	3	1	1.800	0.27%	5.4	RP
	V5	L	15.0	45.0	6.03	0.97%	34.7	165	17	50	1.20	3	1	1.800	0.44%	4.6	RC
Beber [38]	VR3	L	12.0	25.0	1.57	0.57%	33.6	230	15	100	0.11	1	1	0.111	0.04%	5.6	RC
	VR4	L	12.0	25.0	1.57	0.57%	33.6	230	15	100	0.11	1	1	0.111	0.04%	7.1	RC
	VR5	L	12.0	25.0	1.57	0.57%	33.6	230	15	100	0.11	1	4	0.444	0.15%	7.1	RP
	VR6	L	12.0	25.0	1.57	0.57%	33.6	230	15	100	0.11	1	4	0.444	0.15%	7.5	RP

Table 2. Continued...

Author	Exp. Data	Type	Reinforced concrete element					CFRP System									
			b	h	A_s	ρ_s	f^{cil}_{cm}	E_{f1}	ε_{fk1}	b_{f1}	t_{f1}	n_{bf1}	n_{lf1}	A_{f1}	ρ_f	ε_{fu}	Type
			(cm)	(cm)	(cm²)	(%)	(MPa)	(GPa)	(‰)	(mm)	(mm)			(cm²)	(%)	(‰)	Rupt.
	VR7	L	12.0	25.0	1.57	0.57%	33.6	230	15	100	0.11	1	7	0.777	0.26%	5.2	RP
	VR8	L	12.0	25.0	1.57	0.57%	33.6	230	15	100	0.11	1	7	0.777	0.26%	5.6	RP
	VR9	L	12.0	25.0	1.57	0.57%	33.6	230	15	100	0.11	1	10	1.110	0.37%	4.8	RP
	VR10	L	12.0	25.0	1.57	0.57%	33.6	230	15	100	0.11	1	10	1.110	0.37%	4.7	RP
Travassos [42]	A12	L	20.0	40.0	4.02	0.59%	38.5	242	16	200	0.11	1	3	0.666	0.08%	8.0	RP
	A14	L	20.0	40.0	4.02	0.59%	38.5	242	16	200	0.11	1	1	0.222	0.03%	6.2	RC
	A32	L	20.0	40.0	4.02	0.59%	38.5	242	16	200	0.11	1	3	0.666	0.08%	7.2	RP
	A33	L	20.0	40.0	4.02	0.59%	38.5	242	16	200	0.11	1	1	0.222	0.03%	3.2	RC
	A11	L	20.0	40.0	4.02	0.59%	34.4	242	16	200	0.11	1	1	0.222	0.03%	6.7	RC
	A21	L	20.0	40.0	9.42	1.39%	34.4	242	16	200	0.11	1	1	0.222	0.03%	9.2	RC
	A31	L	20.0	40.0	4.02	0.59%	34.4	242	16	200	0.11	1	3	0.666	0.08%	10.6	RP
	A34	L	20.0	40.0	4.02	0.59%	34.4	242	16	200	0.11	1	1	0.222	0.03%	8.4	RC
Matthys [40]	BF2	L	20.0	45.0	8.04	0.96%	36.5	159	19	100	1.20	1	1	1.200	0.13%	6.7	RP
	BF3	L	20.0	45.0	8.04	0.96%	34.9	159	19	100	1.20	1	1	1.200	0.13%	7.2	RP
	BF4	L	20.0	45.0	8.04	0.96%	30.8	159	19	100	1.20	1	1	1.200	0.13%	6.8	RP
	BF5	L	20.0	45.0	8.04	0.96%	37.4	159	19	100	1.20	1	1	1.200	0.13%	5.7	RP
	BF6	L	20.0	45.0	8.04	0.96%	35.9	159	19	100	1.20	1	1	1.200	0.13%	7.1	RP
	BF8	L	20.0	45.0	4.02	0.48%	39.4	159	19	100	1.20	1	1	1.200	0.13%	5.8	RC
	BF9	S	20.0	45.0	4.02	0.48%	33.7	233	13	100	0.11	1	2	0.222	0.02%	10.0	RP
Brosens [39]	A1	S	12.5	22.5	1.01	0.41%	41.0	235	15	75	0.17	1	2	0.251	0.09%	-	RP
	B1	S	12.5	22.5	1.51	0.62%	46.0	235	15	75	0.17	1	2	0.251	0.09%	-	RP
	C1	S	12.5	22.5	1.51	0.62%	43.0	235	15	75	0.17	1	2	0.251	0.09%	-	RP
	C2	S	12.5	22.5	1.51	0.62%	43.0	235	15	75	0.17	1	2	0.251	0.09%	-	RP
	D1	S	12.5	22.5	1.51	0.62%	38.0	235	15	75	0.17	1	2	0.251	0.09%	-	RP
	E1	S	12.5	22.5	1.51	0.62%	33.0	235	15	75	0.17	1	2	0.251	0.09%	-	RP
	F1	S	12.5	22.5	1.29	0.52%	43.0	235	15	75	0.17	1	2	0.251	0.09%	-	RP
	G1	S	12.5	22.5	2.07	0.85%	43.0	235	15	75	0.17	1	2	0.251	0.09%	-	RP
Gamino et al. [21]	VR01	L	7.5	15.0	0.62	0.62%	45.0	230	15	75	0.13	1	1	0.098	0.09%	13.3	RC
	VR02	L	7.5	15.0	0.62	0.62%	45.0	230	15	75	0.13	1	1	0.098	0.09%	-	RC
	VR03	L	7.5	15.0	0.62	0.62%	45.0	230	15	75	0.13	1	1	0.098	0.09%	11.8	RC
	VR04	L	7.5	15.0	0.62	0.62%	45.0	230	15	75	0.13	1	1	0.098	0.09%	12.6	RC
	VR05	L	7.5	15.0	0.62	0.62%	45.0	230	15	75	0.13	1	1	0.098	0.09%	11.4	RC
	VR06	L	7.5	15.0	0.62	0.62%	45.0	230	15	75	0.13	1	1	0.098	0.09%	-	RP
	VR07	L	7.5	15.0	0.62	0.62%	45.0	230	15	75	0.13	1	1	0.098	0.09%	-	RP
	VR08	L	7.5	15.0	0.62	0.62%	45.0	230	15	75	0.13	1	1	0.098	0.09%	-	RP
	VR09	S	7.5	15.0	0.62	0.62%	45.0	235	15	75	0.11	1	1	0.083	0.07%	5.3	RC
	VR10	S	7.5	15.0	0.62	0.62%	45.0	235	15	75	0.11	1	1	0.083	0.07%	6.4	RC
	VR11	S	7.5	15.0	0.62	0.62%	45.0	235	15	75	0.11	1	2	0.165	0.15%	6.6	RC
	VR12	S	7.5	15.0	0.62	0.62%	45.0	235	15	75	0.11	1	1	0.083	0.07%	4.3	RC
	VR13	S	7.5	15.0	0.62	0.62%	45.0	235	15	75	0.11	1	1	0.083	0.07%	4.4	RC
	VR14	S	7.5	15.0	0.62	0.62%	45.0	235	15	75	0.11	1	1	0.083	0.07%	3.9	RC

3.1 Design model in ULS

The calculation methodology indicated in the ACI440.2R-17 [22] and FIB Model Code [23] standards was used to evaluate the bending safety factor of experimental data of reinforced concrete strengthened with CFRP.

Table 3 presents the criteria defined for such analysis, with 2 cases without partial safety factors (for comparison with the experimental data collected) and 2 cases with partial safety factors (verification of global safety).

Table 3. Criteria defined for analysis.

Parameters established for the analysis criteria				
	Partial safety factor			
	C.1	C.2	C.5	C.6
Design equations.	(ACI)	(FIB)	(ACI)	(FIB)
Material properties	(ACI)	(FIB)	(ACI)	(FIB)
Ultimate compressive strain of concrete; (ε_{cu})	3‰	3.5‰	3‰	3.5‰
Limit of tensile strain in steel ($\varepsilon_{s,lim}$)	-	-	-	-
Strength reduction factor (ϕ)	1	1	($\Delta\varepsilon_s$)	Verification
FRP Strength reduction factor (ψ_f)	1	1	0.85	-
Partial safety factor for steel (γ_s)	1	1	1.10	1.15
Environmental reduction factor (C_E)	1	1	0.85	0.74

As indicated in Figure 1, by imposing one of the failure modes and limiting the strain in the conditioning material, it is possible to determine the position of the neutral axis and obtain the effective strain in the FRP. Furthermore, the stresses and strains in the internal reinforcement in the FRP and in the concrete can be determined. However, in these calculations, it is necessary to consider the hypothesis of occurrence of premature failure characteristic in structures strengthened through EBR technique. Owing to the difficulty in detecting them, ACI440 [22] and FIB [23] limit the strain of FRP (ε_{fd}) to increase the reliability of the reinforcement.

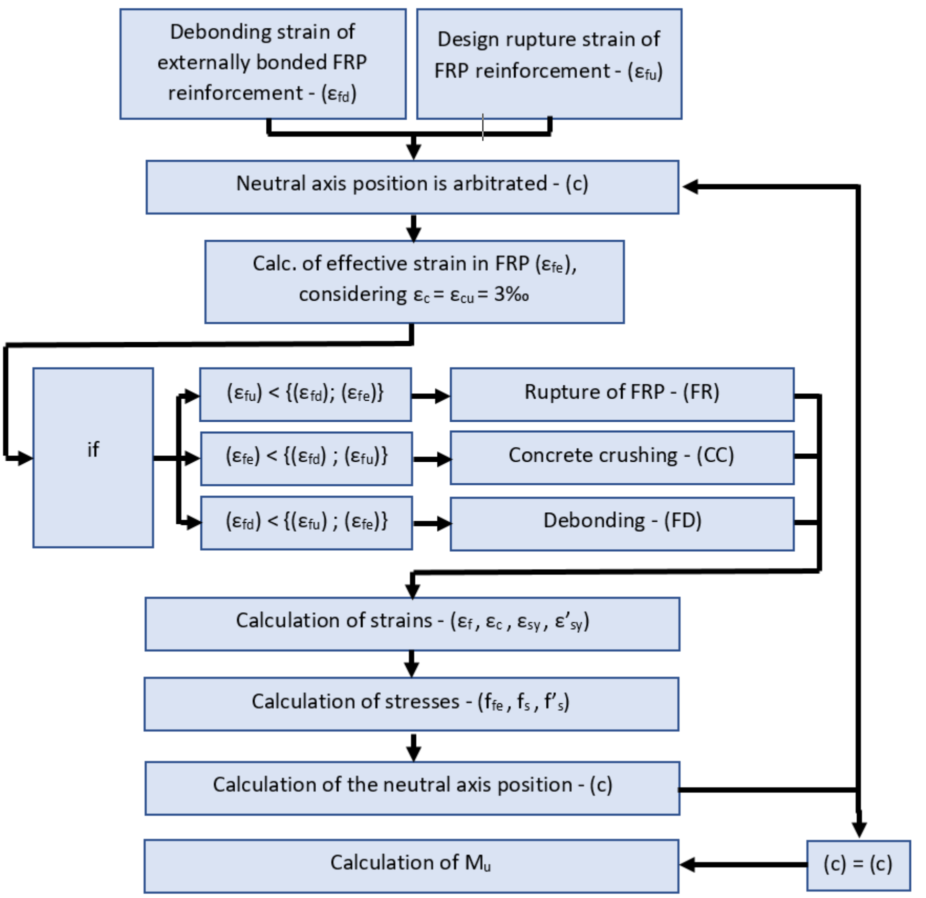

Figure 1. Flowchart of the calculation methodology adopted for the FIB and ACI models.

4 RESULTS AND DISCUSSIONS

4.1 Analysis of collected experimental data

Note in Tables 1 and 2 that both for the slabs and for the beams, approximately 60% of the experimental data present premature rupture. The experimental data show that the slabs present larger strain values (ε_{fu}) when compared to beams strengthened by the same externally bonded technique (EBR).

In the slabs case, given that the shear is not very pronounced in these models, the strain in CFRP shows high values (ε_{med} ≈ 11‰), especially when rupture is controlled by classical failure. However, even in situations of premature failure, accurate results can be observed from these experimental data (ε_{med} ≈ 9‰).

These results are evidenced in studies of several authors, namely ACI-440 [22], Juvandes [24], FIB-14 [35], Brosens [39], Matthys [40], and Azevedo [43], concluding that in beam models the develops lower strain values than in the slab models.

Important to note that the collection of data presented in this paper reveals an interesting variation in reported test results. As presented by Naser et al. [15], this can be attributed to significant variation in tested specimens, material types, loading configurations, experimental procedures, and test arrangements, etc., which make interpretation of test results complex. This demanded a standardization on testing procedures, and some tests are published, [44] and [45].

4.2 Ultimate flexural strength analysis (ACI x FIB)

To perform the statistical analysis of the ratio between the ultimate theoretical and experimental moments, the proportion ($M_{theoretical} / M_{exp.}$) of the 64 experimental data was assessed in this study for the corresponding criteria (C.1 and C.2). Such values are plotted in Figure 2, 3 and 4. The mean, standard deviation (SD), and coefficient of variation (CV) were calculated; they are presented in Table 4.

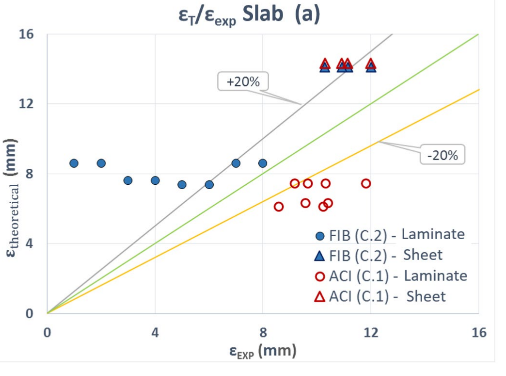

Figure 2. ACI440 x FIB - Analysis of the ultimate strain ($\epsilon_{theoretical} / \epsilon_{exp}$) for slabs (a).

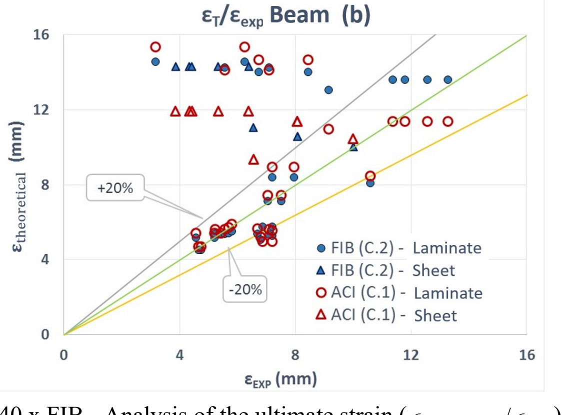

Figure 3. ACI440 x FIB - Analysis of the ultimate strain ($\epsilon_{theoretical} / \epsilon_{exp}$) for beam (b).

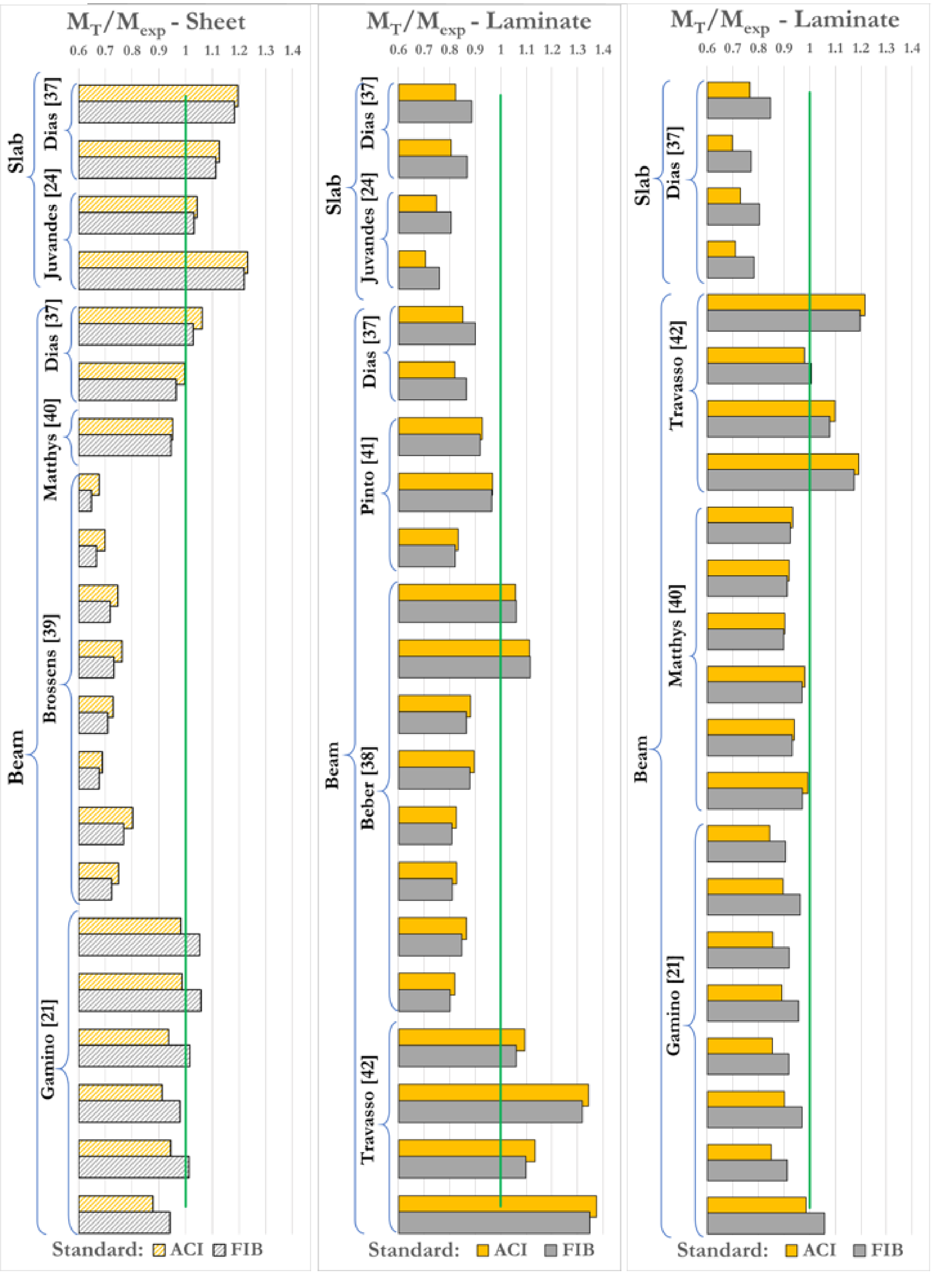

Figure 4. ACI440 x FIB - Analysis of the ultimate moment of the 64 experimental data ($M_{theoretical} / M_{exp}$).

Table 4. Mean, standard deviation (SD), and coefficient of variation (CV) of the ratios $(M_{theoretical}/M_{exp})$ and $(\epsilon_{theoretical}/\epsilon_{exp})$ - FIB x ACI.

$(M_{theoret.}/M_{exp.})$ of 64 experimental data

		ACI (C.1)	FIB (C.2)
Total	Mean	0.92	0.95
	SD	0.15	0.15
	CV(%)	16.73	16.04

		ACI (C.1)	FIB (C.2)
Total Slab	Mean	0.88	0.92
	SD	0.21	0.17
	CV(%)	23.31	18.19
Total Beam	Mean	0.93	0.96
	SD	0.15	0.15
	CV(%)	16.02	15.71

		ACI (C.1)	FIB (C.2)
Slab (Laminates)	Mean	0.75	0.82
	SD	0.05	0.05
	CV(%)	6.28	5.71
Slab (Sheet)	Mean	1.15	1.14
	SD	0.08	0.08
	CV(%)	7.23	7.23
Beam (Laminates)	Mean	0.97	0.98
	SD	0.15	0.13
	CV(%)	15.11	13.73
Beam (Sheet)	Mean	0.85	0.86
	SD	0.13	0.16
	CV(%)	14.88	18.20

$(\varepsilon_{theoret.}/\varepsilon_{exp.})$ of 52 experimental data*

		ACI (C.1)	FIB (C.2)
Total	Mean	1.32	1.38
	SD	0.79	0.84
	CV(%)	60.19	61.08

		ACI (C.1)	FIB (C.2)
Total Slab	Mean	0.89	0.97
	SD	0.31	0.24
	CV(%)	34.65	24.89
Total Beam	Mean	1.44	1.50
	SD	0.85	0.92
	CV(%)	58.82	61.09

		ACI (C.1)	FIB (C.2)
Slab (Laminates)	Mean	0.69	0.81
	SD	0.08	0.08
	CV(%)	11.39	10.17
Slab (Sheet)	Mean	1.30	1.27
	SD	0.08	0.08
	CV(%)	6.27	6.27
Beam (Laminates)	Mean	1.29	1.28
	SD	0.83	0.78
	CV(%)	64.21	60.62
Beam (Sheet)	Mean	1.99	2.27
	SD	0.73	1.00
	CV(%)	36.53	43.99

* 12 of 64 experimental strain data collected (ε_{exp}) are unknown.

According to Figure 4 and Table 4, concerning the cases of slabs, it is observed that the FIB model code [23] yields more consistent results (ratio near to 1.0) than the ACI440 model [22]. In the case of slabs strengthened with laminate, the prediction of the moment capacity of the slab is quite conservative according to these two philosophies, and the ACI440 [22] proved to be more conservative than FIB [23]. Note that while the ACI [22] criterion is generally more conservative than FIB [23], both seem to better reflect the behavior of beams than the behavior of slabs (expressed by a ratio $M_{theoretical}/M_{exp}$ <1,00, and by values closer to the experimental results and with less dispersion). This can be explained by the fact that in slabs the shear is not pronounced, making the FRP more effective in these cases. Since two guidelines do not differentiate between beams and slabs; the estimated failure moment values are over conservative for the slabs case. Itis also noted a difference in the behavior between sheets and laminates, demonstrating the need to separate their specification in a future code.

Concerning beams strengthened with laminates, the ultimate behavior of design models is foreseen with high accuracy ($M_{theoretical}/M_{exp}$ ≈ 1.0) and low dispersion (CV ≈ 15%) according to the ACI and FIB criteria. In contrast, the models reinforced with sheets lead to more conservative ultimate moments average.

As observed in Table 4, the increase on the concrete ultimate strain from 3.0 ‰ (ACI [22]) to 3.5 ‰ (FIB [23]), set out in criterion C.2, resulted in a small increase in the mean ratio $(M_{theoret.}/M_{exp})$ of the 64 elements, due considering the remaining resistance in the compression of the reinforced element. This demonstrates the importance of assessing the strength reserve in the compression of a structure to be strengthened, being, in most cases, the mandatory factor of design to strength a structure. To be noted that ABNT NBR6118 [36] specifies the same concrete ultimate strain value as FIB [23].

In general, when compared to the ACI440.2R-17 model, the FIB model code [23] presents a smaller dispersion of values and analytical results closer to the experimental values, expressed by the ratio $M_{theoretical} / M_{exp}$ near 1 presented on Table 4. Some of these evidences agrees with the studies by Pham and Al-Mahaidi [46] and Toutanji et al. [47].

4.3Analysis of maximum strain of FRP (ACI x FIB)

From Figure 2, Figure 3, and Table 4, comparing beams and slabs, it can be concluded that in both codes the slabs presented ultimate strain with a closer and conservative approximation of the theorical results when compared to experimental results, and with a reasonable dispersion of values, reflected by an average value of 0.89 (ACI) / 0.97 (FIB) and a CV of 34.65% (ACI) / 24.89% (FIB). The beams analyses led to theoretical values higher than those obtained in the experimental tests. This difference in behavior between beams and slabs can be explained because of the occurrence of premature failures earlier than expected in the beam models.

When compared to the FRP sheet models, the FRP laminates showed a better approximation on the ultimate theorical strain compared with experimental results (for beams and slabs).

Comparing the ACI and FIB models, it can be concluded that for slabs the FIB model fits better to the maximum strain of the FRP, with an average of the ratio ($\varepsilon_{theoretical} / \varepsilon_{exp}$) closer to 1 and a smaller dispersion of results than the ACI model. However, in general, as observed in Figure 2 and 3, different from the relation between the ultimate moments ($M_{theoretical} / M_{exp}$), the strain shows remarkable dispersion of values (CV>50%), proving not to be a good parameter for analysis and convergence of values.

4.4 Analysis of the global safety factor (ACI x FIB)

To carry out the analysis of the global safety factor, it was calculated the ratio C.1/C.5 for ACI and C.2/C.6 for FIB, where C.1 and C.2 are the ultimate moment of the strengthened member without consideration of partial safety factor and C.5 and C.6 are the same moment including partial safety factors, as shown in Table 5.

Table 5. Global safety factor obtained - FIB x ACI.

Global safety factor (C.1/C.5) - ACI								
						FR	Mean	1.35
			Slab	Mean	1.31		SD	0.06
				SD	0.07		CV(%)	4.19
Total	Mean	1.28		CV(%)	5.66	FD	Mean	1.27
	SD	0.05					SD	0.04
	CV(%)	3.97	Beam	Mean	1.27		CV(%)	3.20
				SD	0.04	CC	Mean	1.25
				CV(%)	3.12		SD	0.02
							CV(%)	1.24
Global safety factor (C.2/C.6) - FIB								
						FR	Mean	1.35
			Slab	Mean	1.26		SD	0.03
				SD	0.09		CV(%)	2.40
Total	Mean	1.32		CV(%)	7.25	FD	Mean	1.24
	SD	0.08					SD	0.06
	CV(%)	5.88	Beam	Mean	1.33		CV(%)	5.01
				SD	0.07	CC	Mean	1.37
				CV(%)	5.40		SD	0.03
							CV(%)	2.47

Table 5 shows an average value of 1.28 for the global safety factor obtained for the ACI (C.1/C.5). However, when comparing the global safety factors of ACI440, and separating them by the type of failure, note that the largest global safety factor occurs when the analytical mode failure is due to the rupture of the FRP (FR). This can be explained by the environmental reduction factor (CE) being directly associated with this mode of failure. Concrete crushing presented the lowest global safety factor, but still with values within the parameters found in the literature.

From Table 5, the global safety factor obtained (C.2/C.6) for the FIB Model Code [22] is a mean value of 1.32. However, the highest global safety factor occurs when the failure mode of the structure is due to the rupture of the FRP and concrete crushing. This can be explained due to the partial safety factor of the FRP material (y_f), which limits the maximum strain of the FRP, being directly associated with this mode of failure (FR). For concrete crushing, the partial safety factor of concrete y_c is directly associated with the global safety factor values, and according to FIB-14 [35], this value is set as $y_c = 1.5$.

5 CONCLUSIONS

- The design procedures presented in the ACI440 and FIB Model Code design guides have differences in the approach of the FRP subject, however, without large discrepancies of results, considering the FRP to be a recent reinforcement system. The importance of this topic demonstrates the need to create codes on these matters in Brazil.
- The FRP strain analysis ($\varepsilon_{theoretical} / \varepsilon_{exp}$) presented large coefficient of variation, proving not to be a good parameter to be assessed for convergence of values. Therefore, future regulation in Brazil should be mainly based on flexural strength principles.
- For structures strengthened with FRP by the EBR technique, when compared to ACI440 design guide, the design methodology specified by FIB Model Code leads to analytical results closer to the experimental values, with smaller results dispersion, expressed as the ratio $M_{theoret.} / M_{exp}$ close to 1.0.
- Both design models (ACI440 and FIB) seem to better reflect the behavior of beams than slabs. The account for the different element types (slabs/beams and laminates/sheets) is not considered in the FIB neither ACI models nor should be developed in future studies in Brazil.
- It is noted that in 9 of 64 experimental data that the rupture of the member started after excessive steel yielding, and in one of these cases the failure was due only to excessive plastic deformation of steel, pointing to a need to limit the excessive steel yielding, especially in cases where the amount of reinforcement is an important factor for the service life of the structure. ABNT NBR6118 limits the strain of the reinforcement to ($\varepsilon_{sy,lim}$ = 10‰), and this may be an important factor to be adopted in a future Brazilian codes on FRP;
- In general, the Brazilian code for Concrete Structures is like the European standard (Eurocode) one. Therefore, the FIB Model Code 2010 model presents a calculation methodology and partial safety factors that can be more easily related to the future Brazilian code on Reinforced Concrete Structures Strengthened With CFRP.

ACKNOWLEDGEMENTS

The authors are grateful for the support of Brazilian Research Funding Agencies - CNPq (Conselho Nacional de Desenvolvimento Científico e Tecnológico) - scholarship number 152486/2016-0.

REFERENCES

[1] A. Siddika, M. A. A. Mamun, W. Ferdous, and R. Alyousef, "Performances, challenges and opportunities in strengthening reinforced concrete structures by using FRPs: a state-of-the-art review," *J. Eng. Fail. Anal.*, vol. 111, pp. 104480, 2020, http://dx.doi.org/10.1016/j.engfailanal.2020.104480.

[2] H. Toutanji, L. Zhao, and E. Anselm, "Verifications of design equations of beams externally strengthened with FRP composites," *J. Compos. Constr.*, vol. 10, no. 3, pp. 254–264, 2006, http://dx.doi.org/10.1061/(ASCE)1090-0268(2006)10:3(254).

[3] U. Meier and H. Kaiser, "Strengthening of structures with CFRP laminates," in *Proc. Adv. Compos. Mater. Civ. Eng. Struct.*, New York, 1991, pp. 224–232.

[4] P. Ritchie, D. Thomas, L. Lu, and G. Conneley, "External reinforcement of concrete beams using fiber reinforced plastics," *ACI Struct. J.*, vol. 88, no. 4, pp. 490–500, 1991, http://dx.doi.org/10.14359/2723.

[5] A. Sharif, G. Al-Sulaimani, I. Basunbul, M. Bakuch, and B. Ghaleb, "Strengthening of initially loaded reinforced concrete beams using FRP plates," *ACI Struct. J.*, vol. 91, no. 2, pp. 160–168, 1994, http://dx.doi.org/10.14359/4594.

[6] A. Siddika, M. A. A. Mamun, R. Alyousef, and Y. H. M. Amran, "Strengthening of reinforced concrete beams by using fiber-reinforced polymer composites: a review," *J. Build. Eng.*, vol. 25, pp. 100798, 2019, http://dx.doi.org/10.1016/j.jobe.2019.100798.

[7] L. Huang, C. Zhang, L. Yan, and B. Kasal, "Flexural behavior of U-shape FRP profile-RC composite beams with inner GFRP tube confinement at concrete compression zone," *Compos. Struct.*, vol. 184, pp. 674–687, 2018, http://dx.doi.org/10.1016/j.compstruct.2017.10.029.

[8] U. Meier, "Carbon fiber-reinforced polymers: modern materials in bridge engineering," *Struct. Eng. Int.*, vol. 2, no. 1, pp. 7–12, 1992, http://dx.doi.org/10.2749/101686692780617020.

[9] L. Sorrentino, S. Turchetta, and C. Bellini, "In process monitoring of cutting temperature during the drilling of FRP laminate," *Compos. Struct.*, vol. 168, pp. 549–561, 2017, http://dx.doi.org/10.1016/j.compstruct.2017.02.079.

[10] J. Huo, Z. Li, L. Zhao, J. Liu, and Y. Xiao, "Dynamic behavior of CFRP-strengthened reinforced concrete beams without stirrups under impact loading," *ACI Struct. J.*, vol. 115, no. 3, pp. 775–787, 2018, http://dx.doi.org/10.14359/51701283.

[11] Y. Ou and D. Zhu, "Tensile behavior of glass fiber reinforced composite at different strain rates and temperatures," *Constr. Build. Mater.*, vol. 96, pp. 648–656, 2015., http://dx.doi.org/10.1016/j.conbuildmat.2015.08.044.

[12] D. A. Bournas, A. Pavese, and W. Tizani, "Tensile capacity of FRP anchors in connecting FRP and TRM sheets to concrete," *Eng. Struct.*, vol. 82, pp. 72–81, 2015, http://dx.doi.org/10.1016/j.engstruct.2014.10.031.

[13] B. H. Osman, E. Wu, B. Ji, and S. S. Abdulhameed, "Repair of pre-cracked reinforced concrete (RC) Beams with openings strengthened using FRP sheets under sustained load," *Int. J. Concr. Struct. Mater.*, vol. 11, no. 1, pp. 171–183, 2017., http://dx.doi.org/10.1007/s40069-016-0182-3.

[14] Y. H. Mugahed Amran, R. Alyousef, R. S. M. Rashid, H. Alabduljabbar, and C.-C. Hung, "Properties and applications of FRP in strengthening RC structures: a review," *Structures*, vol. 16, pp. 208–238, 2018, http://dx.doi.org/10.1016/j.istruc.2018.09.008.

[15] M. Z. Naser, R. A. Hawileh, and J. A. Abdalla, "Fiber-reinforced polymer composites in strengthening reinforced concrete structures: a critical review," *J. Eng. Struct.*, vol. 198, pp. 109542, 2019, http://dx.doi.org/10.1016/j.engstruct.2019.109542.

[16] L. Czarnecki, M. Kaproń, and D. Van Gemert, "Sustainable construction: challenges, contribution of polymers, research arena," *Restor. Build Monuments*, vol. 19, no. 2–3, pp. 81–96, 2013, http://dx.doi.org/10.1515/rbm-2013-6583.

[17] M. F. Humphreys, "The use of polymer composites in construction," in *Int. Conf. Smart & Sustain. Built Environ.*, Brisbane, Australia, 2003.

[18] R. A. Hawileh, W. Nawaz, and J. A. Abdalla, "Flexural behavior of reinforced concrete beams externally strengthened with Hardwire Steel-Fiber sheets," *Constr. Build. Mater.*, vol. 172, pp. 562–573, 2018, http://dx.doi.org/10.1016/j.conbuildmat.2018.03.225.

[19] R. A. Hawileh, J. A. Abdalla, and M. Z. Naser, "Modeling the shear strength of concrete beams reinforced with CFRP bars under unsymmetrical loading," *Mech. Adv. Mater. Structures*, vol. 26, no. 1, pp. 1–8, 2018.

[20] H. Rasheed, J. A. Abdalla, R. Hawileh, and A. Al-Tamimi, "Flexural behavior of reinforced concrete beams strengthened with externally bonded aluminum alloy plates," *Eng. Struct.*, vol. 147, no. 15, pp. 473–485, 2017, http://dx.doi.org/10.1016/j.engstruct.2017.05.067.

[21] A. L. Gamino, T. N. Bittencourt, and J. L. A. O. Sousa, "Estruturas de concreto reforçadas com PRFC. Parte I: análise dos modelos de flexão," *Rev. IBRACON*, vol. 2, no. 4, pp. 326–355, 2009, http://dx.doi.org/10.1590/S1983-41952009000400003.

[22] American Concrete Institute, *Guide for the Design and Construction of Externally Bonded FRP Systems for Strengthening Concrete Structure*, ACI 440.2R-17, 2017.

[23] Federation International Du Béton, *FIB Model Code for Concrete Structures 2010*, 2010.

[24] L. F. P. Juvandes, "Reforço e reabilitação de estruturas de betão usando materiais compósitos de CFRP," Ph.D. dissertation, Fac. Eng., Univ. Porto, 1999.

[25] H. A. Rasheed, *Strengthening Design of Reinforced Concrete with FRP*. Boca Raton: CRC Press, 2014.

[26] L. C. Hollaway, "A review of the present and future utilization of FRP composites in the Civil infrastructure with reference to their important in service properties," *Constr. Build. Mater.*, vol. 24, no. 12, pp. 2419–2445, 2010, http://dx.doi.org/10.1016/j.conbuildmat.2010.04.062.

[27] L. De Lorenzis and J. G. Teng, "Near-surface mounted FRP reinforcement: an emerging technique for strengthening structures," *Compos. B. Eng.*, vol. 38, no. 2, pp. 119–143, 2007., http://dx.doi.org/10.1016/j.compositesb.2006.08.003.

[28] R. Kalfat, R. Al-Mahaidi, and S. T. Smith, "Anchorage devices used to improve the performance of reinforced concrete beams retrofitted with FRP composites: stateof- the-art review," *J. Compos. Constr.*, vol. 17, no. 1, pp. 14–33, 2013., http://dx.doi.org/10.1061/(ASCE)CC.1943-5614.0000276.

[29] H. Pham and R. Al-Mahaidi, "Experimental investigation into flexural retrofitting of reinforced concrete bridge beams using FRP composites," *Compos. Struct.*, vol. 66, no. 1–4, pp. 617–625, 2004., http://dx.doi.org/10.1016/j.compstruct.2004.05.010.

[30] E. del Rey Castillo, M. Griffith, and J. Ingham, "Straight FRP anchors exhibiting fiber rupture failure mode," *Compos. Struct.*, vol. 207, pp. 612–624, 2019.

[31] A. M. Okeil, Y. Bingol, and T. Alkhrdahi, *Analyzing Model Uncertainties for Concrete Beams Flexurally Strengthened with FRP Laminates.* Washington, DC., 2007.

[32] M. Arduini and A. Nanni, "Parametric study of beams with externally bonded FRP reinforcement," *ACI Struct. J.*, vol. 94, no. 5, pp. 493–501, 1997, http://dx.doi.org/10.14359/499.

[33] H. Toutanji, L. Zhao, and Y. Zhang, "Flexural behavior of reinforced concrete beams externally strengthened with CFRP sheets bonded with an inorganic matrix," *Eng. Struct.*, vol. 28, no. 4, pp. 557–566, 2006, http://dx.doi.org/10.1016/j.engstruct.2005.09.011.

[34] A. K. Al-Tamimi, R. Hawileh, J. Abdalla, and H. A. Rasheed, "Effects of ratio of CFRP plate length to shear span and end anchorage on flexural behavior of SCC RC beams," *J. Compos. Constr.*, vol. 15, no. 6, pp. 908–919, 2011, http://dx.doi.org/10.1061/(ASCE)CC.1943-5614.0000221.

[35] Federation International Du Béton, *Bulletin 14: Externally bonded FRP reinforcement for RC structures*, 2001.

[36] Associação Brasileira de Normas Técnicas, *Projeto de Estruturas de Concreto*, NBR 6118, 2014.

[37] S. Dias, “Verificação experimental do reforço com CFRP de estruturas de betão à flexão,” M.S. thesis, Fac. Eng., Univ. Porto (FEUP), Porto, 2001.

[38] A. Beber, “Avaliação do Desempenho de Vigas de Concreto Armado Reforçadas com Lâminas de Fibra de Carbono,” Ph.D. dissertation, Univ. Fed. Rio Grande do Sul (UFRGS), Porto Alegre, 1999.

[39] K. Brosens, “Anchorage of externally bonded steel plates and CFRP laminates for the strengthening of concrete elements,” Ph.D. dissertation, Katholieke Univ. Leuven, Leuven, Bélgica, 2001.

[40] S. Matthys, “Structural behaviour and design of concrete members strengthened with externally bonded FRP reinforcement,” Ph.D. dissertation, Ghent Univ., Ghent, 2000.

[41] C. Pinto, “Reforço à flexão de vigas de concreto armado com fibras de carbono,” M.S. thesis, Univ. Fed. Rio de Janeiro, Rio de Janeiro, 2000.

[42] N. Travassos, “Caracterização do comportamento da ligação CFRP-Betão,” M.S. thesis, Inst. Superior Técnico (IST), Lisboa, 2005.

[43] D. M. M. Azevedo, “Reforço de estruturas de betão com colagem de sistemas compósitos de CFRP - Recomendações para dimensionamento,” M.S. thesis, Fac. Eng., Univ. Porto (FEUP), Porto, 2008.

[44] American Society for Testing and Materials, *Standard Guide for Testing Polymer Matrix Composite Materials*, ASTM D4762-16, 2016.

[45] International Organization for Standardization, *Fibre-Reinforced Plastics – Methods of Producing Test Plates – Part 1: General Conditions*, ISO 1268-1:2001, 2001.

[46] H. Pham and R. Al-Mahaidi, "Assessment of available prediction models for the stength of FRP retrofitted RC beams," *Compos. Struct. J.*, vol. 66, no. 1–4, pp. 601–610, 2004.

[47] H. Toutanji and L. Zhao, “Review of design equations of beams externally strengthened with FRP composites,” in *Intl. Wksh. Innov. Mater. Des.*, Cairo, Egypt, 2005. https://doi.org/10.1061/(ASCE)1090-0268(2006)10:3(254).

Author contributions: IDGO: conceptualization, analysis, methodology, data curation, writing, TNB and LCM: conceptualization, analysis, methodology, reviewer, supervision;

Editors: Mark Alexander, Guilherme Aris Parsekian.

Rev. IBRACON Estrut. Mater., vol. 15, no. 2, e15205, 2022

IBRACON Structures and Materials Journal
Revista IBRACON de Estruturas e Materiais
ISSN 1983-4195 ismj.org

ORIGINAL ARTICLE

Eco-efficient concrete, optimized by Alfred's particle packing model, with partial replacement of Portland cement by stone powder

Concreto ecoeficiente, otimizado pelo modelo de empacotamento de Alfred, com substituição parcial do cimento Portland por pó de pedra

Heloisa Fuganti Campos[a]
André Lucas Bellon[a]
Eduardo Reis de Lara e Silva[a]
Maurício Villatore Junior[a]

[a]Universidade Federal do Paraná – UFPR, Departamento de Construção Civil, Curitiba, PR, Brasil

Received 08 April 2021
Accepted 11 August 2021

Abstract: The partial replacement of clinker by complementary cementitious materials can significantly contribute to the reduction of carbon emissions in the production of concrete. Another alternative to reduce these emissions is to increase the efficiency of the concrete, achieving higher compressive strength with lower consumption of cement. Particle packing models are efficient tools to optimize the composition of the matrix and contribute to the production of more eco-efficient concretes. In this context, the objective of the present study is evaluating the production of concretes with partial replacement of cement by stone powder, optimized by Alfred's particle packing model, seeking to reduce cement consumption and CO_2 emissions per MPa of compressive strength. The replacement content of cement by stone powder was 20% by mass (equivalent to 22.4% by volume). Concretes were produced with different distribution factor (q) - 0.37; 0.21; 0.45 - to verify the influence of fines on the flow between particles and on the efficiency of the produced concrete. The analyses were carried out in terms of properties in the fresh state, hardened state, and sustainability parameters (cement consumptions and CO_2 emissions). The application of the proposed method resulted in a higher compressive strength than the expected for the water/cement ratio used (0.5). The most efficient concrete reached the compressive strength of 68 MPa with 240 kg/m^3 of cement, which represents 3.5 kg of cement/m^3/MPa and 3.1 kg of CO_2/m^3/MPa, a value below the references found in the literature for conventional concretes. Therefore, the proposed method allows to produce more eco-efficient concrete, contributing to the use of waste and reducing CO_2 emissions.

Keywords: particle packing, Alfred model, stone powder, eco-efficient concrete.

Resumo: A substituição parcial do clínquer por adições pode contribuir de maneira significativa na mitigação da pegada do carbono dentro da cadeia produtiva do concreto. Outra alternativa para reduzir essas emissões é o aumento da eficiência do concreto, atingindo maiores resistências com menores consumos de cimento. Modelos de empacotamento de partículas são ferramentas eficientes para otimizar a composição da matriz e contribuir para a produção de concretos mais ecoeficientes. Nesse contexto, o objetivo do presente estudo é avaliar a produção de concretos com substituição parcial do cimento por pó de pedra, otimizados pelo modelo de empacotamento de partículas de Alfred, buscando reduzir o consumo de cimento e as emissões de CO_2 por MPa de resistência à compressão. O teor de substituição do cimento Portland por pó de pedra foi de 20% em massa (equivalente a 22.4% em volume). Foram produzidos traços com diferentes módulos de distribuição (q) - 0,37; 0,21; 0,45 – a fim de verificar a influência dos finos no escoamento entre as partículas e na eficiência dos concretos produzidos. A análise foi realizada em termos de propriedades no estado fresco, estado endurecido e parâmetros de sustentabilidade (consumo de cimento e emissões de CO_2). A aplicação do método proposto permitiu obter resistências superiores às esperadas para a relação água/cimento utilizada (0,5). O traço mais eficiente atingiu a resistência à compressão de 68 MPa com 240 kg/m^3 de consumo de cimento, o que representa 3,5 kg de cimento/m^3/MPa e 3,1 kg de CO_2/m^3/MPa, valores abaixo das referências encontradas

Corresponding author: Heloisa Fuganti Campos. E-mail: heloisacampos@ufpr.br
Financial support: None.
Conflict of interest: Nothing to declare.

na literatura para concretos convencionais. Portanto, o método proposto permite produzir concretos mais ecoeficientes, contribuindo para a utilização de um resíduo e reduzindo as emissões de CO_2.

Palavras-chave: empacotamento de partículas, modelo de Alfred, pó de pedra, concreto ecoeficiente.

How to cite: H. F. Campos, A. L. Bellon, E. R. Lara e Silva, and M. Villatore, "Eco-efficient concrete, optimized by particle packing models, with partial replacement of Portland cement by stone powder". *Rev. IBRACON Estrut. Mater.*, vol. 15, no. 2, e15205, 2022, https://doi.org/10.1590/S1983-41952022000200005

1 INTRODUCTION

Civil construction has a high participation in the world economic and social, being the concrete its main input. However, this activity represents a major environmental impact, mainly in Portland cement (PC) production, which that may reach up to 5% to 7% of the global CO_2 release [1]–[4]. These values are expected to increase to 30% by 2050, if no action is taken [5]. The strategy used by PC producers to reduce the environmental impact involves promoting the production of cement types with lower clinker content. This strategy is based on the hypothesis that some additions, which are waste from other production chains, reach the cement industry with zero environmental impact [4], [6]–[12]. A material that has shown great potential for the replacement of PC is the waste generated during the aggregate production process in quarries: the stone powder (SP), due to its continuous granulometry, which contributes to the packing particles [13], [14]. This material typically remains stored in quarries as a waste material, obstructing the drainage of channels and generating dust during crushing operations. Apart from bringing greater profitability to companies, taking advantage of this SP would also benefit the environment.

In the same context, a subject studied by materials microstructure engineering that has the purpose of optimizing the concrete mixes reducing cement consumption without compromising mechanical performance, while still being ecological and economical is in the packing particles [15]. Concrete mixtures with better-accommodated particles tend to reduce the space required for filling with cement paste, demonstrating less PC consumption per m^3 of concrete and theoretically indicating higher compressive strength [16]. Highly efficient packing reduces the intergranular voids in the paste through the combination of fines materials with different particle sizes and optimizes the granular skeleton of the aggregates to reduce paste consumption [17]. Additionally, particle packing optimization provides a guided replacement of fine materials to primarily control matrix fracture properties.

Particle packing models are divided into two main types: discrete and continuous. Discrete models consider multimodal distributions containing ''n" discrete size classes of particles rearrange by- themselves to reach the maximum packing density [3]. Some models, such as the compressible packing model (CPM), present good precision in their results [14]. This model defines the packing density of granular assemblies from the granulometric distribution and allows the consideration of the type of compaction applied. It also allows the consideration of aspects such as grain morphology, the presence of water and admixtures in an indirect manner since the packing density of each class of the grains component of mixtures must be determined experimentally. Recent studies have demonstrated the efficiency of this model in the production of high-strength and eco-efficient concretes [13], [17]. Conversely, continuous models consider continuously sized particles. Moreover, it assumes a similarity condition for particle packing; i.e. the array of particles (granulation image) surrounding every particle in the distribution should be similar, regardless the size of the particle [3].

The search for the ideal granulometric curve for the continuous models aroused the interest of several researchers in the early twentieth century. The first model, proposed by Fuller and Thompson [18], is a power curve that accounts for two variables: the distribution factor (q) and the largest particle size (D). The curve is described by Equation 1, with a distribution coefficient (q) equal to 0.5 to obtain a curve with minimum voids.

$$\frac{CPFT}{100} = \left(\frac{d}{D}\right)^q \tag{1}$$

where CPFT = the cumulative (volume) percent finer than d, d = the particle diameter, D = the larger particle diameter, and q = the distribution coefficient.

Some researchers tried to improve this curve, like Andreasen and Andersen [19]. They proposed the use of an exponent q in the range of 0.33-0.50. This adjustment factor q had to be determined experimentally and, therefore, can vary according to the characteristics of the particles. However, Ortega et al. [20] concluded that besides the above two parameters, the smallest particle size would also influence the packing density of granular systems. Therefore, in 1980, Funk and Dinger [21] improved Equation 1 by accounting for the smallest particle diameter (DS). The latter was defined as Alfred model and is presented by Equation 2. They proposed an adjustment factor q = 0.37, determined by computer simulations, which provides the maximum packing density.

$$\frac{CPFT}{100} = \left(\frac{DP^q - Ds^q}{DL^q - DS^q} \right)^q \tag{2}$$

where CPFT = the cumulative (volume) percent finer than DP, DP = the particle diameter, DL is the larger particle diameter, Ds = the smaller particle diameter, and q = the distribution coefficient.

Among the particle packing models, Alfred's is considered the one that best adapts to the real conditions of particle size distribution and is widely used in the manufacture of ceramics and porcelain tiles [22].

With the possibilities listed, research aimed at reducing CO_2 emissions and the use of SP, optimized by particle packing models can add significant progress towards obtaining more eco-efficient concretes. In this context, the objective of the present study is evaluating the production of concretes with partial replacement of PC by SP, optimized by Alfred’s particle packing model, seeking to reduce cement consumption and CO_2 emissions per MPa of compressive strength .

2 MATERIALS AND EXPERIMENTAL PROGRAM

2.1 Materials

The PC used was the Brazilian cement type CP V-ARI, whose characteristics are described by the standard ABNT NBR 16697:2018 [23]. This type of cement is composed of up to 10% limestone filler in addition to the clinker. Its specific gravity is equal to 3,090 kg/m^3. The SP used is a waste material from the limestone sand production process. It was obtained from the quarry and then dried in a laboratory oven at 60ºC. Its specific gravity is equal to 2,670 kg/m^3. The SP was classified as inert according to the Brazilian standards that determine the pozzolanic activity with lime [24] and the performance index with PC [25]. Table 1 presents the chemical compositions of both materials, as obtained by the X-ray fluorescence (XRF) (Panalytical, model Axios Max with Rhodium tube 4 kV).

Table 1. X-ray fluorescence of the fine materials.

Chemical composition		
Parameter analyzed	**PC**	**SP**
Al_2O_3	4.1%	3.0%
SiO_2	18.7%	6.1%
Fe_2O_3	2.8%	1.3%
CaO	60.6%	48.6%
MgO	4.1%	1.2%
SO_3	3.0%	0.2%
CaO free	0.6%	-
Insoluble residue	0.7%	-
Alkaline equivalent	0.7%	-
K_2O	-	0.6%
SrO	-	0.2%
Na_2O	-	0.1%
TiO_2	-	0.1%
P_2O_5	-	0.1%
Cl		-
MnO	-	< 0.1%

In Table 1, it is evident that PC and the SP exhibit high calcium oxide content in their chemical compositions. Figure 1 presents the particle size distribution of the PC and the SP. The test was performed by laser diffraction (equipment Malvern 2000) after 1 minute of ultrasound. Artificial limestone sand (S) and two limestone coarse aggregates were used: gravel with a maximum particle size equal to 9.5 mm (G9.5) and gravel with a maximum particle size equal to 19 mm (G19). The particle size distribution of the three aggregates, tested according to the standard ABNT NBR NM 248: 2003 [26] are also presented in Figure 1. The matrix rock of all aggregates is limestone. The characterization of the aggregates is shown in Table 2 according to: ABNT NBR NM 248: 2003 [26]; ABNT NBR NM 46: 2033 [27]; ABNT NBR NM 45: 2006 [28]; ABNT NBR NM 52: 2009 [29] ; ABNT NBR NM 53: 2009 [30]; ABNT NBR 7211: 2009 [31].

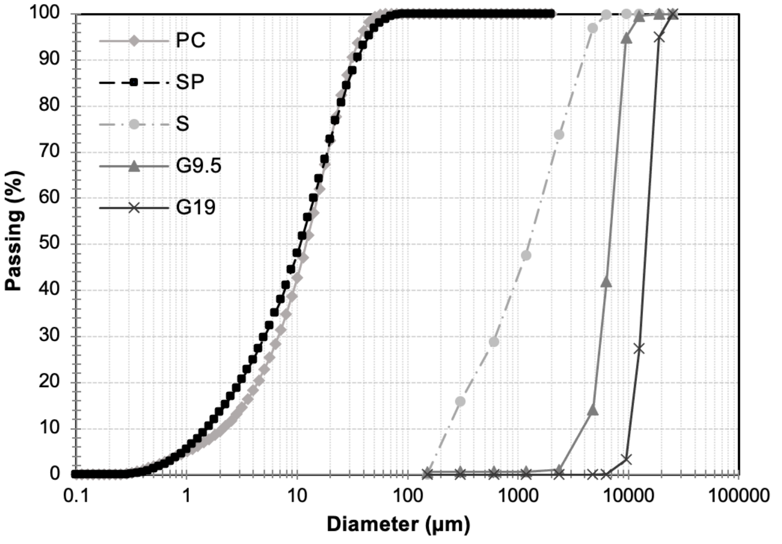

Figure 1. Particle size distribution of the materials.

Table 2. Physical characteristics of the aggregates.

	PROPERTY	S	G9.5	G19
Specific gravity (g/cm^3)	G9.5 and G19: ABNT NBR NM 53 (ABNT 2009b) S: ABNT NBR NM 52 (ABNT 2009c)	2.4	2.7	2.6
Bulk density (g/cm^3)	ABNT NBR NM 45: 2006	1.8	1.5	1.5
Void index (%)		26.7	42.2	42.6
Material finer than 75 µm (%)	ABNT NBR NM 46: 2003	11.9	0.2	0.1

S: Artificial limestone sand. G9.5: Gravel with a maximum particle size equal to 9.5 mm. G19: Gravel with a maximum particle size equal to 19 mm

As evident in Figure 1, the particle size distribution of the PC and the SP are continuous and like each other. The diameter D50 is equal to 12.0 mm for the PC and 10.6 mm for the SP. It was also noted that the coarse aggregates showed grain uniformity, which can be verified by the small slope of the granulometric curve. On the other hand, sand presents a more continuous distribution.

In Table 2, as expected, it is noted that the artificial limestone sand had the highest amount of material finer than 75 µm. Artificial sands tend to present granulometry different from natural ones, generally with a higher content of fines [13]. This artificial limestone sand was chosen because it is common in the region and it is an artificial sand, considering the environmental impact related to the extraction of natural sand. Informality in natural sand extraction processes aggravates the environmental impact of concrete production. As an alternative, replacing natural sand with artificial one reduces environmental impacts. In addition, its production is carried out in the quarries, which reduces transport costs. The amount of material finer than 75 µm observed in the artificial limestone sand was high, thus helping to fill voids in the larger grains and, consequently, increasing the packing density. The same reasoning can be observed in G9.5, which obtained a powdery material content higher than that of G19.

The chemical admixture used consists of a third-generation superplasticizer with a density of 1,100 kg/m^3 and a solid content of 46.68%, according to the manufacturer. It meets the requirements of ABNT NBR 11768: 2011 [32], being compatible with all types of Brazilian PC. Superplasticizer content was fixed at 0.9% relative to the weight of the solids. This value was obtained from the saturation dosage test [13].

2.2 Experimental program

To define the content of each material in the composition of the concretes, to reduce the empty spaces in the cementitious matrix and increase the compactness, the action of increasing the packing of the particles was adopted. This action was obtained through the more efficient distribution of the grain sizes of the materials and using a theoretical distribution model [17], [33]. The model adopted for the packing curve was Alfred's, according to Equation 2, with three different distribution-factors (q): 0.37; 0.21; 0.45. As previously explained, the value of q = 0.37, through experimental checks, has been shown to result in maximum particle packing [34]. The values below the value of q=0.37 favor an increase in the amount of fines, while values above provide residual porosity. Thus, the lowest value analyzed (q = 0.21) seeks to evaluate the mixture with the highest content of fines. The highest value used (q = 0.45) intends to evaluate mixtures with lower levels of fine materials and the results in terms of efficiency (cement consumption/MPa), even knowing that in these mixtures, there is probably a lack of paste to involve the aggregates. With this discrepancy in values for the granulometric distribution module, it became possible to check the influence of fines on the flow between the particles and in terms of the efficiency of the produced concrete. For all mixtures, it was decided to keep the water/cement (w/c) constant and equal to 0.5, with the expected resistance of about 31 MPa, due to the empirical relationship of Abrams' Law [35].

In the first mixture, only PC was considered as a fine material, without the use of SP, as a reference mixture and with the value q = 0.37. From the second mixtures and for the others, the objective of the study was achieved with the partial replacement of CP by SP. SP was used as a PC partial replacement by percentage, since the particle size curve of the materials (Figure 1) were quite similar. The literature indicates the replacement content of 20% by mass as being ideal to produce more eco-efficient concretes [14], [17]. It is important to highlight that the models are applied in volume, since the packing is related to the spatial occupation by the particles in the composition, and not directly to its weight. Subsequently, applications will be made in weight, to ensure the necessary precision. Correlating with the appropriate specific gravity of the materials (section 2.1), in volume the substitution is equivalent to 22.4% of SP and 77.6% of PC.

For a better distribution of the theoretical curve, 15 different diameters were considered, the smallest in the series 10 µm and the largest 19000 µm, considering the diameter through which 50% of the smallest particles pass (SP, with D50 = 10.649 µm) and 50% of the largest particles (G19, with D50 = 19000 µm). Then, using Equation 2, the accumulated percentage of particles for each diameter of the series was determined. So that the proportion of each component material in the concrete could be defined, being divided into fines, sand, and coarse aggregate. Three distinct zones were considered in the model: a) fine materials: all material up to 100 µm; b) sand: from 100 to 4800 µm; c) coarse aggregates: from 4800 to 9500 µm (G9.5) and the remaining G19 (up to 19000 µm). Other authors have also used this methodology in applying Alfred's model [11].

Table 3 shows the application of the model considering q = 0.37.

Table 3. Application of the Alfred model with q = 0.37.

Diameter (µm)	CPFT (%)	Discrete (%)	Volume (%)	
10	0%	1%	11%	PC
15	1%	2%		
30	3%	3%		
60	6%	3%		
100	9%	2%		
150	11%	5%	46%	S
300	16%	7%		
600	23%	9%		
1200	32%	11%		
2400	43%	14%		
4800	58%	7%	27%	G9.5
6300	64%	12%		
9500	76%	9%		
12500	85%	15%	15%	G19
19000	100%	0%		

Table 4 shows the application of the model with q = 0.21.

Table 4. Application of the Alfred model with q = 0.21.

Diameter (µm)	CPFT (%)	Discrete (%)	Volume (%)	
10	0%	2%	20%	PC + SP
15	2%	4%		
30	7%	5%		
60	12%	4%		
100	16%	4%		
150	20%	7%	49%	S
300	27%	8%		
600	35%	10%		
1200	45%	11%		
2400	56%	13%		
4800	68%	6%	21%	G9.5
6300	74%	9%		
9500	83%	6%		
12500	89%	11%	11%	G19
19000	100%	0%		

Table 5 presents the volumes obtained with the application of the model with q = 0.45.

Table 5. Application of the Alfred model with q = 0.45.

Diameter (µm)	CPFT (%)	Discrete (%)	Volume (%)	
10	0%	1%	8%	PC + SP
15	1%	2%		
30	2%	2%		
60	4%	2%		
100	6%	2%		
150	8%	4%	44%	S
300	13%	6%		
600	18%	8%		
1200	26%	11%		
2400	37%	15%		
4800	52%	7%	30%	G9.5
6300	59%	13%		
9500	72%	10%		
12500	82%	18%	18%	G19
19000	100%	0%		

From each corresponding diameter and discrete percentage of particles, the curve of the model was done. It is shown in Figure 2 for all the q values (0.37; 0.21; 0.45).

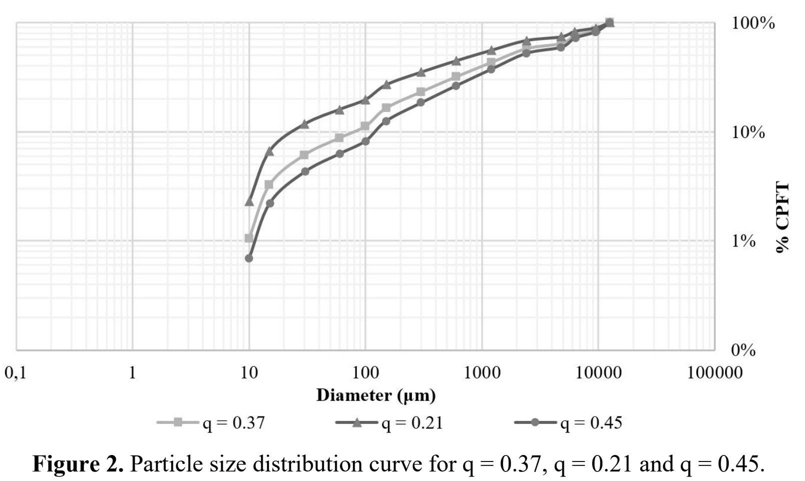

Figure 2. Particle size distribution curve for q = 0.37, q = 0.21 and q = 0.45.

It is important to highlight the increase in the content of fines (PC and SP) evidenced by the lower value of q, from 11% with q = 0.37 (Table 3) to 20% with q = 0.21 (Table 4). The same occurred with the sand, from 46% (q=0.37) to 49% (q=0.21). As for the coarse aggregates, the levels increased with the reduction of the value of q, from 27% to 21% (G9.5) and 15% to 11% (G19). As expected, the increase in the q value (q=0.45) caused a smaller volume of fines (8% PC + SP and 44% S) and an increase in the content of coarse particles (30% G9.5 and 18% G19) in the mixture composition, as shown in Table 5 and Figure 2.

With the volume of different materials defined for each curve plotted, the study proceeded to effectively obtain the mixtures in weight. The ratio of PC to other materials was calculated in weight from the volume contents and the respective specific gravity. Equation 3 was used to calculate the PC per m^3 of concrete, using the specific gravity of the materials that make up the concrete. The air content of 1.5% was considered, due to the packing of the particles, which provides a lower void content [13].

$$C = \frac{1000 - \left(air\% x10\right)}{\frac{1}{\gamma PC} + \frac{a/c}{\gamma water} + \frac{a}{\gamma sand} + \frac{p}{\gamma graves}} \tag{3}$$

where C = PC content (kg/m^3); γ = specific gravity; a = sand content, related to PC (PC: S) in mass; p = graves content, related to PC (PC: G) in mass.

Table 6 shows the consumption of materials in each mixture obtained with the application of the method.

Table 6. Consumption of materials in each mixture

Mixture	Volume (m^3)		Content related to PC		Weight (kg)
M1	PC	0.11	1	1	300.31
	S	0.46	3.21	a	964.15
	G9.5	0.27	2.08	p	623.45
	G19	0.15	1.16		347.67
	Chemical admixture	0.0025	-	-	2.7
	TOTAL	1.00	6.44	m	-
M2	PC	0.09	1	1	240.32
	SP	0.03	0.25		59.94
	S	0.46	4.14	a	994.25
	G9.5	0.27	2.68	p	642.91
	G19	0.15	1.49		358.53
	Chemical admixture	0.0020	-	-	2.7
	TOTAL	1.00	8.30	m	-
M3	PC	0.15	1	1	390.07
	SP	0.04	0.25		97.29
	S	0.49	2.48	a	967.75
	G9.5	0.21	1.17	p	458.12
	G19	0.11	0.59		229.51
	Chemical admixture	0.0032	-	-	4.39
	TOTAL	1.00	4.24	m	-
M4	PC	0.06	1	1	181.60
	SP	0.02	0.25		45.29
	S	0.44	5.36	a	973.48
	G9.5	0.30	4.02	p	729.63
	G19	0.18	2.36		429.04
	Chemical admixture	0.0015	-		2.04
	TOTAL	1.00	11.74	m	-

Comparing the consumption of each mix with the replacement of PC by SP, the use of q=0.21 resulted in a CP consumption 62% higher than the mixture with q=0.37. For q = 0.45 consumption was close to 75% if also compared with the mix obtained with q = 0.37. Evidencing the higher and lesser amount of fines in the mixture by applying the Alfred model varying the q value.

The procedure used for mixing the materials to produce the concretes was adapted from Campos [13] and Damineli [5]. The first step consists of manual homogenization of the fine materials in the dry condition and their addition to a concrete mixer. Thereafter, half of the water and superplasticizer volumes are added to the concrete mixer in a constant and controlled flow for approximately 30 seconds with the mixing equipment on. The coarse aggregates are then added to the concrete mixer in a constant flow for approximately 1 minute, followed by 1.5 minutes of mixing time. The next step involves the addition of sand in a constant and controlled flow for 2.5 minutes. The addition of the remaining water and superplasticizer volumes is then performed in a controlled and constant flow for approximately 30 seconds with the mixing equipment on. Finally, the materials were mixed for 10 minutes, resulting in a 16-minute mixture.

After mixing, eight cylindrical specimens were molded for each concrete mix with dimensions of 100 x 200 mm for the tests in a hardened state. The compaction was performed with a vibration table in four layers for 15 seconds each. The specimens were kept at the formworks at laboratory temperature for 24 hours and covered with a plastic film to prevent water loss. Thereafter, the concrete specimens were placed in a chamber with > 95% humidity and temperatures of 23 ± 2 °C until the date of the test.

In the fresh state, specific gravity and consistency were determined. The specific gravity was obtained according to the procedure described in ABNT NBR 9833: 2008 [36]. The consistency was evaluated by the slump test, dictated by ABNT NBR NM 67: 1998 [37]. In the hardened state, the compressive strength test was carried out at 7 and 28 days, performed as established by ABNT NBR 5739: 2007 [38] with a ZwickRoell press with a capacity of 100 tons. The specimens were polished for the test using a concrete surface grinding machine. This process consists of the removal of a thin layer of top material by mechanical means.

The sustainability analyses were performed considering the CO_2 emission factors obtained from the literature for each material used. Efficiencies were calculated considering the cement consumption and CO_2 emissions required to obtain 1 MPa of compressive strength, as proposed by Damineli et al. [39]. The emission factors used were obtained from the following references: PC: 0.863 kgCO_2e/kg [40], [41]; SP: 0.0016 kgCO_2e/kg [42]; S: 0.0016 kgCO_2e/kg [42]; G9.5: 0.00155 kgCO_2e/kg [43]; G19: 0.00155 kgCO_2e/kg [43]; Chemical admixture: 1.133 kgCO_2e/kg [44].

4 RESULTS AND DISCUSSIONS

Table 7 shows the specific gravity and the slump for each mixture.

Table 7. Results in fresh state

Mix	q	Specific gravity (kg/m^3)	PC (kg/m^3)	Chemical admixture (%)	Slump (mm)
M1	0.37	2303.37	300.31	0.9	13.0
M2	0.37	2410.63	240.32	0.9	20.0
M3	0.21	2223.68	390.07	1.2	>250
M4	0.45	2150.13	181.60	0.9	-

The partial replacement of PC by SP in the composition allowed the reduction of cement consumption by 20%, comparing the M1 and M2 mixtures, which have the same q value in the application of the method. However, the greater presence of SP fines demanded more water, which resulted in a lower slump (slump = 2.0 cm), given that the w/c ratio was kept constant, as observed in Table 7. The demand for water is a function of the specific surface of the particles: the larger the specific surface of the particle, the more water will be needed to wet it, consequently the smaller the water layer thickness and workability. For the same amount of water, with a larger surface area, the thickness of the water film will be thinner and the flow capacity will be less and vice versa [45]. In addition, clusters of fine particles act as larger particles, which modifies the particle size distribution and hinders the mobility of flow lines, since clusters move more slowly and act as blocks to smaller particles, increasing viscosity and generating voids [5]. Other studies have also noted the loss of slump with the use of SP [13]. Still comparing mixtures M1 and M2, the greater specific gravity of the second indicates less voids content, therefore greater packing due to the fines of the SP.

In the M3, due to the lower q value, the loss of workability was even more pronounced, which resulted in the choice to increase the chemical admixture content to 1.2%, increasing the slump. It is noteworthy that with the higher amount of PC and SP the larger the specific surface, therefore, requiring more water. To use the w/c ratio for all mixtures, the additive content was increased from 0.9 to 1.2% to avoid difficulties in molding the mixture. As a result, M3 was very viscous, with a slump greater than 25 cm.

The last mixture, with the highest value of q (0.45) obtained a higher volume of aggregates at the expense of fines and cement. The opposite occurred in M3, as q adopts values above 0.37 residual porosity [34] is verified, also evidenced by the low consumption of PC in the mixture. Mixture M4 lacked cement paste, not being enough to cover the aggregates, making them apparent. With the low consistency, it was not possible to measure the slump since the mixture disintegrated when removing the specimens. Also in Table 7, the specific gravity of M4 was the lowest obtained, which demonstrates the highest void content of this mixture, as expected by the q value used. Figure 3 shows the specimens one day after production, illustrating the highest void content in M4.

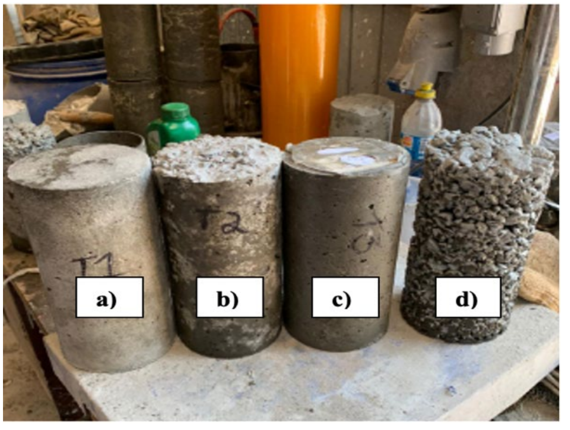

Figure 3. a) M1; b) M2; c) M3; d) M4.

Figures 4 show the results of compressive strength at 7 and 28 days.

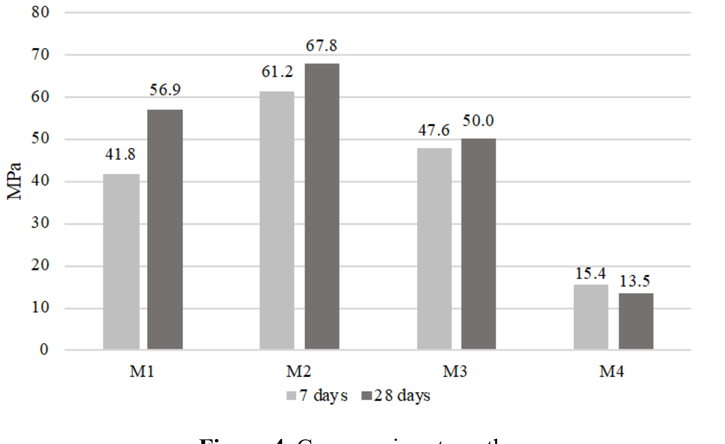

Figure 4. Compressive strength.

Figure 4 shows that, due to the use of high initial strength cement use, the values of compressive strength at 7 days proved to be high. Not only regarding the PC, but the application of the Alfred particle also packing model demonstrated the production of concretes with higher compressive strength than expected by Abrams's Law [35]. Only exception was M4, considering the w/c ratio high for this compressive strength range (w/c = 0.50). Yousuf et al. also verified that concretes optimized by Alfred's model obtained compressive strengths above the target before 28 days [11]. To reach compressive strength close to 50 MPa, the w/c ratio around 0.40 is indicated [46]. The sole use of Abrams' law is not precise enough to predict the behaviour of highly packed systems designed using advanced techniques such as particle packing models [3]. The authors explain that particle packing models may enhance the particle size distribution of granular systems, reducing the material's porosity and consequently increasing the system packing density. Recent studies have shown that the use of particle packing models results in a reduction in concrete porosity, with a significant increase in concrete electrical resistivity and ultrasonic pulse velocities [14], [17]. Therefore, an increase in the compressive strength of the concrete is observed. So, the application of particle packing models, to increase the density of the granular system in cementitious materials, shows as a key parameter for obtaining concrete with high mechanical and durability performance [16].

It also can be seen, in Figure 4, that the mixture with the highest compressive strength was the M2, with 118% of the value expected by Abrams' Law [35]. It is also noted that the replacement the PC by SP in M2 provided greater compressive strength as compared to M1, for the same q value. Even though it is an inert material, the granulometric curve of the SP, and its amount of fines contributed to filling the voids, demonstrated by the compressive strength 19% higher than M2 compared to M1 with less PC consumption. This also indicates greater packing, as observed in other studies that used SP as a partial replacement for PC [13], [14], [17]. M3 obtained a PC consumption 62% higher than M2. However, its average compressive strength was 26% lower, proving that the greater packing (given by q=0.37) resulted in higher compressive strength, even with less PC consumption. Due to the lack of fines, M4 presented many voids and low compressive strength, being 80% lower than M2 with a 24% lower PC consumption.

Figure 5 show the consumption of PC per m^3 of concrete to obtain 1 MPa of compressive strength, to analyze the efficiency of the mixtures produced.

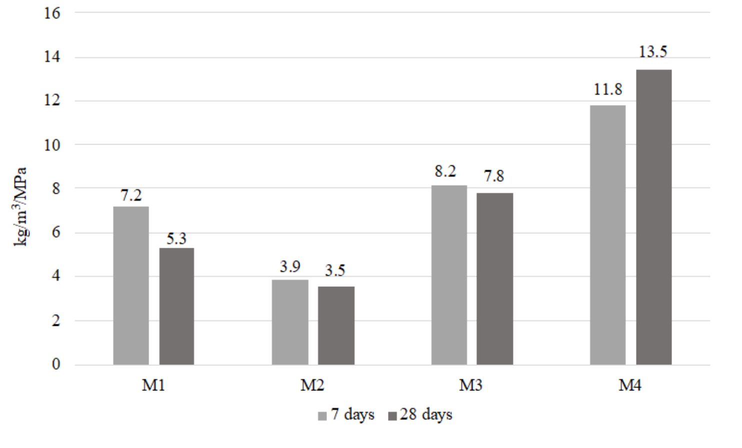

Figure 5. kg/m^3/MPa.

It can be seen, in Figure 5, that M2 is the most efficient, with the lowest consumption of cement/MPa (3.5). Damineli et al. [39] showed that a large part of the Brazilian market for concretes, with most concretes produced in the range of 40 MPa of compressive strength at 28 days, present the index above in the range between 7 and 14 kg/m^3/MPa. The literature commonly presents values from 9 to 14 kg/m^3/MPa for conventional situations [3]. For high-performance concretes, the level is in the range of 5 kg/m^3/MPa [39]. Toralles et al. [47], to compare three mix methods for conventional concrete fixing the same desired compressive strength, show that for the ABCP (Brazilian Portland Cement Association) method the PC consumption of 418 kg/m^3 and w/c ratio of 0.49 reached 36.3 MPa. For the same w/c ratio, the O'Reilly method, with cement consumption of 412 kg/m^3, reached 36.5 MPa. Finally, the last method, from IPT (Institute of Technological Research), for a w/c ratio of 0.59 and cement consumption of 314 kg/m^3, obtained 27 MPa. For these mixtures, the binder index was between 7 and 14 kg/m^3/MPa, confirming the values indicated by Damineli et al. [39]. The most efficient concrete in this study, by the O´Reilly method, reached 11.29kg/m^3/MPa. Lopes [15] analyzed the application of Alfred's particle packing model in the production of optimized concretes, to reduce cement consumption. For comparison, the author opted to produce conventional and high strength concrete using the IPT and modified IPT methodologies. In the study, the concrete with the highest compressive strength, optimized by the Alfred model, resulting in 83.25 MPa with cement consumption of 420.82 kg/m^3. The corresponding reference mixture, produced by the modified IPT method, presented 62.37 MPa with cement consumption of 654.15 kg/m^3. The reference mixture had a binder index of 10.49 kg m^3/MPa and the optimized one reached 5.05kg m^3/MPa. Thus, it is noted that the most efficient mixture of the present study (M2) had lower cement consumption per MPa, compared with data from the literature.

The present study searched the production of optimized concretes in the compressive strength range of conventional ones, but with less consumption of PC necessary to reach this level. The compressive strength achieved by M1 and M2 concretes put them at the same level as high-performance concretes. M1 presents a binder index close to 5 kg/m^3/MPa. In M2, the partial replacement of PC by SP not only provided less cement consumption, but also greater packing and compressive strength gain, as previously mentioned exposed. As a result, M2 received a value of 3.5 kg/m^3 to deliver 1 MPa of compressive strength, the lowest amount observed in the optimized concretes of the study. This value is 50% below the minimum value observed for conventional concretes (7 kg/m^3/MPa) and 29% below that noted for high-performance concretes (5 kg/m^3/MPa). Comparing M1 and M2 mixtures, the replacement of PC by SP in M2 allowed the reduction of the binder index by 45% at 7 days and by 32% at 28 days. Mixtures M3 and M4, the first for presenting the highest PC consumption between the mixtures and the second for the lowest compressive strength achieved, fit in the range of conventional concretes between 7 and 14 kg/m^3/MPa.

Figure 6 shows the kgCO_2e to produce 1 m^3 of concrete.

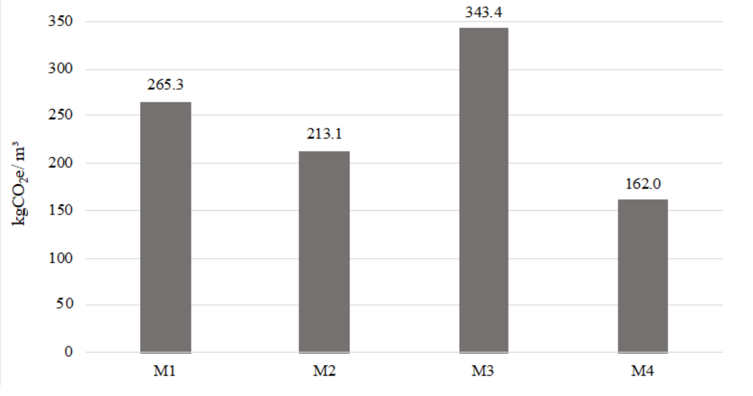

Figure 6. kgCO_2e/ m^3.

It can be seen, in Figure 6, that the mixture that presented the lowest emission index was M4. This fact is linked to its low PC consumption, predicted by the high q value uses (0.45), which represents a lower content of fines (PC+SP). M2 was in second place in this indicator, with M3 remaining in the sequence. Recalling that the q value was the same for the two mixtures (q = 0.37 for M1 and M2), only the replacement of PC by SP in M1 promoted a 20% reduction in the CO_2 emissions per m^3 of concrete. M3, for presenting the highest amount of fines obtained the highest consumption of PC and, consequently, the highest indicator of emissions per m^3.

Figure 7 shows the efficiency of the concretes in terms of CO_2 emissions.

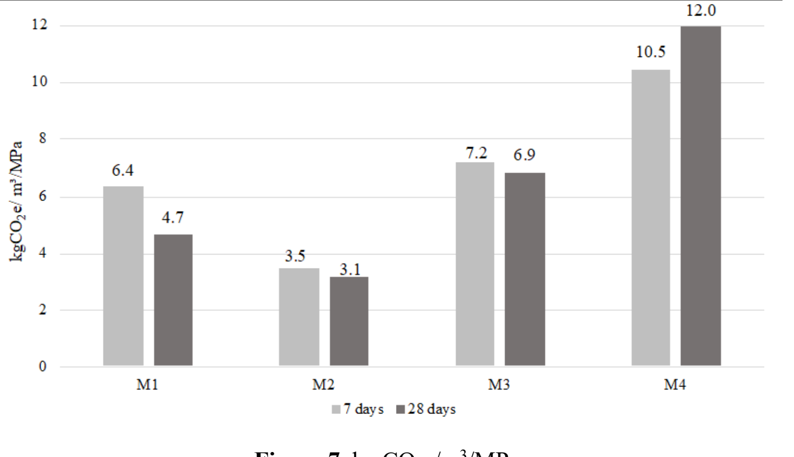

Figure 7. kg CO_2e/m^3/MPa.

It as can be seen in Figure 7, that M4, which obtained the lowest emissions per m^3, now attests to the worst performance due to its low targeted compressive strength. Again, when comparing M1 and M2, the replacement by SP in the second mixture resulting in lower PC consumption and higher compressive strength, resulted in a 33% reduction in $kgCO_2e/m^3/MPa$. The measured compressive strength of M3 was satisfactory when compared to conventional concretes. However, the consumption of PC higher than the other produced mixes made it intermediate in relation to this index over the others, being 54% above M2 (most efficient). In Costa's research [48], the author raised quantities of CO_2 emitted in the production of materials used in civil construction. Concretes produced with CP V ARI in the range of 50 MPa with a standard mixture of cement consumption close to 400 kg/m^3, it would take the level of emissions at 485 $kgCO_2e/m^3$, witch results in 9.7 $kgCO_2e/m^3/MPa$. It is noted that the values obtained in the present research were satisfactory, with the best concrete produced (M2) reaching 213.09 $kgCO_2e/m^3$ and 3.15 $kgCO_2e/m^3/MPa$.

5 CONCLUSIONS

After performing the experiments and analyzing the obtained results, the following conclusions can be made:

- The application of the method resulted in concretes with cement consumption of 300.31 kg/m^3 for M1 (q = 0.37 without replacing PC by SP), 240.32 kg m^3 for M2 (q = 0.37 with the replacement of PC by SP), 390.07 kg/m^3 for T3 (q = 0.21) and 181.60 kg/m^3 for T4 (q = 0.45).
- In the fresh state, the slump was reduced in the mixtures with the replacement of PC by SP due to the higher content of fines in the SP. These fines result in a greater specific surface; therefore, more water was needed to wet the particles, consequently, the water layer thickness and workability were smaller. On the other hand, the use of SP, due to the greater packing provided by the fines of its composition, increased the specific gravity comparing M1 (without SP) and M2 (with replacement of 20% of PC by SP). In the third mixture (M3), due to the lower q value (0.21), the loss of workability was even more accentuated. It is noteworthy that with the greater amount of PC and SP composing the mixture, the larger the specific surface, therefore, requiring more water. To use the same w/c ratio for all mixtures, the additive content was increased from 0.9 to 1.2% to avoid difficulties in molding the specimens. As a result, M3 was very viscous, with a slump greater than 25 cm. In the last mixture (M4), with the highest q value (0.45), residual porosity was noted. This feature exhibited little paste, not enough to cover the aggregates. With the low consistency, it was not possible to measure the slump.
- In the hardened state, the M2 mixture showed the highest compressive strength - 67.8 MPa at 28 days. Comparing the M1 and M2 mixtures (q = 0.37), the first without and the second with the partial replacement of PC by SP, the modified mixture showed higher compressive strength, indicating that the SP favored greater packing. Even though it is an inert material, the SP allowed 19% higher compressive strength with 20% less PC consumption. M3 (q = 0.21) presented compressive strength 16% below M2 (q = 0.37), for a 62% higher PC consumption. This fact demonstrating that the value q = 0.37 resulted in greater packing and, consequently, higher compressive strength, even with less PC consumption. M4 had the lowest compressive strength of the mixtures, due to the lower consumption of PC and higher voids content. The application of the Alfred particle packing obtained highest compressive strength than expected (31 MPa), except for T4, considering the high w/c ratio used (w/c= 0.50).
- In terms of efficiency, the M2 binder index, which showed the best results, was 3.5 kg/m^3/MPa, lower than the values observed in the literature. M1 presented a binder index 48% above M2 due to its higher CP consumption and lower compressive strength, both factors are related to the partial replacement of PC by SP. As cement is the component material of concrete that most emanates CO_2 emissions for its production, the lower consumption of cement in the mix implies lower CO_2e emissions per m^3 of concrete. Thus, the mixture that presented the lowest emission values per m^3 was M4. However, in terms of efficiency, M2 proved to be the most eco-efficient, with only 3.15 $kgCO_2/m^3/MPa$.

It is concluded then that the method proved to be simple to be applied, providing a lower volume of voids in the concrete that resulted in less consumption of paste needed to fill these spaces. Consequently, it was possible to produce concrete with lower cement consumption and CO_2 emissions per MPa. SP as a partial replacement for PC provided greater compressive strength, even though it is an inert material. Sustainable concretes proved to be very efficient, with a lot of potential yet to be explored. So, as a suggestion for future work: verify the method by applying other residual materials in substitution of PC; evaluate the rheological parameters of concretes optimized by the particle packing technique.

ACKNOWLEDGEMENTS

The authors would like to thank the companies Itambe and Grace which kindly provided all necessary materials for the study. The company Votorantim Cimentos, for carrying out the compressive strength test of the studied concrete.

We also thank the Department of Construction Engineering (DCC) and the Post-graduation Program in Civil Engineering at the Federal University of Parana (PPGEC/UFPR) for the infrastructure support provided.

REFERENCES

[1] M. L. Berndt, "Influence of concrete mix design on CO2 emissions for large wind turbine foundations," *Renew. Energy*, vol. 83, pp. 608–614, 2015, http://dx.doi.org/10.1016/j.renene.2015.05.002.

[2] K. Celik, C. Meral, P. A. Gursel, P. Mehta, A. Horvath, and P. Monteiro, "Mechanical properties, durability, and life-cycle assessment of self-consolidating concrete mixtures made with blended portland cements containing fly ash and limestone powder," *Cement Concr. Compos.*, vol. 56, pp. 59–72, 2015, http://dx.doi.org/10.1016/j.cemconcomp.2014.11.003.

[3] M.T. Grazia, L.F.M. Sanchez, R.C.O. Romano, and R.G. Pileggi, "Investigation of the use of continuous particle packing models (PPMs) on the fresh and hardened properties of low-cement concrete (LCC) systems," *Constr. Build. Mater.,* v. 195, p. 524–536, 2019, https://doi.org/10.1016/j.conbuildmat.2018.11.051.

[4] Sindicato Nacional da Indústria do Cimento, *ROADMAP Tecnológico do Cimento: Potencial de Redução das Emissões de Carbono da Indústria do Cimento Brasileira até 2050*. Rio de Janeiro: SNIC, 2019.

[5] B. L. Damineli, "*Conceitos para formulação de concretos com baixo consumo de ligantes: controle reológico, empacotamento e dispersão de partículas*," M.S. thesis, Esc. Politéc., Univ. São Paulo, São Paulo, 2013.

[6] T. Proske, S. Hainer, M. Rezvani, and C. Graubner, "Eco-friendly concretes with reduced water and cement contents - Mix design principles and laboratory tests," *Cement Concr. Res.*, vol. 51, pp. 38–46, 2013, http://dx.doi.org/10.1016/j.cemconres.2013.04.011.

[7] T. Higuchi, M. Morioka, I. Yoshioka, and K. Yokozeki, "Development of a new ecological concrete with CO_2 emissions below zero," *Constr. Build. Mater.*, vol. 67, pp. 338–343, Sep 2014, http://dx.doi.org/10.1016/j.conbuildmat.2014.01.029.

[8] E. Gartner and H. Hirao, "A review of alternative approaches to the reduction of CO_2 emissions associated with the manufacture of the binder phase in concrete," *Cement Concr. Res.*, vol. 78, pp. 126–142, 2015, http://dx.doi.org/10.1016/ j.cemconres.2015.04.012.

[9] R. C. D. O. Romano, D. D. R. Torres, and R. G. Pileggi, "Impact of aggregate grading and air-entrainment on the properties of fresh and hardened mortars," *Constr. Build. Mater.*, vol. 82, pp. 219–226, 2015, http://dx.doi.org/10.1016/j.conbuildmat.2015.02.067.

[10] H. S. Mueller, M. Haist, J. S. Moffatt, and M. Vogel, "Design, material properties and structural performance of sustainable concrete," *Procedia Eng.*, vol. 171, pp. 22–32, 2017, http://dx.doi.org/10.1016/j.proeng.2017.01.306.

[11] S. Yousuf, L. F. M. Sanchez, and S. A. Shammeh, "The use of particle packing models (PPMs) to design structural low cement concrete as an alternative for construction industry," *J. Build. Eng.,* v. 25, p. 100815, Sep. 2019, https://doi.org/ 10.1016/j.jobe.2019.100815.

[12] P. R. Matos, R. D. Sakata, and L. R. Prudêncio Jr., "Eco-efficient low binder high-performance self-compacting concretes," *Constr. Build. Mater.*, vol. 225, pp. 941–955, 2019, http://dx.doi.org/10.1016/j.conbuildmat.2019.07.254.

[13] H. F. Campos, "*Dosagem de concreto sustentável e de alta resistência, otimizada por modelos de empacotamento de partículas, com substituição parcial do cimento Portland por pó de pedra e sílica ativa*," M.S. thesis, Univ. Fed. Paraná, Curitiba, Brazil, 2019.

[14] H. F. Campos, N. S. Klein, J. Marques Fo., and M. Bianchini, "Low- cement high-strength concrete with partial replacement of Portland cement with stone powder and silica fume designed by particle packing optimization," *J. Clean. Prod.*, vol. 261, pp. 121228, 2020, http://dx.doi.org/10.1016/j.jclepro.2020.121228.

[15] H. M. T. Lopes, "*Aplicação do conceito de empacotamento de partículas na otimização de dosagem de concretos de cimento* Portland," M.S. thesis, Universidade Federal de São Carlos, São Carlos, São Paulo, Brazil, 2019.

[16] A. Castro and F. Ferreira, "Effect of particle packing in the durability of high performance concretes," *Ing. Constr.*, vol. 31, no. 2, pp. 91–104, 2016.

[17] H.F. Campos, J Marques Fo, and N.S. Klein, "Proposed mix design method for sustainable high-strength concrete using particle packing optimization," *J. Clean. Prod.*, vol. 265, pp. 121907, 2020, https://doi.org/10.1016/j.jclepro.2020.121907

[18] W. B. Fuller and S. E. Thompson, "The laws of proportioning concrete," in *Transactions of ASCE*, 1907, pp. 67–143.

[19] A. H. M. Andreasen and J. Andersen, "Über die Beziehungzwischen Kornabstufung und Zwischenraum in Produktenauslosen Körnern (miteinigen Experimenten)," *Colloid Polym. Sci.*, vol. 50, pp. 217–228, 1930.

[20] F. D. S. Ortega, R. G. Pileggi, P. Sepúlveda, and V. C. Pandolfelli, "Influência dos modelos de Alfred e de Andreasen sobre a microestrutura e densidade a verde de compactos cerâmicos obtidos por colagem ou prensagem," *Ceramica*, vol. 43, no. 283–284, pp. 185–191, 1997, http://dx.doi.org/10.1590/S0366-69131997000400007.

[21] J. E. Funk and D. R. Dinger, *Grinding and Particle Size Distribution Studies for Coal-Water Slurries at High Solids Content, Final Report*. New York, USA: Empire State Electric Energy Research Corporation (ESEERCO), 1980.

[22] I. R. Oliveira, A. R. Studart, R. G. Pileggi, and V. C. Pandolfelli, *Dispersão e Empacotamento de Partículas: Princípios e Aplicações em Processamento Cerâmico*, São Paulo: Fazendo Arte, 2000, pp. 224.

[23] Associação Brasileira de Normas Técnicas, *Cimento Portland — Requisitos, NBR 16697*, 2018.

[24] Associação Brasileira de Normas Técnicas, *Materiais pozolanicos - Determinacao da Atividade Pozolanica com Cal aos Sete Dias, NBR 5751*, 2015.

[25] Associação Brasileira de Normas Técnicas, *Materiais pozolânicos - Determinação do Índice de Desempenho com Cimento Portland aos 28 dias, NBR 5752*, 2014.

[26] Associação Brasileira de Normas Técnicas, *Agregados - Determinação da Composição Granulométrica, NBR NM 248*, 2003.

[27] Associação Brasileira de Normas Técnicas, *Agregados - Determinação do Material Fino que Passa Através da Peneira 75 um, por Lavagem, NBR NM 46*, 2003.

[28] Associação Brasileira de Normas Técnicas, *Agregados - Determinação da Massa Unitária e do volume de vazios, NBR NM 45*, 2006.

[29] Associação Brasileira de Normas Técnicas, *Agregado miúdo - Determinação de Massa Específica e Massa Específica Aparente, NBR NM 52*, 2009.

[30] Associação Brasileira de Normas Técnicas, *Agregado graúdo - Determinação de Massa Específica, Massa Específica Aparente e Absorção de Água, NM 53*, 2009.

[31] Associação Brasileira de Normas Técnicas, *Agregados para Concreto — Especificação, NBR 7211*, 2009.

[32] Associação Brasileira de Normas Técnicas, *Aditivos para Concreto de Cimento Portland, NBR 11768*, 2011.

[33] R. Yu, P. Spiesz and H. J. H. Brouwers, "Development of an eco-friendly Ultra-High Performance Concrete (UHPC) with efficient cement and mineral admixtures uses," *Cement Concr. Compos.*, vol. 55, pp. 383–394, 2015, http://dx.doi.org/10.1016/j.cemconcomp.2014.09.024.

[34] A. L. Castro and V. C. Pandolfelli, "Revisão: conceitos de dispersão e empacotamento de partículas para a produção de concretos especiais aplicados na construção civil," *Ceramica*, vol. 55, no. 333, pp. 18–32, 2009, http://dx.doi.org/10.1590/S0366-69132009000100003.

[35] D. A. Abrams, *Design of Concrete Mixtures*. Chicago, USA: *Structural Materials Research Laboratory,* 1924.

[36] Associação Brasileira de Normas Técnicas, *Concreto Fresco – Determinação da Massa Específica, do Rendimento e do Teor de Ar pelo Método Gravimétrico*, ABNT NBR 9833, 2009.

[37] Associação Brasileira de Normas Técnicas, *Concreto - Determinação da Consistência pelo Abatimento do Tronco de Cone*, ABNT NBR NM 67, 1998.

[38] Associação Brasileira de Normas Técnicas, *Concreto - Ensaio de Compressão de Corpos-de-prova Cilíndricos*, ABNT NBR 5739, 2007.

[39] B. L. Damineli, F. M. Kemeid, P. S. Aguiar, and V. M. John, "Measuring the eco-efficiency of cement use," *Cement Concr. Compos.*, vol. 32, no. 8, pp. 555–562, 2010.

[40] V. C. H. C. Oliveira, "Estratégias para a minimização da emissão de CO2 de concretos estruturais," M.S. thesis, Escola Politécnica da Universidade de São Paulo, São Paulo, Brazil, 2015.

[41] Votorantim Cimentos, *EPD – Environmental Product Declaration*. Portland, USA: PCA, 2016.

[42] C. M. B. D. B. Falcão, *Análise da Qualidade do Investimento e Emissões de CO_2 Associadas à Produção de Agregados Reciclados na Região Metropolitana de São Paulo*. São Paulo: Escola Politécnica, Universidade de São Paulo, 2013.

[43] E. Rossi, "*Avaliação do ciclo de vida da brita para a construção civil: estudo de caso*," M.S. thesis, Universidade Federal de São Carlos, São Carlos, Brazil, 2013.

[44] F. Ma, A. Sha, P. Yang, and Y. Huang, "The greenhouse gas emission from portland cement concrete pavement construction in China," *IJERPH.*, vol. 13, no. 7, pp. 632, 2016. https://doi.org/10.3390/ijerph13070632.

[45] L. G. Li and A. K. H. Kwan, "Concrete mix design based on water film thickness and paste film thickness," *Cement Concr. Compos.*, vol. 39, pp. 33–42, 2013, http://dx.doi.org/10.1016/j.cemconcomp.2013.03.021.

[46] B. F. Tutikian and P. Helene, "Dosagem dos concretos de cimento Portland," in *Concreto: Ciência e Tecnologia*, G. C. Isaia, Ed., São Paulo: Ibracon, 2011.

[47] B. M. Toralles et al., "Estudo comparativo de diferentes métodos de dosagem de concretos convencionais," *Rev. Eng. Tecnol.*, vol. 10, no. 1, pp. 184–198, 2018.

[48] B. L. C. Costa, "*Quantificação das emissões de CO_2 geradas na produção de materiais utilizados na construção civil*," M.S. thesis, Universidade Federal do Rio de Janeiro, Rio de Janeiro, 2012.

Author contributions: HFC.: Conceptualization (Lead), Formal analysis (Equal), Investigation (Equal), Methodology (Lead), Project administration (Lead), Supervision (Lead), Writing (Lead); ALB: Formal analysis (Equal), Investigation (Equal), Methodology (Equal), Validation (Equal), Writing (Supporting). ERDLS.: Formal analysis (Equal), Investigation (Equal), Methodology (Equal), Writing (Supporting). VMVJ: Formal analysis (Equal), Investigation (Equal), Methodology (Equal), Writing (Supporting).

Editors: Bernardo Tutikian, Guilherme Aris Parsekian.

IBRACON Structures and Materials Journal
Revista IBRACON de Estruturas e Materiais
ISSN 1983-4195 ismj.org

ORIGINAL ARTICLE

Application of MEMS accelerometer of smartphones to define natural frequencies and damping ratios obtained from concrete viaducts and footbridge

Uso de acelerômetros MEMS de smartphones para o conhecimento de frequências naturais e taxas de amortecimento de viadutos e passarela em concreto

Jorge Dalmas Braido[a]
Zacarias Martin Chamberlain Pravia[a]

[a]Universidade de Passo Fundo – UPF, Programa de Pós-graduação em Engenharia Civil e Ambiental – PPGEng, Passo Fundo, RS, Brasil

Received 27 March 2021
Accepted 14 August 2021

Abstract: The continuous development of smartphones has garnered considered research attention owing to the possibility of its use in different engineering applications. MEMS accelerometers available on smartphones are useful for structural health monitoring. This study is aimed at determining the use of smartphones in the calibration and correction of the sampling rate for natural frequency and damping identification. Three concrete bridges were used in the case studies. The results indicate that smartphones can be used to understand some dynamic parameters.

Keywords: accelerometers, smartphones, calibration, MEMS, modal.

Resumo: a contínua evolução dos smartphones despertou o interesse da comunidade científica para aplicações deste aparelho em situações ligadas à engenharia estrutural. Em um caso mais específico, os acelerômetros MEMS que equipam aparelhos de telefonia móvel tem se mostrado úteis para a realização de monitoramentos da saúde estrutural SHM. O objetivo deste trabalho é apresentar o uso de MEMS do celular junto à calibração e correção da taxa de amostragem, as quais são necessárias para a identificação dos parâmetros modais de frequência natural e amortecimento. Os estudos de caso são três estruturas – dois viadutos em concreto armado e uma passarela em concreto protendido. Os resultados indicam que é possível utilizar este aparelho em casos onde é necessário o conhecimento de algumas propriedades dinâmicas ao alcance da mão.

Palavras-chave: acelerômetros, celular, calibração, MEMS, modal.

How to cite: J. D. Braido and Z. M. C. Pravia, "Application of MEMS accelerometer of smartphones to define natural frequencies and damping ratios obtained from concrete viaducts and footbridge," *Rev. IBRACON Estrut. Mater.*, vol. 15, no. 2, e15206, 2022, https://doi.org/10.1590/S1983-41952022000200006

1 INTRODUCTION

Structural health monitoring (SHM) has undergone continuous development in civil infrastructure since the 1970s. This methodology, also known as St-Id, uses nondestructive methods composed of numerical models and experimental data to assess structural performance and aid in decisions regarding structural management and rehabilitation [1].

The evolution of SHM can also be seen on mobile sensors and wireless devices; for example, current smartphones are embedded with MEMS accelerometers. The use of wireless devices has become more appealing because it allows faster monitoring and is feasible in both public and private infrastructures.

Corresponding author: Jorge Dalmas Braido. E-mail: jorgebraido@gmail.com
Financial support: None.
Conflict of interest: Nothing to declare.

MEMS accelerometers in smartphones have been studied [2]–[12]. In some of these studies they show monitoring using smartphones at different levels and situations, not necessarily from an SHM approach. These examples consider the adaptability and capability of smartphones.

When smartphones are used for SHM, concerns arise regarding data accuracy and calibration. According to Kuhlmann et al. [13], if the angle installation is in the range of 0.5° to 3°, the data accuracy can be compromised. Moreover, civil structure strains are in the range of −5° – 5° [14]. Therefore, in extreme situations where the device is installed incorrectly, the data from smartphones can correspond to an 8° inclination. Data accuracy can also be jeopardized by incorrect device operation, resulting in the disposal of samples taken using the smartphone. Other error sources include inadequate manufacturing, voltage instability, and temperature effects [15].

The calibration of the MEMS accelerometer of a smartphone can be performed before any sample extraction and has simple computational steps that do not require special training [16]. The approach uses two special fixtures to record the acceleration in six positions, assuming constant gravitational force (*g*). The position angle of the smartphone during calibration has been previously defined [14].

Moreover, smartphone sensors show low quality at a frequency range below 0.5 Hz. This behavior is characteristic of colored noise, where the low-frequency spectrum is predominant [17]. Thus, a 1 Hz first-order natural frequency higher pass filter should be used to reduce unwanted frequency components [4], [18].

Another potential problem is that the smartphone's real sampling rate is lower than the target frequency [19]. This characteristic does not change the answers in the frequency peaks but modifies the amplitude values. A correction should be performed considering the ratio of the target frequency to the real frequency.

Although the mobile accuracy degree is lower than that of commercial accelerometers, their results are very similar [20]. Professional sensors have a 10^{-9}g resolution and measurement range below ± 1 g, while smartphone resolution is in the range of 0.1 to 15 mg with the measurement range of ± 4 g [5]. In this study, signals were assessed using the Root Mean Square (RMS) power data from before and after the filter application phases, and decibels are used to define attenuation or gain.

Smartphone mounting is performed by using double-sided tape to pin the smartphone to the structure to avoid local vibration during structural vibration measurement [3]. Stud mounting of accelerometers was used to analyze extremely high natural frequencies, as in the case of mechanical systems [21], [22]. Civil structures generally have very low natural frequencies. To avoid the interference from mounting the smartphone, a nondestructive method, such as structural adhesives or magnetic mounting, is ideal. This allows for more accurate assessments of structural damage, human comfort, and ground-borne noise applications; therefore, these techniques are more convenient and widely used.

The use of smartphones in monitoring activities is not restricted to one specific model or manufacturing company, which can expand the use of this device. Simple operation based on friendly applications is another reason for their implementation. Moreover, data can be saved, stored, and sent to data clouds, and some apps allow the definition of dynamic parameters, such as natural frequencies and damping rates, immediately after the measurements are taken.

According to Debona and da Silva [23], wired devices may cause involuntary accidents, such as the dragging of the device owing to pedestrian walking. To avoid these types of accidents, wireless devices must be implemented.

Studies have used different apps, such as the Accelerometer analyzer app developed by Mobile Tools [20], iDynamics app [5], and the phyphox app [12], in a controlled environment; however, in [24]. Phyphox was created to aid physics teaching using the smartphone sensors.

Because of the low costs associated with the use of MEMS accelerometers, they have been widely considered in the monitoring of civil structures. Considering that this type of device is found in most mobile devices, it can easily be applied to engineering issues.

In this study, one measurement point was adopted as nonofficial to discard commercial accelerometers. This configuration can present the influence of different vibration modes on the acceleration readings according to specific traffic conditions [25].

Three study cases located in Passo Fundo/RS were used to validate the process: two reinforced concrete bridges and a prestressed concrete footbridge. The bridges were 22.5m in width and 36.0m in length, with a common structural solution in Brazil: two cantilever girders simply supported with one span. The dimensions of the bridges were obtained from the structural design and retro analysis. The footbridge has a T cross-section and a length of 23.4m; although its dimensions were provided by the builder company, no additional information, such as cable positions, prestress force magnitude, or concrete strength class, was supplied. To verify the experimental dynamic parameters, finite element models and literature values were used as references.

Among the study cases, a minimum degree of comfort must be attained for the footbridge. Researchers and design standards have provided natural frequency values that guide this study. For instance, concrete footbridges with a span length of 23 m have a natural frequency in the range of 3.05 – 5.05 Hz [26]; natural frequencies higher than 5 Hz do not demand deeper evaluation related to pedestrian effects [27]; according to the Brazilian concrete standard [28], critical natural frequency (f_{crit}) should be 4.5 Hz and reach a design stage of ($f > 1,2f_{crit}$) vertical natural frequencies lower than 5 Hz should be avoided [29]; and finally, natural frequencies should be higher than 2 Hz, which is the natural frequency of human walking [30].

In the case of the footbridge, its maximum damping ration is 1.7% [30]. Low damping ratios can vary in the range of 0.5% – 1% [26].

In the case of bridges, natural frequencies are directly related to the span length [30]. The damping ratios cannot exceed 2%. In the case of simply supported, reinforced concrete bridges, damping should not exceed 3.5% [31].

The goal of this study was to demonstrate the use of a smartphone in infrastructure monitoring. The steps for calibration and frequency sampling rate correction are explained by considering the natural frequency and damping ratios from the case study definitions. To verify the results, numerical models were created obeying the real dimensions obtained from the structural designs and the national standard of the material properties [28], [32]. In addition, this paper presents a high-pass filter application. The authors have only defined two angles for calibrating the vertical positions related to the gravitational force axis: first, with the screen upward, and the second, with the screen upside-down.

The results showed that it is feasible to define the dynamic parameters from the case studies. However, smartphone limitations must also be considered. Thus, an indication of the behavior of the dynamic parameters can be reached with the MEMS accelerometers of smartphones in a simplified manner.

2 MATERIALS AND EXPERIMENTAL PROGRAM

2.1 Measurement points

Figure 1 shows the measurement points used in the case studies and smartphone positions. As shown in Figure 1a, the smartphone's position had already been identified, and 'X' represents the vandal load application point on the footbridge. In Figure 1b, the smartphone's position on the bridges has already been identified.

The excitation force on the footbridge was exerted by one person jumping over three different points: 1/2 L, 1/4 L, and 3/4 L. This excitation force is known as the vandal load [33] and was used because of the low population density (people/m^2) and the difficulty in exciting the footbridge. The jumps were performed only once at a point. Although the continuous jumping over the structure is an application of forced excitation force, the vibration source was applied only once over the structure, and the vibration decreases until it reaches the resting state.

In the case studies, the measurement point was located at the middle of the bridge span. Measurement points closer to the boundary conditions exhibit higher stiffness than the central regions [34]. This is because superstructure and mesostructure elements interact and can influence the natural frequency values.

In the bridges, the measurement point was located at the middle of the span, more precisely, on the lateral walkway.

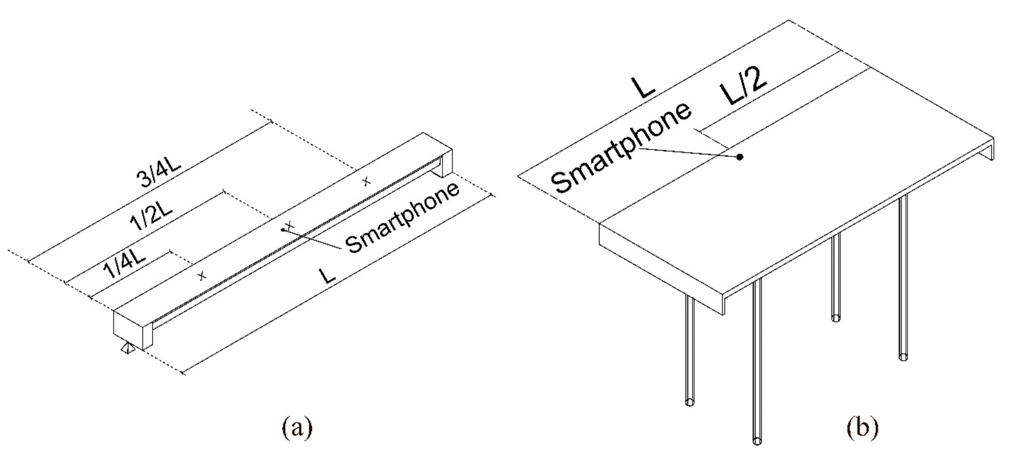

Figure 1: Measurement points on the (a) footbridge and (b) the bridges

Figure 2a shows the total length of the footbridge and Figure 2b shows its T cross-section on AA'.

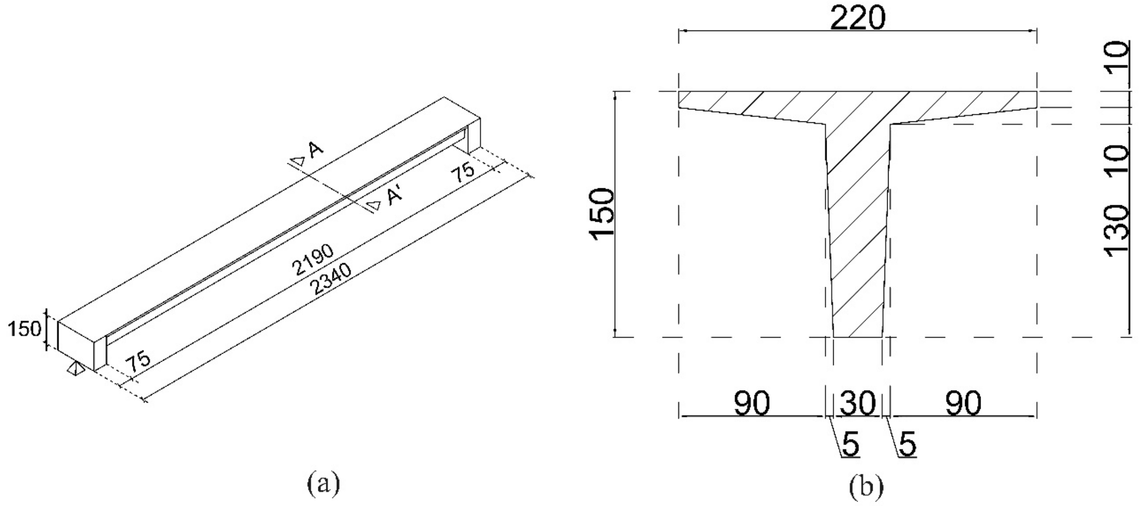

Figure 2: Footbridge length and cross-section (dimensions in centimeters).

2.2 Materials

The vibration test was performed using a Motorola Moto Z Force 2 smartphone, which has an LSM6DSM accelerometer with a 0.0023956299 m/s^2 resolution and a 428 Hz sampling rate.

This accelerometer can be used for vibration monitoring [35], and can function at 0.65 mA, be used to record the triaxial acceleration, . In addition, it operates in the temperature range of −40 – +85°C.

In this study, we used the Vibration Alarm app, developed and distributed for free by MobileTools, because it can record and store acceleration data. The version used in this study has four different sampling rates, namely 7, 27, 33, and 428 Hz; sampling rate of 428 Hz was used in this study.

Acceleration data processing was performed using Microsoft Excel and Scilab, through which we selected the acceleration data, its processing, and the definition of the dynamic parameters. ANSYS Mechanical APDL 2020 R2 Academic was used to create finite element models.

2.3 Methods

2.3.1 Extraction data

Six data extractions were performed for each case. For bridges, the samples were 5 min in length. The beginning of the vibration test did not follow any special traffic conditions. On the footbridge, the samples have a shorter duration following jump execution. The smartphone was mounted using a double-sided tape on the back of the smartphone. Thus, during the vibration test, the smartphone was oriented such that its screen was in the upward direction.

2.3.2 Calibration

The calibration was performed using two fixtures created in a lathe machine using industrial nylon, with dimensions to couple the phone during the calibration operation. Using this apparatus, the smartphone's alignment is guaranteed to be in the three orthogonal axes: X, Y, and Z. The fixtures allowed the touchscreen to remain operable. Figure 3 shows the smartphone and the fixtures used in the calibration.

Figure 3: Smartphone during calibration

The calibration explores the fact that the gravitational force, *g*, is constant for a resting sensor. The method determines six positions for smartphone placement: three with positive gravitational force and three with negative gravitational force. In each position, one axis reads the acting *g* force. Figure 4 shows the six positions of the smartphone during calibration.

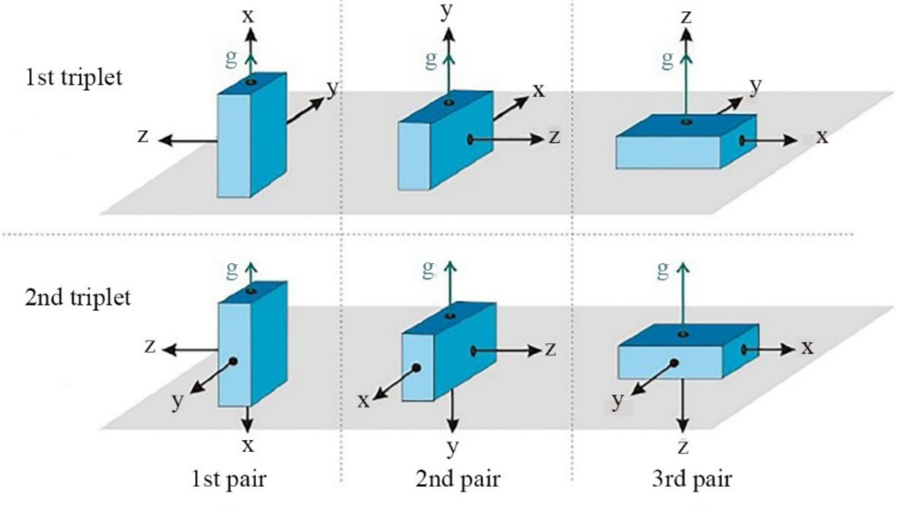

Figure 4: Calibration method [16]

Twelve calibration parameters were defined from the calibration matrix, Cs, and zero-level offset a_0 to correct the acceleration values from the case studies. This method performs static compensation, which is considered a source of invariant time errors.

The calibration matrix, Cs, is obtained through the combination of the positive and negative static acceleration matrices, A_{s+} and A_{s-}. These are 3 × 3 matrices, and they assume the same value as the mean acceleration values for each axis. The calibration matrix, Cs, is defined as,

$$C_S = 2\left(A_{S+} - A_{S-}\right)^{-1} \tag{1}$$

where Cs is the calibration matrix (m/s^2), A_{s+} is the static matrix considering a positive force, g, acting on the X, Y, and Z axes on the first set of calibration measurements (m/s^2), and A_{s-} is the static matrix considering a negative force, g, acting on axes X, Y, and Z on the second set of calibration measurements (m/s^2).

The other parameters were obtained from the zero-level offset a_0, which requires the determination of the A_0 matrix. Each A_0 matrix column presents a zero-level offset a_0 obtained from a measurement pair. The A_0 matrix is determined as follows:

$$A_0 = \frac{A_{s+} + A_{s-}}{2} \text{ (m/s}^2\text{)} \tag{2}$$

The zero-level offset a_0 is

$$a_0 = \frac{\left(A_{s+} + A_{s-}\right)i}{6} \text{ (m/s}^2\text{)} \tag{3}$$

where i is a 3x1 order vector of 1.

The Cs matrix and a_0 parameter are inserted in equation 4 to correct the acceleration data from the case studies:

$$a = C_s\left(a_s - a_0\right) \tag{4}$$

where a is the corrected acceleration (m/s^2), Cs is the calibration matrix (m/s^2), a_s is the acceleration data from the structure (m/s^2), and a_0 is the zero-level offset (m/s^2).

In this study, only the data from vertical acceleration was corrected. The calibration samples had a one-minute length and 28,597 acceleration reads for each axis. Better calibration results would be obtained if the calibration samples were larger.

2.3.3 Angle between the smartphone vertical axis and gravitational acceleration vector during calibration

Angles were defined using the gravity vector and vertical axis acceleration. The inverse tangent function provides more accuracy [14].

Angles refer to the calibration step, and their purpose is to verify the effectiveness of the special fixtures that were built for this application. Considering that only the vertical axis acceleration is used in the processing phase, the angles used in this study are those related to the positive and negative vertical positions. This assumes that the calibration matrix and the zero-level offset are known, because their values are combined from the other two matrices. Angles from the mean acceleration are defined as

$$ø = tan^{-1} \frac{\sqrt{A_{x,ot}^2 + A_{y,ot}^2}}{A_{z,ot}} \tag{5}$$

where Ø is the angle between the smartphone vertical axis and the gravitational acceleration vector in degrees (°), and $A_{x,ot}$, $A_{y,ot}$, and $A_{z,ot}$ are the acceleration means obtained from the vertical positions extracted during calibration (m/s^2).

2.3.4 Data processing

A Butterworth High-Pass filter (BHP), which has a 1 Hz natural frequency and one pole, was applied to minimize the influence of the colored noise influence. This is the simplest filter configuration [36].

The signal power was defined from the relation between RMS [37] using the ratio before and after the application of the BHP filter. This procedure gives a result in voltage, which is later converted into decibels and defines the attenuation or grain of the signal.

Peak picking was used to identify the natural frequencies. This method was applied owing to the simplicity and fastness of the application, but it is very difficult to determine the natural frequency with a greater degree of accuracy [38].

The damping ratios were defined using the logarithmic decrement method in the time domain. The property's definition was based on the visual recognition of the logarithmic decrement pattern in one of the acceleration peaks. Eleven acceleration peaks were used to minimize identification errors [39].

2.3.5 Sampling rate corretion

This correction is necessary because of the measurement quality variation, which considers the accelerometer's sampling rate and sampling delay [19]. Real sampling can be defined from timestamp analysis, total time, and acceleration readings in one sample. The sampling correction factor, $k_{correction}$, considers the target and achieved sampling rates of the smartphone:

$$k_{corrction} = \frac{f_{s\,achieved}}{f_{s\,target}} \tag{6}$$

where $k_{correction}$ is the sampling rate correction ratio, $fs_{achieved}$ is the real sampling rate, *and* fs_{target} is the smartphone app sampling rate.

The correction is performed by multiplying the amplitude values that are already available in the frequency domain. Real frequency, f_{real} (Hz), is defined as

$$f_{real} = f_{identified} \times k_{correction} \tag{7}$$

where $f_{identified}$ is the natural frequency identified by the sensor (Hz).

2.3.6 Numeric models

The meshes of the numeric models of the study cases were defined with the aid of mesh tests, which started with a size of 50 × 50 cm, decreasing 5 cm each time. The testing was stopped when the modal parameters did not show a significant variation. Moreover, meshes obeyed the nodal limitations from the student version and avoided mesh errors.

The numerical model of the footbridge was a solid created in two stages: first, the T cross-section was built from the PLANE183 element. Second, the area was extruded longitudinally, transforming PLANE183 into SOLID186. This element is a 3D element with 20 nodes and exhibits a quadratic displacement behavior. It has three degrees of freedom per node: translation in the x, y, and z directions [40].

The material properties of the footbridge were a 33 GPa Young's modulus, with a density of 2500.00 N/m^3. The footbridge is simply supported at the ends, and transversal displacement is avoided through the boundary conditions in the flange. Tension stress was not considered. Mesh size was 15 × 15cm.

Bridges V1 and V2 were created from shell elements using SHELL181. The material properties of the V1 bridge have a Young's modulus of 25 GPa according to Brazilian concrete standard correlations [28], with a density of 2533.58 N/m^3, which considers the pavement depth, New-Jersey concrete barrier, railings, girders, beams, and decks. Simply supported boundary conditions were applied to the nodes that matched the abutments. The boundary conditions avoided transverse displacements on the first and last transverse beams. Mesh size was 15 × 15 cm.

The material properties of the V2 bridge were a 20 GPa Young's Modulus and 2536.78 N/m^3 density, considering their masses as existing, as done previously in the other study cases. The boundary conditions and mesh size are the same as those applied at the V1 bridge. The Poisson's ratio was 0.2.

3 RESULTS AND DISCUSSION

3.1 Calibration

Calibration was performed on a planar surface. The Cs calibration matrix results are as follows:

$$C_S = \begin{bmatrix} z_1 & y_1 & x_1 \\ z_2 & y_2 & x_2 \\ z_3 & y_3 & x_3 \end{bmatrix} = \begin{bmatrix} 0.1017656 & 0.0006339 & -0.0003295 \\ -0.0003608 & 0.101254 & 0.0004612 \\ 0.0045794 & -0.0009603 & 0.1031238 \end{bmatrix}$$

The zero level offset a_0 was

$$a_0 = \begin{bmatrix} za_0 \\ ya_0 \\ xa_0 \end{bmatrix} = \begin{bmatrix} -0.0521225 \\ -0.0093539 \\ -0.0224103 \end{bmatrix}$$

The Cs and a_0 matrices were placed to correct the acceleration data from the study cases.

3.2 Angles between the smartphone vertical axis and gravitational force during the calibration process

The angle obtained with the positive position with the screen upward was:

$$ø = tan^{-1} \frac{\sqrt{(-0.0765406)^2 + (-0.043384)^2}}{9.7588723} = 0.5165°$$

The angle obtained with the negative position with the screen upside-down was:

$$ø = tan^{-1} \frac{\sqrt{(0.0458722)^2 + (-0.1067092)^2}}{-9.8908458} = -0.6728°$$

As shown above, the angles are lower than 1°. However, values greater than 0.5° can influence the vibration data [13]. Therefore, the fixtures require further improvement, or the manufacturing method may need to be altered to yield a higher level of accuracy.

3.3 Natural frequency correction

Text files from the acceleration app were analyzed. The timestamp identification was not properly discovered because the app only presented the first millisecond algorithm. Thus, for a 428 Hz sampling rate, the timestamp was 0.002336 s. In the text file, only the “2” algorithm is presented.

In the same text file, the timestamp failed to create an algorithm equal to 3 in several readings. Therefore, the timestamp that considers this millisecond algorithm can vary in the range between 255 Hz and 0.003922 s to 333 Hz and 0.003033 s.

Data processing was performed with both timestamps, but they did not change the resultant natural frequency from the study cases. Sampling rates vary from the 428 Hz sampling rate from a range of 18.69% to 8.88% for 348 Hz to 390 Hz, respectively. This behavior is expected because the natural frequency correction remains the same [19]. The results shown in this study refer to a sampling rate of 390 Hz.

The results show that the sampling rate decreases after each sample in 0.07%.

3.4 Experimental vibration parameters

The mean natural frequency obtained from the footbridge was 4.90 Hz. The difference between the highest and lowest natural frequencies was 2.41%. An additional vibration mode was identified to be closer to 35 Hz.

The mean footbridge damping ratio was 1.32%. The results vary between the ranges of 1% and 1.7%; this damping range is greater than the lowest damping e, which is lower than the maximum damping. Therefore, the damping obtained in this study is acceptable.

The footbridge's natural frequency is greater than 2 Hz [30], [26]. However, it requires a deeper evaluation [27]. Moreover, it does not meet specifications [28], [29]. Figure 5 shows the footbridge samples in the time domain after the BHP filter application in (a), frequency domain in (b), and samples for damping estimation in (c). Acceleration peaks refer to the execution of one jump, with 0.08 m/s^2 as the highest value. The power spectral density (PSD) showed a frequency peak close to 4.9 Hz and another with a dip close to 35 Hz.

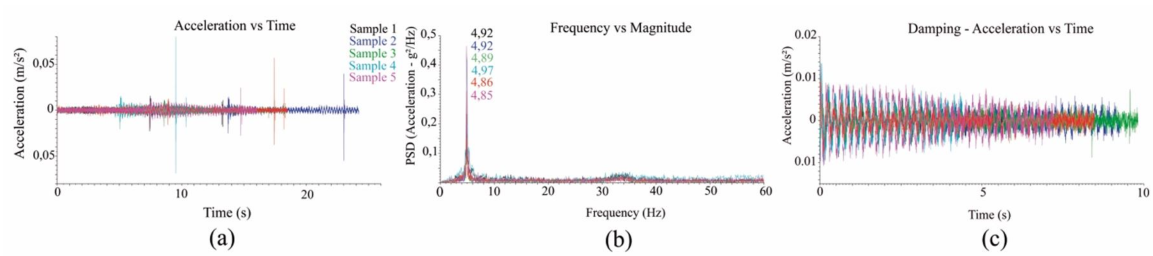

Figure 5: Footbridge accelerations recorded and PSD

Table 1 lists the experimental results of the footbridge. RMS showed lower results after the application of the filter and of the attenuations of −4 and −9 dB, the minimum and maximum values, respectively, between the six samples.

Table 1: Footbridges' experimental results

Sample	Excitation source point	*sampling frequency* (Hz)	ξ (%)	*f* (Hz)
1	½ L	389.72	1.64	4.92
2	¾ L	389.58	1.58	4.92
3	¼ L	389.46	1.34	4.89
4	½ L	389.37	1.28	4.97
5	¾ L	389.26	1.23	4.86
6	¼ L	389.17	0.81	4.85
		Mean	1.32	4.90
		Standard deviation	0.298	0.044
		Variance	0.089	0.002

The mean natural frequency of the V1 bridge was 12.20 Hz. The difference between the highest and lowest values was 4.86%. The mean damping of the V1 bridge was 2.17%. Damping fell between the range of 2% and 3.5% [30], [31].

Figure 6 shows the V1 bridge samples in the time domain that followed the BHP filter application in (a), frequency domain in (b), and samples for damping estimation in (c). The highest acceleration peak was 0.2 m/s^2. Moreover, it was possible to identify peaks closer to 17 and 35 Hz.

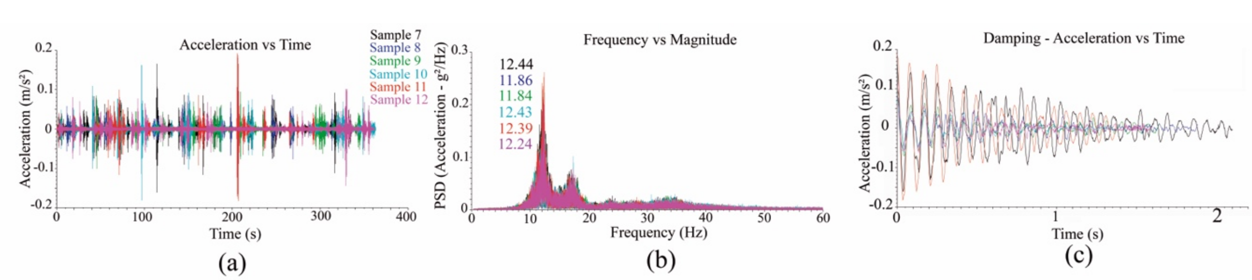

Figure 6: V1 bridge accelerations recorded and PSD

Table 2 shows the V1 experimental results. RMS showed lower results after the application of the filter and the attenuations of −1 and −2 dB, minimum and maximum values, respectively.

Table 2: V1 experimental results

Sample	*Sampling frequency* (Hz)	ξ (%)	*f* (Hz)
7	390.61	1.09	12.44
8	390.56	1.46	11.86
9	390.44	2.58	11.84
10	390.42	2.70	12.43
11	390.24	2.58	12.39
12	390.11	2.60	12.24
	Mean	2.17	12.20
	Standard deviation	0.702	0.282
	Variance	0.493	0.079

The V2 bridge exhibited different vibration modes with respect to its natural frequency. Two samples provided natural frequencies close to 5.30 Hz, while the other four samples presented natural frequencies closer to 16.70 Hz. These two natural frequency peaks can be easily identified among the acceleration samples from this bridge. These different natural frequency peaks from the same measurement points can cause the need to create additional modal identification methods or planning for additional measurement activities.

In addition to these two peaks, there were low peaks close to 25 Hz. Owing to different results, the mean natural frequency, standard deviation, and variance are not presented. Figure 7 shows the V2 bridge samples in the time domain following the BHP filter application in (a), frequency domain in (b), and samples for damping estimation in (c). The highest acceleration peak was 0.06 m/s^2.

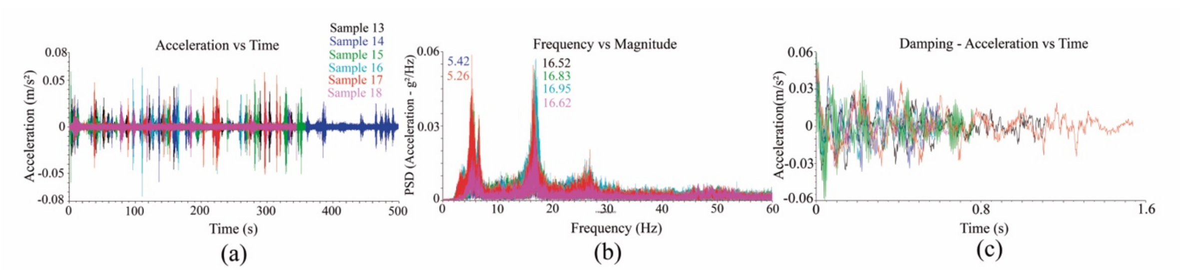

Figure 7: V2 bridge accelerations recorded and PSD

Table 3 shows the V2 experimental results. RMS showed lower results after the application of the filter and of the attenuations of −4 and −8 dB, minimum and maximum values, respectively.

Table 3: V2 experimental results

Samples	*Sampling frequency* (Hz)	ξ (%)	*f* (Hz)
13	390.57	1.62	16.52
14	390.36	2.04	5.42
15	390.22	1.99	16.83
16	390.13	1.66	16.95
17	390.14	2.71	5.26
18	389.94	2.91	16.62

3.5 Numeric models

For the footbridge, the first natural frequency presented is 4.01 Hz with a torsion modal shape; the second natural frequency is 6.99 Hz, with a bending modal shape; the third natural frequency is 13.69 Hz, with a lateral modal shape.

The numerical footbridge model was created from a constant T cross section; however, this representation is a simplification. The real structure has a rectangular cross section above the abutments. In this case, the results were preliminary and therefore were not useful for comparisons or structural behavior assessments. Moreover, no prestressed normal force is considered in the model.

For the V1 bridge, the first modal shape is torsion, with a natural frequency of 11.50 Hz; while the second modal shape was bending, with a natural frequency of 11.83Hz, and the third modal shape is torsion, presenting a natural frequency of 13.39 Hz.

For the V2 bridge, the first modal shape is torsion, and its natural frequency is 6.60 Hz; the second modal shape is bending, with a natural frequency of 6.84 Hz . The third modal shape is lateral, with a natural frequency of 8.57 Hz. The fourth bending modal shape has a natural frequency of 15.14 Hz.

The numerical models applied in the study case were created following Brazilian concrete standards. Destructive tests were not performed. Moreover, it is possible to verify that there are simplifications in the models that can influence the behavior; thus, only preliminary observations should be made regarding dynamic parameters.

Figure 8 shows the modal shapes from the study cases, which had numerical natural frequencies closer to the experimental values. The modal shapes of the footbridges are as follows: (a) footbridge torsional modal shape, (b) V1 bending modal shape, and (c) V2 bending modal shape.

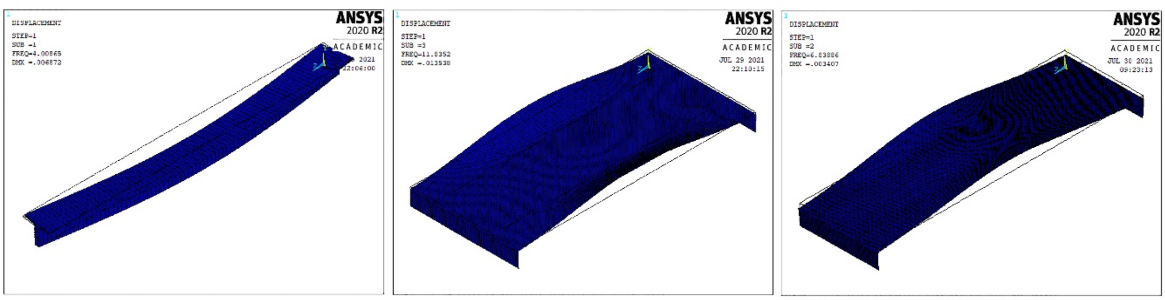

(a) (b) (c)

Figure 8: Study cases modal shapes

3.6 Applied methods assessment

The process assessment showed that the smartphone could define the natural frequencies and damping ratios in the case studies. However, calibration and sampling rate corrections are necessary.

The calibration method was straightforward and its execution was simple; the nylon industrial fixtures did not interfere with the touch screen, allowing the smartphone to operate normally. However, they did not guarantee precise readings; therefore, they did not present an acceptable degree of accuracy, which influenced the acceleration values.

The correction of the natural frequency resulted in a lower real sampling rate than the value indicated by the app. A negative aspect of the app refers to the timestamp presentation in the acceleration text file, which only provides the first millisecond algorithm. This feature can help one choose which app should be used: the ideal app should present the complete timestamp for each reading.

The experimental results from the study cases show that the footbridge and V1 bridge have similar natural frequencies to the numerical models. The footbridge also showed values that were close to those reported in previous literature. The V2 bridge showed two different natural frequencies and thus demands a different method of measurement or the modal identification method.

Attenuation was higher on the footbridge and on V2 than on V1, and it represented a greater noise reduction before the modal identification phase. Small vibration amplitudes are characteristics that indicate low signal quality [5]. Furthermore, structures with larger amplitudes result in better vibration parameter results when monitored with smartphones.

Numerical models, especially footbridges, are simplifications of the real structure and can represent non-official behavior. The obtained numerical values were close to the experimental values, but destructive tests were not performed to define the real properties of the materials. Thus, experimental vibration parameters prevail against the numerical results because they present the real behavior of the structure.

4 CONCLUSIONS

The purpose of this study was to demonstrate the use of one smartphone for monitoring vibration activities. Three study cases were used: two bridges and one footbridge. Calibration and frequency sampling rate corrections were presented, and errors from accelerometer mounting and timestamp imperfections were minimized. After analyzing the results, we can conclude the following:

- A MEMS accelerometer embedded in a smartphone is an alternative for obtaining natural frequencies and damping ratios.
- The calibration method and sampling rate correction are essential because smartphones are not specifically designed for monitoring operations.
- The calibration results should improve the accuracy degree by using more precise calibration devices.
- Experimental vibration parameters are very similar to numerical results.

The smartphone was able to record acceleration data for natural frequencies and damping ratios after definition from study cases and corrections on calibration and sampling rate.

However, professional accelerometers should not be replaced by smartphones' MEMS accelerometers. This alternative could be useful for the engineering team if method limitations and corrections are considered before its application.

The use of the procedure shown in this paper, attests that the use of smartphones' MEMS accelerators can provide a less accurate alternative structural behavior definition at one's fingertips.

REFERENCES

[1] P. Cawley, "Structural health monitoring: closing the gap between research and industrial deployment," *Struct. Health Monit.*, vol. 17, no. 5, 1225, 2018, http://dx.doi.org/10.1177/1475921717750047.

[2] Y. Yu, X. Zhao, and J. Ou "A new idea: mobile structural health monitoring using smart phones", in *Int. Conf. Intell. Control Inf. Process.*, China, 2012. http://dx.doi.org/10.1109/ICICIP.2012.6391524.

[3] M. Feng, Y. Fukuda, M. Mizuta, and E. Ozer, "Citizen sensors for shm: use of accelerometer data from smartphones," *Sensors*, vol. 15, no. 2, pp. 2980–2998, 2015, http://dx.doi.org/10.3390/s150202980.

[4] Y. Yu et al., "J. Ou. "Initial validation of mobile-structural health monitoring method using smartphones," *Int. J. Distrib. Sens. Netw.*, vol. 11, no. 2, 274391 2015, http://dx.doi.org/10.1155/2015/274391.

[5] A. Feldbusch, H. Sadegh-Azar, and P. Agne, "Vibration analysis using mobile devices (smartphones or tablets)," *Procedia Eng.*, vol. 199, pp. 2790–2795, 2017, http://dx.doi.org/10.1016/j.proeng.2017.09.543.

[6] S. Castellanos-Toro, M. Marmolejo, J. Marulanda, A. Cruz, and P. Thomson, "Frequencies and damping ratios of bridges through Operational Modal Analysis using smartphones," *Constr. Build. Mater.*, vol. 188, pp. 490–504, 2018, http://dx.doi.org/10.1016/j.conbuildmat.2018.08.089.

[7] A. B. Noel, A. Abdaoui, T. Elfouly, M. H. Ahme, A. Badawy, and M. S. Shehata, "Structural health monitoring using wireless sensor networks: a comprehensive survey," *IEEE Commun. Soc.*, vol. 19, no. 3, pp. 1403–1423, 2017. http://dx.doi.org/10.1109/COMST.2017.2691551.

[8] T. J. Matarazzo, V. Vazifeh, S. Pakzad, P. Santi, and C. Ratti, "Smartphone data streams for bridge health monitoring," in *Int. Conf. Struct. Dyn - EURODYN*, Italy, 2017. http://dx.doi.org/10.1016/j.proeng.2017.09.203.

[9] T. J. Matarazzo et al., "Crowdsourcing bridge vital signs with smartphone vehicle trips", *Comput. Soc. Appl. Phys.*, 2020.

[10] B. K. Muliterno, F. Muliterno Jr., and Z. M. C. Pravia, "Avaliação da irregularidade longitudinal do pavimento sobre pontes usando acelerações medidas por smartphones," *Transportes*, vol. 27, no. 2, pp. 182–193, 2019., http://dx.doi.org/10.14295/transportes.v27i2.1686.

[11] A. H. Alavi and W. G. Buttlar, "An overview of smartphone technology for citizen-centered, real-time and scalable civil infrastructure monitoring," *Future Gener. Comput. Syst.*, vol. 93, pp. 651–672, 2019, http://dx.doi.org/10.1016/j.future.2018.10.059.

[12] K. G. Manikandan, K. Pannirselvam, J. J. Kenned, and C. S. Kumar, "Investigations on suitability of MEMS based accelerometer for vibration measurements," *Mater. Today Proc.*, vol. 45, pp. 6183–6192, 2021, https://doi.org/10.1016/j.matpr.2020.10.506.

[13] T. Kuhlmann, P. Garaizar, and U. Reips, "Smartphone sensor accuracy varies from device to device in mobile research: the case of spatial orientation," *Behav. Res. Methods*, vol. 53, no. 1, pp. 22–33, 2021, http://dx.doi.org/10.3758/s13428-020-01404-5.

[14] J. Zhu, W. Wang, S. Huang, and W. Ding, "An improved calibration technique for MEMS accelerometer-based inclinometers," *Sensors*, vol. 20, no. 2, pp. 452, 2020, http://dx.doi.org/10.3390/s20020452.

[15] L. Cao and J. Chen, "Online investigation of vibration serviceability limitations using smartphones," *Measurement*, vol. 162, 107850, 2020, http://dx.doi.org/10.1016/j.measurement.2020.107850.

[16] S. Stančin and S. Tomažič, "Time and computation-efficient calibration of MEMS 3D accelerometers and gyroscopes," *Sensors*, vol. 14, no. 8, pp. 14885–14915, 2014, http://dx.doi.org/10.3390/s140814885.

[17] S. V. Vaseghi, *Advanced Digital Signal Processing and Noise Reduction*, 2nd ed. England: John Wiley & Sons, 2000.

[18] R. R. Ribeiro and M. R. Lameiras, "Evaluation of low-cost MEMS accelerometers for SHM: frequency and damping identification of civil structures," *Lat. Am. J. Solids Struct.*, vol. 16, no. 7, e203, 2019, http://dx.doi.org/10.1590/1679-78255308.

[19] E. Ozer, D. Feng, and M. Q. Feng, "Hybrid motion sensing and experimental modal analysis using collocated smartphone camera and accelerometers," *Meas. Sci. Technol.*, vol. 28, no. 10, 105903, 2017, http://dx.doi.org/10.1088/1361-6501/aa82ac.

[20] G. M. Guzman-Acevedo, G. E. Vazquez-Becerra, J. R. Millan-Almaraz, H. E. Rodriguez-Lozoya, A. Reyes-Salaza, and J. R. Gaxiola-Camacho, "GPS, accelerometer, and smartphone fused smart sensor for SHM on real-scale bridges," *Adv. Civ. Eng.*, vol. 29, pp. 1–15, 2019, http://dx.doi.org/10.1155/2019/6429430.

[21] A. Miller, D. Sburlati, and D. Duschlbauer, “Accelerometer mounting: comparison of stud and magnetic mounting methods”, in *Hear to Listen: Acoust.*, Australia, 2018.

[22] A. Miyamoto, R. Kiviluoma, and A. Yabe, "Frontier of continuous structural health monitoring system for short & medium span bridges and condition assessment," *Front. Struct. Civ. Eng.*, vol. 13, no. 3, pp. 569–604, 2019, http://dx.doi.org/10.1007/s11709-018-0498-y.

[23] G. L. Debona and J. G. S. Silva, "Assessment of the dynamic structural behavior of footbridges based on experimental monitoring and numerical analysis," *IBRACON Struct. Mater.*, vol. 13, no. 3, pp. 563–577, 2020, http://dx.doi.org/10.1590/s1983-41952020000300007.

[24] S. Staacks, S. Hütz, H. Heinke, and C. Stampfer, "Advanced tools for smartphone-based experiments: phyphox," *Phys. Educ.*, vol. 53, no. 4, 045009, 2018, http://dx.doi.org/10.1088/1361-6552/aac05e.

[25] A. Elhattab, N. Uddin, and E. Obrien, "Extraction of bridge fundamental frequencies utilizing a smartphone mems accelerometer," *Sensors*, vol. 19, no. 14, pp. 3143, 2019, http://dx.doi.org/10.3390/s19143143.

[26] C. S. Oliveira, "Fundamental frequencies of vibration of footbridges in Portugal: from in situ measurements to numerical," *Shock Vib.*, vol. 2014, pp. 1–22, 2014, http://dx.doi.org/10.1155/2014/925437.

[27] E. Caetano and A. Cunha, “Dynamic design of slender footbridges”, in *Proc. 2nd Int. Conf. Struct. Archit. - ICSA 2013*, Guimarães, 2013. http://dx.doi.org/10.1201/b15267-154.

[28] Associação Brasileira de Normas Técnicas, *Projeto de Estruturas de Concreto – Procedimento*, NBR 6118, 2014.

[29] Service d'Études Techniques des Routes et Autoroutes. *Footbridges: Assessment of Vibrational Behaviour of Footbridges Under Pedestrian Loading*, 1st ed. Paris: Association Française de Génie Civil, 2006, pp. 1–127.

[30] H. Bachmann et al., *Vibration Problems in Structures: Practical Guidelines*, 1st ed. Basel: Birkhäuser Verlag, 1995. http://dx.doi.org/10.1007/978-3-0348-9231-5.

[31] P. Li, Y. Wang, B. Liu, and L. Su, "Damping properties of highway bridges in China," *J. Bridge Eng.*, vol. 19, no. 5, 04014005, 2014, http://dx.doi.org/10.1061/(ASCE)BE.1943-5592.0000578.

[32] Associação Brasileira de Normas Técnicas, *Projeto de Pontes de Concreto Armado e de Concreto Protendido – Procedimento*, NBR 7187, 2003.

[33] E. Caetano, A. Cunha, and C. Moutinho, "Vandal loads and induced vibrations on a footbridge," *J. Bridge Eng.*, vol. 16, no. 3, pp. 375–382, 2011, http://dx.doi.org/10.1061/(ASCE)BE.1943-5592.0000154.

[34] B. Wu, G. Wu, H. Lu, and D. Feng, "Stiffness monitoring and damage assessment of bridges under moving vehicular loads using spatially-distributed optical fiber sensors," *Smart Mater. Struct.*, vol. 26, no. 3, 035058, 2017, http://dx.doi.org/10.1088/1361-665X/aa5c6f.

[35] STMicroelectronics. *LSM6DSM - iNEMO Inertial Module: Always-on 3D Accelerometer and 3D Gyroscope*, 2017, pp. 1–126.

[36] G. Ellis, *Control System Design Guide: a Practical Guide*, 3rd ed. London, UK: Elsevier Academic Press, 2004.

[37] K. B. Ginn, *Architectural Acoustics*, 2nd ed. Nærum: Brüel & Kjær, 1978.

[38] J. He and Z. Fu, *Modal Analysis.* 1st ed. UK: ButterWorth-Heinemann, 2001.

[39] D. J. Tweten, Z. Ballard, and B. P. Mann, "Minimizing error in the logarithmic decrement method through uncertainty propagation," *J. Sound Vibrat.*, vol. 333, no. 13, pp. 2804–2811, 2014., http://dx.doi.org/10.1016/j.jsv.2014.02.024.

[40] ANSYS, Inc., *ANSYS Mechanical APDL Element Reference*. South Pointe: SAS IP, Inc., 2013.

Author contributions: JDB: conceptualization, acquisition, writing. ZMCP: conceptualization, acquisition, writing, supervision.

Editors: Samir Maghous, Guilherme Aris Parsekian.

IBRACON Structures and Materials Journal
Revista IBRACON de Estruturas e Materiais
ISSN 1983-4195 ismj.org

ORIGINAL ARTICLE

Distribution of load effects and reliability of reinforced concrete frames: intact and with columns removed

Distribuição de esforços e confiabilidade de pórticos de concreto armado: íntegro e com remoção de colunas

Pedro Henrique Preto Facholli[a]
André Teófilo Beck[a]

[a]Universidade de São Paulo – USP, Escola de Engenharia de São Carlos, São Carlos, SP, Brasil

Received 11 May 2021
Accepted 18 August 2021

Abstract: The design of reinforced concrete (RC) frames is made on a member-by-member basis. Similarly, in the literature, the reliability of RC beams and columns is often studied in isolation from the rest of the structure. Yet, in the construction of regular frames, symmetry and regularity are often exploited, resulting in the same design for each element type. This is despite of different load effects on different parts of the structure, which leads to significant variations in the failure probability of the elements. Hence, in this paper, we investigate the reliability of members and the distribution of load effects in regular RC frame buildings, considering intact and column loss cases, where symmetry is lost. Results show that the ratios of normal-to-bending loads change significantly along building height, and this has a significant impact on reliability of individual columns.

Keywords: structural reliability, regular frame structures, reinforced concrete structures, discretionary column removal.

Resumo: O projeto de estruturas aporticadas de concreto armado é feito elemento a elemento. Da mesma forma, a confiabilidade de vigas e pilares de concreto armado é frequentemente estudada, na literatura, considerando elementos isolados do restante da estrutura. Entretanto, na construção de pórticos regulares, é usual explorar a simetria e regularidade, resultando no mesmo dimensionamento para cada tipo de elemento. Porém, com esforços solicitantes diferentes atuando em diferentes partes da estrutura, variações significativas podem ocorrer na probabilidade de falha dos membros. Neste trabalho, é investigada a confiabilidade dos elementos e a distribuição de esforços em estruturas aporticadas de concreto armado, considerando casos intactos e com remoção de colunas, nos quais a simetria é perdida. Os resultados mostram que as razões normal – momento fletor variam significativamente ao longo da altura do edifício, exercendo um impacto considerável na confiabilidade dos pilares de cada lance.

Palavras-chave: confiabilidade estrutural, estruturas aporticadas regulares, estruturas de concreto armado, remoção discricionária de coluna.

How to cite: P. H. P. Facholli and A. T. Beck, "Distribution of load effects and reliability of reinforced concrete frames: intact and with columns removed," *Rev. IBRACON Estrut. Mater*., vol. 15, no. 2, e15207, 2022, https://doi.org/10.1590/S1983-41952022000200007

1 INTRODUCTION

In the design of building structures, one needs to consider the uncertainties affecting the strength of structural materials, the expected loads on the structure, and the accuracy of engineering calculation models. The design of building structures is made using design codes, which employ partial safety factors to overcome the uncertainties and produce safe and reliable structures. More recently, structural reliability theory has allowed a more comprehensive understanding of the impacts of uncertainties in structural design.

Corresponding author: André Teófilo Beck. E-mail: atbeck@sc.usp.br
Financial support: CAPES; CNPq (grant n. 309107/2020-2); FAPESP (grant n. 2019/13080-9).
Conflict of interest: Nothing to declare.

Loading in structures include those that the structure will certainly be exposed to, although of unknown intensity, but also exceptional loads due to accidental or malevolent actions, to which the structure is exposed to with smaller probability. One exceptional loading condition is loss of a load-bearing element due to accidental or malevolent action. Accidental actions include traffic accidents (impact of moving truck on a wall or column), accidental explosions (like gas, for instance), major fire, or gross human error. Malevolent actions include bomb detonations, as in terrorist acts. Some recent occurrences of whole frame collapses, following initial damage of limited proportions, have raised the necessity for robust structural design. A structure is said to be robust if it can withstand local damage, which does not propagate in a manner which is disproportional to the extent of the initiating damage event.

Brazilian design codes do not have specific requirements with respect to structural robustness, other than the requirement for appropriate binding of slabs, and for continuity of lower beam reinforcements [1]; see a review of Brazilian normative in [2]. Yet, progressive collapse events have been observed in Brazil, for example: rupture of balconies of 15 floors of Edifício Don Gerônimo, Maringá PR (2008); full collapse of Edifício Real Class, 34 floors, Belém do Pará AM (2011); full collapse of the Liberdade building in Rio de Janeiro RJ (2012); partial collapse of Edifício Senador, 13 floors, São Bernardo do Campo SP (2012); the almost-complete collapse of Poty Shopping Center, Teresina PI (2013), during construction; and more recently, the full collapse of Andrea building in Fortaleza CE (2019) due to inadequate maintenance of columns.

Under multiple hazards, the probability of structural collapse is given by [3]–[5]:

$$p_c = P\left[C\right] = \sum_{H}\sum_{LD} P\left[C|LD,H\right]P\left[LD|H\right]P\left[H\right] \tag{1}$$

where C is for collapse, LD is local damage, and H is a hazard, like fire, traffic accident, explosion, etc. In Equation 1, $P\left[H\right]$ is the probability of occurrence of hazard H, $P\left[LD|H\right]$ is the conditional probability of local damage, given occurrence of a hazard, and $P\left[C|LD,H\right]$ is the conditional probability of collapse, given hazard and local damage. The sum over H and LD considers all relevant hazards and local damages a structure may be exposed to. Local damage may be in terms of localized strength reduction, due to a fire or vehicle impact; or the loss of load-bearing structural elements, such as walls or columns.

Following Equation 1, it is possible to reduce the probability of collapse in three ways: a) by limiting the threat probability (installing screening barriers, limiting speed of vehicles, prohibiting inflammable and explosive substances); b) by limiting the probability of local damage, given hazard (safety barriers for impact, local strengthening measures); and c) by reducing or arresting damage propagation (by proper design including alternate load paths). This paper addresses damage propagation by looking into the conditional failure probability of neighboring beams and columns, considering discretionary column loss events.

Many works in the published literature have addressed the resisting mechanisms, and formulated methodologies for modelling and verification of structures exposed to progressive collapse due to local damage: Starossek [6] studied and classified the damage propagation in buildings, Izzuddin et al. [7] proposed a simplified dynamic assessment for progressive collapse, Khandelwal and El-Tawil [8] investigated the robustness of building systems by the *pushdown* analysis, Masoero et al. [9] presented an analytical model for PC of 2D frames, Oliveira et al. [10] used a high-fidelity FE model to investigate the safety of structures after the loss of a column.

International design codes present both direct and indirect measures for design against progressive collapse. Indirect measures address the problem qualitatively, by prescribing minimal levels of ductility, strength, and continuity [11]. Direct design measures against progressive collapse are presented in North-American guidelines such as [12] and [13], which include local strengthening and design for alternate load paths. In the so-called *Alternate Load Path Method* (APM), it is warranted that the structure has the required strength to re-distribute loads initially sustained by the damaged column, bridging over it, for a period sufficient for repair action to be taken. This “bridging” strength refers to the term $P\left[C|LD,H\right]$ in Equation 1. Following [3]–[5], the conditional collapse probability can be accepted to be between about 0.01 and 0.1 since, even if local damage is certain given hazard ($P\left[LD|H\right]=1$), hazard probabilities are usually small (between 10^{-6} and 10^{-5} for typical hazards like explosions and fire). References [14]–[16] address the hazard probabilities for which the APM design becomes cost-effective, from a risk-management perspective.

Based on APM requirements, many studies have addressed the behavior of beams and slabs, responsible for the reserve strength, and considered as the last line of defense against progressive collapse [17]. However, in column loss situations, the overload on adjacent columns is also significant. As the main elements in bearing the vertical loads, special attention also needs to be given to columns in PC situations.

Interestingly, most studies on the reliability of RC beams and columns address individual elements which are “detached” from the main structure. This may be a consequence of the usual design procedures, where elements are designed on an element-by-element basis. Focusing on results published in Brazil, studies on the reliability of “detached” beam elements include [18]–[23] and “detached” columns include [24]–[29]. Studies addressing “detached” beams and/or columns, based on Brazil and elsewhere, include [30]–[32]. Yet, to facilitate construction of regular RC buildings, it is usual to consider the same beams and slabs throughout the building, and to produce similar columns (same cross section dimensions) over the height of the building, perhaps differentiating interior and facade columns. As load effects and normal-to-bending action ratios are not the same throughout the building, design for beam and column regularity produces variations in the reliability of elements located in different parts of the building. These variations have not been thoroughly studied in the literature. Importantly, building regularity is lost in case of a column failure.

Within this framework, this paper presents a study on the spatial distribution of load effects in regular RC frames, and the impact on the reliability of beams and columns located in different parts of the structure. We address the cases of intact frames, and the situation of discretionary column removal. The study includes frames of four and eight stories, with removal of internal and external (facade) columns. Under column removal, we consider usual frames (not strengthened), and strengthened following ASCE 7-16 [33] recommendations for abnormal loading condition. Our study is limited to gravitational loads and to linear structural behavior. Albeit simple, the linear model captures the distribution of load effects in the structure, and the interaction between normal and bending load effects in columns. Non-linear material modelling will be considered in future research. Horizontal loading and out-of-plumbness will also be addressed in the future.

2 RELIABILITY ANALYSIS BY FORM

Probabilistic analysis of structures is a field of research that has been extensively developed since the second half of the 20th century, when works of Freudenthal [34], Cornell [35] and Hasofer and Lind [36] revolutionized the assessment of structural safety and laid the foundations for structural reliability.

The reliability of a structure refers to a degree of belief that it meets its technical design requirements during a specified lifetime and respecting operational conditions [37]. The technical design requirements can be defined by limit state equations, which represent a boundary between desirable (safety or service) and undesirable state (failure) of the structure. These limit states are given for each failure mode of each element of the structural system:

$$g(\mathbf{X}) = g(X_1, X_2, \dots, X_n) = 0 \tag{2}$$

where $\mathbf{X}$ is a random variable vector. Negative values of the limit state equation represent failure, whereas positive values represent survival. The boundary between failure (Ω_f) and survival (Ω_s) domains is given by $g(\mathbf{x}) = 0$, such that:

$$\Omega_f = \{\mathbf{x} \mid g(\mathbf{x}) \le 0\} \tag{3}$$

$$\Omega_s = \{x \mid g(x) > 0\} \tag{4}$$

Thus, the failure probability, which is the probability of limit state violation, can be evaluated by a multi-dimensional integration of the joint probability density function $f_{\mathbf{X}}(\mathbf{x})$ over the failure domain:

$$p_f = P[X \in \Omega_f] = P[g(X) \le 0] = \int_{\Omega_f} f_X(x)\, dx \tag{5}$$

The solution of Equation 5 can be performed by Monte Carlo simulation or transformation methods. In this paper, the First Order Reliability Method (FORM) is used, by way of the UQLab software [38] in a MATLAB environment.

The FORM method consists in mapping the joint probability density function from the original design space $\mathbb{X}$ to the standard Gaussian space $\mathbb{Y}$ through the Principle of Normal Tail Approximation [39] and the Nataf transformation [40]. In this space, the limit state equation is approximated by a tangent hyper-plane at the design point. This point represents the most probable point in the failure domain and is obtained by the constrained optimization problem:

$$\begin{aligned}&\text{find}: \mathbf{y}^* \\ &\text{which minimizes}: d = \|\mathbf{y}\| = \sqrt{\mathbf{y}^{\mathbf{t}}\mathbf{y}} \\ &\text{subject to}: g(\mathbf{y}) = 0\end{aligned} \tag{6}$$

where $\mathbf{y}$ is the random variable vector in the standard Gaussian space, $\mathbf{y}^*$ is the design point and d is the distance of a point to the origin. The solution to this problem yields the Hasofer and Lind's [36] reliability index, β, commonly used as a safety metric in structural codes.

The transformation from the original space to the standard space is done as the optimization algorithm moves towards the design point. In this paper, the improved Hasofer-Lind-Rackwitz-Fiessler algorithm [41], [42] is used to ensure unconditional convergence. At the design point, the limit state equation is approximated by a tangent hyper-plane. Using the property of radial symmetry of the normal standard distribution, a first order approximation of the failure probability is given by:

$$p_f \cong \Phi(-\beta) \tag{7}$$

where β is the reliability index and $\Phi(.)$ is the standard gaussian cumulative probability distribution function.

The contribution of each random variable to the calculated failure probabilities can be found by:

$$\boldsymbol{\alpha}\left(\mathbf{y}^*\right) = \frac{\nabla g\left(\mathbf{y}^*\right)}{\|\nabla g\left(\mathbf{y}^*\right)\|} \tag{8}$$

where $\nabla g = \left\{\frac{\partial g}{\partial y_i}\right\}$ is the gradient vector containing the partial derivatives of the limit state equation with respect to each random variable. The component α_i^2 provides a linear approximation of the sensibility of the p_f to random variable X_i, which is composed by a combination of its distribution, mean value and standard deviation [37]. Through the sensibility, it is possible to identify more or less significant variables in a structural reliability problem in order to inform relevant aspects that deserve more attention of the designer, mainly in the statistical treatment of the variables, which can reduce the uncertainties and increase the accuracy of the analysis.

2.1 Limit state equation for beams

The rectangular beams considered herein are subjected to pure bending caused by gravity loads. The resistance to formation of a plastic hinge is given by the classical equations of equilibrium and recommendations of the ABNT NBR 6118 [1]:

$$M_R = A_s\, f_y\, (d - x) + 0.408\, x^2 f_c\, b_w \tag{9}$$

$$x = 1.25\left(\frac{A_s f_y}{0.85\, f_c\, b_w}\right) \tag{10}$$

where M_R is the bending moment resistance of the cross section, A_s is the steel reinforcement area, f_y is the yield strength of steel, d and b_w are the effective height and width of the cross section, f_c is the compressive strength of concrete and x is the neutral axis position, given by Equation 10. Equation 9 is valid for concrete with less than 50 MPa of characteristic compressive strength and simple reinforced beams.

Thus, the limit state equation for beams (g_B) is given by:

$$g_B(\mathbf{X}) = E_B\, M_R\left(f_c, f_y, d, b_w\right) - M_s\left(d, b_w, D, L\right) \tag{11}$$

where E_B is the model error variable for beam bending, M_s is the maximum bending moment on the beam, given by the FE model, and the random variable vector is $\mathbf{X} = \left\{E_B, f_c, f_y, d, b_w, D, L\right\}$, where D and L are the dead and live loads, respectively.

2.2 Limit state equation for columns

The rectangular columns were subjected to normal loads combined with bending. Unlike beams, column resistance cannot be assessed directly as it represents a nonlinear system resulting from the imposition of the equilibrium equations between the internal load effects and strengths [43]. These relations are considered by shifting the neutral axis position in the cross section, allowing the construction of an interaction curve that separates the safe and failure regions, as depicted in Figure 1, evaluated following prescriptions of [1].

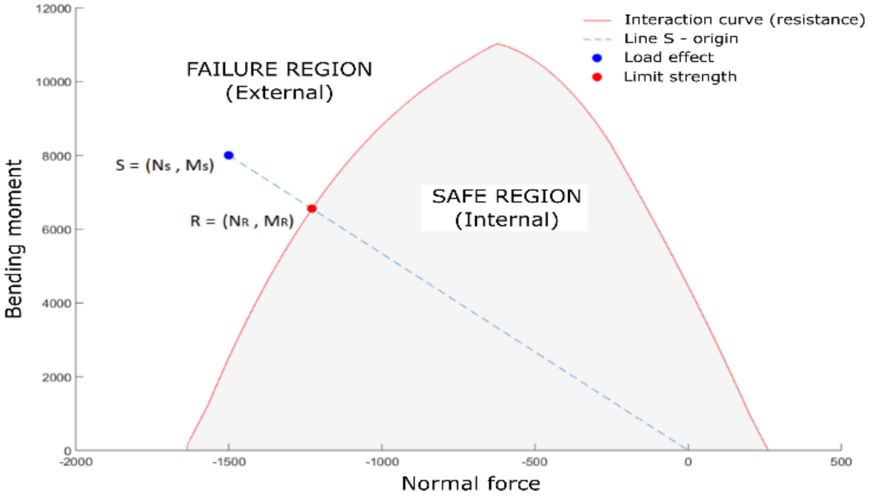

Figure 1. Normal load times bending Moment (NM) interaction diagram for strength of RC columns.

Formulation of the limit state for RC columns follows [30], and is based on the shortest load path criterion. Let *S* be the load effect, given as a point of normal force and bending moment (N_S , M_S) in the diagram (Figure 1). The line joining this point to the origin is the "load path". This line defines the limit strength point *R*, given as (N_R , M_R), and which can be obtained by a curve intersection algorithm. The limit state function for columns (g_C) is established by comparing the distance between points *R* and *S* to the origin:

$$g_C(\mathbf{X}) = E_C\sqrt{(N_R)^2 + (M_R)^2} - \sqrt{(N_S)^2 + (M_S)^2} \tag{12}$$

where E_C is the model error variable for columns. For a point inside the safe region, the distance from S to the origin is smaller than the distance from R to the origin, leading to a positive value for the limit state function. In Equation 12, the strength is a function of resistance variables ($N_R(f_c, f_y, d, \ldots)$, $M_R(f_c, f_y, d, \ldots)$), and the load effects are functions of the loads: $N_S(D, L, d, b_w)$, $M_S(D, L, d, b_w)$.

The formulation presented herein assumes that load effects N_S , M_S vary in proportion to the loads (D, L) , which is valid in case of dependent gravity loads. When lateral (wind or earthquake) loads are considered, load effects may change independently, and a more complex "out-crossing rate" formulation is required [44].

2.3 Collapse probabilities

In this paper, we conduct reliability analyses of intact frames and frames with discretionary column removals, representing situations in which local damage has occurred. The failure probabilities given through the limit state equations for beams and columns (Equations 11 and 12) for the damaged structures represent the conditional collapse probability $P[C \mid LD, H]$, following Equation 1. The $P[C]$ term needs to be evaluated considering a risk analysis to determine $P[H]$ and $P[LD \mid H]$ terms. For the intact structures, in which local damage has not occurred, the failure probabilities represent the term $P[C]$ related to the usual loading condition.

3. FINITE ELEMENT MODELLING FOR LOAD EFFECTS

The load effects in the studied frames are assessed through a linear static analysis. A mechanical model based on the finite element method (FE) is used, with elastic material behavior and 2D frame elements. A linear static analysis is sufficient for an approximate study of the load distribution in regular frames, and for its redistribution across the floors and spans. A study of the ultimate collapse loads requires mechanical models which incorporate geometric and material nonlinearities behavior and are out of the scope of this paper.

Each frame element in the model has two nodes with three degrees of freedom in each node: one rotation and two displacements, as depicted in Figure 2.

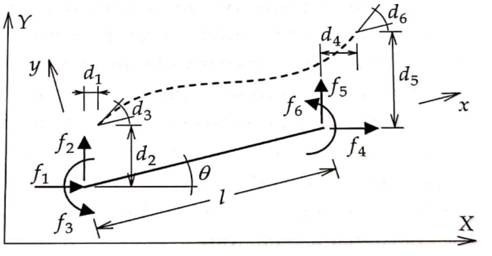

Figure 2. Degrees of freedom of the frame element [45].

The nodal displacements vector $\mathbf{u}$ is obtained by a system containing the global stiffness matrix $\mathbf{K}$ and the nodal forces vector $\mathbf{f}$:

$$\mathbf{K} \cdot \mathbf{u} = \mathbf{f} \tag{13}$$

With the displacements, the load effects can be found through equilibrium equations. The model used herein was validated by comparing the results with academic software Ftool [46]. In the FE model, one element is used for each column in each floor and one element is used for each spam of the beams.

3.1 Limitations of linear analysis

The mechanical model used herein is limited to elastic behavior of the materials and does not consider geometric nonlinearity and dynamic effects. Therefore, as a phenomenon that causes large deformations in the structure, the collapse mechanism is considered in a simplified and conservative approach.

Figure 3 depicts the nonlinear behavior of a reinforced concrete beam which suffered a midspan column removal. The first part of the load-displacement curve is the linear elastic stage or approximated as such; this is followed by the arch effect, the snap-through and the catenary (or membrane) action. Catenary action only occurs if columns at both ends of the beam element provide enough horizontal restraint. The end of the curve, point D, represents the ultimate load capacity of the beam, which can be quantified by nonlinear procedures. The bending moment resistance in the linear stage, used herein as the limit state (Equations 9–11), corresponds to point A, where the limits of material and geometrical linearities are valid. Therefore, a great reserve of strength is still available in the elements, which is not captured in the simplified analyses carried out in this paper. Hence, the reliability index values computed in this paper are minimum values, corresponding to the strength at point A in Figure 3.

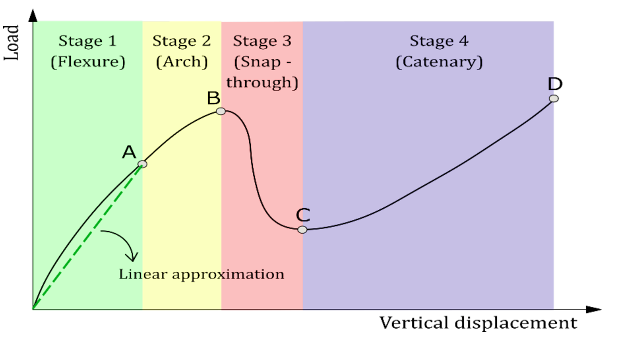

Figure 3. Nonlinear behavior in the collapse of a reinforced concrete beam.

4. STUDIED FRAMES, DESIGN AND LOAD CASES

The analyses presented in this paper are based on the buildings illustrated in Figure 4: a 4-story and an 8-story reinforced concrete frames with four bays, spans of 5.0 meters and story height of 3.0 meters. Five different situations were analyzed in each frame, one intact, two with removal of an external column and two with removal of an internal column, as shown in Figure 5. For the frames with column removal, we consider a normal design (no strengthening for column loss) and a strengthened APM design, i.e., a frame reinforced to bridge over a failed column, as detailed in the next section.

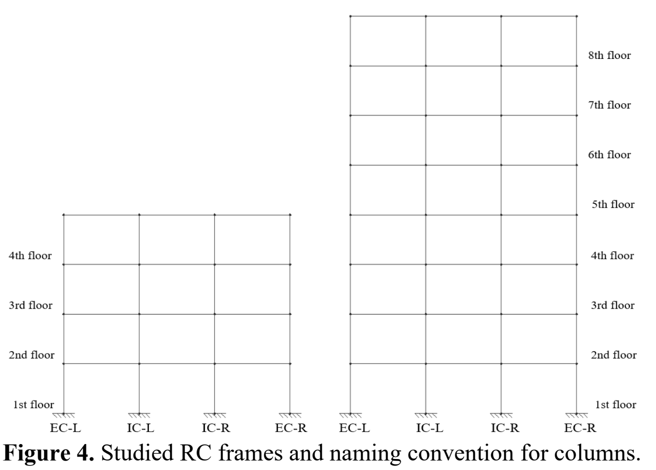

Figure 4. Studied RC frames and naming convention for columns.

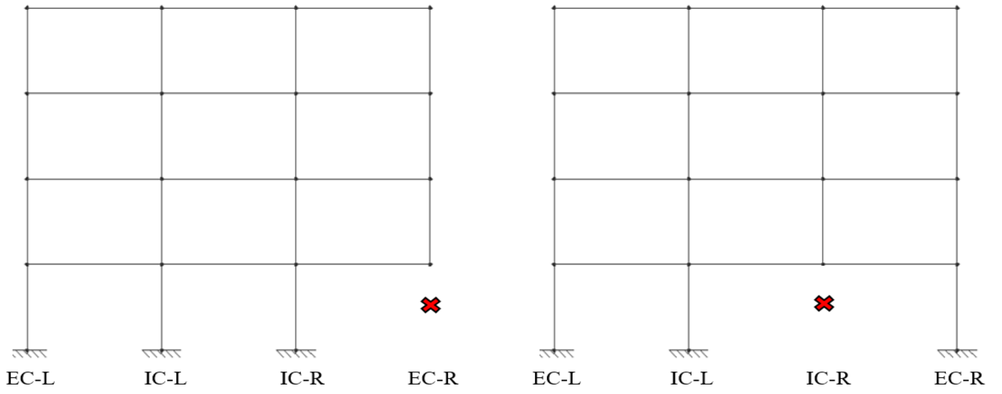

Figure 5. Illustration of the considered column loss conditions: external (left) and internal (right).

4.1 APM design

The Alternate Path Method is specified in documents UFC 4-023-03 [13] and GSA [12]. In this direct design approach against progressive collapse, the structure is designed such as to be able to bridge over a removed load-carrying element. This is achieved by ensuring that alternate load paths are available in the structure in cases where local damage occurs, confining disproportionate collapse.

The method is applied by notionally removing key load-bearing structural elements, followed by a structural analysis. One at a time, internal and external columns are removed, as well as columns at critical locations, as determined by engineering judgment. The elements which do not resist the load redistribution need to be strengthened. The analysis can be linear static, nonlinear static or nonlinear dynamic. The use of linear static procedures is limited to regular structures that are 10-stories or less.

In light of Equation 1, the APM design is done by considering $P\left[LD|H\right]=1$, in which the local damage corresponds to a column loss. Recall that the failure probabilities obtained by a reliability analysis in a damaged structure (column loss) refers to the term $P[C\,|\,LD,H]$. To find the term $P\left[C\right]$, one needs to use Equation 1, as commented in Section 2.3.

4.2 Load combinations and design

The loads applied in the structures are quantified based on an influence area with a total depth of 8.0 meters, 4.0 meters in each side of the frame. All nominal values of the loads are based on ABNT NBR 6120:2019 – Design loads for structures [47]. The live loads are established considering a residential building, with the rooms classified as "Pantry and laundry area", with 2.0 kN/m^2. For the dead loads, only the self-weight of the structural elements is considered, with slabs of 0.12 meters height.

The design code ABNT NBR 8681 [48] specifies an exceptional loading combination arising from the occurrence of actions that can cause catastrophic effects. These actions are transitory and extremely brief in duration. Following ABNT NBR 8681, the required design strength R_D is given by:

$$R_D \geq 1.2\,D_n + 1.0\,L_n \tag{14}$$

where D_n is the nominal dead load and L_n is the nominal live load.

Although the definition of exceptional loads in the Brazilian standard [48] may be in convergence with events that can cause severe local damage, it does not specifically recommend any loading condition for design or strengthening of structures that already suffered damage, which is the case of the Alternate Path Method. In the APM design, the residual capacity of the structure must be assessed, which is conditional to the occurrence of local damage (column loss). Hence, to maintain coherence between our analysis for the cases of intact frame and column loss, the design factors for loads are taken from ASCE 7 [33], for usual loading (intact frame) and abnormal loading (column loss – residual capacity).

For demonstration purposes, in Section 5.2 we show how use of load combinations given in ABNT NBR 8681 (Equation 14) results in overdesigned elements when an external column is removed. Although Equation 14 may not be fitted for the progressive collapse assessment through the Alternate Path Method, it may be well suited for the Enhanced Local Resistance method, where collapse is prevented by reinforcing specific elements to resist initial abnormal loads.

As a consequence of using ASCE 7 load combinations, the reliability index results obtained herein for the intact structure are not the same as those obtained using design factors of codes [1] or [48]. Yet, the analysis is justified as we are more interested in the variation of reliability indexes for different points of the structure. Moreover, the recent study on reliability-based calibration of Brazilian design codes [49] has suggested that the partial load factor for dead load should be reduced (to $\gamma_D = 1.25$) and for live load should be increased (to $\gamma_L = 1.70$). These values are somewhat closer to the values given by ASCE 7, as reported below.

Following ASCE 7, under normal loading condition, the required design strength R_D is given by:

$$R_D \geq 1.2\,D_n + 1.6\,L_n \tag{15}$$

The design strength R_D is evaluated following ABNT NBR 6118:2014, with $\gamma_c = 1.4$ and $\gamma_S = 1.15$.

The column loss condition corresponds to an extraordinary event. Following the Alternate Path Method (APM) and the ASCE 7 "Residual capacity" load combination, beams and columns of the regular building are strengthened such that:

$$R_D \geq 1.2\,D_n + 0.5\,L_n \tag{16}$$

Under column loss condition, a reduced design value is considered for the live load: the damaged frame is not expected to withstand the lifetime maximum live load, but it should support the sustained part of the live load, until repair action is taken. Accordingly, in the reliability analysis, the fifty-year extreme value of the live load is considered for the intact frame, and the arbitrary-point-in-time value of the live load is considered under column loss condition, as detailed in the sequence.

Beam elements are designed considering pure bending, and columns are designed considering normal loads plus bending. Second-order effects were not considered, to simplify the reliability analysis, and to respect the limitations of the linear finite element model. Tables 1 and 2 present the cross-section and reinforcement area for beams and columns of the 4 and 8-story buildings, respectively. In the columns, the reinforcement is placed near the top and the bottom of the cross-section. All elements are designed with concrete with 30 MPa of characteristic compressive strength (f_{ck}) and steel with 500 MPa of characteristic yield strength (f_{yk}). The structural analysis was performed with a modulus of elasticity (E) of 20 GPa. Table 3 shows the loading considered, as well as the resulting live-to-dead load ratios, which are relevant to interpret the results of reliability analysis.

Table 1. Cross-section dimensions and reinforcement for 4-story building ("CL" means column loss).

Loading case	Width (cm)	Beams		Internal columns		External columns	
		Height (cm)	Steel reinf. (cm^2)	Height (cm)	Steel reinf. (cm^2)	Height (cm)	Steel reinf. (cm^2)
Normal loading	19.0	50.0	6.80	40.0	5.00	40.0	7.50
Strengthened for external CL	19.0	70.0	16.00	50.0	8.00	50.0	13.00
Strengthened for external CL (ABNT *NBR 8681*)	19.0	80.0	18.00	50.0	10.00	50.0	17.00
Strengthened for internal CL	19.0	70.0	15.00	50.0	10.00	50.0	14.50

Table 2. Cross-section dimensions and reinforcement for 8-story building ("CL" means column loss).

Loading case	Width (cm)	Beams		Internal columns		External columns	
		Height (cm)	Steel reinf. (cm^2)	Height (cm)	Steel reinf. (cm^2)	Height (cm)	Steel reinf. (cm^2)
Normal loading	19.0	50.0	8.50	60.0	12.00	60.0	6.60
Strengthened for external CL	19.0	80.0	16.00	70.0	12.00	70.0	12.00
Strengthened for internal CL	19.0	80.0	14.00	70.0	20.00	70.0	12.00

Table 3. Nominal values for loads (in kN/m) and ratio L_n / D_n .

Frame	Case	Live load on beams (q_n)	Dead load on beams ($g_{v,n}$)	Self-weight of columns ($g_{p,n}$)	L_n / D_n on beams	L_n / D_n on columns
4-story	Intact	16.00	26.38	1.90	0.61	0.56 - 0.58
	Column loss	16.00	27.33	2.38	0.59	0.52 - 0.56
8-story	Intact	16.00	26.38	2.85	0.61	0.54 - 0.57
	Column loss	16.00	27.80	3.33	0.58	0.51 - 0.56

4.3 Random variables for reliability analysis

The reliability analysis of the frames is performed considering ten random variables, presented in Table 4. The live load random variable in column loss scenarios follows [14], taken with arbitrary-point-in-time values and Gamma distribution, as the damaged frame is not expected to withstand its lifetime maximum live load. All the beams were loaded by the same live load random variable simultaneously.

Table 4. Random variables considered in the reliability analysis and their parameters ("Variable" means "in terms of the standard deviation").

Variable (symbol)	Distribution	Mean	C.o.V.	Standard deviation	Reference
Cross-section dimensions (B, H)	Normal	d_n	Variable	$4 + 0.006 d_n$ (mm)	[50]
Self-weight of columns (G_p)	Normal	$1.06 g_{p,n}$	0.12	$0.1272 g_{p,n}$	[32]
Dead load on beams (G_v)	Normal	$1.06 g_{v,n}$	0.12	$0.1272 g_{v,n}$	[32]
Live load on beams, intact frame (Q_{50})	Gumbel	q_n	0.40	$0.40 q_n$	[32]
Live load on beams, column loss $(Q_{a.p.t.})$	Gamma	$0.25 q_n$	0.55	$0.1375 q_n$	[32]
Concrete compressive strength (f_c)	Normal	$1.22 f_{ck}$	0.15	$0.183 f_{ck}$	[32]
Steel yield strength (f_y)	Normal	$1.22 f_{yk}$	0.04	$0.0488 f_{yk}$	[32]
Model error for beam bending (E_B)	Lognormal	0.99	0.024	0.02376	[19]
Model error for columns (E_C)	Normal	1.15	0.145	0.16675	[49]

5. RESULTS FOR THE 4-STORY FRAME

5.1 Normal design, intact frame

Reliability index results for the intact 4-story frame are presented in Figure 6. Calculated values of reliability indexes are shown besides each element. The elements highlighted in yellow color are those which controlled the regular design.

Reliability indexes observed in Figure 6 are around 3.0 for beams and 4.0 for columns. Note that the element which controls design, for which design strength is smaller, is also always the element with smaller reliability index. The largest variations in reliability indexes are observed for columns of different floors. Design of internal columns is controlled by larger normal loads at the first floor. Significant reserve in safety is observed for internal columns of higher floors, when the same detailing is considered: this is expected, as normal loads are significantly smaller. Design of external columns is controlled at the highest floor, where bending moments prevail over normal loads. As observed in Figure 7, the external columns of different floors correspond to quite different points in the NM interaction diagram: the design is controlled at the fourth floor, where normal load is small, hence the load trajectory is very stepped and bending strength is limited (Figure 7 right); for the third floor (and those below), the normal load is much larger, the load trajectory is less stepped, leading to much larger bending strength. The ratio of bending moment to normal force, M/N, for external columns, is shown in Figure 8, which confirms that the load effects change significantly from the third to the fourth floor.

The results presented herein can be better interpreted by looking at the sensitivity coefficients, which show the contribution of each random variable to the calculated failure probabilities. Figure 9 shows the reliability indexes and the sensitivity coefficients for the external and internal columns of the 4-story frame. We start by noting that the model error random variable (E_C) has a greater role for all columns. For those columns which control the design, role of E_C is around 40 to 50%; for other columns, it approaches 100%. This points out to the importance of developing better probabilistic models for the model error of columns. Considering the behavior observed in Figure 7, one significant improvement would be to evaluate model error statistics for "zones", corresponding to similar values of the ratio M/N.

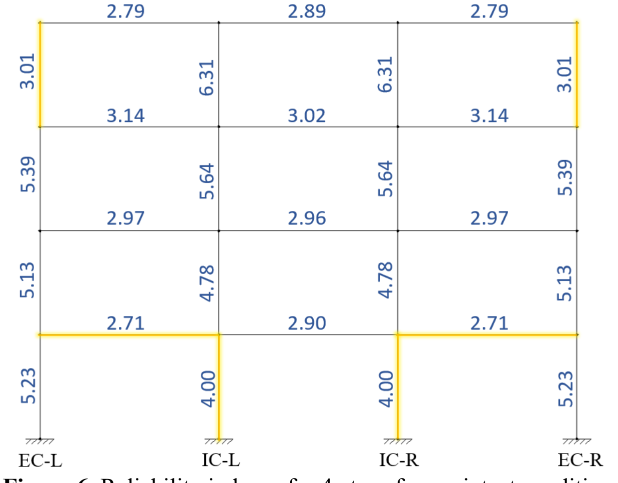

Figure 6. Reliability indexes for 4-story frame, intact condition.

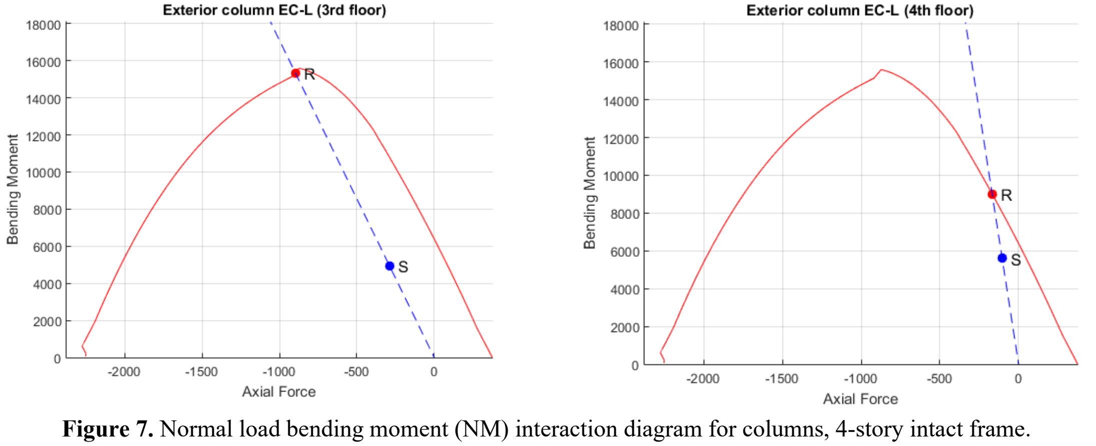

Figure 7. Normal load bending moment (NM) interaction diagram for columns, 4-story intact frame.

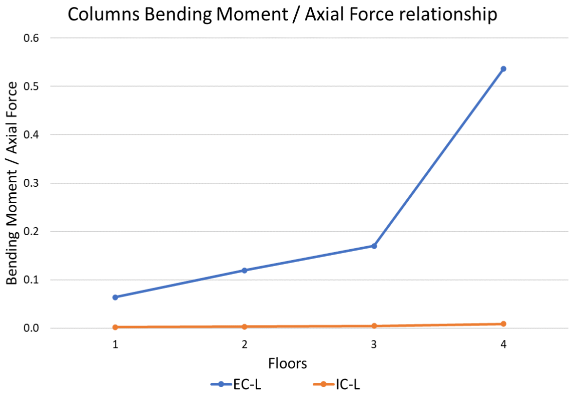

Figure 8. Ratio between bending moment and normal force (M/N) for columns at different floors, 4-story intact frame.

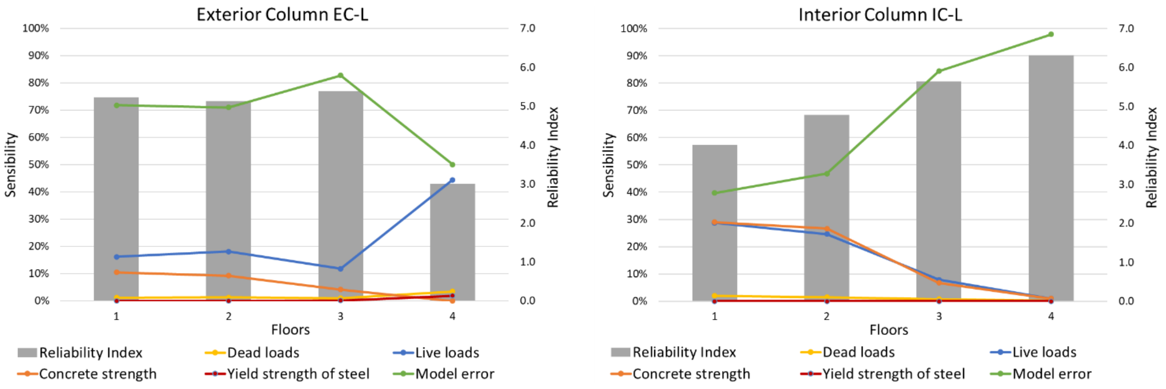

Figure 9. Reliability index and sensitivity coefficients for columns of different floors, 4-story intact frame, external columns (left) and internal columns (right).

One intuitive behavior is observed for the internal columns, with the reliability index increasing from bottom to top: for lower floor columns, with greater normal load, the contribution of concrete strength and live load rivals that of the model error; as normal loads are reduced, the importance of other variables vanishes, and E_C dominates failure probabilities, which become very small.

For external columns, the influence of live load exceeds that of concrete strength, and becomes relevant at the fourth floor, which controls the design. Recall that the normal force bending moment interaction diagram for external columns of 3rd and 4th floors is shown in Figure 7.

5.2 Discretionary removal of external column

Figure 10 illustrates the reliability indexes for the 4-story frame, when the external column is removed: left in figure, results for the original frame; right, results for the strengthened frame (APM method). All reliability indexes shown in Figure 10 are conditional on column removal (local damage). Highlighted in red are the elements for which the failure probability is larger than 0.1, which corresponds to the maximum accepted value for the conditional collapse probability (term $P[C|LD,H]$ in Equation 1). Negative reliability indexes shown in figure correspond to $P[C|LD,H] > 0.5$.

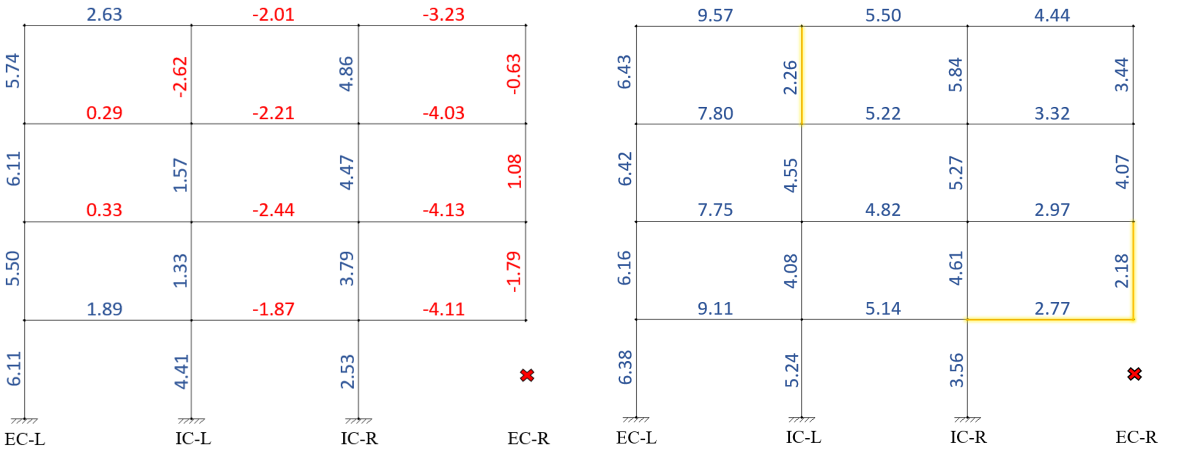

Figure 10. Reliability indexes for 4-story frame, removal of external column, original frame (left) and strengthened frame (right).

As observed in Figure 10 (left), the original (non-strengthened) frame does not withstand loss of an external column. Beams of the affected bay would most certainly form plastic hinges. External columns above the removed one (EC-R) and the internal column at the top floor (IC-L) also present unacceptably low reliability index. As noted in Figure 10 (right), the strengthened frame would likely support loss of the external column, with the weakest column presenting $\beta = 2.18$, which corresponds to a failure probability of $p_f = 0.015$.

Sensitivity indexes for the strengthened frame are shown in Figure 10. Again, the model error random variable controls failure probabilities, with around 70% dominance for those elements which control the design. For external left (EC-L) column, model error contributed alone to the failure probability: this deterred the reliability index from becoming larger than 7. Behavior of column IC-L is observed to be like the case of internal columns of the intact frame, with the reliability index decreasing at the top floor, such as the influence of the model error (Figure 11). At the top floor, an increase in the sensibility of dead and live load actions, as well as yield stress, is observed. This hints to the greater contribution of bending moments at this top column.

For column IC-R, reliability indexes become smaller for lower floors, with larger participation of concrete strength, as well dead and live loads; this occurs due to larger participation of normal loads, for this damaged structure condition. Figure 12 confirms this observation, as it shows the ratio of bending moment to normal loads, for the three remaining columns of the damaged building.

Relating results in Figure 12 to those in Figure 10, we observe that M/N ratios up to 0.4 contribute to greater strength and larger β's, whereas values above 0.6 lead to smaller β's (as is the case for column IC-L at the top floor).

The collapse probability given by Equation 1 for the elements with the lowest reliability indexes are shown in Table 5, for all the analyses conducted. The values were obtained considering hazard probability $P[H]$ of 10^{-5} and that local damage is certain due to hazard ($P[LD|H]=1$). As expected, the collapse probabilities are small for the strengthened structures, since the hazard probabilities are usually small. For the intact structures, the collapse probability refers to the usual loading condition, and cannot be compared directly with the cases of column loss.

At last, as commented in Section 4.2 of this paper, the reliability analysis of the building redesign with the ABNT NBR 8681 "Exceptional load combination" is shown in Figure 13. The reliability indexes of the elements which control the design are much larger than those of the frame strengthened using ASCE 7 "Residual capacity" load combination. The most critical beam's β goes from 2.77 to 4.31, whereas the internal column's goes from 2.26 to 3.94 and the external column's goes from 2.18 to 3.46. As one can observe in Table 5, the order of magnitude of the failure probability of the elements designed following ABNT NBR 8681 are around 10^{-10}, excessively lower than the 10^{-7} of the ASCE 7 load combination, which indicates that the Alternate Path method assessed with Brazilian load factors will likely overdesign the elements.

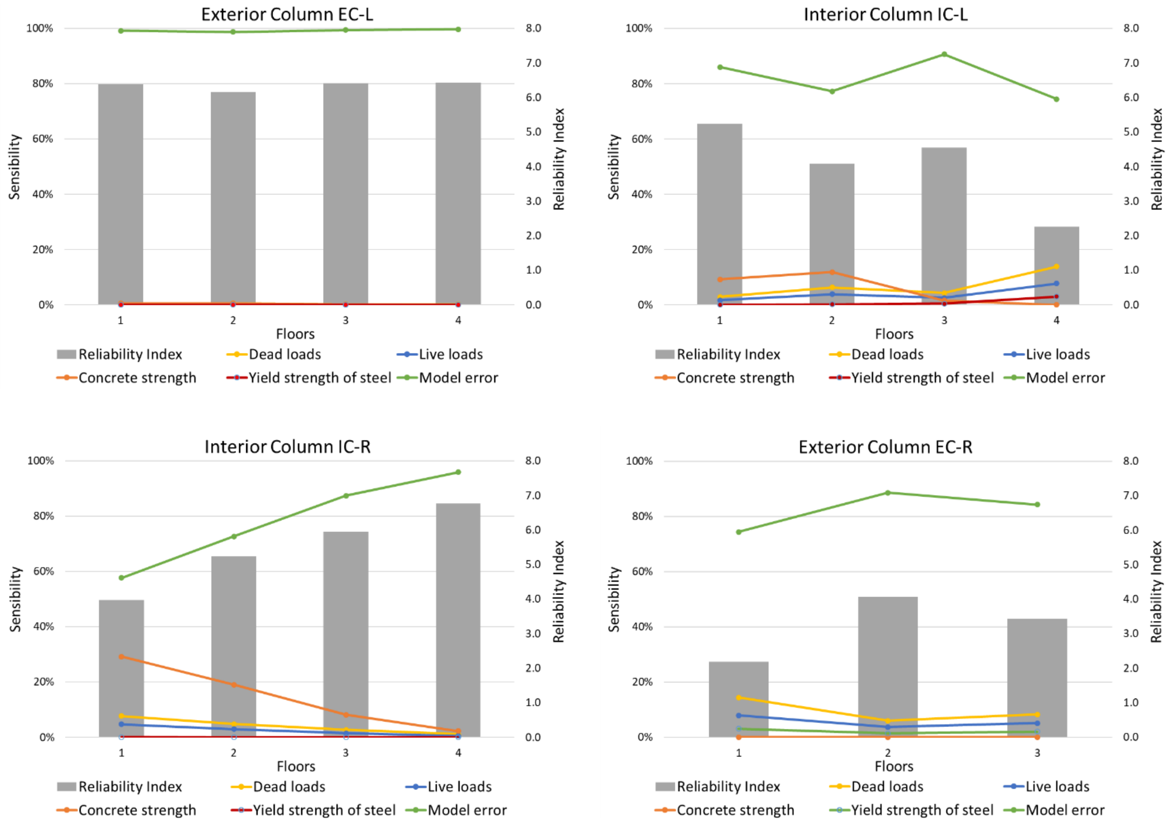

Figure 11. Reliability index and sensitivity coefficients for columns of different floors, strengthened 4-story frame with removal of external column.

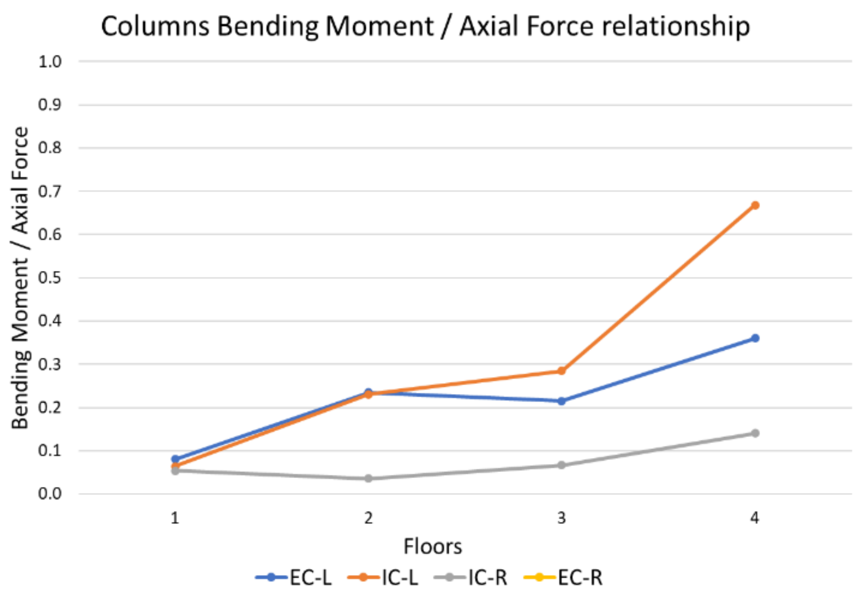

Figure 12. Ratio M/N for columns at different floors, strengthened 4-story frame with removal of external column.

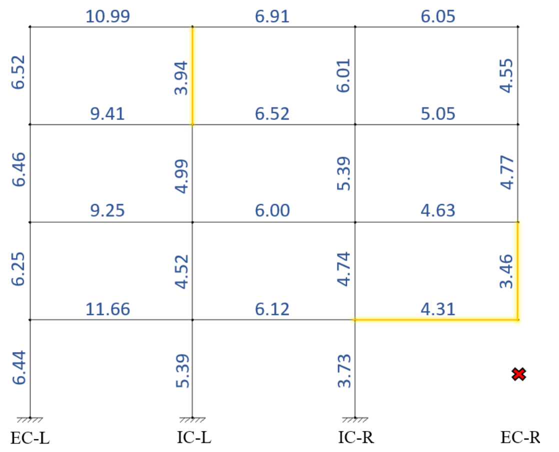

Figure 13. Reliability indexes for 4-story frame, removal of external column, designed with exceptional load combination of ABNT NBR 8681 [48].

Table 5. Collapse probability of the most critical elements, calculated through Equation 1 using $P[H]=10^{-5}$ and $P[LD|H]=1$ (in boldface, values that exceed 10^{-6}, corresponding to $P[C|LD,H]>0.1$).

Structure		Beam	External Column	Internal Column
4-story	Intact	3.36E-03	1.31E-03	3.17E-05
	ECL - O	**1.00E-05**	**9.63E-06**	**9.96E-06**
	ECL - S	2.80E-08	1.46E-07	1.19E-07
	ECR - S (ABNT NBR 8681)	8.16E-11	2.70E-09	4.07E-10
	ICL - O	**1.00E-05**	**9.98E-06**	**7.91E-06**
	ICL - S	9.35E-09	9.14E-08	4.07E-10
8-story	Intact	6.57E-03	5.39E-03	2.70E-04
	ECL - O	**1.00E-05**	**9.79E-06**	1.66E-07
	ECL - S	**1.66E-06**	**1.64E-06**	1.69E-08
	ICL - O	**1.00E-05**	**9.73E-06**	1.44E-08
	ICL - S	1.22E-08	1.99E-08	3.49E-09

ECL: external column loss; ICL: internal column loss; O: original (non-strengthened); S: strengthened

5.3 Discretionary removal of internal column

Figure 14 illustrates the reliability indexes for the 4-story frames, when the internal column is removed. Again, the original frame does not withstand column loss as beams and most of column EC-R present unacceptably low reliability indexes. However, in the first floor, the columns right next to the removed one were not significantly affected by the overload.

In the strengthened frame, all elements present acceptable reliability indexes. In this scenario, there is a reduction in the β's of the EC-R column at the 4th floor. This again occurs due to the excessive steepness of the load path, indicating a prevalence of bending moment action. This same phenomenon is observed in the IC-L and EC-L columns, but with less intensity.

As depicted in the graphs of Figure 15, the influence of the model error is preponderant, ranging from 65 to 75% in the elements that control the design and up to 100% in the others. In the IC-L and EC-R columns, the importance of the concrete strength is significant, especially on the first floor, where the increase in compression relieves the effects of bending moment, reducing the steepness of the load path and increasing reliability. On the other hand, in the last floor, the sensitivity of the concrete drastically decreases, being surpassed by the dead and live loads. In Figure 16, we observe that M/N ratios above 1.0 lead to smaller values of reliability indexes (as is the case for column EC-R at the top floor).

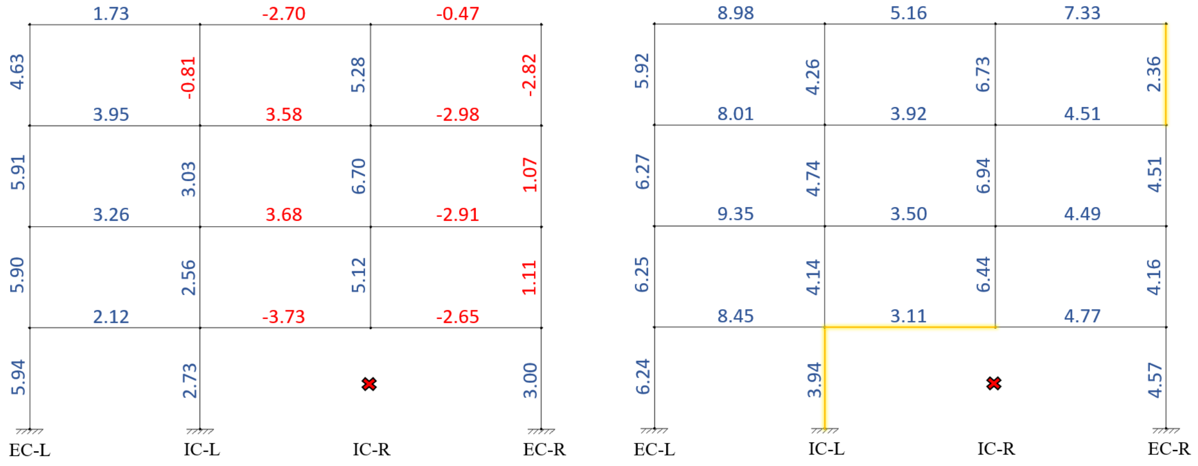

Figure 14. Reliability indexes for 4-story frame, removal of internal column, *original frame (left) and strengthened frame (right).*

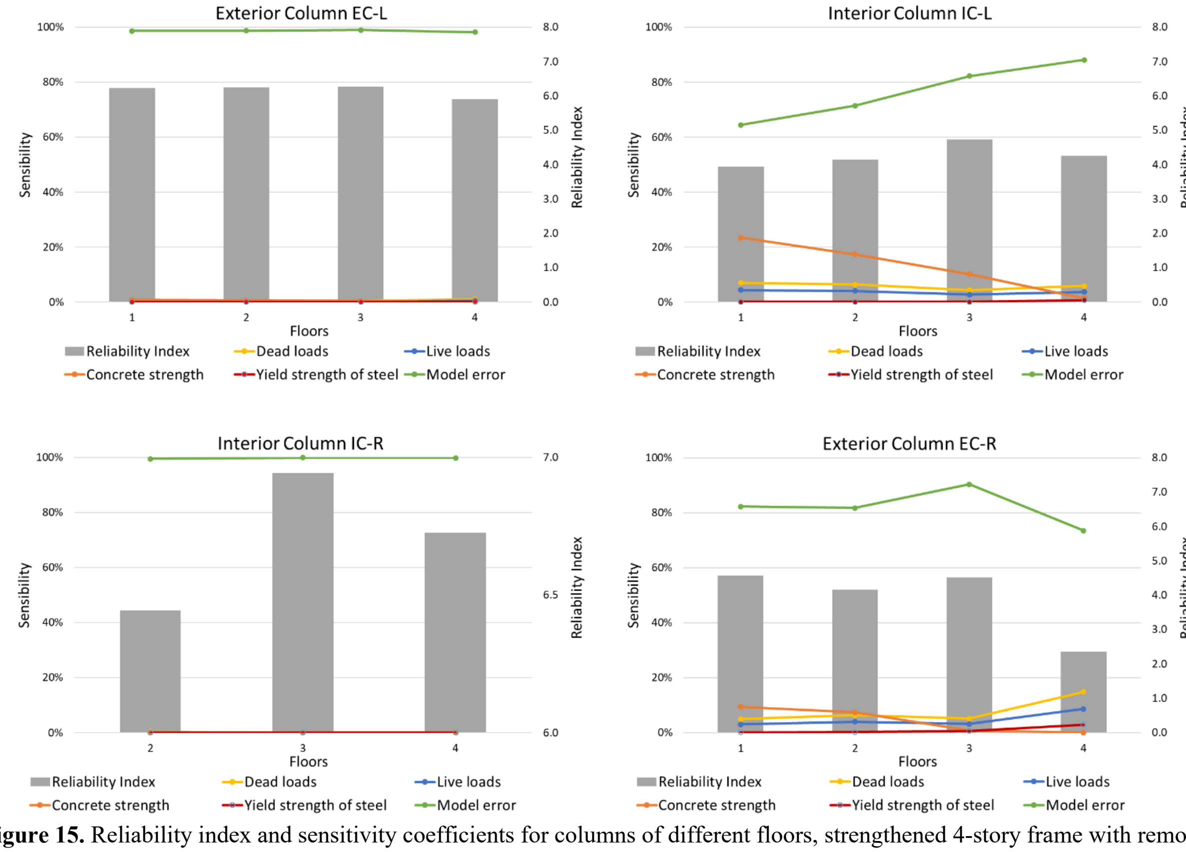

Figure 15. Reliability index and sensitivity coefficients for columns of different floors, strengthened 4-story frame with removal of internal column.

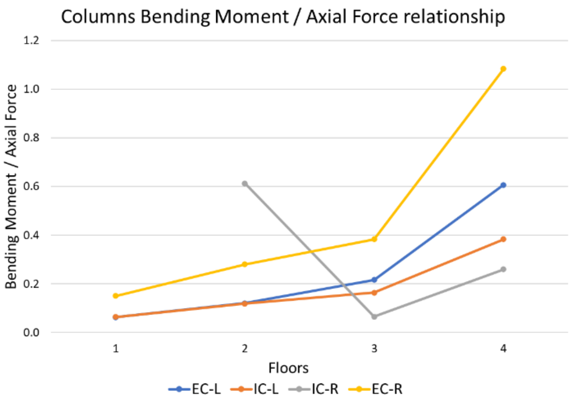

Figure 16. Ratio M/N for columns at different floors, strengthened 4-story frame with removal of external column.

6. RESULTS FOR THE EIGHT-STORY FRAME

The 8-story frame presents similar results to the 4-story frame w.r.t. the columns behavior and the inability of the non-strengthened structure to withstand column loss. Hence, due to space constraints, detailed results are not presented herein. Figure 17 depicts the reliability indexes for the intact and for the strengthened frames with column removal. The model error variable sensibility prevails in all columns. For the elements that control the design, values around 50% in the intact frame and up to 80% in the column loss frames were found.

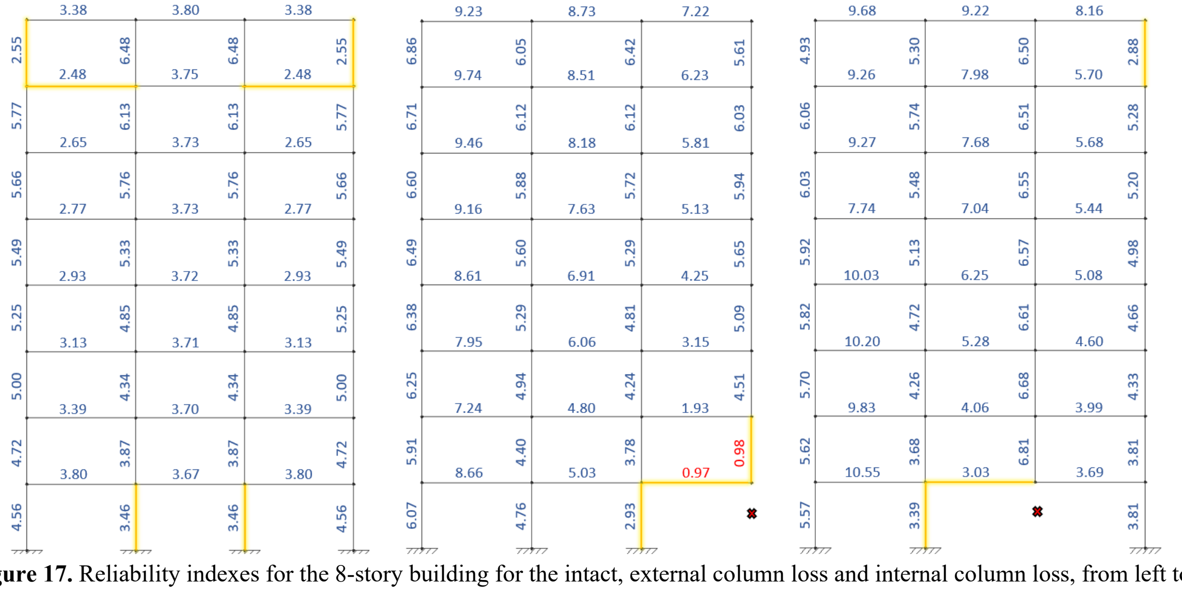

Figure 17. Reliability indexes for the 8-story building for the intact, external column loss and internal column loss, from left to right.

7. CONCLUSIONS

In this paper, we addressed the spatial distribution of load effects and reliability index of beams and columns of RC plane frames, built considering symmetry and regularity. The analysis is limited to gravitational loads, and to linear material modelling; yet it considers usual and abnormal “column loss” loading conditions. Using load combinations recommended by ASCE and partial safety factors for concrete and steel strength by ABNT NBR 6118, we found reliability indexes around $\beta \approx 3$ for beams, and $\beta \approx 4$ for the critical columns of the intact frame.

We observed that the design of internal columns is controlled by the base (first floor) column, at which normal gravity loads are largest. The reliability index for the base column is around $\beta \approx 3$, and this value increases for upper internal columns. The design of external columns was found to be controlled by the fourth (or upper) floor, where the ratio of bending moment to normal load effect (M/N) is largest. For lower external columns, the normal load increases, the load trajectory becomes less stepped in the MN diagram, and the reliability index increases significantly.

Among all random variables considered, the model error for column strength was found to be the most significant source of uncertainty for the reliability of columns. For those columns controlling design, the contribution of model error was found to be around 40 to 70%; for other columns with greater reserve strength (due to design regularity), the contribution of model error reached 100%. This points out to the importance of developing better models for column strength, and more refined probabilistic models for the model error variable. One significant improvement would be to evaluate model error statistics for “zones”, corresponding to similar values of the M/N ratio, in the MN interaction diagram.

For the discretionary column removal loading condition, it was observed that conventional design leads to unacceptable failure probabilities. The beams would most likely fail, due to exceptional bending moments generated by cantilever or double-spam effects. This conclusion does not consider the eventual compressive arch or catenary effects. For the strengthened frames, following the APM design philosophy, the conditional failure probabilities were found to be acceptable. In column loss condition, symmetry is lost, but regular design also leads to significant differences in reliability index and sensitivity coefficients of beams and columns located in different parts of the building.

Investigations are underway to include horizontal loads, non-linear material modelling, and to consider system effects like compressive arch and catenary actions, in the reliability analysis of RC frames subject to column loss loading.

ACKNOWLEDGEMENTS

Funding of this research project by Brazilian agencies CAPES (Brazilian Higher Education Council), CNPq (Brazilian National Council for Research, grant n. 309107/2020-2) and joint FAPESP-ANID (São Paulo State Foundation for Research - Chilean National Agency for Research and Development, grant n. 2019/13080-9) is cheerfully acknowledged. Valuable comments by the anonymous reviewers are also cheerfully acknowledged

REFERENCES

[1] Associação Brasileira de Normas Técnicas, *Design of Concrete Structures – Procedure*, ABNT NBR 6118, 2014.

[2] I. V. Melo, S. H. S. Nóbrega, and P. G. B. Nóbrega, “Progressive collapse in concrete structures and the Brazilian design codes (in Portuguese),” in *An. 58º Congr. Bras. Concreto*, Belo Horizonte, MG, 2016.

[3] B. R. Ellingwood and D. O. Dusenberry, "Building design for abnormal loads and progressive collapse," *Comput. Aided Civ. Infrastruct. Eng.*, vol. 20, no. 3, pp. 194–205, 2005, http://dx.doi.org/10.1111/j.1467-8667.2005.00387.x.

[4] B. R. Ellingwood, "Mitigating risk from abnormal loads and progressive collapse," *J. Perform. Constr. Facil.*, vol. 20, no. 4, pp. 315–323, 2006, http://dx.doi.org/10.1061/(ASCE)0887-3828(2006)20:4(315).

[5] B. R. Ellingwood, "Strategies for mitigating risk to buildings from abnormal load events," *Int. J. Risk Assess. Manag.*, vol. 7, no. 6–7, pp. 828–845, 2007, http://dx.doi.org/10.1504/IJRAM.2007.014662.

[6] U. Starossek, "Typology of progressive collapse," *Eng. Struct.*, vol. 29, no. 9, pp. 2302–2307, 2007, http://dx.doi.org/10.1016/j.engstruct.2006.11.025.

[7] B. A. Izzuddin et al., "Progressive collapse of multi-storey buildings due to sudden column loss - Part I: Simplified assessment framework," *Eng. Struct.*, vol. 30, no. 5, pp. 1308–1318, 2008, http://dx.doi.org/10.1016/j.engstruct.2007.07.011.

[8] K. Khandelwal and S. El-Tawil, "Pushdown resistance as a measure of robustness in progressive collapse analysis," *Eng. Struct.*, vol. 33, no. 9, pp. 2653–2661, 2011, http://dx.doi.org/10.1016/j.engstruct.2011.05.013.

[9] E. Masoero, P. Darò, and B. M. Chiaia, "Progressive collapse of 2D framed structures: An analytical model," *Eng. Struct.*, vol. 54, pp. 94–102, 2013, http://dx.doi.org/10.1016/j.engstruct.2013.03.053.

[10] C. E. M. Oliveira, E. A. P. Batelo, P. Z. Berke, R. A. M. Silveira, and T. L. Massart, "“Computational assessment of the progressive collapse of reinforced concrete planar frames using a nonlinear multilayered beam formulation”, *RIEM* -," *Rev. IBRACON Estrut. Mater.*, vol. 7, no. 5, pp. 845–855, 2014, http://dx.doi.org/10.1590/S1983-41952014000500007.

[11] B. Ellingwood and E. V. Leyendecker, "Approaches for design against progressive collapse," *J. Struct. Div.*, vol. 104, no. 3, 1978.

[12] General Services Administration, *Alternate Path Analysis & Design Guidelines for Progressive Collapse Resistance*, 2013, p. 143.

[13] Unified Facilities Criteria, Design of Buildings to Resist Progressive Collapse, UFC 4-023-03, 2009, p. 227.

[14] A. T. Beck, L. R. Ribeiro, and M. Valdebenito, "Risk-based cost-benefit analysis of frame structures considering progressive collapse under column removal scenarios," *Eng. Struct.*, vol. 225, 2020, http://dx.doi.org/10.1016/j.engstruct.2020.111295.

[15] A. T. Beck, L. R. Ribeiro, and M. Valdebenito, “Cost-benefit analysis of design for progressive collapse under accidental or malevolent extreme events,” in *Engineering for Extremes: Decision-making in an Uncertain World*, M. G. Stewart and D. V. Rosowsky, Eds., Switzerland: Springer, 2021. ISBN 978-3-030-85017-3.

[16] A. T. Beck, L. R. Ribeiro, M. Valdebenito, and H. Jensen, "Optimal design of regular frame structures subject to column loss events: a conceptual study," *J. Struct. Eng.*, 2021. https://doi.org/10.1061/(ASCE)ST.1943-541X.0003196.

[17] J. M. Adam et al., "Research and practice on progressive collapse and robustness of building structures in the 21st century," *Eng. Struct.*, vol. 173, pp. 122–149, 2018, http://dx.doi.org/10.1016/j.engstruct.2018.06.082.

[18] F. R. Stucchi and S. H. C. Santos, "Reliability based comparison between ACI 318-05 and NBR 6118," *Rev. Ibracon Estrut.*, vol. 3, no. 2, 2007.

[19] E. S. Santos, “Avaliação estatística do erro de modelos de resistência para elementos lineares de concreto armado da ABNT NBR 6118:2007,” in M.S. thesis, São Carlos Sch. Eng., Univ. São Paulo, São Carlos, 2012.

[20] D. M. Santos, F. R. Stucchi, and A. T. Beck, "Confiabilidade de vigas projetadas de acordo com as normas brasileiras," *Rev. IBRACON Estrut. Mater.*, vol. 7, pp. 723–746, 2014, http://dx.doi.org/10.1590/S1983-41952014000500002.

[21] D. A. San Martins, “Confiabilidade de vigas pré-tracionadas de concreto protendido”, M.S. thesis, Eng. Civ., Univ. Fed. Rio Grande do Sul, 2014.

[22] C. G. Nogueira and M. D. T. Pinto, "Safety variability assessment of reinforced concrete beams subjected to bending moment considering the NBR 6118:2014 safety partial factors," *Rev. IBRACON Estrut. Mater.*, vol. 9, no. 5, pp. 682–709, 2016, http://dx.doi.org/10.1590/S1983-41952016000500003.

[23] M. Scherer, I. B. Morsch, and M. V. Real, "Reliability of reinforced concrete beams designed in accordance with Brazilian code NBR-6118:2014," *Rev. IBRACON Estrut. Mater.*, vol. 12, no. 5, pp. 1086–1125, 2019, http://dx.doi.org/10.1590/s1983-41952019000500007.

[24] J. M. Araújo, "A confiabilidade no projeto de pilares de concreto armado," *Teor. Prat. na Eng. Civ.*, no. 2, pp. 1–8, 2001.

[25] H. A. T. Nogueira, “Avaliação da confiabilidade de pilares curtos em concreto armado projetados segundo a NBR 6118:2003,” in M.S. thesis, Esc. Eng., Univ. Fed. Minas Gerais, 2006.

[26] W. L. A. Oliveira, A. T. Beck, and A. L. H. C. El Debs, "Safety evaluation of circular concrete-filled steel columns de-signed according to Brazilian building code NBR 8800:2008," *IBRACON Struct. Mater. J.*, vol. 1, pp. 212–236, 2008, http://dx.doi.org/10.1590/S1983-41952008000300001.

[27] P. M. Tramontini, “Estudo de confiabilidade para seções de concreto armado submetidas a diversos tipos de esforços,” in M.S. thesis, Esc. Politéc., Univ. Fed. Rio de Janeiro, 2012.

[28] F. C. Magalhães et al., “Avaliação da confiabilidade de pilares de concreto armado com base nos resultados oriundos de distintos locais de ensaio”, in *An. 56º Cong. Bras. Concr.*, Natal, 2014.

[29] M. F. Pereira, A. T. Beck, and A. L. H. C. El Debs, "Reliability of partially encased steel-concrete composite columns under eccentric loading," *IBRACON Struct. Mater. J.*, vol. 10, pp. 298–316, 2017, http://dx.doi.org/10.1590/s1983-41952017000200003.

[30] H. P. Hong and W. Zhou, "Reliability Evaluation of RC Columns," *J. Struct. Eng.*, vol. 125, no. 7, pp. 784–790, 1989., http://dx.doi.org/10.1061/(ASCE)0733-9445(1999)125:7(784).

[31] M. M. Szerszen and A. S. Nowak, "Calibration of design codes for buildings (ACI 318): Part 2 – Reliability analysis and resistance factors," *ACI Struct. J.*, vol. 100, no. 3, pp. 383–391, 2003.

[32] W. C. Santiago, “*Reliability-based calibration of partial safety factors from main Brazilian codes*,” D.Sc. thesis, São Carlos Sch. Eng., Univ. São Paulo, São Carlos, 2019.

[33] American Society of Civil Engineers, *Minimum Design Loads and Associated Criteria for Buildings and Other Structures*, ASCE/SEI 7-16, 2016, 822 p.

[34] A. M. Freudenthal, "The safety of structures," *Trans. Am. Soc. Civ. Eng.*, vol. 112, pp. 125–180, 1947., http://dx.doi.org/10.1061/TACEAT.0006015.

[35] C. A. Cornell, "A probability-based structural code," *J. ACI*, vol. 66, no. 12, pp. 974–985, 1969.

[36] A. M. Hasofer and N. C. Lind, "An exact and invariant first-order reliability format," *J. Eng. Mech.*, vol. 100, pp. 111–121, 1974.

[37] A. T. Beck, *Confiabilidade e Segurança das Estruturas*, 1. ed. Rio de Janeiro: Elsevier, 2019.

[38] S. Marelli and B. Sudret, “UQLab: a framework for uncertainty quantification in MATLAB”, in: *The 2nd Int. Conf. Vulnerability and Risk Anal. Manage. (ICVRAM 2014)*, p. 2554–2563, 2014.

[39] O. Ditlevsen, "Principle of normal tail approximation," *J. Eng. Mech.*, vol. 107, pp. 1191–1208, 1981., http://dx.doi.org/10.1061/JMCEA3.0002775.

[40] A. Nataf, "Détermination des distributions dont les marges sont données," *C. R. Acad. Sci. Paris*, vol. 225, pp. 42–43, 1962.

[41] Y. Zhang and A. Der Kiureghian, *Finite Element Reliability Methods for Inelastic Structures – Report UCB/SEMM - 97/05*. Berkeley: Dep. Civ. Environ. Eng., Univ. California, 1997.

[42] B. Sudret and A. Der Kiureghian, *Stochastic Finite Element Methods and Reliability: A State-of-the-Art Report, Research Report No. UCB/SEMM-2000/08*. Berkeley: Dep. Civ. Environ. Eng., Univ. California, 2000.

[43] W. S. Venturini and R. O. Rodrigues, *Dimensionamento de Peças Retangulares de Concreto Armado Solicitadas à Flexão Reta*. São Carlos: São Carlos Sch. Eng., Univ. São Paulo, 1987.

[44] R. E. Melchers and A. T. Beck, *Structural Reliability Analysis and Prediction*, 3rd ed. Hoboken: Wiley, 2018.

[45] L. F. Martha, *Análise de Estruturas - Conceitos e Métodos Básicos*, 2ª. ed. Editora GEN LTC, 2017, 600 p.

[46] L. F. Martha, "Ftool: a structural analysis educational interactive tool", in *Proc. Workshop Multimed. Comput. Tech. Eng. Educ.*, 1999, pp. 51–65.

[47] Associação Brasileira de Normas Técnicas, *Design Loads for Structures*, ABNT NBR 6120, 2019, 60 p.

[48] Associação Brasileira de Normas Técnicas, *Actions and Safety of Structures – Procedure*, ABNT NBR 8681, 2003, 18 p.

[49] W. C. Santiago, H. M. Kroetz, S. H. C. Santos, F. R. Stucchi, and A. T. Beck, "Reliability-based calibration of main brazilian structural design codes," *Lat. Am. J. Solids Struct.*, vol. 17, no. 1, pp. 1–28, 2020, http://dx.doi.org/10.1590/1679-78255754.

[50] Joint Committee on Structural Safety, *Probabilistic Model Code*, 2001. [Online]. Available: https://www.jcss-lc.org/jcss-probabilistic-model-code/

Author contributions: PF: resources, computer programming, data manipulation, writing original draft; ATB: conceptualization, funding acquisition, methodology, supervision, writing original draft, writing review and editing.

Editors: Mauro Real, Guilherme Aris Parsekian.

IBRACON Structures and Materials Journal
Revista IBRACON de Estruturas e Materiais
ISSN 1983-4195 ismj.org

ORIGINAL ARTICLE

Curved bridges live load bending moment distribution using straight and curved girders

Distribuição de momento fletor devido a carga móvel em pontes curvas utilizando longarinas retas e curvas

Arthur da Silva Rebouças[a]
José Neres da Silva Filho[b]
Rodrigo Barros[b]
Yngrid Rayane Freitas Nascimento[b]
Pedro Mitzcun Coutinho[b]

Received 11 September 2020
Accepted 20 August 2021

[a]Instituto Federal de Educação, Ciência e Tecnologia do Rio Grande do Norte – IFRN, São Paulo do Potengi, RN, Brasil
[b]Universidade Federal do Rio Grande do Norte – UFRN, Programa de Pós-Graduação em Engenharia Civil – PEC/UFRN, Natal, RN, Brasil

Abstract: The present study focuses on comparative parametric analysis of curved precast concrete bridges using straight and curved I-girders. The live load bending moment distribution for girders was studied using the bridge curvature and its relationship with the results obtained for a straight bridge. FEM 3D models were developed with restrictions on the transverse live load positions and with two different load models types: HL-93 (AASHTO) and TB-450 (NBR 7188, 2013). The parametric analysis results were calculated using the Modification Factor (MF) and the Bending Moment Distribution Factor (BMDF), calculated from the structural analysis of each model at the midspan. Globally, an increase was found in the total bending moment for the curved bridge models in relation to the straight bridge. In the examples herein studied, the larger the bending radius, the larger the maximal bending moment in the bridge center. For the external girders, the MF increases with the increase of the L/R. For the internal ones, the MF decreases with the increase of the L/R. In addition, the occurrence of "Load Shift" was different from the rigid body behavior, for there was demonstrated a different bending moment variation between external girder (G1) in relation to its adjacent (G2). Therefore, the structural behavior of straight (SG) and curved girders (CG) was analyzed, revealing that, in the SG, a significant gap occurred in the BMDF between G1 and G2 girders for all curvatures. For L/R = 0.6, it caused a difference of 17.8% in the BMDF between the G1 and G2 girders, while on the curved girders, a difference of only 6.6% was found.

Keywords: bridges, live loads, curvature, bending moment distribution, FEM.

Resumo: o presente estudo foca na análise paramétrica comparativa de pontes curvas utilizando utilizando longarinas retas e curvas pré-moldadas. As análises foram baseadas na distribuição transversal de momento fletor para a longarinas, na variação da curvatura da ponte e na relação desses parâmetros com os resultados obtidos em uma ponte reta. Foram desenvolvidos FEM 3D models com restrições nas posições transversais da carga-móvel e com dois tipos diferentes de modelos de carga: HL-93 e NBR 7187. Os resultados da análise paramétrica foram determinados utilizando o Fator de Modificação (FM) e o Fator de Distribuição de Momento Fletor (FDMF), calculadas a partir da análise estrutural de cada modelo na posição longitudinal do meio do vão. No âmbito global, contatou-se um aumento do momento fletor total nos modelos de ponte curva em relação à reta. Nos exemplos estudados, quanto maior o raio de curvatura, maior foi o momento fletor máximo no meio do vão da ponte. O valor de FM varia linearmente. Para as longarinas externas o

Corresponding author: Arthur da Silva Rebouças. E-mail: arthur.reboucas@ifrn.edu.br
Financial support: None.
Conflict of interest: Nothing to declare.

FM aumenta com o aumento do L/R, já para as internas, o FM diminui com o aumento do L/R. Além disso, foi comprovada a ocorrência de "Load Shift" diferente do comportamento de corpo rígido, tendo em vista a variação diferenciada de momento fletor para a longarina externa G1 em relação a sua adjacente G2. Constatou-se uma diferença considerável de comportamento estrutural entre as longarinas retas e curvas, tendo em vista que nas SG ocorreu uma diferença significativa de FDMF entre a longarina G1 e a G2 para todas as curvaturas, o que não ocorreu para as CG. Para L/R=0.6, observou-se uma diferença de 17.8% no FDMF entre as longarinas G1 e G2 retas, já nas longarinas curvas, a diferença foi de apenas 6.6%.

Palavras-chave: pontes, cargas móveis, curvatura, distribuição de momento fletor, Método dos Elementos Finitos.

How to cite: A. S. Rebouças, J. N. Silva Filho, R. Barros, Y. R. F. Nascimento, and P. M. Coutinho, "Live Load Radial Moment Distribution for curved bridges using straight and curved girders," *Rev. IBRACON Estrut. Mater.*, vol. 15, no. 2, e15208, 2022, https://doi.org/10.1590/S1983-41952022000200008

1. INTRODUCTION

According to the World Economic Forum [1], the number of cars in the world was 1.1 billion. It is expected that this number will continue to grow, possibly doubling until 2040, reaching over 2.0 billion. In such a scenario, more robust and efficient transportation logistics is required, which must be met by building roads, railroads, bridges, and viaducts. In large cities, the need for mobility and the difficulty of interposing obstacles in restricted spaces makes the specification of bridges and curved viaducts designs frequent.

Previously, according to Amorn et al. [2], curved bridges were usually built using a set of straight rails, forming a sequence of straight stretches within the curve. The fabrication of curved rails in the plane was very laborious, costly, and the structural analysis of this type of geometry was considered complex. Nowadays, with the development of the manufacturing equipment and industry, the curvature in the plane does not impose as many difficulties. In addition, in relation to structural analysis, the advance of software tools allows the modeling and analysis of curved bridges in a relatively simple manner.

According to Alawneh [3], in the last thirty years, steel girder bridges have dominated the construction of curved bridges due to advantages such as speed of construction, relative flexibility and light weight. However, the prestressed concrete girders bridges are a viable alternative since they are widely used in bridges with straight longitudinal design and are considerably stiffer than steel ones.

Hence, the present study focuses on the parametric comparative analysis of bridges with curved longitudinal layout using prefabricated "I" section, straight girders, and curved ones. The analyses were based on the cross-sectional distribution of the girders bending moment, the variation of the bridge curvature and the relationship of these parameters with the results obtained in a straight bridge. The results were obtained from 3D models executed with restrictions on the transverse positions of the live load and applying two different vehicle types. They indicated several advantages in the structural behaviour of curved girders compared to straight girders.

2. STRUCTURAL BEHAVIOR OF CURVED BRIDGES

The bridge with curved longitudinal layout has different structural behaviour from the straight due to the center of gravity's position being located outside the line connecting the extreme supports, generating an eccentricity in relation to this axis, and consequently an overall torsional trend around the supports (Figure 1). The main property of the superstructure of curved bridges is curvature, which can be measured as the ratio between the arc length of the bridge centerline (L_a) and the radius between this arc and the center (R). According to PCI Bridge Design Manual [4], although it is an arch, the center of gravity of the surface of bridge deck is different from the center of gravity of an arch due to the portion of area on the part of the deck that is above the center line. This portion of area is larger than the lower portion, moving the center of gravity closer to the center line and increasing the eccentricity in relation to the line connecting the supports.

In addition, due to the eccentricity between the CG of the bridge and the line connecting the supports, the torsion will be maximum in the supports, which generates the need to design supports that have torsional stiffness.

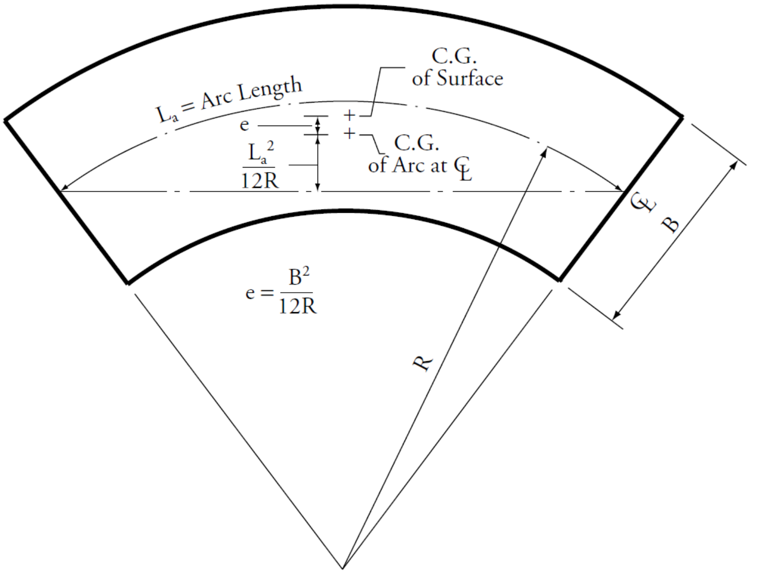

Figure 1. Geometric Properties of a curved bridge deck. PCI Bridge Design Manual [4].

Accordingly, for any load applied in the vertical plane, bending and torsion forces arise in a coupled way, along the structural element. This interaction between torsion and bending is mandatory, since it comes from the equilibrium conditions of a curved beam element, which in this case represents the global equilibrium of the bridge. Figure 2 shows an infinitesimal element of a curved beam loaded only in the normal direction to the horizontal plane, as well as the internal forces generated by this loading. Equations (1), (2) and (3) denote the structural behavior of a curved beam element. Equations (1) and (2) depend directly on the radius of curvature (R)

$$\frac{dV}{ds} = -p \quad (1)$$

$$\frac{dM}{ds} = V - \frac{T}{R} \quad (2)$$

$$\frac{dT}{ds} = t + \frac{M}{R} \quad (3)$$

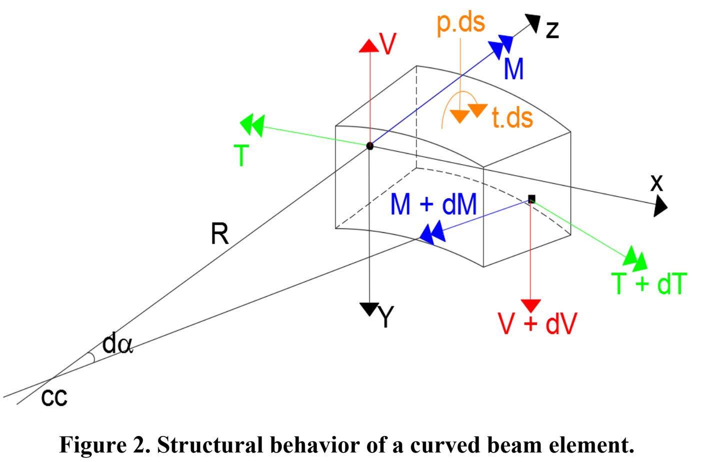

Figure 2. Structural behavior of a curved beam element.

3. EXISTING SYSTEMS FOR CURVED PRECAST CONCRETE GIRDERS BRIDGES

To design prestressed concrete curved bridges the designers can use various structural configurations. In bridges with open cross section, in most cases, straight beams are used within the curved bridge layout due to their simplicity of construction. However, it is also possible to use precast concrete curved girders for this layout. As already mentioned, Alawneh [3] developed a methodology for the construction of precast concrete curved girders with straight sections connected in predefined positions to achieve the desired curvature. Figure 3 shows the proposed geometry.

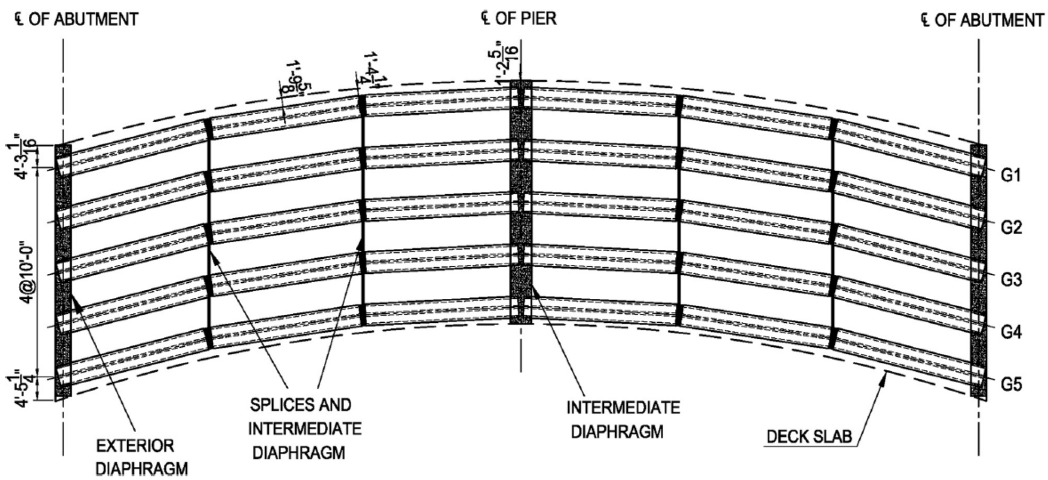

Figure 3. Geometry of Curved Precast Concrete Girders Bridges. Alawneh et al. [3]

According to Cho et al. [5], the application of curvature in precast prestressed concrete girders is very advantageous, since the steel girders, mostly used in this type of curved layout, have low stiffness to warping. Another factor that contributes to the use of concrete girders is better stability during assembly compared to steel girders.

4. BENDING MOMENT DISTRIBUTION PARAMETERS IN CURVED BRIDGES

In bridges with more than two girders, the distribution of internal forces depends on the stiffness of the structural elements. It was initially decided to investigate which are the main factors influencing the bending moment distribution for the curved bridges girders, especially regarding the magnitude of the effect that is allocated to each of them.

Brockenbrough [6] tested the impact of several parameters on the distribution of effort in open section curved bridges and concluded that variations in the girder stiffness and in the spacing of the diaphragms have a small effect on this distribution, but that the central angle per span, which includes the combined effect of curvature and span length, and the girders spacing, have the greatest effects. Kim et al. [7] pointed out that the key parameters to study the distribution of bending moment in curved bridges are the radius, the girders spacing, the span length and the spacing between the diaphragms.

Therefore, it was decided to focus on the curvature (relation between span length (L) and radius (R)) according to Figure 1, varying it within limit parameters and fixing all other parameters mentioned above, to analyze the direct impact of the curvature on the bending moment distribution for each girder

5. MODELS

A curved bridge is basically a straight bridge to which an eccentricity applied in relation to the line connecting the extreme supports. In most cases, this curvature is imposed using a fixed curvature along the entire length of the bridge.

The AASHTO [8] defines that the central angle of the bridge should vary from 12° to 34°, due to the limitation of torsion stiffness in open sections. These conditions were used as the basis for the development of the models under study. Four groups of bridge models were created maintaining all physical and geometric parameters while varying solely the curvature (L/R).

In each curved bridge model, straight girders (SG) and curved girders (CG) geometries defined with the same height and cross section were applied. In addition, a bridge model with straight longitudinal layout (SB) was used as a reference for the comparative analyses that were performed. In this group, only one model was created, with the same cross section as the curved bridge models. All models are shown in Table 1.

5.1. Materials

The same material properties, defined according to current design practices, were used in all models. The structural analysis was carried out in the linear static analysis, with the properties adopted for all models presented in Table 2.

Table 1. Structural analysis models

L/R	Central angle	Girders Geometry
0.2	12°	Straight Girder (SG)
	12°	Curved Girder (CG)
0.4	23°	Straight Girder (SG)
	23°	Curved Girder (CG)
0.6	34°	Straight Girder (SG)
	34°	Curved Girder (CG)
0	∞	Straight Bridge (SB)

Table 2. Materials Properties

Concrete	
Compressive strength of concrete	40 MPa
Modulus of elasticity	31870 MPa
Poisson's Ratio	0.2
Specific Weight	25 kN/m^3

5.2. Geometry

Figure 4 shows the adopted cross section and their geometric characteristics, calculated using the CSIBridge v17 structural analysis software. The parameters in Figure 4 correspond to: (a) Area of the entire cross section (A); (b) Polar Moment of Inertia (J); (c) Moment of inertia in relation to the y-axis of the center of gravity (Iycg); (d) Moment of inertia in relation to the z-axis of the center of gravity (Izcg); (f) Section center of gravity's position, in the y direction (ycg) and (g) Section center of gravity's position, in the z direction (zcg).

A (m^2)	J (m^4)	Iy_{cg} (m^4)	Iz_{cg} (m^4)	Y_{cg} (m)	Z_{cg} (m)
6.3250	0.1893	3.5641	122.8937	7.50	-1.5293

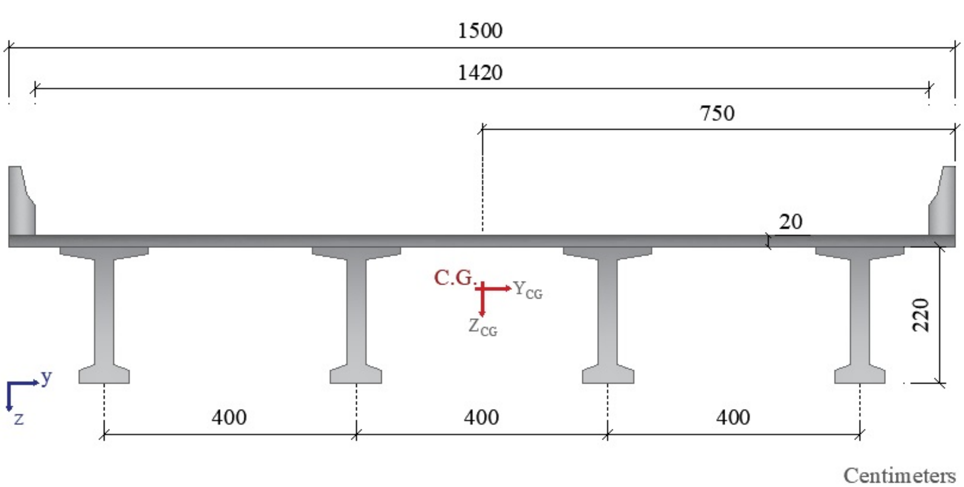

Figure 4. Cross section and geometric parameters.

Regarding the evaluation of the stiffness of the cross-section, the paving surface of the bridge and the area related to the protective barriers were not considered. The cross-section has an overhang equal to 1.50 meters, measured from the axis of the outer beam to the ends of the slab.

In the curved bridge models, the longitudinal layout of the deck follows the center line ("layout line") of the bridge, maintaining a fixed radius. The girders were numbered from the external part to the curve, that is, the external girder was named G1 and the internal one G4 (Figure 5).

All models have a midspan diaphragm, measuring 1.80m high and 0.30m wide, due to the need for its insertion to ensure efficiency in the bending moment distribution and the overall balance of the structure.

5.3. Bearings and boundary conditions

The model used was the one proposed by Samaan et al. [9], maintaining the girders directly supported on the abutments using restricting only the vertical translation. Two of the girders have different restrictions (Figure 6). Thus, when evaluating the whole bridge , it is possible to consider an overall restriction of rotation of torsion, since all support devices prevent vertical translation.

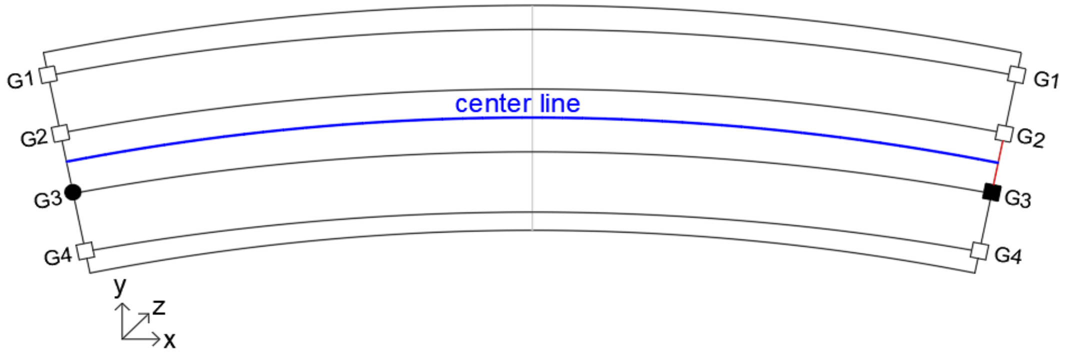

Figure 5. Bridge deck superior view and girder’s identification.

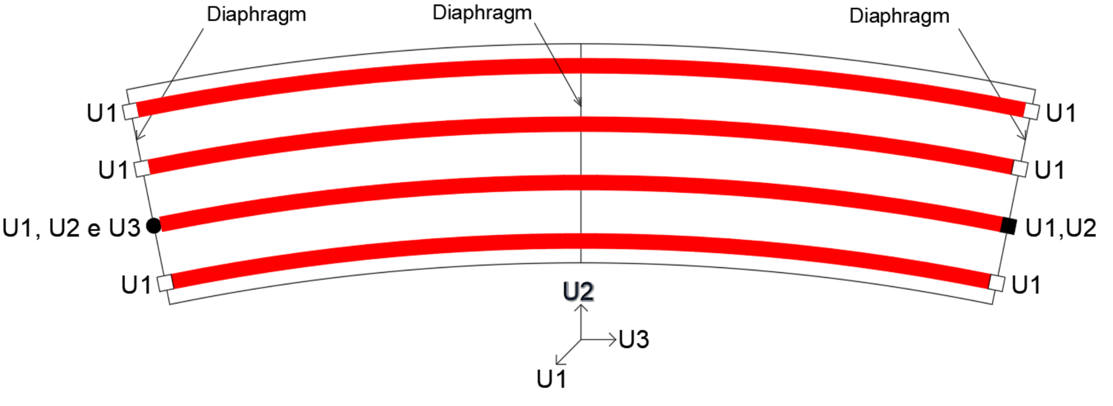

Figure 6. Boundary conditions.

5.4. Load cases

In this study two types of live loads were considered: the HL-93 (Figure 7) used by AASHTO [8] and the TB-450 (Figure 8) defined by ABNT NBR 7188 [10], applied to the deck using only mobile concentrated loads, without crowd loading.

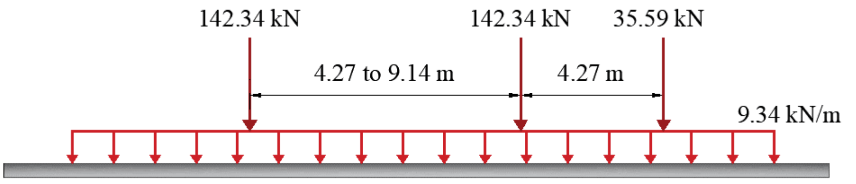

Figure 7. Vehicle type HL-93

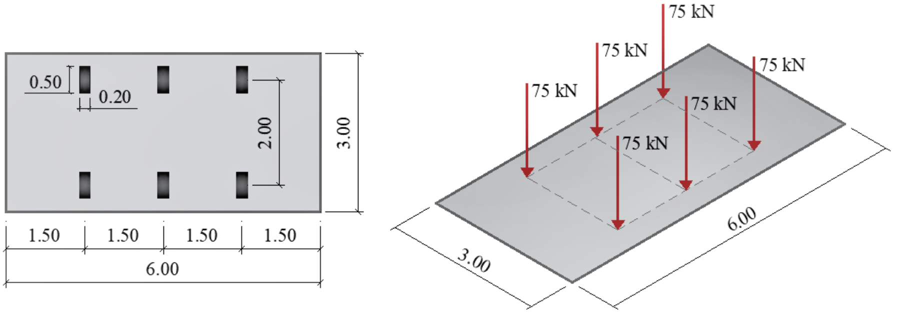

Figure 8. Vehicle type TB-450. Adapted by ABNT NBR 7188 [10].

To verify the impact of the passage of the vehicles in restricted regions, four types of load cases have been developed, named: general load case and load cases 01, 02 and 03. It should be noted that in the general load case, the vehicle-type walked, both in the transverse and longitudinal direction, all over the bridge deck. For this, a usual procedure of passing the vehicle type in the width of the load line predefined by the software CsiBridge v17 was used. A width of 14.2 meters respecting only the transverse application limitations of each standard vehicle was defined to delimit the crossing area of the vehicle. The general load case provided the bending moment envelops, from the influence surface. For this case, the maximum bending moment on the girders during the passage of the standard vehicle throughout the bridge was obtained.

In complement, to be able to compute exactly the bending moment portion captured by each girder in relation to the total obtained on the bridge, the vehicle-type was fixed in certain transverse positions, varying from position only along the length of the bridge. Each loading's position case can be seen in Figure 9.

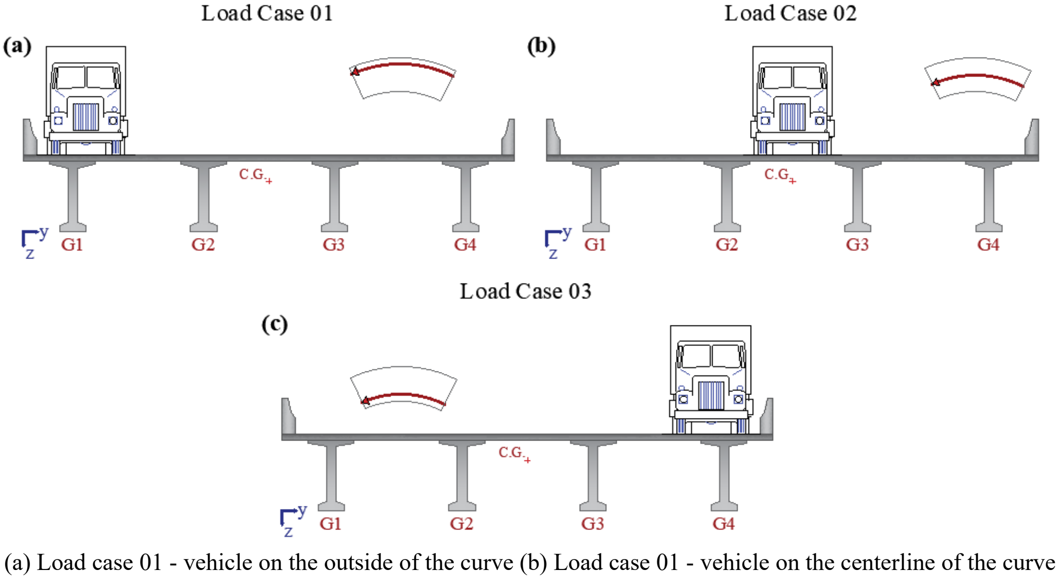

Figure 9. (a) Load case 01 - vehicle on the outside of the curve (b) Load case 01 - vehicle on the centerline of the curve (c) Load case 03 - vehicle on the inner side of the curve.

6. 3D FEM MODELS

The numerical modeling of this study (Figure 10 and Figure 11) was based on the 3D model proposed and validated by Cho et al. [5], similar to those proposed by Nevling et al. [11] in the level 2 model and by Kim et al. [7], which uses shell elements (four nodes and six degrees of freedom at each node) for the deck and frame elements (with two nodes and six degrees of freedom at each node) for the girders, connected by rigid links.

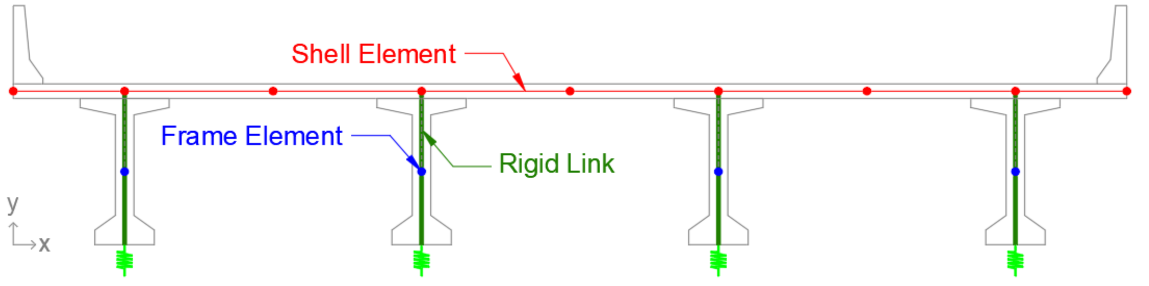

Figure 10. Numerical modeling discretization of bridge cross section.

The numerical modeling of this research was done with the CsiBridge v17 software. Since the aim was to analyze the bending moment transverse distribution in curved bridges, the decision was to use linear three-dimensional models, due to its good precision in relation to field tests, already tested by other researchers and mainly due to its capacity of concise visualization of the results.

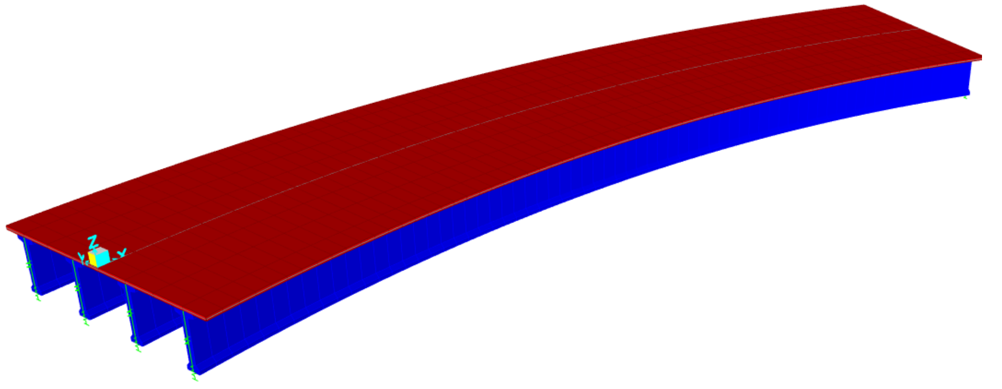

Figure 11. Example of a 3D finite-element bridge model used in the analysis

In all models a maximum element length of 1.20 meters in the longitudinal direction of the bridge was defined, maintaining the aspect ratio of the element at a maximum of 2.50, since the use of smaller elements implied a high computational effort with low precision gains. Thus, the element length was within the limits suggested by Fu and Wang [12] and Fatemi et al. [13].

7. PARAMETRIC ANALYSIS

The results of the parametric analysis were determined in two methods: using the Modification Factor (MF) like that proposed by Acosta et al. [14], as well as the Bending Moment Distribution Factor (BMDF), calculated from the structural analysis of each model in the middle of the span.

7.1. Modification Factor (MF)

The Modification Factor (MF) was obtained by the relationship between the maximum bending moment of the curved bridge on the study girder (Mc) and the maximum bending moment of the straight bridge on the study girder (Ms). This analysis factor aims to contribute as a design reference factor, where it would be possible to obtain an estimated maximum bending moment value in the curved bridge using the maximum moment obtained in a straight bridge model, with equivalent dimensions (same cross section and same span length).

$$MF = \frac{Max.\,girder\,bending\,moment\left(curved\,bridge\right)}{Max.girder\,bending\,moment\left(straight\,bridge\right)} = \frac{M_c}{M_s} \quad (4)$$

7.2. Bending Moment Distribution Factor (BMDF)

The Bending Moment Distribution Factor was calculated through the relationship between the bending moment results in the middle of the span (critical longitudinal section) for each girder, obtained through 3D models, and the bending moment results for the cross section, obtained through a spine model with equivalent stiffness, in the same critical section, submitted to the same live loads. This analysis method was used to understand the radial bending moment distribution for each bridge girder.

$$BMDF = \frac{Bending\,moment\,in\,the\,curved\,girder}{Total\,Bending\,moment\left(cross\,section\right)} = \frac{BM_{3D,\,girder}}{BM_{1D,total}} \quad (5)$$

8. PARAMETRIC RESULTS ANALYSIS

8.1. Global Analysis

Initially analyzing the bending moment values in the global scope, an increase in the total bending moment (sum of the bending moments of the 4 girders) was observed in the models of curved bridge in relation to the straight line. In the examples studied, with an increase in the radius of curvature, the maximum bending moment in the middle of the bridge span was greater. The results obtained corroborate those found by Nevling et al. [11] and Cho et al. [5]. This is due to the portion of torsion coupled to the bending moment, arising from the balance formulations of a curved bridge. Thus, the torsion amplifies the bending moment making it larger than the bending moment in a straight bridge of the same total length.

Regarding the transverse position of the vehicle, it was observed from the load cases studied (01, 02, 03 and general) that the maximum bending moment values on the girders G1 and G2 occurred when the vehicle was in loading position 01 and on the girders G3 and G4 when the vehicle was in loading position 03 for all curved bridge models. That is, regardless of the radius of curvature, the loading migrated to the girders closest to it. This result guided the analysis, because it was possible to define the use of the general load case to obtain the maximum bending moment in the girders. On the other hand, the load cases 01, 02 and 03 were used in the bending moment distribution analysis, to study the behavior of the bridge with respect to the radial distribution.

8.2. Modification factor results comparison for curved and straight girders

The difference in the Modification Factor (MF) between the two types of girders can be seen in the graphs of Figures 12-15, which show the curvature values on the horizontal axis and their corresponding MF value on the vertical axis. Figure 12 shows the values for the external girder (G1) and internal girder (G4) for the two types of girders geometry used in the curved bridge. In both cases a linear growth was observed in the MF value. For the external girders, the MF increases with the increase of the curvature (L/R), while for the internal girders, the MF decreases with the increase of the L/R. This behavior is consistent with the results found by Zhang et al. [15] and Acosta et al. [14]. Therefore, it was possible to verify that even with the application of different vehicle-types (TB-450 and HL-93) and with the use of different girders geometries (straight and curved) the behavior was maintained.

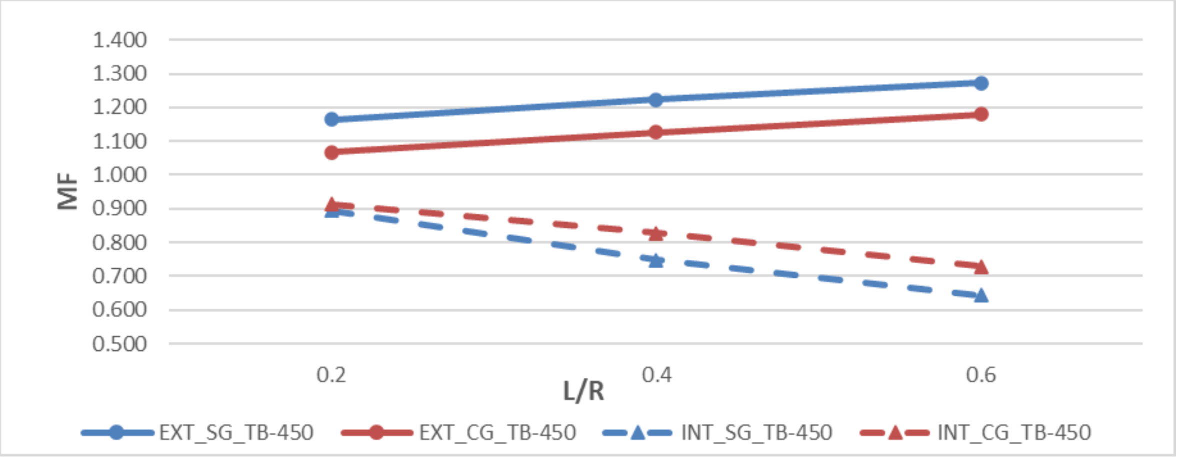

Figure 12. MF growth in relation to the external (G1) and internal (G4) girders.

The MF values for straight girders were higher than for curved girders. Figure 13 shows that the straight girder of the bridge with L/R equal to 0.6 had an MF equal to 1.273. A difference of approximately 0.10 was then observed between the girders with the same corresponding L/R. This difference is probably due to the greater overhang in the straight ones, which increases the negative bending moment in the deck slab, boosting the torsion in the outer girder. The latter is considerably impacted due to the coupling between torsion and bending moment. This indicates that the use of straight girders in bridges with curved layout can have a higher material consumption than the use of curved girders, for all the usually practiced radius, since from the maximum bending moment the passive and active reinforcement of the girders are dimensioned. In addition, this increase in consumption will be multiplied by four, since all the elements of the bridge will be sized for that same maximum bending moment, resulting in a significant reflection in the total cost of the bridge.

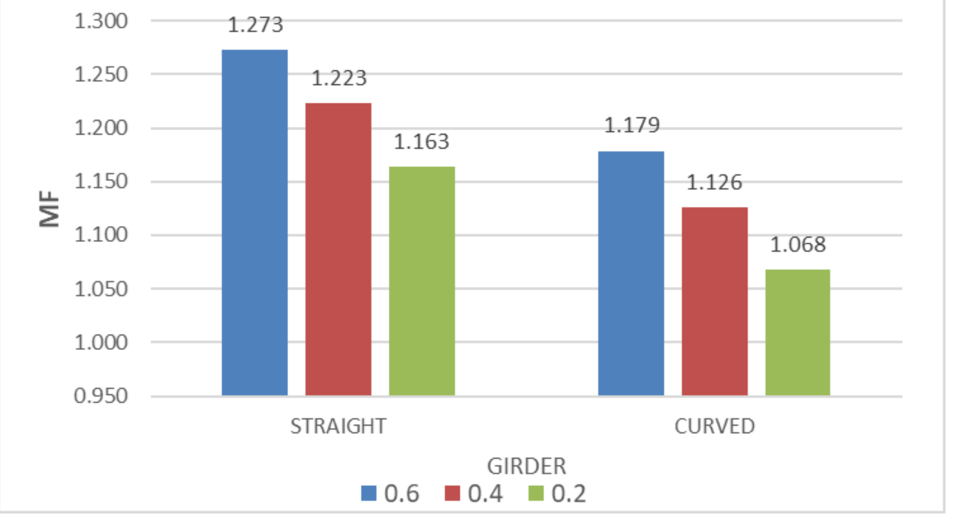

Figure 13. MF growth with vehicle type TB-450 for the most loaded girder (V1).

8.2.1. Comparison between HL-93 and TB-450 using the Modification Factor (MF)

The maximum values of the Modification Factor (MF) for all bridge models were compared with the HL-93 and TB-450 vehicles. The graphs in Figures 14 and 15 show the values found for the vehicle type HL-93 as well as the comparison between the values obtained for both.

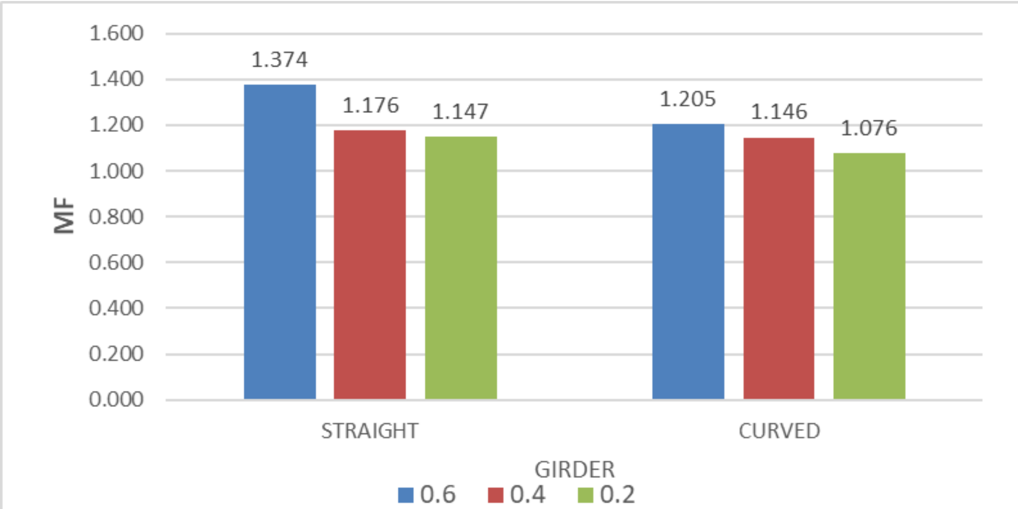

Figure 14. MF growth with vehicle type HL-93 for the most loaded girder.

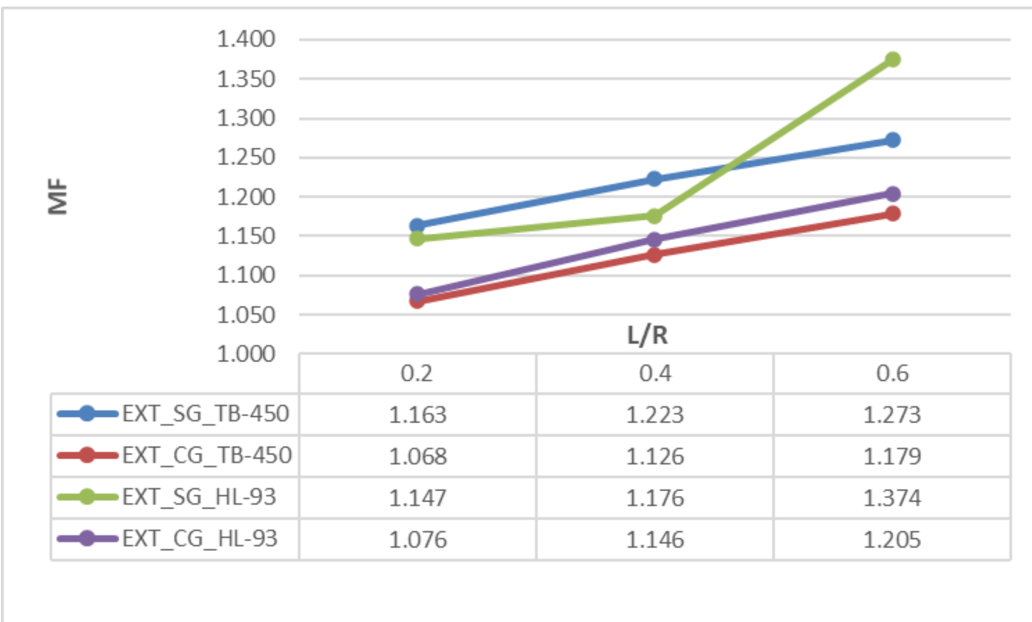

Figure 15. Comparison between HL-93 and TB-450 for the most loaded girder (V1).

It was found from these results that HL-93 generally provided greater bending magnitudes than TB-450. Moreover, the growth of the MF values for the HL-93 did not remain linear for the cases of L/R studied, however, in all results, the values of MF were higher for SG in relation to CG.

8.3. Bending moment distribution for the girders (BMDF)

To analyze the bending moment distribution for the girders and later compare the structural behavior between straight and curved girders, the vehicle was positioned at both ends (load cases 01 and 03) and at the center of the bridge (center of gravity of the cross section), load case 02. The Bending Moment Distribution Factor (BMDF) was used as parameter.

For load case 01 (Figures 16-18) the BMDF values for girders G1 and G2 in the curved bridges were higher than those obtained in the straight bridge. For girders G3 and G4, there was a reduction in BMDF values in relation to the straight bridge. Except for the girder G3 for L/R=0.4 and 0.6, there was a small increase of BMDF in relation to the straight bridge. A greater uniformity was also observed (less difference between girders) in the BMDF values for CG, when compared to SG, mostly between girders G1 and G2 (Figure 19).

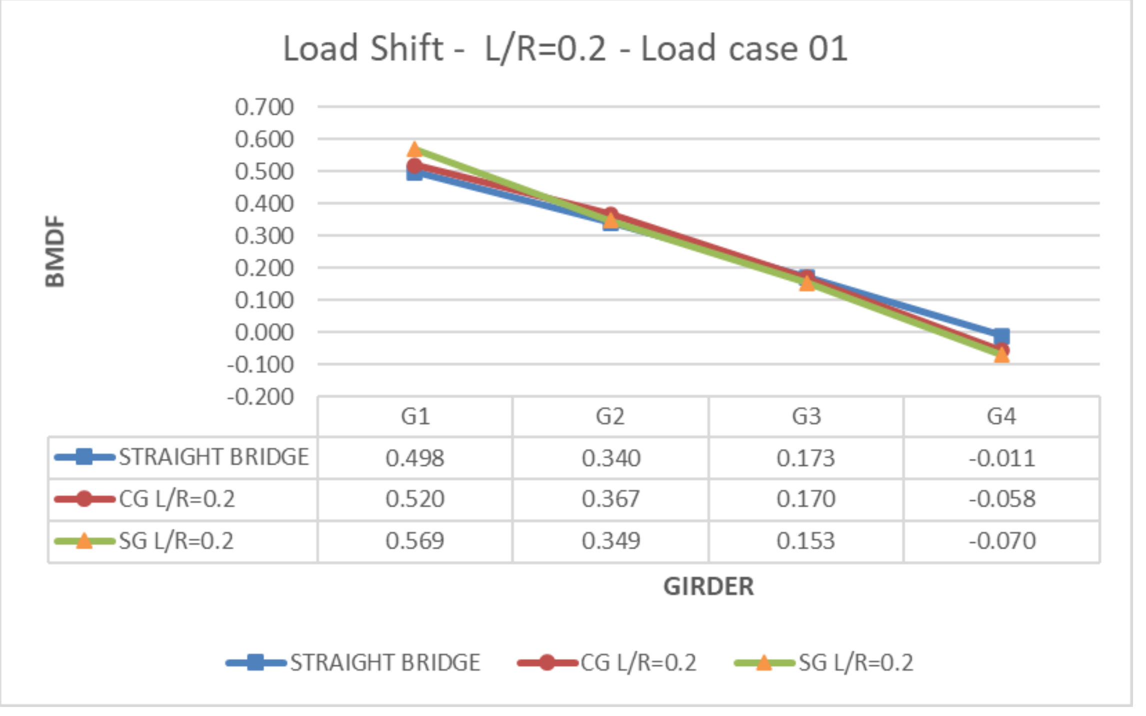

Figure 16. BMDF comparison between straight-bridge girders and curved and straight girders of 0.2 curvature and load-case-01-bridges.

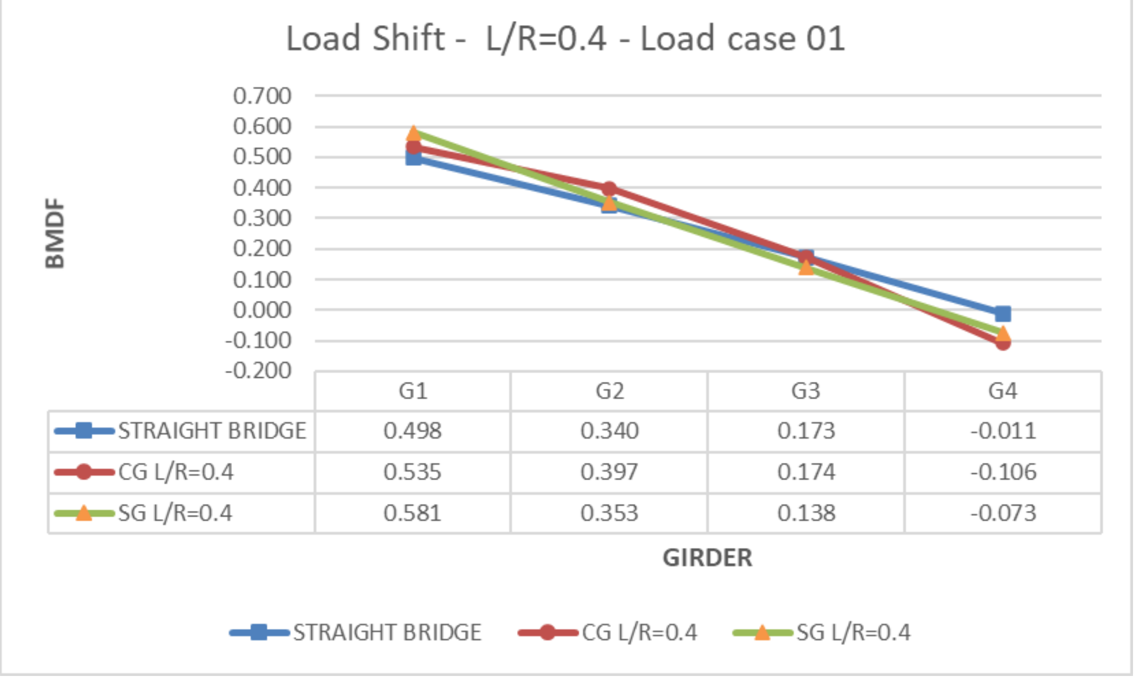

Figure 17. BMDF comparison between straight bridge girders and curved and straight girders of 0.4 curvature and load case 01 bridges.

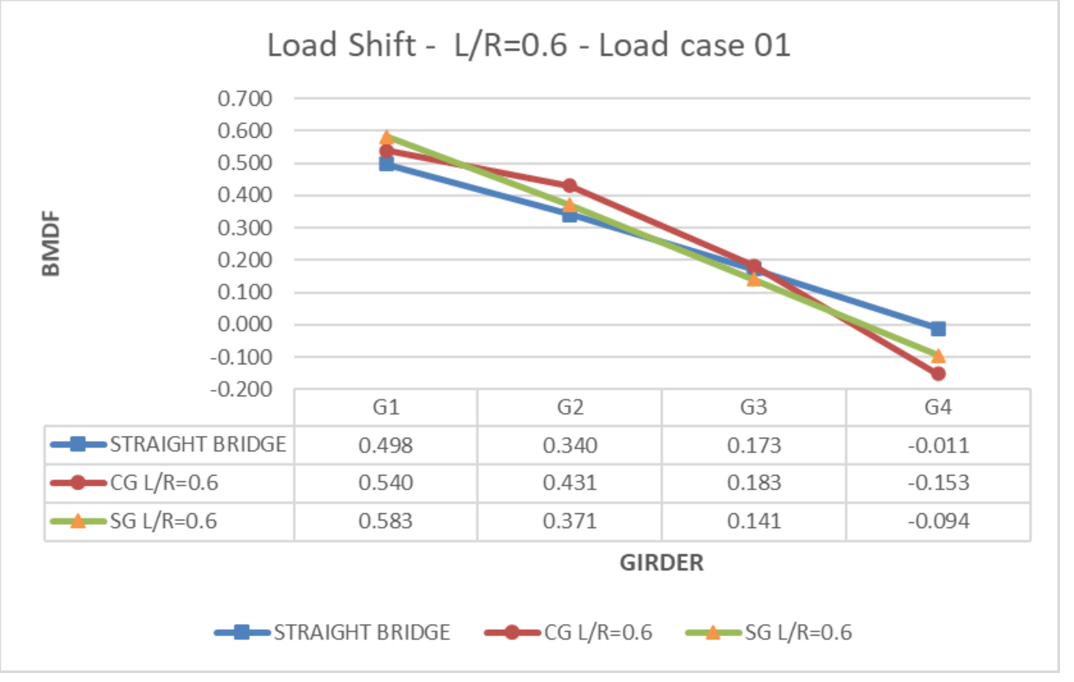

Figure 18. BMDF comparison between straight-bridge girders and curved and straight girders of 0.6 curvature and load-case-01-bridges.

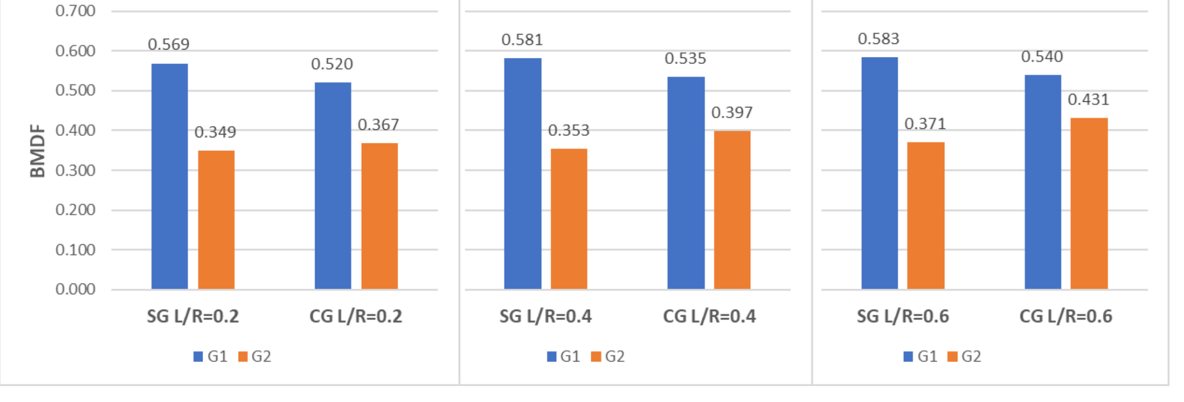

Figure 19. BMDF comparison between straight and curved girders for all studied curvatures.

In load case 03 (Figures 20-22) a different behavior from load case 01 was observed, as the BMDF values on the girders closest to the vehicle crossing region (G3 and G4) were reduced compared to the BMDF values on the straight bridge. Moreover, it was observed that with the increase in curvature a reduction in BMDF of G3 and G4 and an increase in G1 and G2 occurred. This structural behavior is not observed in bridges with straight geometry and needs attention, considering that in curved bridges with heavy curvature a tendency of uniformity may occur between the BMDF of all the girders of the cross section, even with a vehicle fixed in the inner region of the curve.

Still relative to load case 03, it was found that the BMDF values for the SG external to the curve (G1 and G2) were higher than the BMDF of the CG for all curvatures studied. In the internal stringers (G3 and G4) the opposite behavior was observed. This confirms the tendency already observed in the Modification Factor (MF) analysis, where the SG presented maximum bending moments higher than CG in these girders. In a certain way, it establishes a relationship between the two types of analysis with different parameters.

Figure 20. BMDF Comparison between straight bridge girders and both straight and curved girders from 0.2 curvature bridges on load case.

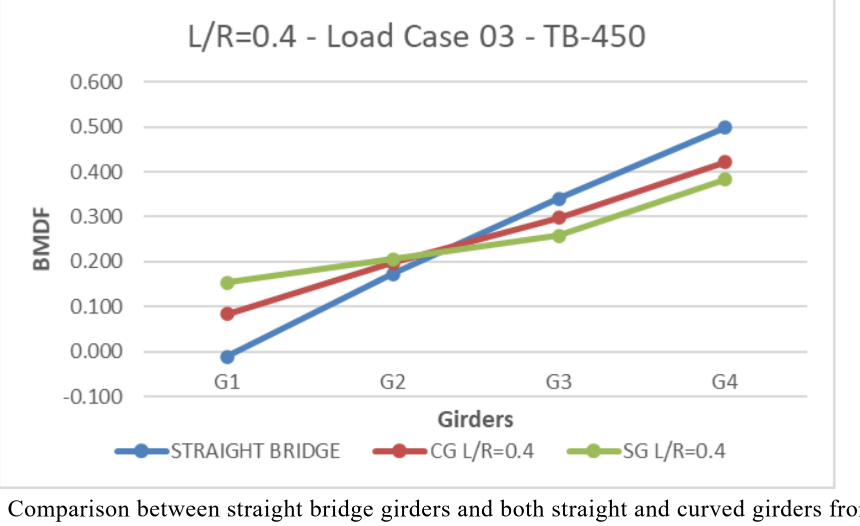

Figure 21. BMDF Comparison between straight bridge girders and both straight and curved girders from 0.4 curvature bridges on load case.

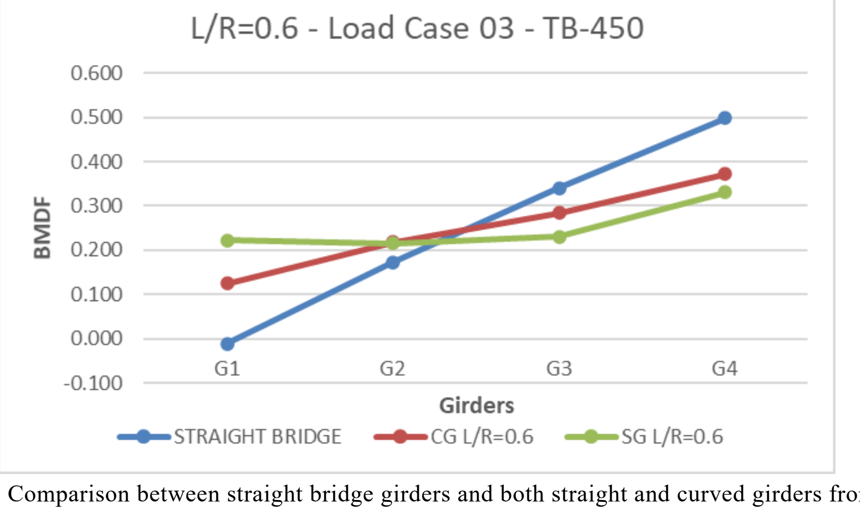

Figure 22. BMDF Comparison between straight bridge girders and both straight and curved girders from 0.6 curvature bridges on load case 03.

On the load 02 case for the straight bridge, it was found that approximately 25% of the total bending moment of the bridge was distributed for each of the girders, that is, there was an equal distribution. However, as shown in Figure 23, when we observed the studied curve bridge models the largest portion of the bending moment is intended for the external girder (G1), which corresponds to the studies of Kim et al. [7], Barr et al. [16] and Acosta et al. [14]. This probably occurs due to the eccentricity in relation to the center of gravity of the deck; the greater length of this girder in relation to the others, and the greater portion of area around its extension.

Moreover, from Figure 23 it was observed that there was an increase in the portion of the bending moment in the outer girder with the increase in the curvature. In the curved bridge with lower L/R, for example, there was an increase of 4% in the bending moment in the outer girder, even with an increase in the total bending moment of only 2%.

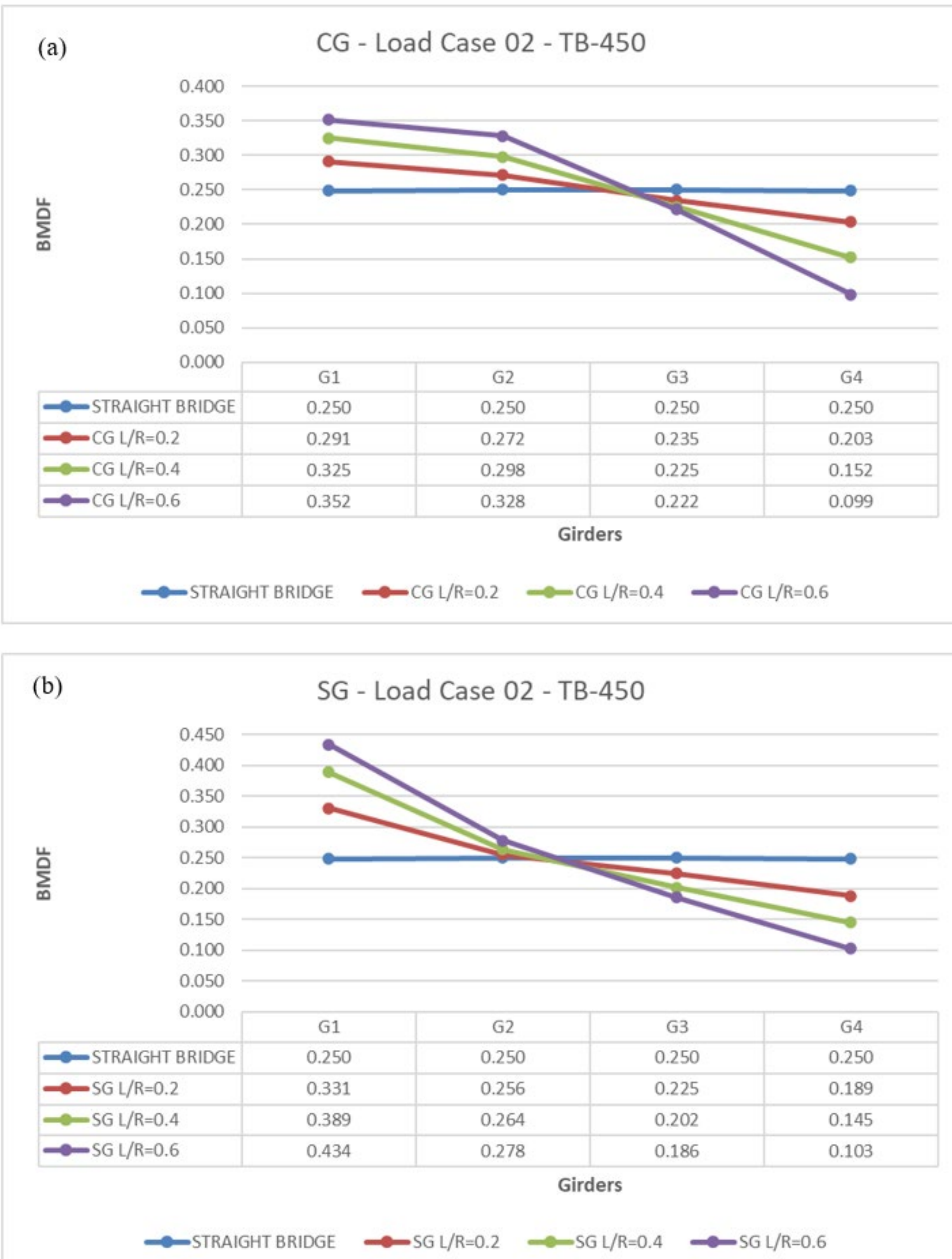

	G1	G2	G3	G4
STRAIGHT BRIDGE	0.250	0.250	0.250	0.250
CG L/R=0.2	0.291	0.272	0.235	0.203
CG L/R=0.4	0.325	0.298	0.225	0.152
CG L/R=0.6	0.352	0.328	0.222	0.099

	G1	G2	G3	G4
STRAIGHT BRIDGE	0.250	0.250	0.250	0.250
SG L/R=0.2	0.331	0.256	0.225	0.189
SG L/R=0.4	0.389	0.264	0.202	0.145
SG L/R=0.6	0.434	0.278	0.186	0.103

Figure 23. BMDF variation with curvature. Load Case 02 (a) Curved girders, (b) Straight girders.

This confirms the occurrence of Load Shift in curved bridges for the bending moment, as emphasized in Guidelines for steel girder bridge analysis [17]. However, observing the results found, a rigid body behavior was not obtained, considering the differentiated variation of the bending moment for the external girder G1.

For this placement, it was observed a considerable difference in structural behavior between the straight and curved girders, considering that in SG there was a significant difference in bending moment between the girder G1 and G2 for all curvatures, which did not occur for CG. One can observe on Figure 24, for L/R=0.6, a difference of 17.8% between the straight girders G1 and G2, while for the curved girders, the difference was only 6.6%. In addition, it was observed from Figure 24 that there was a reduction of this difference with the reduction of the curvature. This structural behavior is quite favorable for CG, because a more uniform bending moment distribution is obtained between the girders, mainly regarding the condition of the bridge in service, aiming at the maintenance and prevention of cracks.

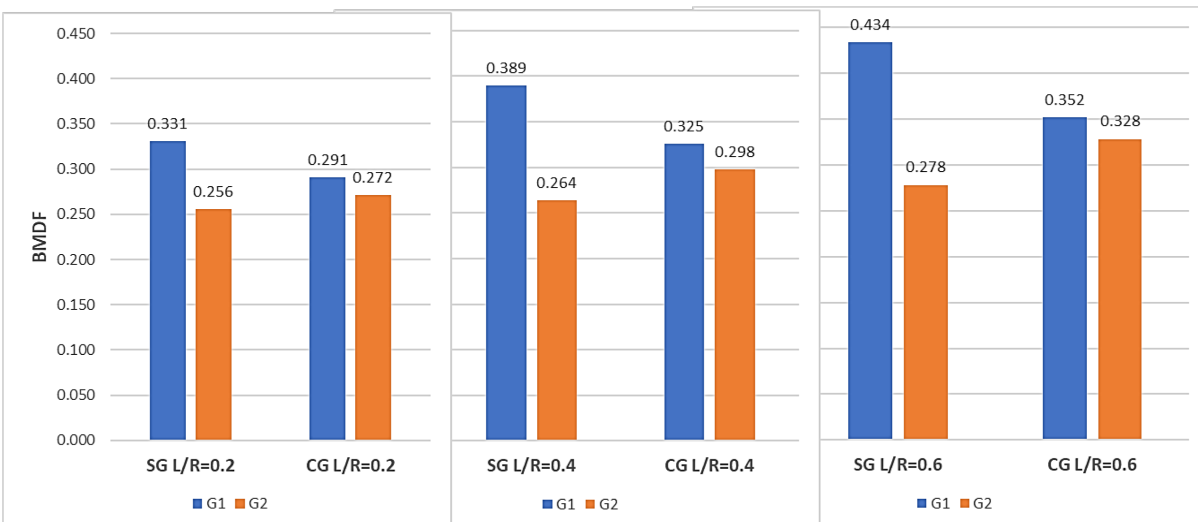

Figure 24. BMDF Comparison between straight and curved girders (V1 and V2) for all studied curvatures on load case 02.

When the relationship of this impact on all the cross-sectional beams was assessed, the graphs of Figures 25-27 were obtained, which show the bending moment distribution for bridges with SG and CG of the same L/R, comparing them with the straight bridge.

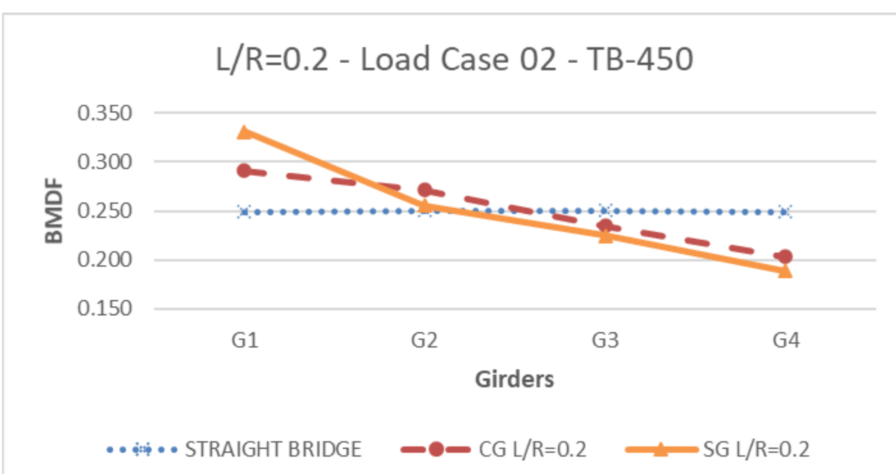

Figure 25. BMDF comparison between straight bridge girders and curved and straight girders from 0.2 curvature bridges on load case 02.

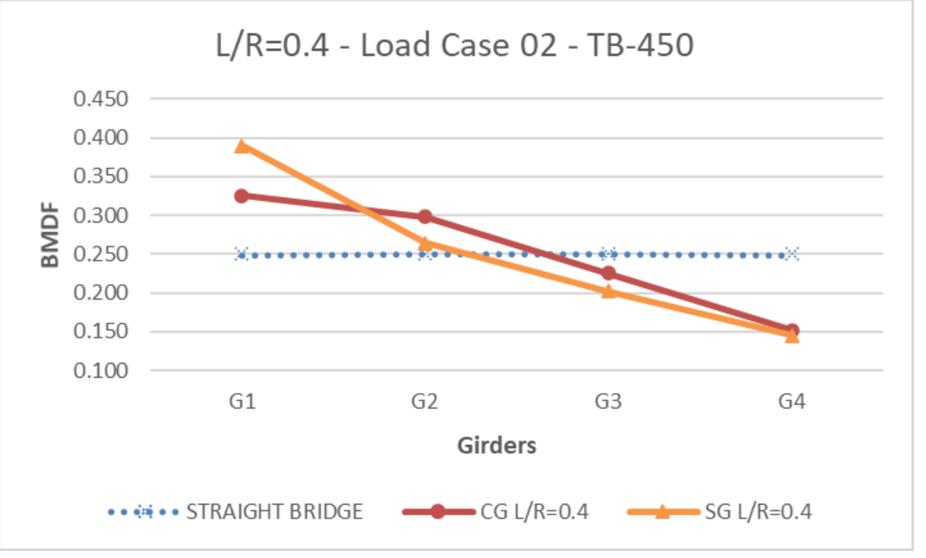

Figure 26. BMDF comparison between straight bridge girders and curved and straight girders from 0.4 curvature bridges on load case 02.

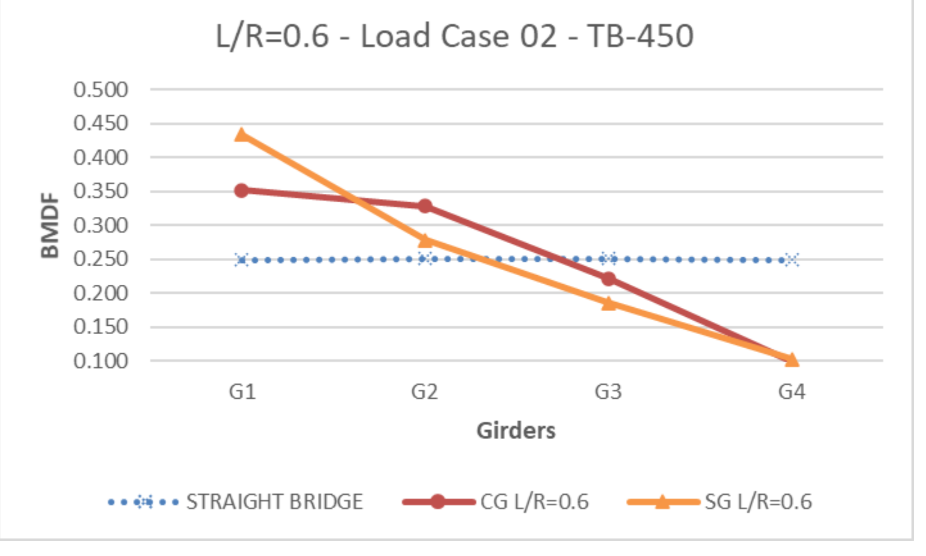

Figure 27. BMDF comparison between straight bridge girders and curved and straight girders from 0.6 curvature bridges on load case 02.

8.3.1. Comparison between HL-93 and TB-450 using MF

BMDF results for HL-93 were also analyzed and compared with those obtained by TB-450 (Figures 28-30). For all curvatures studied, as well as the two types of girders (SG and CG), the values obtained for G1 with HL-93 were higher than those obtained with TB-450. However, for the other girders the behavior of the bending moment distribution between the two types of vehicles underwent variations without a clear observable tendency.

As the load shift of the bending moment to the external girders on the curve, it was found that this behavior was maintained even with the use of HL-93, since even applying the loading to the central line of the bridge (middle of the cross section), the largest portion of the bending moment found by BMDF was precisely for the G1, in all curvatures studied. Moreover, even in this study, where the distribution was studied, it was found that this portion of BDMF grew with the increase in curvature, which resembled the results of the trend for MF found previously.

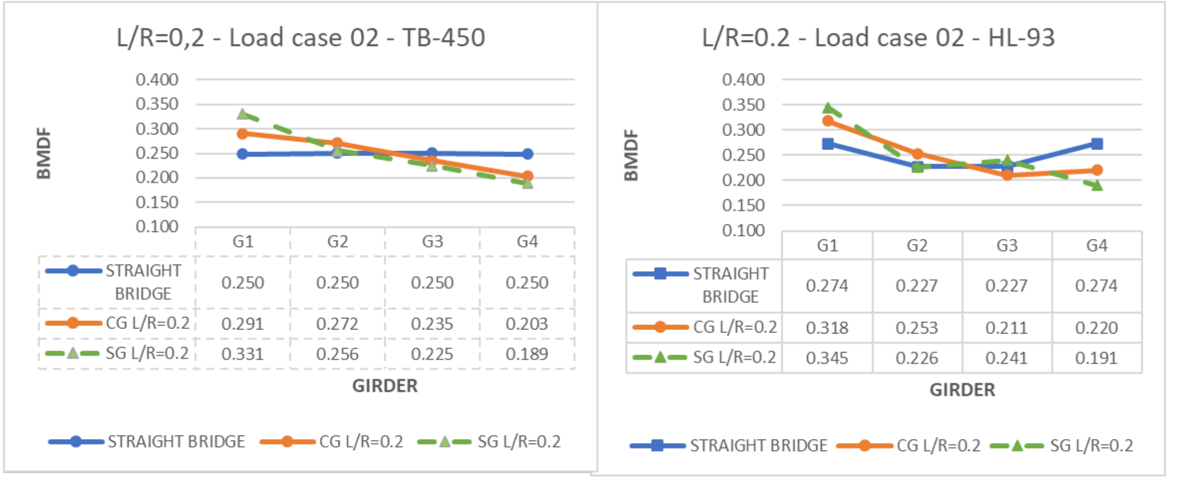

Figure 28. TB-450 and HL-93 comparison, load case 02, L/R=0.2.

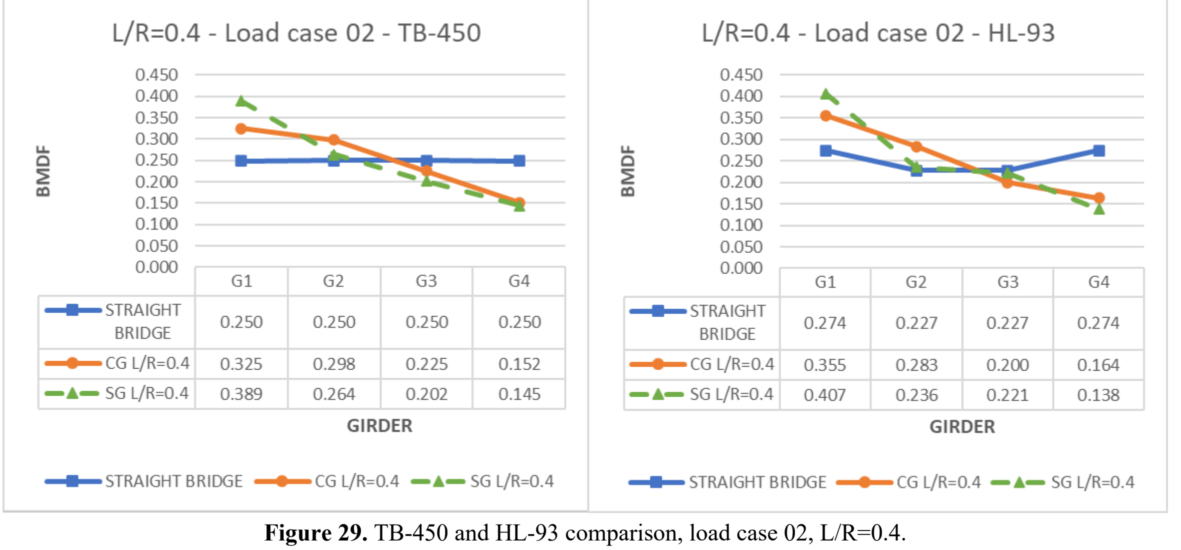

Figure 29. TB-450 and HL-93 comparison, load case 02, L/R=0.4.

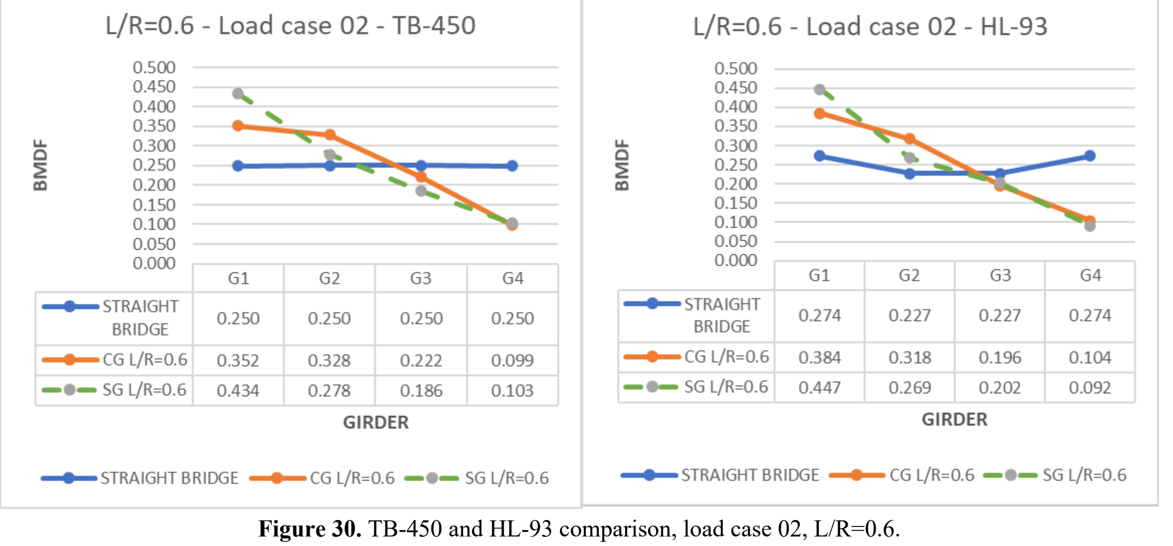

Figure 30. TB-450 and HL-93 comparison, load case 02, L/R=0.6.

9. CONCLUSION

This article aimed to conduct a parametric comparative analysis of bridges with curved longitudinal layout comparing the transverse bending moment distribution, with straight and curved geometry girders. Three types of curvature (0.2, 0.4 and 0.6) were analyzed with the application of two different vehicle-types in four specific load cases (01, 02, 03 and general). Comprehensively analyzing the bridge, it was found that the maximum total bending moment in the cross section is higher in curved bridges than in straight bridges. However, this increase is unequally distributed for the girders, with the maximum bending moment always occurring in the outer beam (G1).

In analysis using the general load case, for both standard vehicles (HL-93 and TB-450), there is a gradual increase in the bending moment in G1 and a reduction in G4, with an increase in the curvature. In addition, it was found that the straight girders (SG) were underestimated at a greater bending moment than the curved girders (CG) in all curvatures studied. This statement points to a possible material saving when using curved girders, considering only the bending moment distribution, given the 0.10 difference in the MF value, which represents approximately a 10% difference in the bending moment value between these two girder geometries.

In the study of the bending moment distribution for the girders, using the case of load 02, it was found that even with the application of the load on the central line of the board, the coupled effect of torsion with the bending moment, made the external girder (G1) the most requested in all curvatures studied. Comparing between SG and CG, a greater difference in bending moment was detected between the straight G1 and G2.

In short, considering only the bending moment distribution, it was possible to observe from the structural and economic point of view, from the results presented, that the use of curved girders in reinforced and/or prestressed concrete bridges with curved longitudinal design (curvatures between 0.2 and 0.6) is more advantageous than the use of straight ones. It is worth mentioning that for most detailed economic analysis, it would be necessary to extend the studies to other girder effects, such as torsion and shear.

REFERENCES

[1] World Economic Forum. “Annual Report 2015-2016.” WEforum.com. https://www.weforum.org/reports/annual-report-2015-2016 (accessed Mar. 3, 2020).

[2] W. Amorn, C. Y. Tuan, and M. K. Tadros, "Curved, precast, pretensioned concrete I-girder bridges," *PCI J.*, vol. 53, no. 6, pp. 43–66, 2008.

[3] M. Alawneh, M. Tadros, and G. Morcous, "Innovative system for curved precast posttensioned concrete i-girder and U-Girder bridges," *J. Bridge Eng.*, vol. 21, no. 11, pp. 04016076, 2016.

[4] Precast Concrete Institute, *Bridge Design Manual*, 3rd ed. Chicago: PCI, 2011.

[5] D. Cho, S. Park, and S. Hong, "Evaluation of girder distribution factor in PSC girder bridge with curved concrete slab based on AASHTO specifications," *Arab. J. Sci. Eng.*, vol. 39, pp. 7635–7646, 2014.

[6] R. L. Brockenbrough, "Distribution factors for curved I-Girder bridges," *J. Struct. Eng.*, vol. 112, no. 10, pp. 2200–2215, 1986.

[7] W. S. Kim, J. A. Laman, and D. G. Linzell, "Live load radial moment distribution for horizontally curved bridges," *J. Bridge Eng.*, vol. 12, no. 6, pp. 727–736, 2007.

[8] American Association of State Highway Transportation Officials, *AASHTO LRFD Bridge Design Specifications*, 8th ed. Washington: AASHTO, 2017.

[9] M. Samaan, K. Sennah, and J. B. Kennedy, "Positioning of bearings for curved continuous spread-box girder bridges," *Can. J. Civ. Eng.*, vol. 29, pp. 641–652, 2002.

[10] Associação Brasileira de Normas Técnicas, *Carga móvel rodoviária e de pedestres em pontes, viadutos, passarelas e outras estruturas, ABNT NBR 7188*, 2013.

[11] D. Nevling, D. Linzell, and J. Laman, "Examination of level of analysis accuracy for curved I-Girder bridges through comparisons to field data," *J. Bridge Eng.*, vol. 11, no. 2, pp. 160–168, 2006.

[12] C. C. Fu and S. Wang, *Computational analysis and design of bridge structures*. 1st ed. Boca Raton: CRC Press, 2015.

[13] S. J. Fatemi, M. S. M. Ali, and A. H. Sheikh, "Load distribution for composite steel-concrete horizontally curved box girder bridge," *J. Construct. Steel Res.*, vol. 116, pp. 19–28, 2016.

[14] R. A. Acosta and J. V. González, "Structural Response of Plan-Curved Steel I-Girder bridges from an equivalent straight bridge analysis," *J. Bridge Eng.*, vol. 23, no. 3, pp. 04017143, 2018.

[15] H. Zhang, D. Huang, and T. Wang, "Lateral load distribution in curved steel I-Girder bridges," *J. Bridge Eng.*, vol. 10, no. 3, pp. 281–290, 2005.

[16] P. J. Barr, M. W. Yanadon, and M. Hailing, "Live-load analysis of a curved I-Girder bridge," *J. Bridge Eng.*, vol. 12, no. 4, 477–484, 2007.

[17] American Association of State Highway Transportation Officials, *Guidelines for Steel Girder Bridge Analysis*. 2nd ed. Washington: AASHTO, 2016.

Author contributions: AR: conceptualization, methodology, data curation, software, formal analysis, writing; JN: formal analysis, project administration, supervision, writing-review & editing; RB: conceptualization, supervision, visualization; YN: data curation, writing-review & editing; PC: conceptualization, visualization.

Editors: Luís Oliveira Santos, Guilherme Aris Parsekian.

IBRACON Structures and Materials Journal
Revista IBRACON de Estruturas e Materiais
ISSN 1983-4195 ismj.org

ORIGINAL ARTICLE

Effect of the connecting beam stiffness on the bracing limit for reinforced concrete slender columns in single and multi-story frames

Efeito da rigidez do feixe de conexão no limite de preparação para colunas esbeltas de concreto armado em quadros únicos e multi-andares

Mohamed Gamal Aboelhassan[a]
Mohie Eldin Shoukry[a]
Said Mohamed Allam[a]

[a]Alexandria University, Faculty of Engineering, Department of Structural Engineering, Alexandria, Egypt

Received: 20 June 2021
Accepted: 31 August 2021

Abstract: The main purpose of this paper is to study analytically the behavior of slender reinforced concrete columns existing in sway and non-sway structures. The studied variables were the stiffness of the beam connected to the slender columns, the stiffness of the bracing columns, and the number of bays and stories in the structure model. The stability of slender columns was studied and the required limits for the lateral bracing were determined using a finite element program to perform buckling analysis, linear analysis, and geometric nonlinear analysis for the different frame structural models. All the results obtained in this study were compared to the available methods included in the different building codes and the methods suggested by other researchers. The results indicated that the minimum value of the bracing limit, required to restrain the slender column against the side-sway, depends on the stiffness of the connecting beams, number of stories, and number of bays. The required bracing limit decreases with increasing the beam stiffness and with increasing the number of bays. However, the required bracing limit increases with the increase of the number of stories in the structure.

Keywords: slender columns, reinforced concrete, beam stiffness, buckling analysis, geometric nonlinearity.

Resumo: O objetivo principal deste artigo é estudar analiticamente o comportamento de pilares esbeltos de concreto armado em estruturas deslocáveis e não deslocáveis. As variáveis estudadas foram a rigidez da viga conectada aos pilares esbeltos, a rigidez dos pilares de contraventamento e o número de vãos e andares no modelo de estrutura. A estabilidade de pilares esbeltos foi estudada e os limites exigidos para o contraventamento lateral foram determinados usando um programa de elementos finitos para realizar análise limite de flambagem, análise linear, e análise não linear geométrica para os diferentes modelos estruturais de pórticos. Todos os resultados obtidos neste estudo foram comparados com os métodos disponíveis incluídos nas diferentes normas de construção civil e os métodos sugeridos por outros pesquisadores. Os resultados indicaram que o valor mínimo do limite de contraventamento, necessário para restringir o pilar esbelto contra a deslocabilidade lateral, depende da rigidez das vigas de conexão, número de andares e número de vãos. O limite de contraventamento necessário diminui com o aumento da rigidez da viga e com o aumento do número de vãos. No entanto, o limite de contraventamento necessário aumenta com o aumento do número de andares na estrutura.

Palavras-chave: pilares esbeltos, concreto armado, rigidez de viga, análise de flambagem, não linearidade geométrica.

How to cite: M. G. Aboelhassan, M. E. Shoukry, and S. M. Allam "Effect of the connecting beam stiffness on the bracing limit for reinforced concrete slender columns in single and multi-story frames," *Rev. IBRACON Estrut. Mater.*, vol. 15, no. 2, e15209, 2022, https://doi.org/10.1590/S1983-41952022000200009

Corresponding author: Mohamed Gamal Aboelhassan. E-mail: mgamalhussien@yahoo.com
Financial support: None.
Conflict of interest: Nothing to declare.

1 INTRODUCTION

Reinforced concrete framed structures might fail by lateral instability caused by excessive inter-story drift, particularly when subjected to extreme earthquake motions. More than 200 years ago, Euler demonstrated that a long, straight, pin-jointed, and concentrically loaded column would remain stable until a critical load is reached at which lateral deflection increases rapidly with a small amount of increase in axial load. For a column with different boundary conditions, the critical buckling load is expressed by Equation 1 (which is a modification of the well-known Euler's equation). The degree of slenderness in a column is expressed in terms of slenderness ratio; λ as defined in Equation 2.

$$P_{cr} = \frac{\pi^2 EI}{\left(l_{eff}\right)^2} \quad (1)$$

$$\lambda = \frac{l_{eff}}{i} = \frac{Kl_u}{i}, i = \sqrt{I / A} \quad (2)$$

where, P_{cr} is the critical buckling load, EI is the bending stiffness of the column in the direction under consideration, l_{eff} is the effective buckling length of the column, l_u is the unsupported column length (or clear length), K is the effective length factor reflecting end restraint and lateral bracing conditions of a column which expressed by the parameter ψ in Equation 6, i is the radius of gyration reflecting the area and shape of a column cross-section, I is the cross-sectional moment of inertia, and A is the cross-sectional area.

MacGregor [1] showed that for the same reinforced concrete cross-section, different types of failure could happen as shown in Figure 1. Failure of a slender column is initiated by the material failure of a section, or the instability failure of the column, depending on the level of slenderness ratio of the column and its end restraints. In the case of instability failure, buckling occurs in columns, and failure is reached before material failure and develops at any cross-section along the column. Large values of lateral deformations are observed with a slight increase in axial load acting on the column. This type of failure can only occur with columns of high values of slenderness ratio.

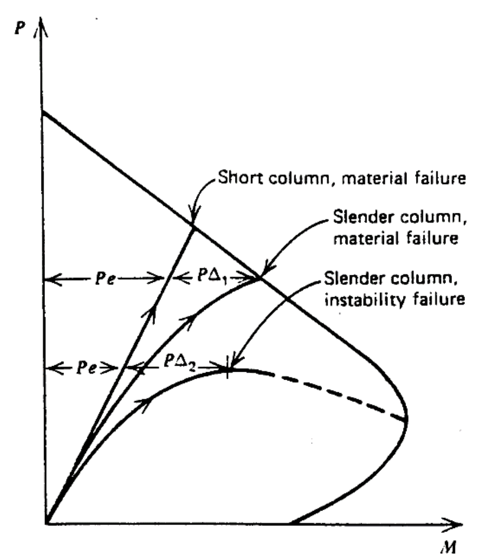

Figure 1. Types of failure for reinforced concrete columns [1].

Structures or structural members may be classified as braced or unbraced depending on the provisions or not of bracing elements and as non-sway or sway depending on their sensitivity to second-order effects due to lateral deflections. According to ACI 318-14 [2], It shall be permitted to assume a column in a structure is non-sway if the increase in column end moments due to second-order effects (P - Δ effect) does not exceed 5% of the first order end moments as given by Equation 3 introduced by MacGregor and Hage [3]. However, according to the Egyptian code (ECP 203-2018) [4] and the British Standards (BS 8110-97) [5], a building is considered non-sway if it has lateral stiffness of bracing elements. The bracing element should be continuous at the whole height of the building and should be symmetrically arranged in the plan, and completely fixed to the foundations. The bracing elements should satisfy the criteria in Equations 4 and 5.

$$Q = \frac{\Sigma P_u \Delta_0}{H_u l_c} \leq 0.05 \tag{3}$$

Where, Q is the stability index for the building, ΣP_u is the total factored vertical load on all columns of the story, H_u is the story shear, respectively, l_c is the length of compression member in a frame, measured from center to center of the joints in the frame, and Δ_o is the first-order relative deflection between the top and bottom of that story due to H_u.

$$\alpha = H_b \sqrt{\frac{N}{\Sigma EI}} < 0.2 + 0.1n \qquad \left(\textit{for a building less than 4 stories}\right) \tag{4}$$

$$\alpha = H_b \sqrt{\frac{N}{\Sigma EI}} < 0.6 \qquad \left(\textit{for a building 4 stories or more}\right) \tag{5}$$

Where, H_b is the total height of the building above foundations, N is the sum of the vertical loads acting on the building, ∑EI is the sum of flexural rigidities of all vertical bracing elements acting in the direction considered, and n is the number of stories in the building.

According to the commentary of ACI 318-14 [2], the effective length factor K may be taken as the smaller of Equations 7 and 8 for compression members in non-sway frames, which were first suggested by Cranston [6]. However, for sway frames, the effective length factor K may be taken from Equations 9 and 10 developed by Furlong [7]. In the Egyptian code (ECP 203-2018) [4] and the British Standards (BS 8110-97) [5], the effective length factor K is as given by Equations 7 and 8 for braced columns, and by Equations 11 and 12 introduced by Cranston [6] for unbraced columns. Also, the American Institute of Steel Construction (ANSI/AISC 360-16) [8] introduced a general formula for the K-factor as shown in Equation 13.

$$\Psi = \frac{\Sigma\left(EI_c / l_c\right)}{\Sigma\left(EI_b / l_b\right)} \tag{6}$$

$$\mathrm{K} = 0.70 + 0.05\left(\Psi_1 + \Psi_2\right) \leq 1.0 \tag{7}$$

$$\mathrm{K} = 0.85 + 0.05\left(\Psi_{\min}\right) \leq 1.0 \tag{8}$$

$$\text{For } \Psi_m < 2 \qquad \mathrm{K} = \frac{20\text{-}\Psi_m}{20}\sqrt{1+\Psi_m} \tag{9}$$

$$\text{For } \Psi_m \geq 2 \qquad \mathrm{K} = 0.90\sqrt{1+\Psi_m} \tag{10}$$

$$\mathrm{K} = 1.0 + 0.15\left(\Psi_1 + \Psi_2\right) \geq 1.0 \tag{11}$$

$$\mathrm{K} = 2.0 + 0.3\left(\Psi_{\min}\right) \geq 1.0 \tag{12}$$

$$K_2 = \sqrt{\frac{P_{story}}{P_r} \times \frac{I_i}{\Sigma\left(I_i / K_{n2}^2\right)}} \geq \sqrt{\frac{5}{8}} \times K_{n2} \tag{13}$$

where, ψ is the end restraint of the column, EI_c is the bending stiffness of column in direction under consideration, EI_b is the bending stiffness of beam in direction under consideration, l_c is the height of column measured between centers of restraints, l_b is the span length of the beam measured center to center of joints, the symbol Σ indicates the summation for all members stiffness connected at the joint and lying in the plane at which buckling of the column is being considered, Ψ_1 and Ψ_2 are the values of Ψ at the two ends of the column, Ψ_{min} and Ψ_m are the smaller and the average values of the two ends of the column, respectively, K_2 is the modified effective length factor for i^{th} rigid partially braced column, I_i is the moment of inertia in plane of bending for i^{th} rigid column, K_{n2} is the effective length factor for i^{th} rigid column based on classic alignment charts, P_r is the required axial compressive strength for i^{th} rigid column, and P_{story} is the total axial loads of the story.

On the other hand, Aristizabal-Ochoa [9], [10] presented a practical approach to calculating the effective length factor for a single column as well as for a multi-column system. In multi-column systems with side-sway uninhibited or partially inhibited, every column is defined as having reached its critical load when side-sway buckling of the frame occurs, the load distribution among the columns is as specified by the designer. In this approach, the effective length factor of each column is a function of its properties, the properties of the entire frame, and the distribution of loads among the columns in the frame. Hellesland and Bjorhovde [11] introduced an improved method to calculate the effective length factor and, at the same time, the method satisfies general system instability for the whole structure. The primary attention in that study was concentrated on non-sway structures. The effective length factors for all columns are first calculated using traditional methods. These values are then used as input data to obtain the modified effective length factors. Furthermore, Bendito et al. [12] developed an equation to calculate the effective length factor for reinforced concrete columns considering the geometric and the material nonlinear performance of these columns. Ma et al. [13] presented another method to calculate the effective length of slender columns elastically restrained at the column top and fixed at the base using the ANSYS program to perform buckling analysis of a slender reinforced concrete column on the bottom floor. Results proved that the obtained effective length factor based on this method was higher than the design code by more than 20%. On the other hand, Farouk [14] suggested an approximate equation to calculate the additional moment for braced slender columns in the elastic analysis. The additional moment calculated from this equation and the finite element analysis showed a good agreement. Marí and Hellesland [15] derived analytical expressions for the lower slenderness limits of reinforced concrete columns with different reinforcement distributions. Excellent agreement was found between the numerical results and those obtained by the proposed expression. Fawzy [16] carried out an analytical study considering the nonlinear material and geometric analyses to determine the sufficient lateral stiffness required to ensure full bracing conditions in one-story frame structures. For a single-bay, single-story frame, beams of high moment of inertia can possess a full fixation for columns and thus increase the critical buckling loads for these columns, this increase was found to be from three to five times of the corresponding buckling loads obtained for the same column when it is free to rotate at its end joints. However, the required lateral stiffness of a bracing column, given as a ratio of the sum of stiffness of other columns in the story, decreases with increasing the number of bays of structure and increases with increasing number of stories of structure. Khuntia and Ghosh [17], [18] introduced an analytical and the experimental research. Which stated that the moment of inertia for column is independent of the reinforcement ratio ρ, the axial load P, the eccentricity ratio e/h (bending moment to axial load ratio), and the compressive strength of concrete f_c'. Similarly, the moment of inertia for beams does not take the effect of reinforcement ratio ρ_g into account. This simplification may not be appropriate in many practical cases. Analysis shows that the column inertia can vary from $0.5I_g$ to $1.0I_g$ and the beam inertia from $0.3I_g$ to $0.5I_g$ in most practical cases. Based on the results, it was recommended that the effective EI of beams and columns to be used in the lateral analysis of frames in general and of frames including slender columns.

2 RESEARCH OBJECTIVE

The restraining effect of beams has a major effect on slender column behavior, such as limiting the horizontal displacement resulting from lateral loads. Also, there is no clear and definite criterion available to determine the necessary and sufficient required stiffness for the bracing elements to guarantee a full non-sway condition. The main objective of this study is:

(1) To study the effect of beam stiffness on the required limits for the lateral stiffness of the bracing elements. This limit is called the bracing limit and it is defined as the stiffness of the bracing element above which the structure can be considered a non-sway structure.
(2) To obtain the effect of the increasing number of bays and number of stories of the structure on the required bracing limit.

In the current analytical study, many variables were considered which affecting the stability of structures. These variables were:

- The beam stiffness connecting to the slender columns.
- The stiffness of the bracing column.
- The number of bays and stories in the structural frame model.

It should be noted that as stated in the analytical study conducted by Fawzy [16], the value of the horizontal loads, applied on the studied frames, did not affect the critical buckling loads of the slender columns. Therefore, the presence of horizontal loads was ignored in the current analytical study. Also, to ensure the accuracy of the current buckling model was verified with the nonlinear material and geometric model presented by Fawzy [16] and the obtained results were very similar. The buckling analysis was selected to reduce the time of solving the model in the computer program.

3 STABILITY MODEL

In the current analytical study, eigenvalue buckling analyses were performed using ANSYS software. Generally, the ANSYS program includes models to solve linear and nonlinear static and dynamic structural problems [19]. A two-dimensional beam element (BEAM3) was used for modeling the frame members. BEAM3 is a uni-axial element with tension, compression, and bending capabilities for two-dimensional structural models. The element has three degrees of freedom at each node; translations in the nodal x and y directions and rotation about the nodal z-axis. After performing linear and nonlinear analysis, the output results for this element for geometric nonlinear analysis can be read in the form of axial forces, moments, shears, displacements, deformed shapes, and stresses in the element local coordinate system. However, the output results for this element for buckling analysis can be read in the form of the critical axial buckling load. The buckling problem is formulated as an eigenvalue problem, see Equation 14. It should be noted that the ANSYS program used some assumptions and restrictions for the buckling analysis which were:
(1) The analysis is valid for structural degrees of freedom only.
(2) The structure fails suddenly with a horizontal force-deflection curve.
(3) The structure has constant stiffness effects.
(4) A static solution with pre-stressed effects included was run.

$$\left(\left[K\right]+\lambda_i\left[S\right]\right)\left\{\Psi\right\}_i=\left\{0\right\} \tag{14}$$

where, [K] is the stiffness matrix, [S] is the stress stiffness matrix, λ_i is the i^{th} eigenvalue used to multiply the loads generated [S], and $\{\psi\}_i$ is the i^{th} eigenvector of displacements. The eigenvectors are normalized so that the largest component is 1. Thus, the stresses (when output) may only be interpreted as a relative distribution of stresses. If the first eigenvalue closest to the shift point is negative (indicating that the loads applied in a reverse sense will cause buckling), the program will terminate.

Figure 2 presents the frame model used in the analysis. This two-dimensional frame model consisted of a slender column with inertia I_o and a bracing column with inertia I_{br}. Each column was completely fixed at its bottom end and was restrained at the top end by a horizontal beam with inertia I_b. Several cases were studied by increasing the moment of inertia of the bracing column, in each case, as a ratio of the moment of inertia of the slender column according to a specified value of beam moment of inertia. Bucking analysis was performed for each case by applying a unit vertical load at each column. The unit vertical load was applied equally to all floors for the multi-story model. The obtained values of critical buckling loads for the sway frame model (Figure 2a) were compared, for each case, with the corresponding values obtained for the same model when being completely restrained against side-sway (Figure 2b). To ensure that the buckling occurs in columns and the instability failure is reached before the material failure, the dimension of the story height was selected to have a column with high values of slenderness ratio which is not accepted by most building codes.

In the current analytical study, the minimum amount of stiffness of the bracing columns for which the critical buckling load of the slender column reaches 95% of the corresponding value obtained when the same structure is completely restrained against side-sway is defined as the bracing limit according to ACI 318-14 [2]. This minimum required stiffness is introduced as a ratio between the stiffness of the bracing column to that of the slender column (I_{br} / I_o) or as a ratio between the stiffness of the bracing column to the sum of all other slender columns forming the structure for multi-bay frames (I_{br} / ΣI_o). Also, multi-story, multi-bay frames with 1, 2, and 3 stories or/and 1, 2, and 3 bays were analyzed, as shown in Figure 3.

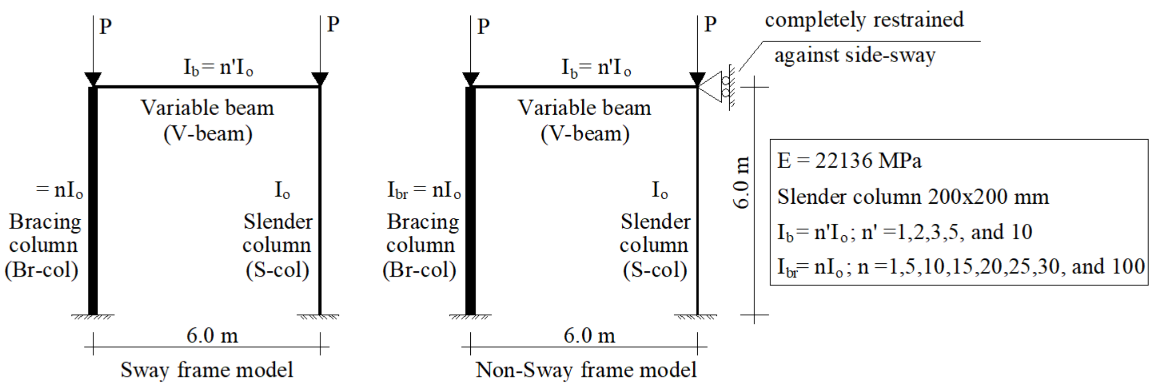

Figure 2. One-story, one bay-frame model.

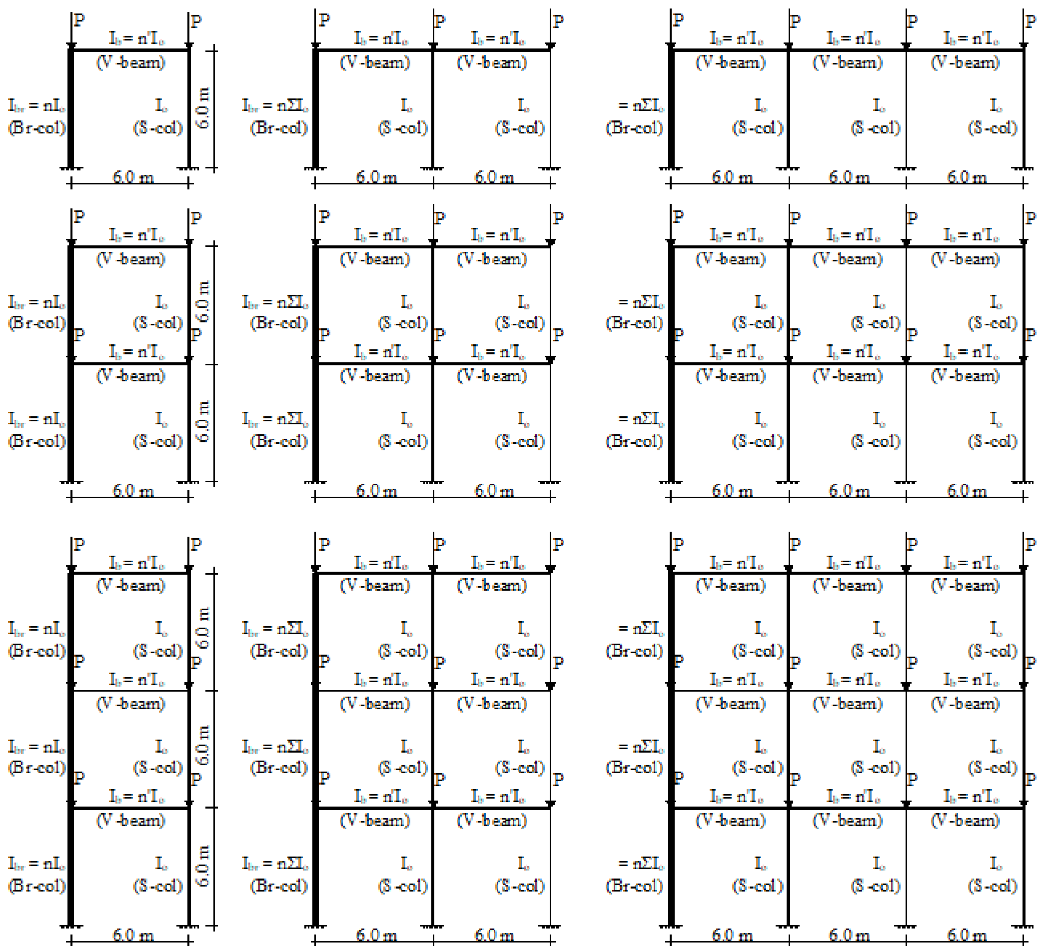

Figure 3. Multi-stories, multi-bays frame models.

4 RESULTS AND DISCUSSIONS

Based on the obtained results, the required bracing limit and the effective length factors of all studied frames are summarized in Tables 1, 2, and 3. The effective length factor K of slender columns was calculated by substituting the critical buckling load, obtained from buckling analysis, in Equation 1 (Euler's equation).

Table 1. Required bracing limit and effective length factors for the one-story frames.

n'= (I_b/I_o)	**Required bracing limit n = (I_{br}/I^o)**			**Effective length factor (K)**			
	One bay frame	***Two bays frame***	***Three bays frame***	***Buckling analysis***	***ANSI/AISC 360-16***	***ACI 318-14***	***ECP 203-2018 and BS 8110-97***
1	***18.8***	***13.87***	***12.78***	0.59	0.91	1.19	1.30
2	***18.67***	***13.76***	***12.50***	0.56	0.85	1.10	1.23
3	***18.48***	***13.53***	***12.39***	0.55	0.84	1.07	1.20
5	***17.37***	***13.18***	***12.12***	0.53	0.82	1.04	1.19
10	***13.39***	***9.67***	***9.43***	0.52	0.81	1.02	1.17

Table 2. Required bracing limit and effective length factors for the two-stories frames.

n'= (I_b/I_o)	**Required bracing limit n = (I_{br}/I^o)**			**Effective length factor (K)**			
	One bay frame	***Two bays frame***	***Three bays frame***	***Buckling analysis***	***ANSI/AISC 360-16***	***ACI 318-14***	***ECP 203-2018 and BS 8110-97***
1	***74.41***	***25.00***	***22.73***	0.60	1.01	1.34	1.45
2	***29.20***	***24.10***	***21.20***	0.56	0.91	1.19	1.30
3	***24.85***	***23.05***	***19.83***	0.56	0.88	1.14	1.25
5	***19.39***	***19.03***	***17.76***	0.53	0.85	1.08	1.21
10	***13.96***	***12.68***	***12.68***	0.52	0.82	1.04	1.18

Table 3. Required bracing limit and effective length factors for the three-stories frames.

n'= (I_b/I_o)	**Required bracing limit n = (I_{br}/I^o)**			**Effective length factor (K)**			
	One bay frame	***Two bays frame***	***Three bays frame***	***Buckling analysis***	***ANSI/AISC 360-16***	***ACI 318-14***	***ECP 203-2018 and BS 8110-97***
1	***88.21***	***76.34***	***53.40***	0.62	1.01	1.34	1.45
2	***81.59***	***66.70***	***36.20***	0.58	0.91	1.19	1.30
3	***73.34***	***54.59***	***29.46***	0.56	0.88	1.14	1.25
5	***29.05***	***27.16***	***26.25***	0.54	0.85	1.08	1.21
10	***18.67***	***16.73***	***17.77***	0.52	0.82	1.04	1.18

3.1 Effect of degree of lateral bracing on the behavior of slender columns

The results of the analysis given in Tables 1 to 3 indicated that increasing the stiffness of the bracing column, i.e., the increasing degree of lateral bracing (I_{br} / I_o) increases the critical buckling load for the slender column until this load reaches approximately the buckling load for the corresponding column in a non-sway model. The minimum values of the bracing limit required to restrain the slender column against the side-sway vary according to the number of bays, number of stories, and stiffness of the connecting beam. Although, a value of I_{br} / I_o = 18.8 is sufficient to restrain the slender column in the one-story, one-bay frame model, the required value for three-stories, one-bay frame model is increased to 88.2. This great effect for the number of stories on the behavior of slender columns was obtained for the columns connected with the small stiffness of the connecting beams. This effect may be explained by the increase of the buckling length of the slender column with the increase of the number of stories. Similarly, for models with beams of small stiffness (I_b / I_o < 5), increasing the number of bays for the frame models decreases the degree of bracing required to restrain the slender column. For example, for I_b / I_o = 1.0 in the two-stories, one-bay frame model, the required bracing limit was 74.4 while the above limit was only 22.7 for the two-stories, three-bays frame model.

MacGregor [1] stated that the structure can be considered as a non-sway structure if the stiffness of the bracing column is six times that of the slender column. This limit is conservative when compared to the limits obtained from the currently obtained results and the results of Fawzy [16]. Also, Equations 4 and 5 recommended by the Egyptian Code (ECP 203-2018) [4], for the classification of columns as sway or non-sway, gives very conservative values when compared to the results of the analysis presented in this study. For example, for the one-story, one-bay frame model the analysis gives a value of 18.8 for I_{br} / I_o while the limit obtained by the Egyptian Code is 85.

3.2 Effect of beam stiffness on the required bracing limit

The results obtained from the analysis indicated that the increase of the stiffness of the beam connecting the slender column at the top decreased the bracing limit required to consider the structure as a non-sway one. The bracing limit is defined as the ratio of the bracing column inertia I_{br} to that for the slender column I_o. For the one-story, one-bay frame model, increasing the ratio of the beam inertia to that for the slender column (I_b / I_o) from 1.0 to 10 decreased the required bracing limit from 18.8 to 13.4 (i.e., a reduction of about 28.7%). Figure 4 displays the relationship between the ratio of the beam stiffness (I_b / I_o) and the degree of lateral bracing for all the cases studied. The figure indicates that for stiff beams (i.e., I_b / $I_o \geq 5$), the change in the values of the required bracing limit is small. It should be noted that the effect of beam stiffness, on the classification of the structure as non-sway or sway, is not included in most building codes.

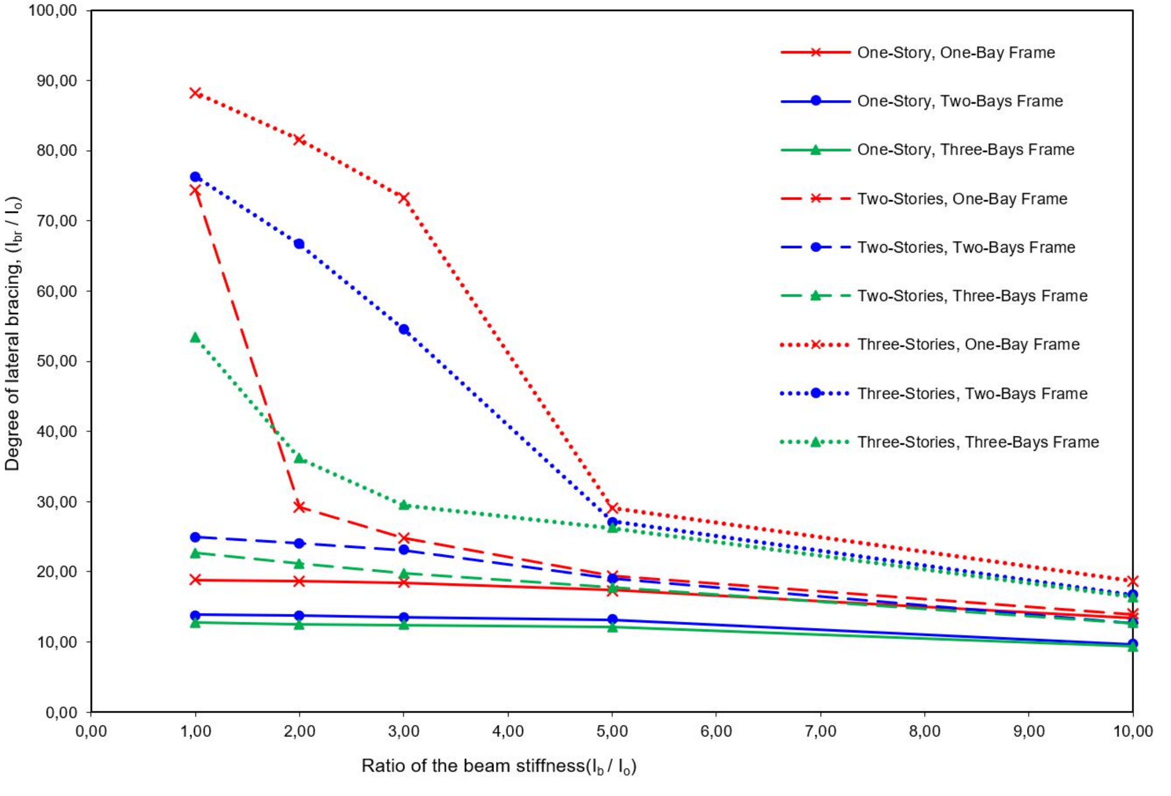

Figure 4. Relation between the ratio of the beam stiffness (I_b / I_o) and the degree of lateral bracing.

3.3 Effective length factor

Figure 5 presents the relation between the effective length factor (K) and the ratio of the beam stiffness (I_b / I_o). Generally, with the increase of moment of inertia for the bracing columns; I_{br}, the effective length factor decreases, and the structure changes from a sway-structure (K>1.0) to a non-sway one (K<1.0). It should be noted that most building codes do not consider the degree of lateral bracing when calculating the effective length factor. The equations recommended by building codes give only two values for the effective length factor; one for non-sway frames and the other for sway frames and neglect the fact that most structures are to be considered partially braced. However, the best results for the effective length factor from the considered building codes were obtained using Equation 13 defined by ANSI/AISC 360-16. The effect of changing the moment of inertia of the connecting beam on the value of the effective length factor was small. This effect was large with increasing the number of stories and/or the number of bays, and for the bracing columns with inertia I_{br} / I_o > 1.0. According to the Egyptian Code (ECP 203-2018) [4], the value of the rotational restraints at column joint (Ψ) should not be taken less than 1.0. However, in this study, the value of Ψ was changed from 0.1 (I_b / I_o = 10) to 1.0 (I_b / I_o = 1.0). In addition, the Egyptian Code gives a minimum value of K = 0.7 for a braced (non-sway) column, while the present analysis gives values for the effective length factor K = 0.5 to 0.6 when the slender columns were restrained against side-sway.

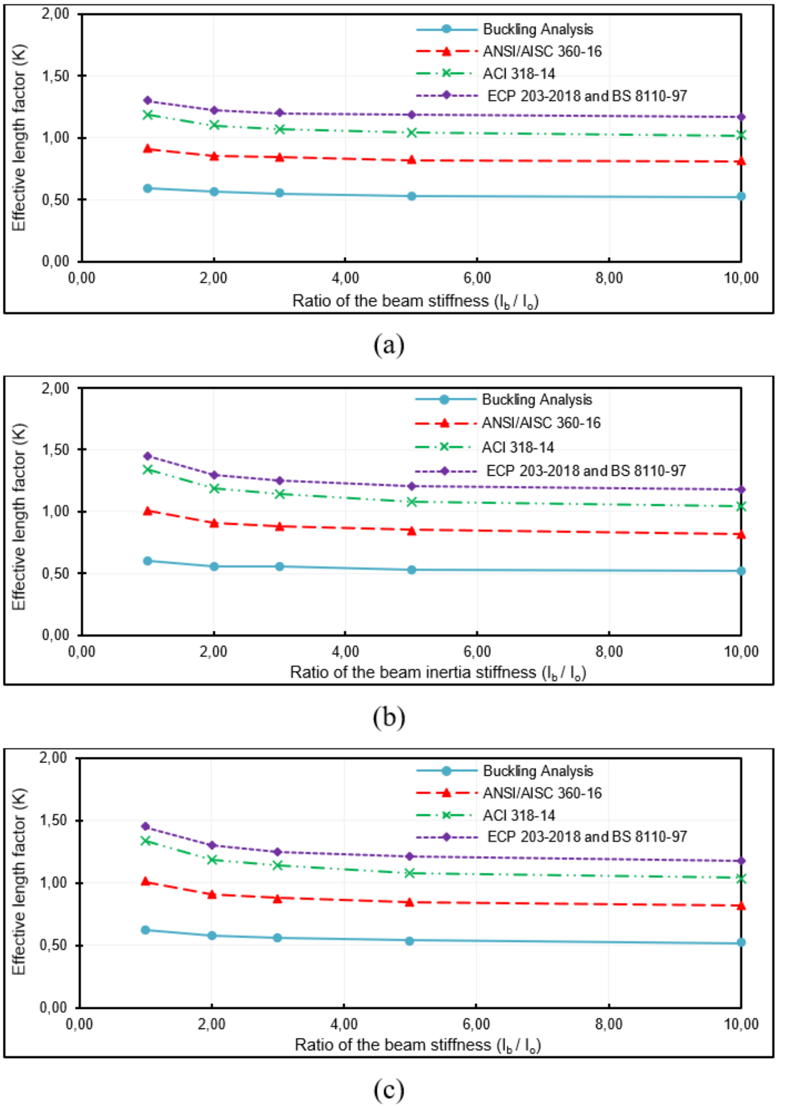

Figure 5. Relation between the effective length factor and the ratio of the beam stiffness (I_b / I_o). a) one-story frames; b) two-stories frames; c) three-stories frames.

5 CONCLUSIONS

The main purpose of this paper was to study the behavior of slender reinforced concrete columns existing in sway and non-sway structures. The stability of slender columns was studied and the required limits for the lateral bracing were determined. The Finite Element program ANSYS was used to perform buckling analysis, linear analysis, and geometric nonlinear analysis for the different frame structural models. Many variables were studied affecting the stability of the structures. These variables were the beam stiffness connecting to the slender columns, the stiffness of the bracing column, and the number of bays and stories in the structural frame model. From the results obtained from the theoretical work presented in this study, the following conclusions may be drawn:

- The minimum value of the bracing limit required to restrain the slender column against the side-sway depends on the number of stories, number of bays, and stiffness of the connecting beam. Effect of beam stiffness was clearly observed for beams with stiffness ratio I_b / I_o more than 2.
- Increasing the number of stories increases the required degree of lateral bracing. However, increasing the number of bays decrease the degree of lateral bracing.
- The equation recommended by the Egyptian Code for the classification of the columns as sway or non-sway gives very conservative values when compared to the present analyses.
- Most building codes give only two values for the effective length factor; one for non-sway columns and the other for sway columns and neglect the fact that most structures in practice are to be considered partially braced. Also, the Egyptian Code recommends conservative values for the effective length factor for both braced and unbraced columns.

REFERENCES

[1] J. MacGregor, "Design of slender columns revisited," *Struct. J.*, vol. 90, no. 3, pp. 302–309, 1993.

[2] American Concrete Institute, *Building Code Requirements for Structural Concrete (ACI 318-14) and Commentary on Building Code Requirements for Structural Concrete*, ACI 318R-14, 2014.

[3] J. G. MacGregor and S. E. Hage, "Stability analysis and design of concrete frames," *J. Struct. Div.*, vol. 103, no. 10, pp. 1953–1970, 1977.

[4] Housing and Construction National Research Center, *Egyptian Code for Design and Construction of Reinforced Concrete Structures*, ECP203-2018, 2018.

[5] British Standards Institution, *Structural Use of Concrete, Part 1: Code of Practice for Design and Construction*, BS 8110-97, 1997.

[6] W. Cranston, *Analysis and Design of Reinforced Concrete Columns* (Research Report 20). London: Cement and Concrete Association, 1972.

[7] R. W. Furlong, "Column slenderness and charts for design," *ACI J. Proc.*, vol. 68, no. 1, pp. 9–19, 1971.

[8] American Institute of Steel Construction, *Specification for Structural Steel Buildings*, ANSI/AISC 360-16, 2016.

[9] J. D. Aristizabal-Ochoa, "Story stability and minimum bracing in RC framed structures: a general approach," *ACI Struct. J.*, vol. 92, no. 6, pp. 735–744, 1995.

[10] J. D. Aristizabal-Ochoa, "Story stability of braced, partially braced, and unbraced frames: classical approach," *J. Struct. Eng.*, vol. 123, no. 6, pp. 799–807, 1997.

[11] J. Hellesland and R. Bjorhovde, "Improved frame stability analysis with effective lengths," *J. Struct. Eng.*, vol. 122, no. 11, pp. 1275–1283, 1996.

[12] A. Bendito, M. L. Romero, J. Bonet, P. Miguel, and M. Fernandez, "Inelastic effective length factor of nonsway reinforced concrete columns," *J. Struct. Eng.*, vol. 135, no. 9, pp. 1034–1039, 2009.

[13] H. Ma, L. Ye, and L. Lin, "A Study on Effective Length of Slender Column with Elastic Restraints," *Procedia Eng.*, vol. 210, pp. 228–234, 2017.

[14] M. A. Farouk, "Second-order analysis in braced slender columns part I: approximate equation for computing the additional moments of slender columns," *JES: J. Eng. Sci.*, vol. 45, no. 2, pp. 118–141, 2017.

[15] A. R. Marí and J. Hellesland, "Lower slenderness limits for rectangular reinforced concrete columns," *J. Struct. Eng.*, vol. 131, no. 1, pp. 85–95, 2005.

[16] A. Fawzy, "Study of column slenderness in reinforced concrete buildings," M.S. thesis, Dept. Struct. Eng., Fac. Eng., Alexandria Univ., Egypt, 2002.

[17] M. Khuntia and S. K. Ghosh, "Flexural stiffness of reinforced concrete columns and beams: analytical approach," *ACI Struct. J.*, vol. 101, no. 3, pp. 351–363, 2004.

[18] M. Khuntia and S. K. Ghosh, "Flexural stiffness of reinforced concrete columns and beams: experimental verification," *ACI Struct. J.*, vol. 101, no. 3, pp. 364–374, 2004.

[19] ANSYS Inc., ANSYS Theoretical Manual (for ANSYS Revision 8.04). Canonsburg, PA: ANSYS Inc., 1998.

Author contributions: MGA: methodology, writing, data curation, formal analysis; MES and SMA: conceptualization, supervision, formal analysis.

Editors: Mauro de Vasconcellos Real, Guilherme Aris Parsekian.

IBRACON Structures and Materials Journal
Revista IBRACON de Estruturas e Materiais
ISSN 1983-4195 ismj.org

ORIGINAL ARTICLE

Parametric analysis related to dimensioning of tubular steel columns filled with concrete in a fire situation

Análise paramétrica do dimensionamento de pilares tubulares de aço preenchidos com concreto em situação de incêndio.

Fábio Masini Rodrigues[a]
Armando Lopes Moreno Júnior[a]
Jorge Munaiar Neto[b]

[a]Universidade de Campinas – UNICAMP, Departamento de Estruturas, Campinas, SP, Brasil
[b]Universidade de São Paulo – USP, Escola de Engenharia de São Carlos – EESC, Departamento de Engenharia de Estruturas, São Carlos, SP, Brasil

Received 10 April 2021
Accepted 02 September 2021

Abstract: For the dimensioning of structural elements in fire situation, simplified equations and parameters are commonly used in analytical equations or numerical models. More complex equations or simplified values can be chosen by the designer for determine materials properties in high temperature in numerical models, however, numerical modeling can be quite sensitive to the variation of some of the physical and mechanical properties. In this paper, the sensitivity of the numerical model in relation to the values according to the level of simplification chosen was evaluated, presenting an analysis in relation to the results found to contribute to the choice of these parameters and presenting the indications found in the literature. In this sense, this work presents a study of sensitivity to the variation of the values of steel and concrete properties, presented in the Eurocode and Brazilian standards, in addition to the moisture content and emissivity of the surface exposed to fire, for the dimensioning, in a fire situation, of steel tube columns, of circular and square section, filled with concrete. The studies were carried out via numerical modeling developed in the software ABAQUS. It was verified that the resulting emissivity values equal to 0.7 or 0.8, recommended in the literature, are conservative, and the choice of either does not bring significant changes in the temperature field obtained for the structural elements under analysis. It was also verified that the concrete moisture content is a relevant aspect for the formation of its temperature field, also affecting, but to a lesser extent, the steel temperature. Regarding the physical and mechanical properties of the materials, this sensitivity study suggests the adoption of the values from the equations presented in Eurocodes, without simplifications, and with the specific heat and thermal conductivity of the concrete, adopted in accordance with the Eurocode 4.

Keywords: fire situation, column, steel, concrete, numerical models.

Resumo: Na verificação de elementos estruturais em situação de incêndio por meio de equações analíticas, e mesmo via modelagem numérica, normalmente são empregados parâmetros e propriedades dos materiais simplificados. Entretanto, os resultados obtidos podem ser bastante sensíveis ao grau de simplificação adotado pelo projetista ou mesmo conforme à escolha de uma ou outra opção de propriedade dos materiais envolvidos. No presente artigo foi apresentado um estudo de sensibilidade considerando a variação das propriedades dos materiais; visando auxiliar a escolha desses parâmetros dentre as diversas opções descritas na literatura. O estudo de sensibilidade foi elaborado para pilares compostos por tubos de aço de seção circular e quadrada, vazio e preenchidos com concreto, e com as propriedades do aço e concreto indicadas pelo Eurocode ou por normas brasileiras para o dimensionamento de estruturas em situação de incêndio. Também foi analisado o comportamento do modelo conforme variações no teor de umidade do concreto e variações da emissividade da superfície de aço exposta ao fogo. O estudo foi realizado em modelo numérico desenvolvido no software ABAQUS e os resultados obtidos demonstram que os valores de 0,7 e 0,8, recomendados na literatura para a emissividade resultante, são conservadores e a alternância entre esses dois

Corresponding author: Fábio Rodrigues. E-mail: fabiosecfmr@gmail.com
Financial support: None.
Conflict of interest: Nothing to declare.
Data Availability: The data that support the findings of this study are available from the corresponding author, [FMR], upon reasonable request.

valores não altera, significativamente, o campo de temperaturas na seção transversal do elemento estrutural. Já com relação ao teor de umidade do concreto foram verificadas alterações significativas no campo de temperaturas, inclusive na temperatura do tubo de aço, com a alternância deste parâmetro. Com relação às propriedades físicas e mecânicas dos materiais, o estudo de sensibilidade sugere a adoção dos valores obtidos a partir das equações sem simplificações apresentadas no Eurocode e com o valor do calor específico do concreto determinado conforme Eurocode 4.

Palavras-chave: situação de incêndio, pilares, aço, concreto, modelos numéricos.

How to cite: F. M. Rodrigues, A. L. Moreno Júnior, and J. Munaiar Neto, "Parametric analysis related to dimensioning of tubular steel columns filled with concrete in a fire situation", *IBRACON Struct. Mater. J.*, vol. 15, no. 2, e15210, 2022, https://doi.org/10.1590/S1983-41952022000200010

1. INTRODUCTION

The columns made of steel tube, of circular and square section, filled with concrete, are usually dimensioned for a fire situation by simplified equations of practical application, presented in the literature [1], [2] and in normative codes, such as EN 1994-1-2 [3] and ABNT NBR 14323: 2013 [4]. However, simplified processes do not always provide satisfactory results and are often used very comprehensively.

In the case of steel tubes filled with concrete, the interaction between both materials increases the complexity of the problem, so that the temperatures usually obtained from graphs and tables presented in the literature [2] are not suitable for any type of situation.

Numerical modeling can be a solution for situations not contemplated by simplified processes. However, whatever the sizing method for a fire situation, whether simplified or advanced, it is essential to evaluate correctly and choose the values for the physical and mechanical properties of the materials.

The normative codes indicate complex and simplified formulations to determine the values of the thermal and mechanical properties of steel and concrete, as well as constant values allowing their assessment in simple design methods. However, there are often no specific rules for when to consider such simplifications. The absence of accurate information on the material property can result in remarkable discrepancies among numerical models and reference experimental models result. The validation of numerical modeling is always conditioned by the values considered for the thermal or mechanical properties of the material, which may not necessarily be the real value, but the ones that yields a better adjustment of the numerical model to the validation data. Hence, it is evident the importance of knowing the influence of each property on the response of the model and, consequently, on the strength capacity of the structural element when in a fire situation.

The moisture content in the concrete and the resulting emissivity factor are two important parameters for numerical modeling, but uncertainties remain in the literature.

This work presents a study on the sensitivity of the steel and the concrete properties applied to circular and square steel tubes filled with concrete and in a fire situation. In addition, this paper reports studies on the usual values adopted for the concrete moisture content, concrete density and emissivity of the surface exposed to fire. The analyses take into consideration the complete and simplified equations presented in EN 1992-1-2 [5], EN1993-1-2 [6] and EN1994-1-2 [3] and ABNT NBR 14323:2013 [4].

The parametric sensitivity evaluation was conducted via numerical modeling, using the software ABAQUS (Dassault Systems SIMULIA Corp., 2014), considering initial studies for model adjustments and including the effect of air-gap, as presented in Rodrigues [7].

2. NUMERICAL MODEL

A three-dimensional model and another two-dimensional model were developed in ABAQUS [8], as described below.

2.1. Three-dimensional model

The three-dimensional model (Figure 1) was developed to allow the analyses of transient and mechanical heat transfer, both developed in the same model (joint analysis). The dynamic-explicit solver was used to reduce computational effort and convergence problems [7]. The finite element was the C3D8 (hexahedron).

The fire temperature was applied evenly around all the specimen, considering the initial temperature equal to 20 °C, with the hot gases heating its exposed face by convection and radiation, with a convection coefficient equal to 25 W/m^{2}ºC, and considering the ISO-834 standard fire curve [9]. In the tube-concrete interface a mechanical contact was defined in the normal direction, allowing the separation between the tube and the concrete. Another mechanical contact was defined in the tangential direction, with a coefficient of friction equal to 0.3, as [1].

The concrete behavior was defined by the CDP model (Concrete Damage Plasticity), with the parameter values indicated in the literature [8]. It is worth highlight that, regarding the three-dimensional model (Figure 1), a pinned support was considered at the base of the column, and at its top considered as a weightless adiabatic rigid block.

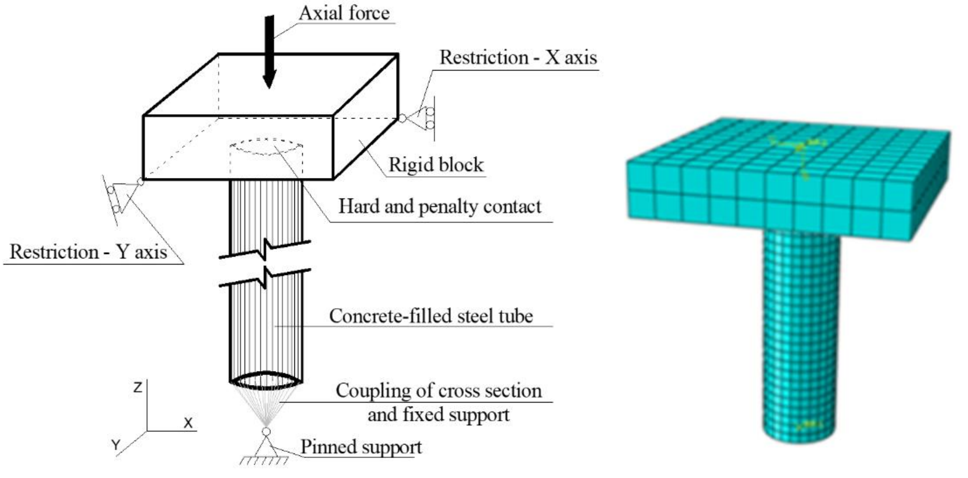

Figure 1. Boundary conditions and connections considered in the model.

2.2. Two-dimensional model

A two-dimensional model was used for the transient heat transfer analyses, resolved with the static-implicit solver, adopting the finite element D2D3 (tetrahedral) for circular section columns and the DC2D4 (quadrilateral) element for the square-section columns (Figure 2).

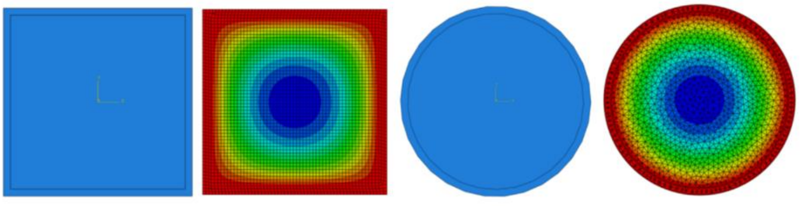

Figure 2. Two-dimensional models with tetrahedral and quadrilateral mesh.

The thermal load was applied directly to the exposed face, according to the standard fire curve, considering a perfect thermal contact in the tube-concrete interface. The intent to building this two-dimensional model was to evaluate the emissivity values of the exposed face, in addition to complementing the studies on the concrete moisture content.

2.3. Materials properties at high temperature

The thermal properties of steel and concrete considered in the numerical models were from EN 1992-1-2 [5], EN 1993-1-2 [6], EN 1994-1-2 [3] and ABNT NBR 14323: 2013 [4], aiming to compare the results considering the properties specification from European or Brazilian standards.

With respect to the steel elastic modulus at high temperature $\left(E_{a,}\right)$ its value is determined by Equation 1, whose respective reduction factors are indicated in EN 1993-1-2 [6], EN1994-1-2 [3] and ABNT NBR 14323 [4], as Table 1.

$$E_{a,} = kE_{a,\theta} \cdot E_a \quad (1)$$

where: $KE_{a,\theta}$ is the reduction factor of the steel elastic modulus at high temperature; E_a is the steel elastic modulus at room temperature equal to 210,000 MPa.

Table 1. Steel yield strength and elastic modulus reduction factor.

Steel temperature θ_a (°C)	Steel yielding strength reduction factor ($Ky_{a,\theta}$)	Steel elastic modulus reduction factor ($KE_{a,\theta}$)
	*1 / 2 / 3	*1 / /2 / 3
20	1.000	1.000
100	1.000	1.000
200	1.000	0.900
300	1.000	0.800
400	1.000	0.700
500	0.780	0.600
600	0.470	0.310
700	0.230	0.130
800	0.110	0.090
900	0.060	0.0675
1000	0.040	0.045
1100	0.020	0.0225
1200	0.000	0.000

* 1- EN 1994-1-2 [3]; 2- ABNT NBR14323:2013 [4] (steel not subject to local buckling); 3-EN 1993-1-2 [6]

The steel constitutive law specified in EN1994-1-2 [3] and ABNT NBR 14323:2013 [4] are the same as EN1993-1-2 [6].

The concrete force is reduced with the temperature increase as shown in Figure 3.

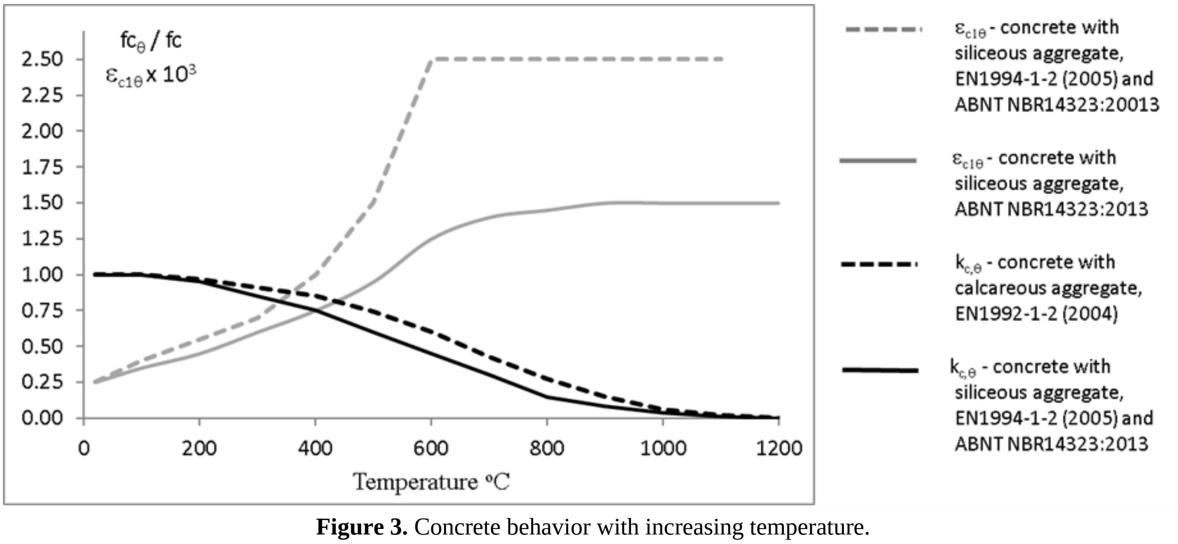

Figure 3. Concrete behavior with increasing temperature.

Equation 2 represents the concrete strength to compression at high temperature, presented in EN 1994-1-1 [3] and ABNT NBR 14323:2013 [4].

$$\sigma_{c,\theta} = \frac{3\varepsilon_{c,\theta} \cdot f_{c,\theta}}{\varepsilon_{c1,\theta}\left[2+\left(\frac{\varepsilon_{c,\theta}}{\varepsilon_{c1,\theta}}\right)^3\right]} \text{ with, } f_{c,\theta} = K_{c,\theta} \cdot f_c \tag{2}$$

In Equation 2, $K_{c,\theta}$ is a factor of concrete strength reduction (Table 2); f_c is the concrete strength to compression at room temperature; $f_{c,\theta}$ is the concrete strength to high temperature (θ) expressed in MPa; $\varepsilon_{c,\theta}$, is the concrete specific strain to high temperature (θ); $\varepsilon_{c1,\theta}$ is the specific strain corresponding to the stress of the concrete maximum strength at high temperature (θ). It is worth mentioning that the term $\varepsilon_{c1,\theta}$ is so called in EN1992-1-2 [5], and in EN1994-1-2 [3] the term is called $\varepsilon_{cu,\theta}$.

The codes EN1994-1-2 [3] and EN1992-1-2 [5] indicate Equation 3 to determine the concrete strength to traction at high temperature.

$$fck,t(\theta) = kc,t(\theta) \cdot fck,t \tag{3}$$

Where: $Kt,_{\theta}$ = 1.0 for 20 °C ≤θ≤ 100 °C; $Kt_{\theta}1-1(\theta-100)/500$ for 100 °C ≤θ≤ 600 °C; Kt_{θ} = 0 for θ> 600 °C.

The reduction factor of the elastic modulus of concrete at high temperature can be determined by Equation 4, based on the constitutive relations presented, for example, in EN1992-1-2 [5].

$$\mathrm{K}_{\mathrm{Ec},\theta} = \mathrm{Kc}_{,\theta} \cdot \frac{\varepsilon_{\mathrm{c1}}}{\varepsilon_{\mathrm{c1},\theta}} \tag{4}$$

Where: ε_{C1}, corresponding specific strain of concrete at room temperature.

Figure 4 shows the factors of reduction determined from the strain corresponding to the stress of the concrete maximum strength to compression, according to Eurocode and to Brazilian standards.

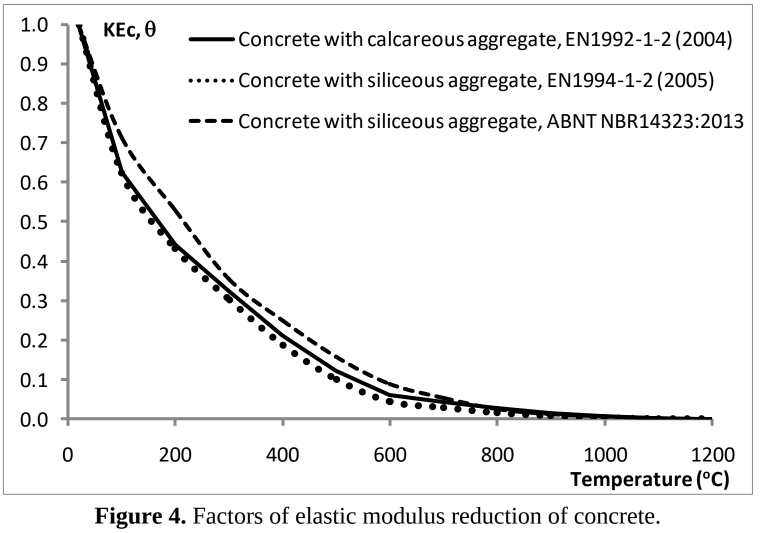

Figure 4. Factors of elastic modulus reduction of concrete.

The Poisson coefficient of steel and concrete is indicated respective as equal to 0.3 and 0.2, regardless of temperature.

4. PARAMETERS AND CONCEPTS FOR NUMERICAL MODELING PURPOSES

4.1. Moisture content in concrete

The moisture content in some materials causes changes in the specific heat; for example, in concrete, there is a considerable increase in specific heat for temperatures about 100 °C. This increase is the result of the latent heat of evaporation of the moisture incorporated into the pores, which is added to the specific heat of the dry material. After evaporation of all the water contained in the material, the specific heat suddenly decreases to remain at the specific heat levels of the dry material. The peak value of the specific heat depends on the moisture content and on the time needed for the water to vaporize [13].

The effect of the moisture content in the concrete is usually considered in the numerical models by values of the specific heat obtained by Equation 7 or 8, considering Cc, peak as a peak value, which occurs between 100 °C and 115 °C, decreasing linearly between 115 °C and 200 °C. From this temperature, the concrete specific heat again follows the values obtained by Equations 5 or 6. The peak value is indicated with values equal to 2020 and 5600 J/kgK for 3% and 10% moisture, respectively, and linear interpolation is valid for intermediate moisture contents.

Equation 7, specified in EN1992-1-2 [5], allows us to determine the specific heat of dry concrete with 0% moisture content (J/kgK).

$$
\begin{aligned}
&C_c = 900 \quad 20\ °C \le \theta c \le 100\ °C \\
&C_c = 900 + (\theta c - 100) \quad 100\ °C < \theta c \le 200\ °C \\
&C_c = 1000 + (\theta c - 200)/2 \quad 200\ °C < \theta c \le 400\ °C \\
&C_c = 1100 \quad 400\ °C < \theta c \le 1200\ °C
\end{aligned} \tag{5}
$$

On the other hand, EN 1994-1-2 [3] indicates Equation 8.

$$C_c(\theta) = 890 + 56.2\left(\frac{\theta_c}{100}\right) - 3.4(\theta_c/100)^2 \tag{6}$$

In the absence of experimental characterization, the considered moisture content is limited to 4% of the concrete mass. However, tubular columns filled with concrete, with calcareous aggregate, may contain higher levels, close to 10% [1].

The area of the concrete section also influences the development of the temperature field, as the larger the concrete area is, the lower the heating speed of the whole section. The decrease in the heating speed occurs due to the greater amount of the material with lower thermal conductivity and due to the amount of vaporized water contained in the concrete layers [2], [13].

It was also observed that the water flow inside the cross section in tubular columns was altered in the presence of longitudinal reinforcement. With the movement of water in the cross section of the column when heated, part of this water is housed around the bars, and therefore, when there are a significant number of steel bars, there is a disturbance in the temperature field [2], [13].

The presence of water in the concrete pores also causes an increase in the thermal conductivity of the material, since the conductivity of water is greater than that of air, which normally occupies the pores in the absence of water, and due to the heating and evaporation of water, since the vapor is diffused through the pore network, transporting heat [19].

The phenomenon called spalling is related to the moisture content in concrete with the increase in temperature. The water contained in the concrete pores vaporizes between 100 and 140 °C; the temperature above the boiling point is reached depending on the pressure of the water inside the pore. Spalling occurs when the water contained in the concrete is not released, causing an excess of internal pressure [1]; however, it was impossible to visually observe this effect in the columns studied here due to the steel tube involving the concrete.

4.2. Emissivity

The definition of the resulting emissivity is fundamental to achieve results with good approximation to the experimental trials. Assuming the surface temperature of the steel element, without fire protection, to be equal to that of the gases of the burning environment $\left(\theta_a = \theta_g\right)$ results in a response that is normally conservative [20]. It is possible to obtain a more realistic scenario when heat transfer from the environment to the surface of the element occurs through convection and radiation mechanisms.The emissivity of a body, which is the ability to transmit and absorb heat, varies in the interval between 0 and 1 in relation to the capacity of the black body, which absorbs and consequently radiates the heat flow according to the rate defined by Stefan-Boltzmann. There are several bibliographic references with values for the emissivity of steel- and concrete-exposed faces and for the emissivity of fire, as Table 2 compiles.

Table 2. Emissivity of steel, concrete and fire.

Reference	Recommended emissivity values			
	Fire ($e_{m,f}$)	Steel ($e_{m,s}$)	Concrete ($e_{m,c}$)	
EN1991-1-2 [10]	1	-	-	
EN1992-1-2 [5]	1	-	0.7	
EN1993-1-2 [6]	1	0.7	-	
EN1994-1-2 [3]	1	0.7	0.7	
Lie and Irwin [11]	0.75	0.7	-	
Irwin and Lie [12]	-	0.8	-	
Rush [13]	0.75	0.7	-	
Drysdale [14]	1	0.2	-	
Chaoming et al. [15]	-	0.8	-	Temperature
Paloposki and Liedquist [16]	-	0.2	-	20 to 385 °C
		0.65		550 to 1200 °C
NIST [17]	1	0.32	-	20 °C
		0.32	-	200 °C
		0.85	-	400 °C
		0.95	-	800 °C
		0.95	-	1200 °C
Sadiq et al. [18]	-	0.28	-	$\theta < 380$ °C
		$0.003040\theta - 0.888$		$380 \leq \theta < 520$ °C
		0.69		$\theta \geq 520$ °C

The literature presents different values adopted for the emissivity of steel- and concrete-exposed faces, but the emissivity of fire is usually specified to be 1.00. The values indicated for the emissivity of steel are usually conservative for initial temperatures and underestimated for higher temperatures, and it is worth highlighting that the value of 1 for the emissivity of the fire is described as overrated for oven testing and realistic for fire situations.

As described in Paloposki and Liedquist [16], between 150 and 385 °C, the steel emissivity is about 0.2, increasing sharply to 0.65 until 550 °C, and from this temperature, it was observed that the emissivity remains constant.

Table 3 shows the coefficients of emissivity at the steel and concrete interface extracted from the literature.

Table 3. Emissivity at the steel-concrete interface.

Reference	Emissivity	
1	Concrete ($\varepsilon_{m,c}$)	Steel ($\varepsilon_{m,s}$)
Han and Gillie [21]	0.92	0.23
O'Loughlin et al.[22]	0.97	0.32

5. PARAMETRIC STUDY

5.1. Parameters and analysis development

The three-dimensional model was used to develop thermal and thermal-mechanical analyses; on the other hand, the two-dimensional model was used only for complementary analysis of heat transfer, considering a more detailed evaluation regarding the variation of the moisture content of the concrete and the emissivity of the exposed face of the steel.

5.1.1. Three-dimensional model

Table 4 shows the specimens used to study the sensitivity of the three-dimensional numerical model.

Table 4. List of three-dimensional specimens.

Reference	Section	L or D	t	Fc	Fya	l
1	Cross-section	(mm)	(mm)	(MPa)	(MPa)	(mm)
1- PQ-100-5	Square	100	5	30	350	500
2- PQ-140-5	Square	140	5	30	350	500
3- PQ-200-5	Square	200	5	30	350	500
4- PQ-250-8	Square	250	8	30	350	500
5- PC-114-5	Circular	114.3	5	30	350	500
6- PC-150-5	Circular	150	5	30	350	500
7- PC-195-5	Circular	195	5	30	350	500
8- PC-250-8	Circular	250	8	30	350	500

The variations of the properties in the model were named M1 to M6 and do correspond to the alternation of the concrete expansion values according to the type of aggregate, of the thermal expansion of steel, to the amount of water and to the density of the concrete, as shown in Table 5.

Table 5. Parameters used in the thermal-mechanical numerical model.

<table>
<tr><th></th><th>Thermal expansion of concrete</th><th>Type of aggregate</th><th>Thermal expansion of steel</th><th>Concrete moisture content</th><th>Concrete density</th></tr>
<tr><td>1</td><td>1</td><td>1</td><td>1</td><td>1</td><td>1</td></tr>
<tr><td>M1</td><td>EN1994-1-2 [3]: 20 °C< $\theta c \leq$ 805 °C: $\Delta l/l,c = -1.2 \cdot 10^{-4} + 6 \cdot 10^{-6} \cdot \theta c + 1.4 \cdot 10^{-11} \cdot \theta c^3$ 805 °C< $\theta c \leq$ 1200 °C: $\Delta l/l,c = 12 \cdot 10^{-3}$</td><td>Calcareous</td><td rowspan="5">EN1994-1-2 [3]: 20 °C < $\theta a \leq$ 750 °C: $\Delta l/l,a = -2.416 \cdot 10^{-4} + 1.2 \cdot 10^{-5} \cdot \theta a + 0.4 \cdot 10^{-8} \cdot \theta a^2$ 750 °C < $\theta a \leq$ 860 °C: $\Delta l/l,a = 11 \cdot 10^{-3}$ 860 °C < $\theta a \leq$ 1200 °C: $\Delta l/l,a = -6.2 \cdot 10^{-3} + 2 \cdot 10^{-5} \cdot \theta a$</td><td rowspan="2">3%</td><td rowspan="3">EN1994-1-2 [3]: 20 °C $\leq \theta c \leq$ 115 °C: $\rho(\theta c) = \rho(20\ °C)$ = 2300 kg/m^3 115 °C < $\theta c \leq$ 200 °C: $\rho(\theta c)=\rho(20\ °C) \cdot (1-0.02 \cdot (\theta c-115)/85)$ 200 °C < $\theta c \leq$ 400 °C: $\rho(\theta c) = \rho(20\ °C) \cdot (0.98-0.03 \cdot (\theta c-200)/200)$ 400 °C < $\theta c \leq$ 1200 °C: $\rho(\theta c) = \rho(20\ °C) \cdot (0.95-0.07(\theta c-400)/800)$</td></tr>
<tr><td>M2</td><td rowspan="4">EN1994-1-2 [3]: 20 °C< $\theta c \leq$ 700 °C: $\Delta l/l,c = -1.8 \cdot 10^{-4} + 9 \cdot 10^{-6} \cdot \theta c + 2.3 \cdot 10^{-11} \cdot \theta c^3$ 700 °C< $\theta c \leq$ 1200 °C: $\Delta l/l,c = 14 \cdot 10^{-3}$</td><td rowspan="5">Siliceous</td></tr>
<tr><td>M3</td><td>10%</td></tr>
<tr><td>M4</td><td rowspan="3">3%</td><td>2300 kg/m^3</td></tr>
<tr><td>M5</td><td>2400 kg/m^3</td></tr>
<tr><td>M6</td><td>simplified: $\Delta l/l,c = 6 \cdot 10^{-6}$</td><td>simplified: $\Delta l/l,a = 12 \cdot 10^{-6}$</td><td>same density of the M1, M2 and M3 models</td></tr>
</table>

The other properties of steel and concrete, not explained in Table 5, remained according to equations presented in EN1992-1-2 [5] and EN1993-1-2 [6].

The fire resistance times were determined according to EN1363-1 [23], with the axial force applied in the models corresponding to 30% of the plastic resistance of the cross section at room temperature.

Figure 5 shows the monitoring points of the temperatures in the specimens.

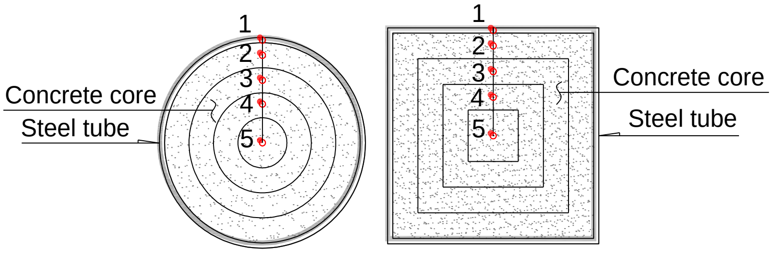

Figure 5. Monitoring points of the temperatures in the cross section.

5.1.2. Two-dimensional model

Using the two-dimensional model, complementary studies were conducted with different values adopted for the specific heat of concrete, according to its moisture content. The models denominated with combinations 1 and 2 refer to Equations 5 and 6, which are used to determine the values of the specific heat of concrete. The influence of moisture in the temperature field was verified considering the specimens indicated in Table 6, with moisture contents alternating between 0, 1.5, 3, 5, 7.5 and 10%.

Table 6. Specimens for modeling with heat transfer analysis.

Reference	Cross section	L or D (mm)	t (mm)	fc (MPa)	Fya (MPa)	l (mm)
1- PC-168-6	Circular	168.3	6.4	-	-	-
2- PC-168-10	Circular	168.3	10	-	-	-
3- PC-300-10	Circular	300	10	-	-	-

The temperatures found with the two-dimensional model were recorded along the track indicated as an example in Figure 6 for specimen 1.

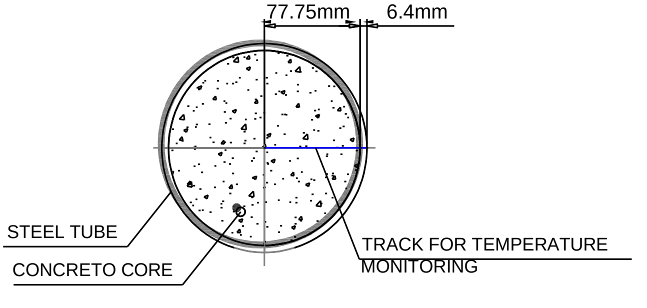

Figure 6. Track for temperature monitoring in the cross section.

The influence of the emissivity adopted for the exposed face in the model was verified by comparing the temperature field, considering the emissivity values of the exposed face as 0.7, 0.8 and 1. In the model, combination two was implemented with dry concrete, a transfer rate by convection of 25 W/m^2 °C, exclusive thermal analysis, and perfect thermal contact in the tube–concrete interface.

5.2. Results and discussions

5.2.1. Three-dimensional model

Table 7 shows, for four specimens, the temperatures in the cross section, along with the fire resistance times, according to the responses of numerical modeling with the alternation of the parameters and properties indicated in Table 5.

Table 7. Response of the parametric analysis of the numerical models.

Specimen (Table 5)	Model M	Fire resistance time (minutes)	Temperature (°C)				
1	1	1	1				
1	1	**1**	**1**	**2**	**3**	**4**	**5**
3-PQ-200-5	1	59.0	905.2	629.8	357.1	219.8	140.9
1	2	50.2	835.5	516.9	243.1	119.6	75.1
1	3	57.0	844.4	471.1	154.3	61.5	43.1
1	4	51.4	833.6	511.5	239.4	118.2	74.7
1	5	52.7	831.1	502.9	229.7	111.3	70.7
1	6	60.9	893.8	612.3	337.8	199.7	123.3
7-PC-195-5	1	45.9	815.1	505.8	250.2	124.4	73.8
1	2	43.2	785.6	458.0	209.7	98.7	61.3
1	3	47.5	804.5	423.3	116.6	55.4	39.4
1	4	43.4	777.0	442.4	198.2	93.7	58.8
1	5	45.9	787.2	451.5	204.1	96.2	60.1
1	6	51.7	852.9	570.0	309.7	174.9	97.2
2-PQ-140-5	1	43.4	815.1	567.7	374.4	254.1	198.0
1	2	36.7	791.3	527.4	332.7	210.4	151.8
1	3	43.7	784.1	453.8	214.9	89.2	62.7
1	4	38.4	789.0	521.1	327.0	206.0	149.0
1	5	38.9	785.9	511.1	315.0	193.2	137.1
1	6	40.7	791.5	529.4	335.1	212.4	153.4
5-PC-114-5	1	31.2	736.3	541.6	344.9	243.2	186.0
1	2	30.0	726.9	524.8	328.1	225.7	164.8
1	3	33.4	725.7	471.4	216.9	89.1	66.3
1	4	30.0	725.0	518.6	322.6	221.5	161.4
1	5	30.0	721.9	508.7	310.5	208.0	146.6
1	6	32.0	753.6	571.5	375.6	275.8	225.4

In this study, it was observed that Model M2, with 3% moisture and concrete density according to the equation described in EN1994-1-2 [3] and EN1992-1-2 [5], presented shorter fire resistance times than those with concrete densities equal to 2300 kg/m^3. For concrete densities equal to 2300 kg/m^3, the fire resistance times increased by up to 10%; the model with 10% moisture content (M3) presented a fire resistance time 16% higher than that with 3% (M2); and the models with constant expansion coefficients showed 18% higher fire resistance times.

Figure 7 graphically shows the results referring to the fire resistance times, as shown in Table 7 for numerical models resolved with the properties and parameters indicated in Table 5 (M1 to M6).

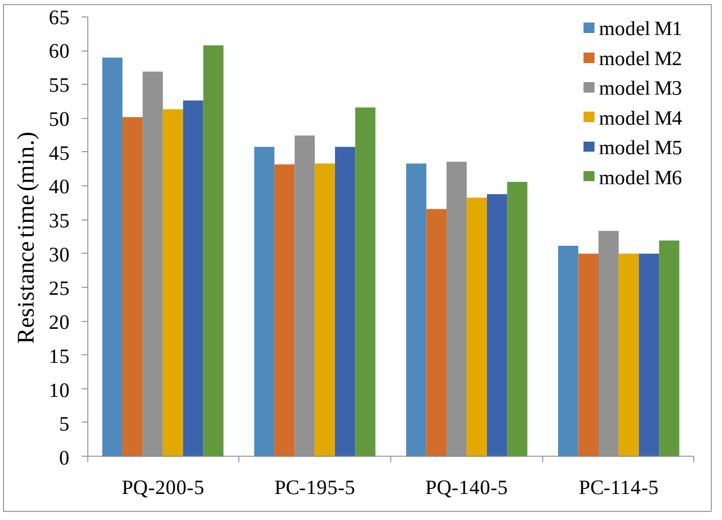

Figure 7. Fire resistance time with alternation of properties in the model.

The thermal properties indicated in ABNT NBR 14323:2013 [4] and EN 1994–1-2 [3] are the same, and the formulations for defining the mechanical behavior are also similar, except for the last deformations and, consequently, the elastic modulus of the concrete.

Experimental studies show that the values of the elastic modulus of concrete determined with the stress–strain diagram at high temperature according to EN19944-1-2 [3] are conservative for concretes of normal strength, and they verified the expressive influence of coarse aggregate types [24]. This suggests that the values determined with the last deformations of concrete at high temperature presented in the Brazilian code are more realistic.

Figure 8 shows that there are small differences in column behavior considering the ultimate deformations and the elastic modulus of concrete, according to EN1994-1-2 [3] and ABNT NBR 14323:2013 [4]. For this analysis, a three-dimensional numerical model was used.

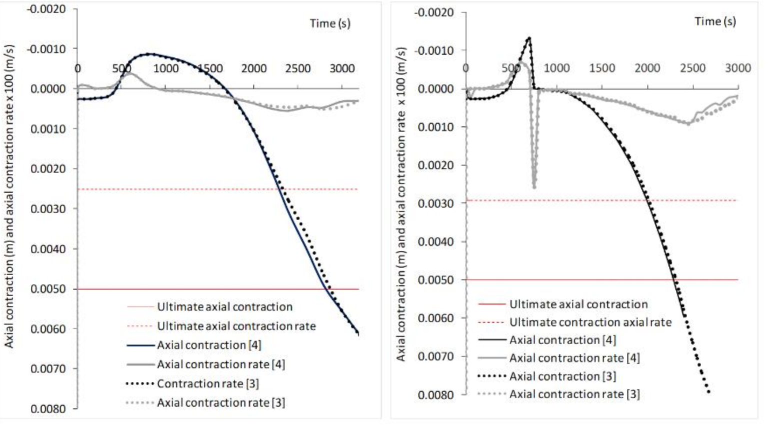

(a) Specimen 3 (b) Specimen 7

Figure 8. The fire resistance time considering the M2 model is indicated in Table 5.

5.2.2. Two-dimensional model

Figure 9 shows the temperatures monitored in the model elaborated with different moisture contents of the concrete and with prefixed times of exposure to fire for specimen 1 (Table 6).

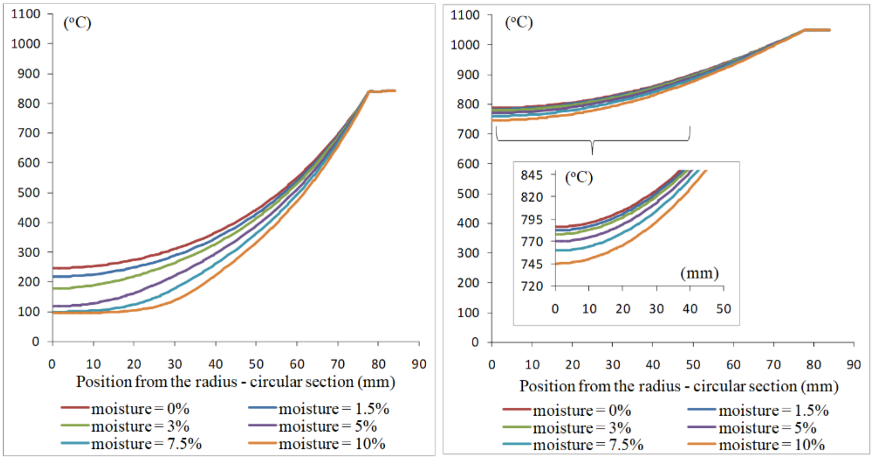

(a) exposure to fire = 30 min (b) exposure to fire = 120 min

Figure 9. Temperature according to the moisture content of the concrete.

Figure 10 shows the temperatures in the center of the concrete and on the inner face of the steel tube.

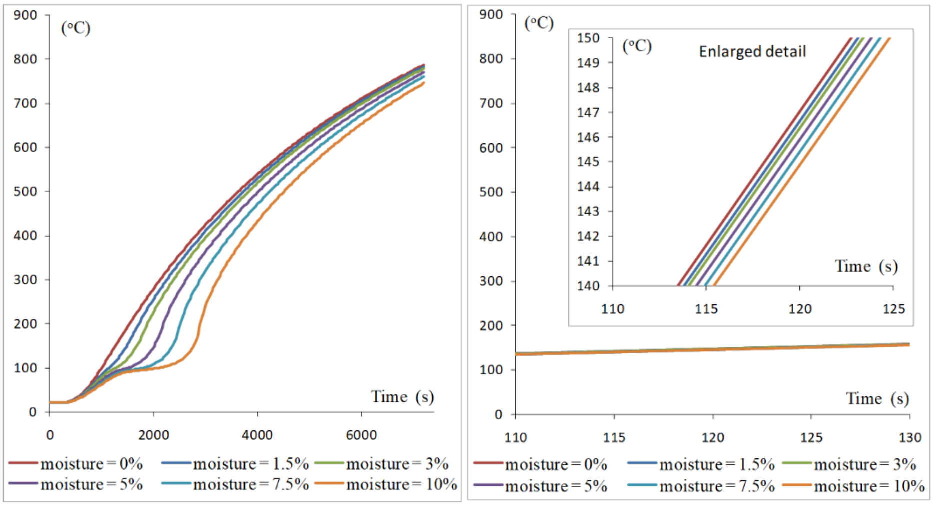

(a) Temperature at the concrete core center (b)Temperature at the internal face of the tube

Figure 10. Evolution of temperature according to the concrete moisture content.

For the evolution of the temperature of sample one, there is a difference in the center of the concrete core between models with moisture contents of 0% and 10% of 150 °C for 30 minutes of exposure to fire and 50 °C for 120 minutes of exposure to fire. For specimen 3 (Table 6), the temperature difference reaches 190 °C for 30 minutes of exposure to fire and 120 °C for 50 minutes. In the steel tube, the change in the moisture content of concrete results in a small variation in its temperature.

Figure 11 shows the temperatures along the monitoring range, comparing the model with combinations 1 and 2 of sample 1 (Table 6), according to the time of exposure to fire (FET).

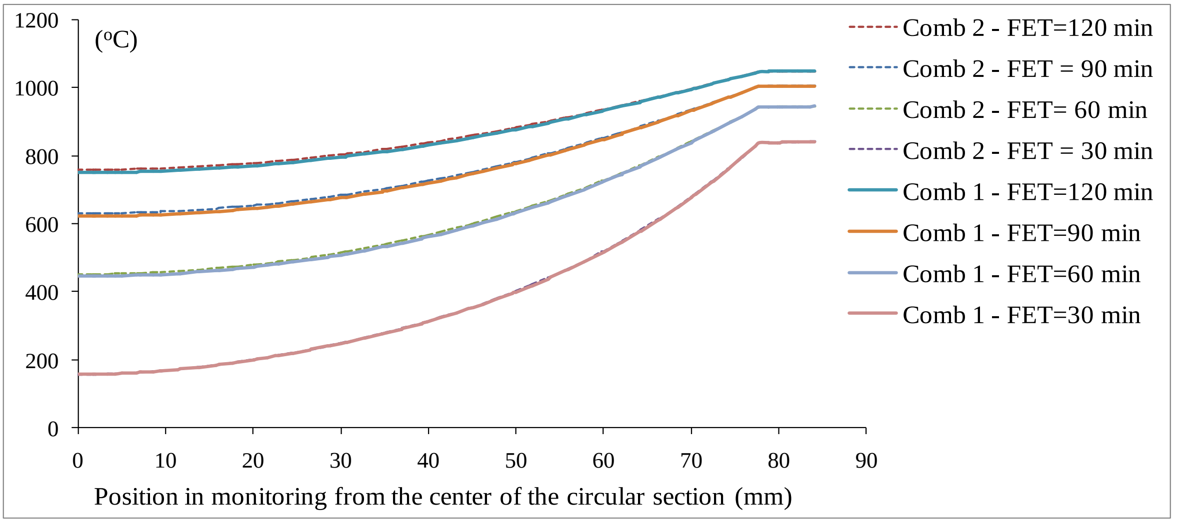

Figure 11. Temperatures along the cross section for combinations 1 and 2.

According to the parametric study, it was found that the responses of the model are coincident; with the combination one or two, but for longer exposure times the combination two presented slightly higher temperatures, but still close.

Figure 12 shows the temperatures over time, on the outer face of the tube and in the center of the concrete core for specimen 1 (Table 6).

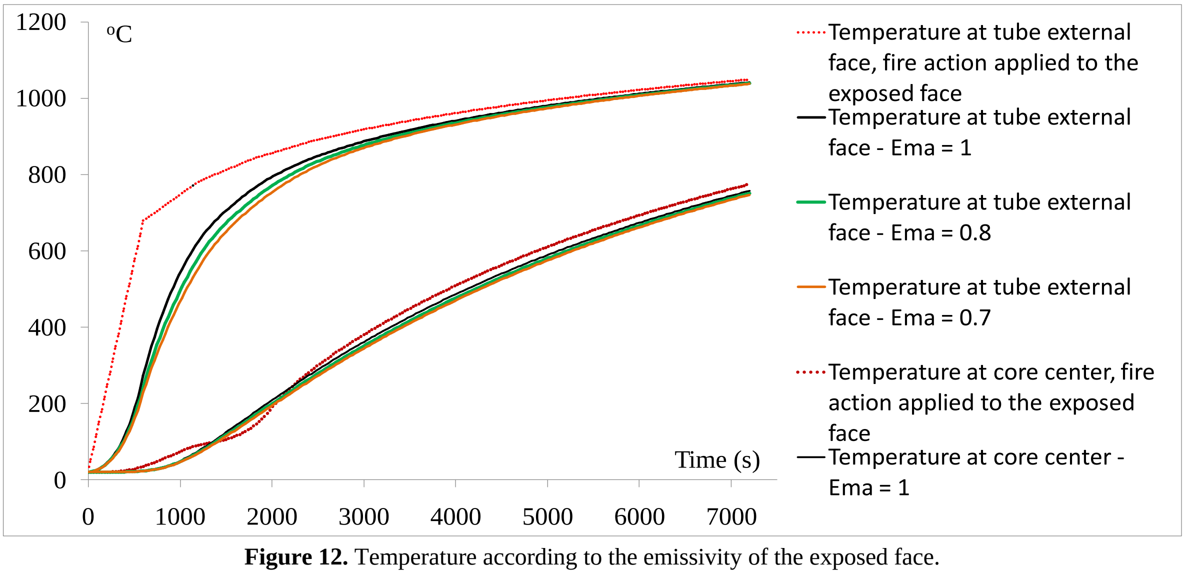

Figure 12. Temperature according to the emissivity of the exposed face.

6. CONCLUSIONS

It was verified that the numerical model was sensitive to the values adopted for the parameters and properties of the materials, and the choice of constant values with a higher degree of simplification should be made judiciously. In this study, it was possible to demonstrate which simplifications most influence the response of the numerical model. Such simplifications seek to facilitate practical applications in numerical and analytical models, but they can reduce the quality of the results. In this sense, some considerations have been presented regarding the study carried out with alternation of modeling parameters and of the properties of steel and concrete.

The equations indicated in the codes EN1992-1-2 [5], EN1993-1-2 [6] and ABNT NBR 14323:2013 [4] should be used preferably without simplifications for determining the values of steel and concrete properties to be adopted in numerical models. The exception is the determination of concrete specific heat, which should favor the equation from EN1994-1-2 [3], which is adjusted for columns composed of tubes filled with concrete. The constant values presented in the Eurocode for the density of concrete and for the coefficients of thermal expansion of steel and concrete should be avoided, since their responses were very divergent from those obtained through the numerical model.

On the other hand, regarding the determination of the mechanical properties of concrete, minimal differences were found between the results of the numerical models according to the Eurocode and the Brazilian code. That is, the results are coincident.

The moisture content considered in the concrete significantly affects the temperature field, especially for the very concrete and for cross sections with greater areas. For the steel tube, the alteration is more discrete, but the decrease in temperature is still perceivable as the moisture content in concrete is increased.

Thus, these results indicate the need for greater knowledge of the concrete moisture content to be adopted in each tubular mixed column. The process used to consider the effect of moisture in the temperature field was also verified to be too simplified. According to bibliographic references, the value of 4% moisture content may be very conservative in some cases but is a reasonable limit when one does not accurately know the moisture effectively contained in concrete; however, for concrete with calcareous aggregate, this limit can be very conservative, evidencing the need for a greater number of experimental tests to generalize these limits.

In numerical models, when considering the heating of the element by the radiation mechanism with the resulting value of the emissivity of the fire and exposed face with alternating values of 0.7 and 0.8, as temperatures undergo small variations. That is, from differences above 15% in the resulting emissivity, the time-temperature curve begins to diverge, presenting a very distinct behavior trend.

7. ACKNOWLEDGEMENTS

The authors thank the support from the University of Campinas and from Catholic University of Santos.

8. REFERENCES

[1] A. Espinòs Capilla, “Numerical analysis of the fire resistance of circular and elliptical slender concrete filled tubular columns,” Ph.D. dissertation, Univ. Politèc. València, Spain, 2012.

[2] C. Renaud, *Report Reference INSI – 04/75b – CR/PB.* France: CTICM, 2004.

[3] European Commitee for Standardization, *Eurocode 4: Design of Composite Steel and Concrete Structures – Part 1.2: Structural Fire Design*, EN 1994-1-2, 2005.

[4] Associação Brasileira de Normas Técnicas, *Fire Design of Steel Structures and Composite Steel and Concrete Structures*, NBR 14323, 2013.

[5] European Commitee for Standardization, *Eurocode 2: Design of Concrete Structures – Part 1.2: General Rules – Structural Fire Design*, EN 1992-1-2, 2004.

[6] European Commitee for Standardization, *Eurocode 3: Design of Steel Structures – Part 1.2: General Rules – Structural Fire Design*, EN 1993-1-2, 2005.

[7] M. F. Rodrigues, “Numerical analysis of short columns composed of steel pipes filled with concrete in fire situation,” M.S. thesis, Univ. Campinas, Campinas, 2017.

[8] Dassault Systèmes. *ABAQUS/CAE User's Guide*. Providence, RI, 2012.

[9] International Organization for Standardization, *Fire-Resistance Tests – Elements of Building Construct: General Requirements*, ISO 834-1:1999, 1999.

[10] European Commitee for Standardization, *Eurocode 1: Actions on Structures – Part 1.2: General Actions - Actions on Structures Exposed to Fire*, EN 1991-1-2, 2002.

[11] T. T. Lie and R. J. Irwin, "Fire resistance of retangular steel columns filled with bar-reforced concrete," *J. Struct. Eng.*, vol. 121, pp. 797–805, 1995.

[12] R. J. Irwin and T. T. Lie, *Fire Resistance of Rectangular Hollow Steel Sections Filled with Bar-Reinforced Concrete* (Internal Report 631). Ottawa, Canada: Natl. Res. Counc. Canada, 1992.

[13] D. Rush, “Fire performance of unprotected and protected concrete filled steel hollow structural sections,” Ph.D. dissertation, Univ. Edinburgh, Edinburgh, 2013.

[14] D. Drysdale, *An Introduction to Fire Dynamics*, 3rd ed. Wiley, 2011, 551 p.

[15] Y. Chaoming, Z. Huang, W. Burgess, and R. J. Plank, “3D modelling of bi-steel structures subject to fire,” in *Proc. Struct. Fire Workshop*, 2006.

[16] T. Paloposki and L. Liedquist, *Steel Emissivity at High Temperatures: Research Notes*. Tampere, Finland: Tech. Res. Cent. Finland, 2005.

[17] D. P. Bentz, L. M. Hanssen, and B. Wilthan, *Thermal Performance of Fire Resistive Materials III. Fire Test on a Bare Steel Column* (NIST Interagency/Internal Report (NISTIR) 7576). Massachusetts, USA: National Institute of Standards and Technology, 2009, pp. 13.

[18] H. Sadiq, M. B. Wong, J. Tashan, R. Al-Mahaidi, and X. L. Zhao, "Determination of steel emissivity for the temperature prediction of structural steel members in fire," *J. Mater. Civ. Eng.*, vol. 25, no. 2, pp. 167–173, 2013.

[19] Y. Mingzhi, S. Xiaofeng, P. Xiaofeng, and F. Zhaohong, "Influence of moisture content on measurement accuracy of porous media thermal conductivity," *Heat Transfer-Asian Res.*, vol. 38, no. 8, pp. 492–500, 2009.

[20] V. K. R. Kodur, "Performance-based fire resistance design of concrete-filled steel columns," *J. Construct. Steel Res.*, vol. 51, no. 1, pp. 21–36, 1999.

[21] Z. G. Han and M. Gillie, “Temperature modeling for concrete-filled steel tube’s cross section in fire,” in *Proc. Int. Conf. Mech. Civ. Eng.*, 2014.

[22] E. O’Loughlin, D. Rush, and L. Bisby, “Concrete-filled structural hollow sections in fire: accounting for heat transfer across a gap,” in *Proc. 15th Int. Conf. Exp. Mech.*, Porto, Portugal, 2012, pp. 1-17.

[23] European Commitee for Standardization, *Fire Resistance Tests - Part 1: General Requirements*, EN 1363-1, 1999.

[24] I. Hager and K. Krzemien, “An overview of concrete modulus of elasticity evolution with temperature and comments to European code provisions,” in *Proc. Int. Fire Saf. Symp*., Coimbra, Portugal, 2015.

Author contributions: FMR: conceptualization, development, methodology, modeling, writing; ALMJ: conceptualization, methodological analysis, supervision and JMN: conceptualization, methodological analysis, supervision.

Editors: Rebecca Gravina, Guilherme Aris Parsekian.